

**Study of Particle Physics Models with Implication
to Neutrino Mass and Dark Matter
Phenomenology in Light of Recent Data**

Nirakar Sahoo

A Thesis Submitted to
Indian Institute of Technology Hyderabad
In Partial Fulfillment of the Requirements for
The Degree of Doctor of Philosophy



Department of Physics

August 2017

Declaration

I declare that this written submission represents my ideas in my own words, and where ideas or words of others have been included, I have adequately cited and referenced the original sources. I also declare that I have adhered to all principles of academic honesty and integrity and have not misrepresented or fabricated or falsified any idea/data/fact/source in my submission. I understand that any violation of the above will be a cause for disciplinary action by the Institute and can also evoke penal action from the sources that have thus not been properly cited, or from whom proper permission has not been taken when needed.

Nirakar Sahoo

(Signature)

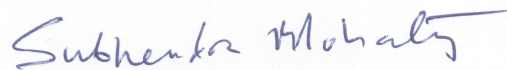
(Nirakar Sahoo)

PH13P1005

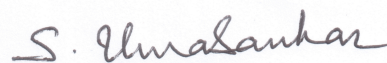
(Roll No.)

Approval Sheet

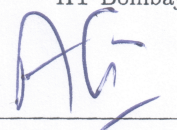
This Thesis entitled Study of Particle Physics Models with Implication to Neutrino Mass and Dark Matter Phenomenology in Light of Recent Data by Nirakar Sahoo is approved for the degree of Doctor of Philosophy from IIT Hyderabad



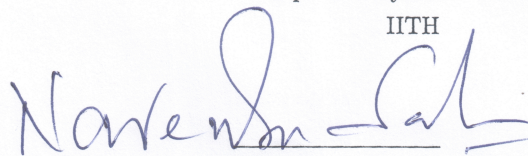
(Prof. Subhendra Mohanty) External Examiner
Theory division
PRL Ahmedabad



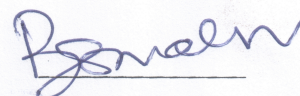
(Prof. S. Umasankar) External Examiner
Dept. of Physics
IIT Bombay



(Prof. Anjan K. Giri) Internal Examiner
Dept. of Physics
IITH



(Dr. Narendra Sahu) Adviser
Dept. of Physics
IITH



(Dr. Bhabani Shankar Mallik) Chairman
Dept. of Chemistry
IITH

Acknowledgements

My warmest thanks to my supervisor Dr. Narendra Sahu, for his guidance, encouragement and support throughout the years. Without his help it would be very difficult for me to work in this particular field of research. He created the enthusiasm in my mind towards free thoughts and research. I would like to express my gratitude to my collaborators Dr. Sudhanwa Patra, Dr. Subhaditya Bhattacharya and Dr. Soumya Rao for their collaboration and fruitful discussions. I am very grateful to Dr. Subhaditya Bhattacharya from whom I learnt software tools like calchep and micrOMEGAs.

My sincere thanks to our HOD Prof. Anjan Giri for his invaluable suggestions. I would also like to thank our HEP group faculties, Dr. P Bandyopadhyay, Dr. S Hundi, Dr. A Tripathy, Dr. S Roy, Dr. S Desai for useful discussions in Physics.

I would like to appreciate my HEP juniors here, Nimmala, Subhasmita, Itishree and Manas for their moral support. I enjoyed a lot while discussing physics with them. My special thanksgivings to my Odia family members, Sonali Apa, Partha, Bunu Bhai, Ponoop, Dwipak and Anjan for making my life easier during the stay in IITH. My Ph.D. career heartily values the dedicated support of my friend Debadeepti for being with me in each and every ups and downs of my life. My profound thankfulness to my friends Jogesh, Suchi, Bisu, Soumendra, Prasant, Sukant, Nihar, Dhani, Anil, Dilip, Alekha Bhai, Shiba Bhai for giving me continuous moral support during these years.

Finally, I would like to praise my family members for their support, without which I would not have reached here. No word can express the sacrifice, love and encouragement of my father. My respectful credits are for Mamee nana, Bapi Bhai, Sami nana, Raju Bhai, Puspa nana and my grandmother for never letting me alone during my struggling days. I am also obliged to Gada Baba for his blessings and love.

Dedication

To my beloved Mother
Late. Manorama Sahoo

Abstract

The presence of a mysterious form of matter constituting 26.8% of the total energy budget of the present universe, is confirmed indirectly by, rotational velocity of spiral galaxies, gravitational lensing and collision of galaxies in bullet cluster. This matter is called as dark matter (DM), because it does not show electromagnetic interaction. The standard model(SM) of particle physics which is a successful theory, explaining many physical phenomena, does not include a particle candidate of DM. It also unable to explain the smallness of neutrino mass as confirmed by neutrino oscillation experiments. In this thesis we explore the viable scenarios of non-zero neutrino mass and DM in beyond the standard model(BSM) frameworks.

In the first attempt we augmented the SM by adding 3 singlet right handed neutrinos and two scalars: one doublet and a charged singlet under $SU(2)_L$. A small mass splitting between the lightest and next to lightest particle among the right handed neutrinos is created. As a result the later can decay to former by emitting a photon of energy 3.5 keV through a transient dipole moment operator. The emitted photon can explain the 3.5 keV X-ray line observed in XMM-Newton X-ray observatory. Both the lightest and next to lightest right handed neutrinos contribute to the relic abundance of the DM. The SM neutrinos can get small mass in a Type I seesaw mechanism.

To explore a further possibility of a DM candidate, we consider a vector-like fermion, which is a mixed state of an additional SM doublet and a singlet lepton. The doublet singlet mixing angle plays an important role in DM phenomenology. Small neutrino mass can be explained in a type II see saw framework by adding a triplet scalar to the model. The triplet scalar also couples to the DM and hence changes the phenomenology accordingly. In a very brief manner we also try to explain the 750 GeV diphoton resonance claimed by the CMS and ATLAS, by adding a singlet scalar and a vector like quark on top of the doublet-singlet fermion to the SM.

We also consider another drawback of SM further to explain the anomalous magnetic moment of muon which is a 3σ discrepancy between theoretical estimation and experimental observation. A gauged $U(1)_{L_\mu-L_\tau}$ extension of the SM is proposed. The model contains additional 3 right handed neutrinos, two singlet scalars and a vector like colourless fermion, as a DM candidate, under the SM gauge group. The magnetic moment of muon gets additional contribution through its coupling to the new Z' gauge boson. The model also predicts an inelastic DM candidate. In the same work we try to explain the positron excess as observed by PAMELA, FERMI-LAT and AMS-02 through the annihilation of DM.

Contents

Declaration	ii
Approval Sheet	iii
Acknowledgements	iv
Abstract	vi
Nomenclature	ix
1 Introduction	6
1.1 What is Dark Matter ?	6
1.1.1 Observational Evidences of Presence of DM	6
1.1.2 Thermal freeze out of DM	10
1.1.3 Experimental Detection of DM	14
1.2 Neutrino mass and See Saw Models	16
1.3 Muon $g - 2$ anomaly	18
1.4 Observed 3.5 keV X-ray line by XMM-Newton Observatory	19
1.5 Aim of the Thesis	20
1.6 Thesis Overview	20
2 Dipolar Dark Matter and 3.5 keV x-ray line	21
2.1 Introduction	21
2.2 The Model	22
2.2.1 Constraints on new particles	23
2.2.2 Mass splitting between N_1 and N_2	23
2.3 Magnetic DM and explanation to 3.5 keV X-ray line	25
2.3.1 Estimation of the new physics scale and collider search	26
2.4 Neutrino mass	27
2.5 Relic abundance of DM	27
2.6 Direct Detection of DM	31
2.7 Summary and Outlook	32
3 Vector like mixed singlet-doublet fermionic Dark Matter and application to 750 GeV diphoton excess signal	34
3.1 Introduction	34
3.2 The Model	35
3.3 Constraints on Model Parameters	39

3.3.1	Invisible Z-decay	39
3.3.2	Invisible Higgs decay	40
3.4	Constraint on Model parameters from Direct Search Experiments of DM	41
3.5	Constraints from Electroweak precision tests on Vector-like leptons	44
3.6	Relic Abundance of DM	46
3.6.1	Relics of Inert fermion doublet DM	46
3.6.2	Relics of Singlet-Doublet mixed fermion DM	47
3.7	Collider Signature	54
3.8	Addition of Scalar triplet to the Inert Fermion DM Model	57
3.8.1	Mixing in the scalar sector	58
3.9	Small neutrino mass	60
3.10	Pseudo-Dirac nature of DM	62
3.10.1	Pseudo-Dirac nature of Inert fermion doublet DM	62
3.10.2	Pseudo-Dirac nature of singlet-doublet fermion DM	63
3.10.3	Relics of Singlet-Doublet mixed fermion DM in presence of scalar triplet	63
3.11	Direct Detection in presence of the scalar triplet	65
3.11.1	Direct Detection of DM through inelastic scattering with the nuclei	65
3.11.2	Direct Detection of DM through elastic scattering with the nuclei	66
3.12	Summary of constraints of the model	68
3.13	Application to Diphoton Excess	69
3.14	The Model for Dark Assisted scalar decay	70
3.14.1	Explanation for Diphoton Excess	72
3.15	Summary and Outlook	76
4	Muon $g-2$ anomaly, neutrino mass and DM phenomenology in U(1) gauged extension of standard model	78
4.1	Introduction	78
4.2	The model	79
4.2.1	Spontaneous breaking of gauge symmetry	80
4.2.2	Interaction Lagrangian	81
4.2.3	Scalar masses and mixing	81
4.2.4	Mixing in the Gauge sector	82
4.3	BBN constraint on $\eta-h$ mixing	83
4.4	Muon $g-2$ anomaly	83
4.5	Neutrino mass	84
4.6	Relic Abundance of DM	86
4.6.1	Relic abundance in absence of η	86
4.6.2	Relic abundance in presence of η	86
4.7	Constraints from Detection of DM in Direct Search Experiments	88
4.7.1	Direct Detection in absence of η	88
4.7.2	Direct Detection in Presence of η	89
4.8	Indirect detection of DM	92
4.9	Conclusion and Outlook	93

5 Conclusion	96
Appendices	98
A Radiative Neutrino Mass	99
B Magnetic Moment of Dipolar DM	101
C 3-Body Decay of N^-	104
D Calculation of $Z - Z'$ mixing	108
References	112

List of Tables

2.1	Particle content of the proposed Model.	22
3.1	Global fit for the electroweak precision parameters taken from ref. [1].	44
3.2	Production Cross-sections $\sigma_{pp \rightarrow N^+ N^-}$ for the benchmark points at LHC for $E_{cm} = 8$ and 14 TeV. The leptonic final states $\sigma_{\ell 2j E_{\cancel{T}}}$ and $\sigma_{2\ell E_{\cancel{T}}}$ are also mentioned. All cross-sections are in fb.	55
3.3	SM background at LHC for $E_{cm} = 8$ TeV for $\ell 2j E_{\cancel{T}}$ and $2\ell E_{\cancel{T}}$ channels before and after missing energy cut $E_{\cancel{T}} > 100$ GeV. All cross-sections are in fb.	56
3.4	SM background at LHC for $E_{cm} = 14$ TeV for $\ell 2j E_{\cancel{T}}$ and $2\ell E_{\cancel{T}}$ channels before and after missing energy cut $E_{\cancel{T}} > 100$ GeV. All cross-sections are in fb.	56
4.1	Particle content of the minimal $U(1)_{L_\mu - L_\tau}$ gauge extension of the SM and their transformation under the SM gauge group.	80
4.2	Benchmark point which satisfies relic density and fits the AMS2 positron fraction data[2].	93

List of Figures

1.1	Rotational velocity curve of spiral galaxy NGC 6503 [3].	7
1.2	Gravitational lensing effect of Abell 2218 galaxy cluster. Picture credit : NASA web page	7
1.3	Image of bullet cluster observed by Chandra X-ray observatory[4]. Picture is taken from NASA web page.	8
1.4	CMB temperature fluctuation as a function of multipole moment l . The picture is borrowed from [5].	9
1.5	Solution to Boltzmann equation for freeze out mechanism. The solid black line corresponds to the Y^{eq} , while the dashed lines corresponds to $\langle\sigma v \rangle = 2.6 \times 10^{-10}\text{GeV}^{-2}$ (Red), $\langle\sigma v \rangle = 2.6 \times 10^{-9}\text{GeV}^{-2}$ (Blue) , $\langle\sigma v \rangle = 2.6 \times 10^{-8}\text{GeV}^{-2}$ (Green) respectively.	13
1.6	Schematic Diagram showing various ways of detection of DM	14
1.7	Constraint on Spin Independent DM-nucleon cross-section. The picture is taken from [6]	15
1.8	Contribution to magnetic moment of muon. (a) corresponds to $g = 2$, (b) corresponds to general diagram showing correction to $g - 2$ value.	18
1.9	The excess of 3.5 keV line as observed in XMM Newton Observatory in the full sample of 73 cluster of galaxies. Picture is borrowed from [7].	19
2.1	Mass splitting between N_1 and N_2 due to radiative correction through breaking of $Z_2 \times Z'_2$ symmetry.	23
2.2	Feynman diagram for magnetic DM decay: $N_2 \rightarrow N_1\gamma$	26
2.3	One loop diagram contributing to Majorana mass of light neutrinos.	27
2.4	r_1 and r_2 as a function of M_{DM} for $Y_\Sigma = Y_H$. For simplicity we set $M_{\text{DM}} = M_X$	29
2.5	Ratio of DM abundance as a function of $M_X - M_{\text{DM}}$ for a typical mass of DM, $M_{\text{DM}} = 1000\text{GeV}$ and $Y_\Sigma = Y_H = 0.55$	30
2.6	Scatter plots for observed relic abundance in the plane of $M_X - M_{\text{DM}}$ versus M_{DM} for different values of the Yukawa couplings: $Y = Y_\Sigma = Y_H$	30
2.7	Elastic scattering of magnetic dipolar DM with target nuclei.	31
3.1	Pictorial presentation of the possible mass spectrum for additional vector-like leptons.	37
3.2	The allowed values of $\sin\theta$ for different DM mass $M_1 < M_Z/2 = 45\text{ GeV}$ from invisible Z decay constraints. We assume here $M_2 = M_z/2 = 45\text{ GeV}$	39

3.3	Scatter plot for allowed parameter space in $\sin 2\theta - M_1$ (GeV) plane from invisible Higgs decay. All possible values of M_2 used that keeps the decay chain open.	40
3.4	Feynman diagrams for direct detection of N_1 DM.	41
3.5	Constraint on $\sin \theta$ (left) from Z mediated direct detection process and $Y \sin 2\theta$ (right) from H mediated direct detection process using Xenon-100 and LUX data for different values of DM mass M_1	42
3.6	Spin independent direct detection cross-section for N_1 DM as a function of DM mass for $\sin \theta = \{0.05 - 0.1\}$ (Green), $\sin \theta = \{0.1 - 0.15\}$ (Purple), $\sin \theta = \{0.15 - 0.2\}$ (Lilac), $\sin \theta = \{0.2 - 0.25\}$ (Red). Fixed values of $\Delta M = \{100, 700\}$ GeV (left and right respectively) have been used. XENON 100, LUX data are shown with XENON 1 T prediction.	43
3.7	In the left panel, \hat{S} is shown as a function of M_2 for $M_1 = 150$ GeV and $\sin \theta = 0.05$ (Green colour, bottom), $\sin \theta = 0.075$ (Blue color, middle) and $\sin \theta = 0.1$ (Red color, top). In the right panel, allowed values of \hat{S} in the plane of $M_2 - M^\pm$ versus M_2 for $\sin \theta = 0.05$	45
3.8	In the left panel, \hat{T} is shown as a function of M_2 for $M_1 = 150$ GeV and $\sin \theta = 0.05$ (Green colour, bottom), $\sin \theta = 0.075$ (Blue color, middle) and $\sin \theta = 0.1$ (Red color, top). In the right panel, allowed values of \hat{T} in the plane of $M_2 - M^\pm$ versus M_2 for $\sin \theta = 0.05$	45
3.9	Relic abundance (green line) of N_0 , the neutral component of the doublet as DM, plotted as a function of doublet mass (M_N) in GeV. Black horizontal line shows the observed relic abundance by PLANCK data. The solid red vertical line is shown to mark $\frac{M_Z}{2} = 45$ GeV; for $M_N > \frac{M_Z}{2}$ the DM does not contribute to the invisible Z decay width.	46
3.10	Dominant Annihilation processes to Higgs and gauge boson productions along with $f\bar{f}$, where f stands for all the SM fermions.	48
3.11	Dominant Coannihilation processes with N_2 to Higgs, gauge boson pair and $f\bar{f}$, where f stands for all fermions.	49
3.12	Dominant co-annihilation contributions from $N_1 N^-$ to Gauge boson and Higgs productions along with $f'\bar{f}$, where f stands for all the SM fermions.	50
3.13	Dominant co-annihilation contributions from $N^+ N^-$ to Gauge boson and Higgs productions along with $f\bar{f}$, where f stands for all the SM fermions.	51
3.14	Relic density of DM as a function of its mass M_1 for different values of $\sin \theta = 0.1, 0.2, 0.3$, shown by red (top), green (middle) and purple (bottom) respectively. The value of the mass splitting: $M_2 - M_1 = 50, 500$ GeV is fixed respectively for left and right panel.	51
3.15	Scatter plot for correct relic density in the plane of M_1 and ΔM , shown by green, red, blue and purple coloured points for $\sin \theta = 0.1, 0.15, 0.2, 0.3$ respectively.	52
3.16	Left : Ωh^2 versus DM mass M_{DM} in GeV for $\sin \theta = 0.1$ and $\Delta M = 10, 20, 30, 40, 100$ GeV (Blue, Green, Orange, Purple, Red respectively from bottom to top). Right : Ωh^2 versus DM mass M_{DM} in GeV for $\sin \theta = 0.0001$ and $\Delta M = 10, 20, 30, 40, 100$ GeV (Blue, Green, Orange, Purple, Red respectively from bottom to top). Horizontal line shows the correct relic density.	53

3.17	Left panel: Feynman graph producing N^+N^- pair at LHC and its subsequent decays. Right panel: Variation in production cross section $\sigma_{pp \rightarrow N^+N^-}$ (pb) at LHC with respect to M_{\pm} for $E_{cm} = 8$ TeV (Green, below) and $E_{cm} = 14$ TeV (Blue, above).	54
3.18	Left panel: Displaced vertex of N^- for $M^{\pm} = 150$ GeV, $m_{\ell} = 105$ MeV and $\sin \theta = 3 \times 10^{-4}$. Right panel: Γ^{-1} values varying between (1 - 10) cm in the plane of ΔM versus M^{\pm} for $\sin \theta = 3 \times 10^{-4}$ (in Green), 2×10^{-4} (in Red) and 10^{-4} (in Black) simultaneously from left to right.	56
3.19	Left panel: Scatter plot showing relic abundance as a function of DM mass with mass splitting less than 50 GeV. Black solid line shows the correct relic abundance as allowed by PLANCK data. Right panel: Displaced vertex (Γ^{-1}) in cm as a function of M^{\pm} (GeV) for relic density allowed points. Value of mixing angle $\sin \theta = 3 \times 10^{-4}$ is used in both the plots for illustration.	57
3.20	Contours of different values of M_{Δ} (in GeV) in the plane of μ versus $\sin \theta_0$	59
3.21	Relic density of DM as a function of its mass M_1 for different values of $\sin \theta = 0.1, 0.2, 0.3$, shown by red (top), green (middle) and purple (bottom) respectively. The value of the triplet mass: $M_{\Delta} = 200, 1000$ GeV is fixed respectively for left and right panel. All these plots are generated keeping a fixed value of the mass splitting $M_2 - M_1 = 500$ GeV. Ratio of Majorana couplings are fixed at : $\frac{f_L}{f_N} = 10^{-3}$ for illustration.	64
3.22	Scatter plot for correct relic density in the plane of M_1 and ΔM , shown by green, red, blue and purple coloured points for $\sin \theta = 0.1, 0.15, 0.2, 0.3$ respectively. Two different triplet masses are chosen $M_{\Delta} = 200$, and 1000 GeV respectively for the left and right panel plots. We fixed the value of Majorana coupling ratio: $f_L/f_N = 10^{-3}$ in both the figures for illustration.	65
3.23	Feynman diagrams for direct detection of N_1 DM via Higgs mediation.	66
3.24	Spin Independent direct detection cross-section for DM as a function of DM mass for $\sin \theta = \{0.05-0.1\}$ (Purple), $\sin \theta = \{0.1-0.15\}$ (Pitch), $\sin \theta = \{0.15-0.2\}$ (Green), $\sin \theta = \{0.2-0.25\}$ (Gray), $\sin \theta = \{0.25-0.3\}$ (Orange), $\sin \theta = \{0.3-0.35\}$ (Red). Black dotted curves show the data from LUX and XENON 1T prediction. Value of $\Delta M = 100, 500$ GeV are fixed for left and right panel figures respectively. The scalar triplet mass is fixed at $M_{\Delta} = 200$ GeV and scalar mixing angle is fixed at $\sin \theta_0 = 0.05$ for the calculation.	68
3.25	Summary of all constraints in the plane of $M_1 - M_2$ using $\sin \theta = 0.1$ (left) and $\sin \theta = 0.3$ (right).	69
3.26	Contours of $M_h = 125$ GeV and $M_S = 750$ GeV in the plane of $\sqrt{2\lambda_H}v$ and $\sqrt{\mu_S^2 + \lambda_{SH}v^2}$ for $\mu_{SH} = 10$ GeV (Solid red), $\mu_{SH} = 750$ GeV (Dashed blue), and $\mu_{SH} = 1400$ GeV (Dotted green).	72
3.27	Feynman diagrams for production of scalar S through gluon gluon fusion mediated by quark-like vector particle Q and its subsequent decay to SM particles mediated by the dark sector particle N^{\pm} . The other decay modes of S via its mixing with the SM Higgs are suppressed in the limit $\theta_{hS} \rightarrow 0$	74
3.28	Contours of $\sigma(pp \rightarrow S \rightarrow \gamma\gamma)$ in the plane of f_N versus M_N for $f_N = f_Q$, $M_N = M_Q$ and $\sin \theta_{hS} = 0$	75

3.29	Contours of $\Gamma(S \rightarrow \text{All})$ (in GeV) in the plane of f_N versus M_N for $f_N = f_Q$, $M_N = M_Q$ and $\sin \theta_{hS} = 0$	76
3.30	Contours of $\text{Br}(S \rightarrow \gamma\gamma)$ in the plane of f_N versus M_N for $f_Q = 5$ and $M_Q = 600$ GeV. We set $\sin \theta_{hS} = 0$	76
4.1	The mixing between the SM gauge boson Z and the $U(1)_{L_\mu-L_\tau}$ gauge boson Z' arising through the exchange of muon and tauon families of leptons.	82
4.2	Possible annihilation channels for relic abundance of DM, where f represents muon and tauon families of leptons while ψ represents the SM fermion.	86
4.3	Parameter space for Z' boson. The region above the red line is allowed by the correct relic abundance of DM, the green shaded region is allowed by null detection of DM at LUX using $Z - Z'$ mixing to be 10^{-3} . Black shaded region is allowed by muon $g - 2$ anomaly. Neutrino trident production [8] forbids the region above the dashed brown curve.	87
4.4	Dominant annihilation channel for relic abundance of DM in the region of small $g_{\mu\tau}$	87
4.5	Constraints on the parameter space satisfying correct relic abundance (shown by Green and Red points) and null detection of dark matter at LUX (shown by Cyan lines). For $M_\eta = 1$ GeV, we have used $\sin \theta_{\eta h} = 5 \times 10^{-6}$ (dashed-line), 1×10^{-5} (solid-line) and 3.5×10^{-5} (dotted-line).	88
4.6	Feynman diagrams for direct detection of DM through scattering with nuclei via the exchange of $Z - Z'$ mixing.	89
4.7	Elastic scattering of DM with nuclei through $\eta - h$ mixing.	90
4.8	Inelastic scattering of DM with the target nucleus through the $Z - Z'$ mixing.	92
4.9	Ratio of positron flux to the total ($e^- + e^+$) flux against energy of the cosmic rays with AMS-02(2014) data[2] for benchmark points listed in Table 4.2. The blue curve is for the benchmark point BP1 while the black curve is for BP2.	94
C.1	Momentum configuration of N^- decay in ℓ, ν_ℓ COM frame.	105

Chapter 1

Introduction

1.1 What is Dark Matter ?

Recent observations in the cosmic microwave background radiation (CMBR) by the satellite borne experiments, such as PLANCK[9] and WMAP[10] reveal that the visible matter constitutes only 4.9% of the total energy budget of the universe. The remaining 95.1% is unseen and yet to be explored. However, it has been shown quantitatively that out of 95.1% of the total energy budget, nearly 26.8% of the universe is made up of some unknown form of matter called Dark Matter (DM) and rest 68.3% is dark energy. DM does not have electromagnetic interaction. The presence of DM is confirmed only by its gravitational interaction. However the properties of a DM, apart from its relic abundance, is not clearly understood yet. There is a huge question mark on DM particle properties like mass, spin, interaction with standard model (SM) particles etc. This thesis focuses on understanding the nature of DM in some beyond standard model (BSM) physics frameworks. In these models we also explore the sub-eV masses of active neutrinos required by oscillation hypothesis.

1.1.1 Observational Evidences of Presence of DM

Rotational velocity of stars in spiral galaxies

The first hint of presence of DM came from the observation of rotational velocity of stars at different distances from the center of the spiral galaxy. The structure of a spiral galaxy is having a central bulge containing almost all the mass and spiral arms extended to fall over a disk. The circular velocity $v(r)$ of a star with mass m at a distance r from the center can be obtained by using virial theorem, which states that:

$$\begin{aligned} \langle K.E \rangle &= -\frac{1}{2} \langle P.E \rangle \\ \frac{1}{2} m v(r)^2 &= \frac{G m M(r)}{2r}, \end{aligned} \tag{1.1}$$

where $M(r)$ is the mass enclosed in a volume with radius r and G is the gravitational constant. Now from eq(1.1) it can be inferred that, the rotational velocity would increase linearly from center to a region enclosed by the central hub i.e. $v(r) \sim r$. It is because the mass is proportional to radius i.e $M(r) = \frac{4}{3} \pi r^3 \rho$ inside the central hub, having average density ρ . As we move far apart

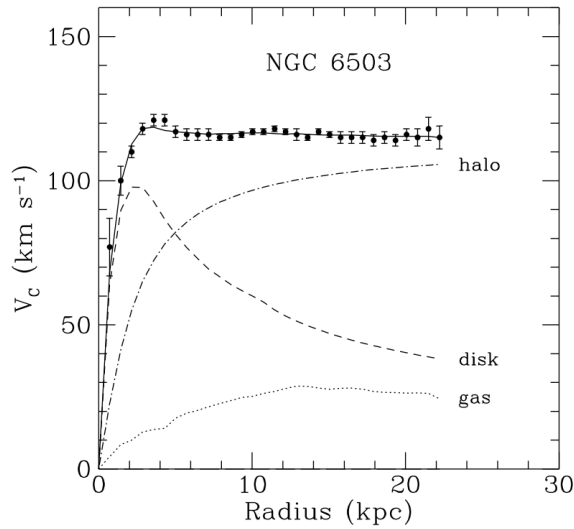


Figure 1.1: Rotational velocity curve of spiral galaxy NGC 6503 [3].

from this region the velocity is expected to fall as $r^{-1/2}$. But the observation suggests that the velocity remains constant as we go far away from the central bulge. This seems that there is a huge amount of unseen matter present so that it compensates the mass with distance. A typical example of rotational velocity of a star as a function of distance, measured in the galaxy NGC6503, is shown in Fig. 1.1. The DM is largely distributed in the halo region and hence gives a good explanation for the flatness of the rotational curves of stars in spiral galaxies.

Gravitational Lensing



Figure 1.2: Gravitational lensing effect of Abell 2218 galaxy cluster. Picture credit : NASA web page

One of the predictions of the General Relativity is that light bends near a heavy gravitational mass and it gives rise to lensing effect. As a result, distorted or multiple images appear for an observer if there exist a source behind the enormous lensing mass. The gravitational lensing effect can be classified into two categories, namely strong and weak lensing. Multiple images of the same object appears in case of strong lensing, while in case of weak lensing the image gets distorted or sheared. The brightness of the background object increases for the observer in the foreground of the

lensing mass in case of weak lensing. This method provides a measurement for the calculation of total mass of the cluster of galaxies causing the lensing effect. By comparing the lensing mass with the luminous mass obtained from the mass to light ratio using X-ray emission, one finds that a huge amount of unseen DM is present in the galaxy cluster. Such an image is shown in Fig. 1.2 for Abell 2218 cluster. In the left central region, a ring like structure is formed due to the lensing effect of Abell 2218 for the background galaxy or cluster.

Bullet Cluster



Figure 1.3: Image of bullet cluster observed by Chandra X-ray observatory[4]. Picture is taken from NASA web page.

The evidence of presence of DM is also further confirmed by studying the gravitational effect of a double galaxy cluster 1E0657-558 named "bullet cluster" [4]. The galaxy is consisting of two distinct subclusters and hot gas (observed through its emission of X-rays and nearly constitutes 90% of luminous matter of the bullet cluster) is concentrated between these subclusters. The cluster of galaxies have collided. The galaxies which have less chance of collision move mostly on their original path. However, the two clouds of hot gas have collided and remained closer to the center of double cluster. Using the gravitational lensing effect of the galaxy cluster the total matter density

is calculated. It is concluded that most of the matter is not associated with the hot gas, but is likely with the galaxies forming two groups of subclusters that have passed through each other without substantial interaction. The associated mass of the bullet cluster is 6 times more as contained in the hot gas. A picture is shown in Fig. 1.3. So this is a kind of strongest evidence of not only the presence of DM, but also its feeble interaction with baryonic matter.

Evidence from Cosmic Microwave Background Radiation (CMBR)

The most recent evidence for the existence of DM came from the observation of temperature anisotropy in the cosmic microwave background radiation (CMBR) which was originated from the Big-Bang during the time of recombination epoch (roughly 200 thousand years after the big-bang). The average temperature of CMBR at present is around 2.7° K. However, there is a small temperature fluctuation in the CMBR, only about $30 \pm 5\mu\text{K}$. This means that the CMBR is uniform to 1 part in 10^5 . On small scales the origin of the anisotropy in CMBR is due to acoustic oscillations. Photons and protons in the early Universe can be modeled as a photon-baryon fluid before the photon decoupling temperature. The fluid is then pass through various cycles: i) while falling into the gravitational potential well (formed due to inflation and further enhanced by the presence of DM), the fluid is compressed, ii) the pressure increases until it makes the fluid to expand outward, iii) the pressure of the fluid decreases as it expands until the gravity pulls it back, iv) the process repeats until the decoupling of the photon. The photons emerging have different temperatures depending upon the location in the cycle on the portion of fluid at decoupling time. Thus any fluctuation in CMBR clearly carries the information about the initial density perturbations that allowed for the formation of early gravitational wells as well as the dynamics of photon-baryon fluid. Thus the temperature fluctuations of the CMBR depend on the amount of baryons and DM present during the time of recombination.

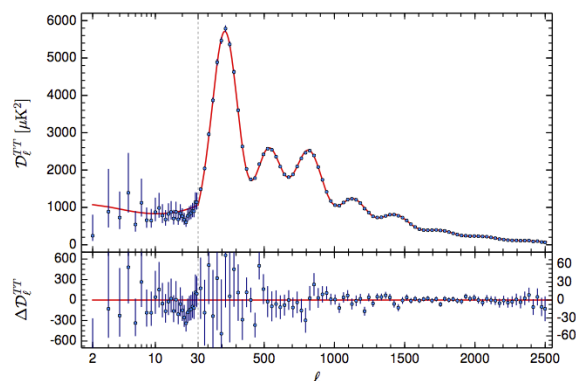


Figure 1.4: CMB temperature fluctuation as a function of multipole moment l . The picture is borrowed from [5].

The satellite borne experiments like PLANCK [9] and WMAP [10] look for this anisotropy in the temperature in CMBR. The temperature fluctuation can be analysed in the form of spherical harmonics so that the angular power spectrum can be obtained. This power spectrum is compared with cosmological models in order to obtain the best fit values of the model parameters. The position and amplitude of peaks of the power spectrum of CMBR anisotropies depend on both the baryon

and DM energy densities. Fitting to 9 year WMAP data [10] one finds $\Omega_c h^2 = 0.1138 \pm 0.0045$ and $\Omega_B h^2 = 0.02264 \pm 0.00050$, where $\Omega_c h^2, \Omega_B h^2$ are the DM energy density and baryon energy density in terms of critical density respectively. The best fit value of $\Omega_B h^2$ also agrees with the results obtained from Big Bang Nucleosynthesis. This result shows that nearly 83% of total matter of the universe is not baryonic but dark. A small change in baryon density is not consistent with the WMAP observation. So the CMBR gives the strongest evidence of presence of DM in the universe. A figure showing the anisotropy in CMBR is shown in fig. 1.4.

Inference about DM properties from astrophysical evidences

So far what we have learnt from the above astrophysical evidences is that the DM is surely present in the universe. However all other interactions of DM except gravity are not known yet. Quantum numbers like mass, charge, spin, etc. are yet to be established for the DM. Its interaction with other SM particles is so feeble that its detection is still a major challenge. Again due to the local DM density being too small, it is very difficult to detect it in the earth bound laboratories. So additional assumption of weak interaction is coined for DM [11]. This weak interaction keeps the DM in thermal equilibrium with the SM particles in the early universe. We will discuss the importance of the weak interaction assumption of DM and will argue about its validity in the next section.

1.1.2 Thermal freeze out of DM

In the early Universe, the DM remains in thermal equilibrium due to its weak interaction with the SM particles. As the temperature falls due to the expansion of the universe the DM decouples from the thermal bath and its density gets diluted afterwards. This happens at a temperature below the DM mass scale. The evolution of the DM in the early universe can be obtained by solving the relevant Boltzmann equation.

Let us consider a DM candidate ψ with f as its distribution function. Then the Boltzmann equation can be written as

$$\hat{L}[f] = C[f], \quad (1.2)$$

where \hat{L} is the Liouville operator and C is the collision operator. The standard model of cosmology which is based on the Friedmann Robertson Walker (FRW) metric assumes that the phase space distribution is spatially homogeneous and isotropic. So the Liouville operator can be given as :

$$\hat{L}[f(E, t)] = E \frac{\partial f}{\partial t} - \frac{\dot{R}}{R} |\vec{p}|^2 \frac{\partial f}{\partial E}, \quad (1.3)$$

where R is the scale factor associated with the expansion of the universe using FRW metric. Now consider the relation:

$$\frac{\partial f}{\partial E} = \frac{\partial f}{\partial p} \frac{dp}{dE} = \frac{E}{p} \frac{\partial f}{\partial p}.$$

Using the above relation in eq. 1.3, we rewrite eq. 1.2 as:

$$\frac{\partial f}{\partial t} - \frac{\dot{R}}{R} p \frac{\partial f}{\partial p} = \frac{C[f]}{E}. \quad (1.4)$$

The number density of the DM species can be defined in terms of the phase space density as:

$$n(t) = \frac{g}{(2\pi)^3} \int d^3p f(E, t). \quad (1.5)$$

Taking momentum space integration of equation 1.4 we get,

$$\frac{\partial n}{\partial t} + 3\frac{\dot{R}}{R}n = g \int \frac{d^3p}{(2\pi)^3} \frac{C[f]}{E}. \quad (1.6)$$

We have used the trick for the integration of the second term in eq. 1.4 as

$$\begin{aligned} & \frac{g}{(2\pi)^3} \int d^3p p \frac{\partial f}{\partial p} \\ &= g \frac{4\pi}{(2\pi)^3} \int_0^\infty dp p^3 \frac{\partial f}{\partial p} \\ &= g \frac{4\pi}{(2\pi)^3} \left[p^3 f - \int_0^\infty f 3p^2 dp \right] \\ &= 0 - g \frac{4\pi}{(2\pi)^3} 3 \int_0^\infty f p^2 dp \\ &= -3g \frac{1}{(2\pi)^3} \int d^3p f \\ &= -3n \end{aligned}$$

Writing Hubble parameter as ($H = \dot{R}/R$), eq. 1.6 takes the form :

$$\frac{\partial n}{\partial t} + 3Hn = g \int \frac{d^3p}{(2\pi)^3} \frac{C[f]}{E}. \quad (1.7)$$

This is the Boltzmann equation governing the number density of the DM particle. We will make it more formal for an annihilation process. Consider there is only one species of DM (ψ) and it is in thermal equilibrium due to the process:

$$\psi + \bar{\psi} \iff \chi + \bar{\chi}.$$

where χ is a very small mass particle and it is very tightly coupled with the thermal plasma. The collision term for this process is given by:

$$\begin{aligned} \frac{g}{(2\pi)^3} \int \frac{d^3p_\psi}{(2\pi)^3} \frac{C[f]}{E_\psi} &= - \int d\Pi_\psi d\Pi_{\bar{\psi}} d\Pi_\chi d\Pi_{\bar{\chi}} \\ &\times (2\pi)^4 \delta^4(p_\psi + p_{\bar{\psi}} - p_\chi - p_{\bar{\chi}}) \\ &\times \left[|\mathcal{M}|_{\psi+\bar{\psi}\rightarrow\chi+\bar{\chi}}^2 f_\psi f_{\bar{\psi}} (1 \pm f_\chi)(1 \pm f_{\bar{\chi}}) \right. \\ &\left. - |\mathcal{M}|_{\chi+\bar{\chi}\rightarrow\psi+\bar{\psi}}^2 f_\chi f_{\bar{\chi}} (1 \pm f_\psi)(1 \pm f_{\bar{\psi}}) \right], \end{aligned} \quad (1.8)$$

where f 's denote the phase space density of the respective particles, and

$$d\Pi \equiv g \frac{1}{(2\pi)^3} \frac{d^3p}{2E} \quad (1.9)$$

with g as the total number of internal degrees of freedom. The $1 + f_i$ represents the Bose enhancement while $1 - f_i$ stands for Pauli Blocking factor. The four dimensional δ function ensures the energy and momentum conservation, while $|\mathcal{M}|^2$ represents the square of the scattering amplitude for the given type of reaction.

Using the standard definition of cross-section, we get

$$\int d\Pi_k d\Pi_l \times (2\pi)^4 \delta^4(p_i + p_j - p_k - p_l) [|\mathcal{M}|_{ij \rightarrow kl}^2] = 4g_i g_j \sigma_{ij} v \times E_i E_j \quad (1.10)$$

Dropping the Bose enhancement and Pauli Blocking factors and substituting the above expression in Eq.1.8, we get

$$\frac{g}{(2\pi)^3} \int \frac{d^3 p_\psi}{(2\pi)^3} \frac{C[f]}{E_\psi} = - \int [dn_\psi dn_{\bar{\psi}} (\sigma_{\psi\bar{\psi} \rightarrow \chi\bar{\chi}}) v - dn_\chi dn_{\bar{\chi}} (\sigma_{\chi\bar{\chi} \rightarrow \psi\bar{\psi}}) v] \quad (1.11)$$

Since cross-section times velocity varies very slowly with change in number density of initial and final state particles it can be taken out of the integrand to give

$$\dot{n}_\psi + 3Hn_\psi = -\langle (\sigma_{\psi\bar{\psi} \rightarrow \chi\bar{\chi}}) v \rangle n_\psi n_{\bar{\psi}} + \langle (\sigma_{\chi\bar{\chi} \rightarrow \psi\bar{\psi}}) v \rangle n_\chi n_{\bar{\chi}} \quad (1.12)$$

The χ particles, which are SM particles, are still in equilibrium in the thermal plasma with the photon. When the DM was also in equilibrium with the SM particles, the principle of detailed balance dictates that

$$\langle (\sigma_{\psi\bar{\psi} \rightarrow \chi\bar{\chi}}) v \rangle (n_\psi^{eq})^2 = \langle (\sigma_{\chi\bar{\chi} \rightarrow \psi\bar{\psi}}) v \rangle n_\chi^{eq} n_{\bar{\chi}}^{eq}.$$

Using the above expression in eq 1.12, we get

$$\dot{n}_\psi + 3Hn_\psi = -\langle \sigma v \rangle [n_\psi^2 - (n_\psi^{eq})^2], \quad (1.13)$$

where $\langle \sigma v \rangle = \langle (\sigma_{\psi\bar{\psi} \rightarrow \chi\bar{\chi}}) v \rangle$

Now we shall use the dimensionless variable $Y \equiv n_\psi/s$ (similarly the equilibrium number with $Y^{eq} \equiv n_\psi^{eq}/s$), which is the actual number of ψ particles in a comoving volume with s being the comoving entropy density. Applying conservation of entropy *i.e.* $sR^3 = \text{constant}$, we get

$$\begin{aligned} R^3 \dot{s} + 3R^3 \frac{\dot{R}}{R} s &= 0 \\ \Rightarrow \dot{s} + 3Hs &= 0 \end{aligned} \quad (1.14)$$

Using new variable Y eq. 1.13 can be rewritten as:

$$\begin{aligned} \dot{s}Y + \dot{Y}s + 3HsY &= -\langle \sigma |v| \rangle [Y_\psi^2 - (Y_\psi^{eq})^2] s^2 \\ \Rightarrow \frac{dY}{dt} &= -s \langle \sigma |v| \rangle [Y_\psi^2 - (Y_\psi^{eq})^2]. \end{aligned} \quad (1.15)$$

We define a new dimensionless variable $x \equiv m/T$ with m being the mass of the ψ particle. In the high temperature limit, $x \ll 1$, the reaction rate is so fast that Y follows its equilibrium value Y^{eq} . For large x the equilibrium number suffers a Boltzmann suppression $\exp(-x)$. So the ψ particles will become so rare that they will never find each other. As a result the reaction rate is too small to

maintain the equilibrium. This is the time when the particle ψ freezes out from the thermal bath and its number in a comoving volume is not changing afterwards. To change the variable from t to x , we have to find the Jacobian as:

$$\frac{dx}{dt} = m \frac{d}{dt} \frac{1}{T} = m \frac{d}{dt} R = Hx \quad (1.16)$$

In the previous expression we used the fact that in radiation dominated era, $R \propto \frac{1}{T}$ as the DM freeze out falls in this era. Also in this era the energy density scales as T^4 , so $H = H(m)/x^2$. After all this information, the evolution equation becomes:

$$\frac{dY_\psi}{dx} = -\frac{s\langle\sigma|v\rangle x}{H(m)} [Y_\psi^2 - (Y_\psi^{eq})^2] \quad (1.17)$$

This is a form of Riccati equation for which no general solution exists. A numerical solution is presented in fig. 1.5.

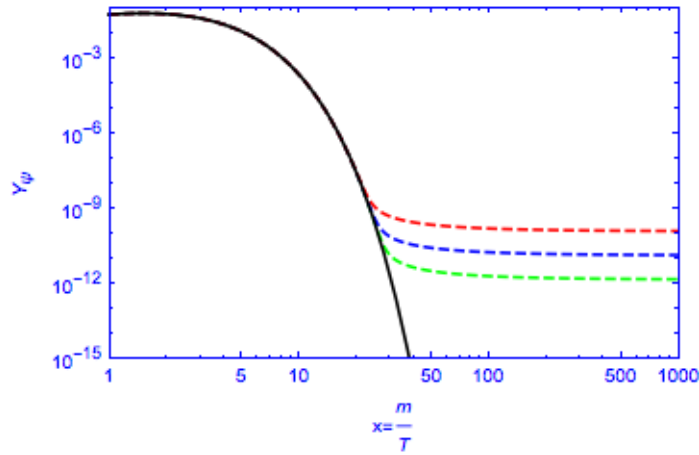


Figure 1.5: Solution to Boltzmann equation for freeze out mechanism. The solid black line corresponds to the Y^{eq} , while the dashed lines corresponds to $\langle\sigma|v\rangle = 2.6 \times 10^{-10} \text{ GeV}^{-2}$ (Red), $\langle\sigma|v\rangle = 2.6 \times 10^{-9} \text{ GeV}^{-2}$ (Blue), $\langle\sigma|v\rangle = 2.6 \times 10^{-8} \text{ GeV}^{-2}$ (Green) respectively.

We can see from the figure that as the cross-section increases, the departure from equilibrium is also delayed. The freeze out occurs nearly at a value of $x_f = \frac{m}{T_f} = 20 - 30$, with T_f as the freeze out temperature. The relic density of the DM ψ can be computed as:

$$\Omega = \frac{\rho_\psi}{\rho_{\text{cr}}}, \quad (1.18)$$

where ρ_{cr} is the critical density today. The DM density at present epoch can be given as

$$\rho_\psi = ms_0 Y_\infty \quad (1.19)$$

where $Y_\infty = Y(x \rightarrow \infty)$, and s_0 is the entropy density today. We can do an order of estimation for

the relic density as observed today:

$$\Omega h^2 \simeq 0.1 \left(\frac{x_f}{20}\right) \left(\frac{m}{100\text{GeV}}\right) \frac{2 \times 10^{-9} \text{GeV}^{-2}}{\langle\sigma|v|\rangle} \quad (1.20)$$

Since the cross-section is falling in the weak interaction range for getting the observed relic abundance, we can safely assume that the DM has weak interaction apart from gravitational interaction. This observation is called WIMP (Weakly Interacting Massive Particle) miracle. It is one of the best choices available for the particle candidates of DM. We will consider some of the very simple WIMP possibilities in this thesis in the subsequent chapters.

1.1.3 Experimental Detection of DM

The detection of DM is very challenging. A concrete evidence of its detection is yet to come. But there are various experiments running globally for its detection. The detection of DM is carried out in three different ways :

- (a) Direct Detection
- (b) Indirect Detection
- (c) Collider signature

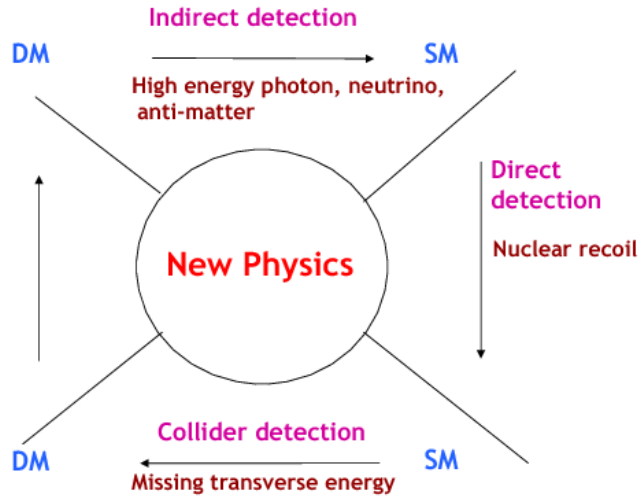


Figure 1.6: Schematic Diagram showing various ways of detection of DM

A schematic diagram has been shown in fig. 1.6 for the detection of DM in experiments. We will briefly discuss the various experimental methods to detect the DM in the following.

Direct Detection

The earth passes through the DM halo as the solar system is rotating around the center of galaxy. So there is a probability that the DM can hit the nucleus whose effect can be read in terms of recoil energy. This method is known as direct detection of DM. The DM velocity in the vicinity of solar system is nearly 200 km/s. So the recoil energy in terms of momentum transfer gives the idea about

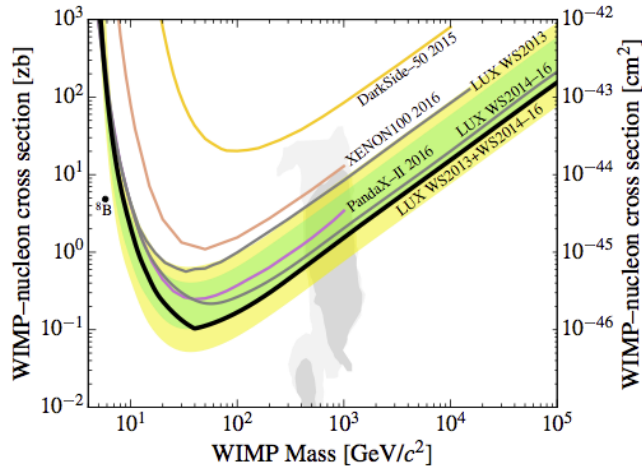


Figure 1.7: Constraint on Spin Independent DM-nucleon cross-section. The picture is taken from [6]

the effective nucleus-DM cross-section. Since the momentum transfer for DM-nucleon scattering is small $\sim \text{keV}$, a detector with low background and threshold is required. The interaction of DM with nucleus is of two types : Spin dependent (SD) and Spin independent (SI) depending on whether the DM interaction with the nucleus depends on its spin or not. Also the interaction can be classified as elastic or inelastic scattering. In case of elastic scattering the DM scatters from the nucleus as a whole and deposits a certain fraction of energy as recoil. However in inelastic scattering the DM either interacts with the electron and ionises the medium or it interacts with the nucleus leaves it in an excited state. The cross-section is enhanced as A^2 , with A being the mass number of the nucleus due to coherent scattering in SI case. Whereas the cross-section depends on $J(J + 1)$ value for SD case for a total spin of the nucleus as J .

There are various DM direct search experiments are looking for a signal of DM like LUX [6], XENON100 [12], DarkSide [13], PandaX-II [14] *etc.* Figure 1.7 is drawn to show the status of various experiments.

In recent times the stringent limit on SI direct detection cross-section (σ_{SI}) is coming from LUX [6] and XENON100 [12] experiments. The null observation of any DM in these experiments puts an upper bound on the DM-nucleon scattering crosssection σ_{SI} .

Indirect Detection

The indirect way of detection of DM is based on its annihilation or decay to SM particles. By looking at any excess of neutrinos, photons, antiparticle or any cosmic rays flux in the universe can probe a possibility of detection of DM. The DM while streaming freely can have a probability to be captured by the heavy massive objects like galactic center (GC), dwarf galaxies core, sun etc due to the strong gravitational force. When the density of the DM increases, they can annihilate or decay to high energetic photons or neutrinos. So these objects become a source of detecting DM through observing the excess of flux in the earth.

There are various experiments running in the world to detect such excesses. In recent times the AMS-02 collaboration declared about an excess in cosmic rays positron flux around 0.5-500 GeV [15, 2]. This result is also further established by excess in positron fraction above 10 GeV by PAMELA [16, 17] collaboration.

Collider Signatures

The DM detection in the colliders is very challenging due to very weak interaction as well as its longer lifetime. Moreover, it is neutral. So it can skip the detector without depositing any energy. The only way to probe DM in colliders by studying the missing energy. If the dark matter is produced due to the high energy collisions, then it can give a significant missing energy and hence can be probed in the colliders. Currently the two experiments, ATLAS and CMS at Large hadron collider (LHC) are focusing on detection of DM. The International Linear Collider (ILC) can probe DM in near future.

1.2 Neutrino mass and See Saw Models

Within the SM, the lepton number is an accidental global symmetry. This leads to exactly zero mass of all the left-handed neutrinos in the SM. However, the long baseline neutrino oscillation experiments [18, 19, 20, 21, 22, 23, 24, 25, 26] confirmed that the neutrinos have non-zero masses and also they mix with each other. But the nature of neutrinos, either Dirac or Majorana is not confirmed yet. Therefore, it is crucial to introduce additional degrees of freedom to the SM to explain non-zero masses of the neutrinos. Assuming that the neutrinos are Majorana (which leads to violation of lepton number by two units), the non-zero masses of left-handed neutrinos can be introduced by using Weinberg's dimension five operator [27]:

$$-\mathcal{L}_\nu^{d=5} = \frac{1}{2}(\bar{l}_L\phi)\kappa(\phi^T l_L^C) + H.c. \quad (1.21)$$

Here κ is a complex matrix having dimension inverse of mass. When the Higgs field ϕ gets a vacuum expectation value (vev), a Majorana mass term is generated for the neutrinos:

$$-\mathcal{L}_M = \frac{1}{2}\bar{\nu}_L M_L \nu_L^C + H.c., \quad (1.22)$$

with $M_L = v^2\kappa$. In general this mass matrix is not diagonal. So one can diagonalize it by taking a transformation of the fields as

$$\nu_L = U\nu'_L \quad (1.23)$$

The matrix U is chosen in such a way that it diagonalises the mass matrix in a way:

$$U^T M_L U = M_{\text{Diag}} \quad (1.24)$$

The see-saw models are an attractive way to explain the sub-eV masses of active neutrinos. These models contain heavy degrees of freedom such that in the low energy limit the heavy degrees of freedom get integrated out and the dimension 5 effective operator is generated. At tree level there are three ways to generate the Weinberg operator.

- (i) The *Type I* see-saw model, where an additional SM singlet fermion per generation, mainly a right handed neutrino, is introduced.
- (ii) The *Type II* see-saw model, where a $SU(2)_L$ scalar triplet is introduced.
- (iii) In *Type III* seesaw model, where an additional $SU(2)_L$ triplet fermion per generation is introduced.

Type I seesaw mechanism

In this case, three right handed neutrinos(RHN) (ν_R fields), which are SM singlet fermions, are introduced to the SM. Then a gauge invariant mass term can be written as :

$$-\mathcal{L}_M = \frac{1}{2} M_R \nu_R^T C^{-1} \nu_R + h.c \quad (1.25)$$

This leads to a Majorana mass for the heavy right-handed neutrinos. Similarly the Yukawa term involving left and right-handed neutrinos is given as:

$$\mathcal{L}_Y = \bar{\ell}_L \tilde{\phi} Y^\dagger \nu_R + h.c. \quad (1.26)$$

where ℓ is the lepton doublet and ϕ is the Higgs doublet. During electroweak symmetry breaking the Higgs acquires a vacuum expectation value (vev) ($v/\sqrt{2}$) and generate a Dirac mass term $M_D = \frac{v}{\sqrt{2}} Y^\dagger$. Hence we get a mass matrix of neutrino as:

$$\mathcal{M} = \begin{pmatrix} 0 & M_D \\ M_D & M_R \end{pmatrix} \quad (1.27)$$

Since $M_R \gg M_D$, the mass eigenvalues are given by a heavy M_R and light $M_\nu = -M_D M_R^{-1} M_D^T$. Assuming $M_R \sim \mathcal{O}(10^{15})$ GeV and a Dirac mass of electroweak scale $M_D \sim \mathcal{O}(10^2)$ GeV, one gets the light neutrino mass $M_\nu \sim \mathcal{O}(10^{-2})$ eV.

Type II seesaw mechanism

In the *Type II* seesaw model a scalar triplet $\Delta(1, 3, 2)$ is added to the SM, where the quantum numbers in the parenthesis are under the gauge group $SU(3)_C \times SU(2)_L \times U(1)_Y$. Due to presence of the triplet Δ , new contribution to Yukawa interaction is given by:

$$\mathcal{L}_Y = Y l^T C^{-1} \tau \cdot \Delta l + h.c \quad (1.28)$$

After electroweak symmetry breaking the neutral component of Δ gets an induced vev u_Δ . This vev gives a mass term to the neutrinos as:

$$-\frac{u_\Delta}{\sqrt{2}} Y \nu_L^T C^{-1} \nu_L \quad (1.29)$$

Thus the neutrino mass is given by :

$$\mathcal{M}_\nu = \sqrt{2} Y u_\Delta \quad (1.30)$$

If $Y \sim \mathcal{O}(1)$, then the sub-eV neutrino mass can be explained if $u_\Delta \sim \mathcal{O}(10^{-1})$ eV.

Type III seesaw mechanism

The *Type III* seesaw mechanism is very similar to the type I seesaw mechanism except that the right handed neutrinos are replaced by fermion triplets ($\Sigma \equiv (\Sigma^+, \Sigma^0, \Sigma^-)^T$) with null hypercharge. The contribution to the Yukawa term due to the additional fermion triplet is:

$$-L_Y = \bar{l}_L Y_\Sigma^\dagger (\tau \cdot \Sigma) \tilde{\phi} + h.c \quad (1.31)$$

After electroweak symmetry breaking this Yukawa term leads to a mass matrix for the neutrinos and is given by :

$$\mathcal{M} = \begin{pmatrix} 0 & M_D^T \\ M_D & M_\Sigma \end{pmatrix} \quad (1.32)$$

where $M_D = \frac{v}{\sqrt{2}} Y_\Sigma$ is the Dirac mass term and M_Σ is the Majorana mass of Σ particle. If $M_\Sigma \gg v$, then the small neutrino mass is given by

$$M_\nu = M_D^T M_\Sigma^{-1} M_D. \quad (1.33)$$

1.3 Muon $g - 2$ anomaly

The magnetic moment (μ) of a particle is given as

$$\vec{\mu} = g \left(\frac{q}{2m} \right) \vec{S}, \quad (1.34)$$

where \vec{S} is the spin of the particle and g being the gyromagnetic ratio. Stern and Gerlach for the first time measured the gyromagnetic ratio of electron. For a spin 1/2 structureless particle, Dirac equation predicts the value of $g = 2$. However due to various effects g is not exactly two. Since muon is a point particle, it must be expected that the gyromagnetic ratio should be equal to 2. However due to quantum corrections, the gyromagnetic ratio differs from 2. All the quantum corrections to

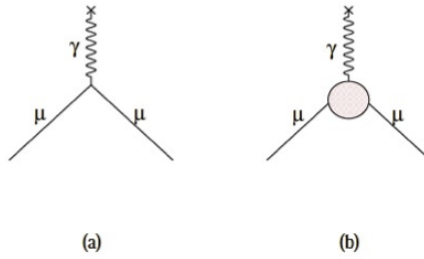


Figure 1.8: Contribution to magnetic moment of muon. (a) corresponds to $g = 2$, (b) corresponds to general diagram showing correction to $g - 2$ value.

the magnetic moment is expressed in

$$a_\mu \equiv \frac{g_\mu - 2}{2} \quad (1.35)$$

where a_μ is called as the anomalous magnetic moment of muon with gyromagnetic ratio g_μ . In the SM the anomalous magnetic moment is coming from corrections from (i) Quantum Electrodynamics

interactions, (ii) Weak interactions , (iii) Hadronic or Quantum chromodynamics interactions. In a simpler way

$$a_{\mu}^{SM} = a_{\mu}^{QED} + a_{\mu}^{Weak} + a_{\mu}^{Had} \quad (1.36)$$

The recent observational evidence suggests that there is more than 3σ discrepancy in the measured value[28] and the SM prediction of a_{μ} value [29]. The difference is given by:

$$\Delta a_{\mu} = a_{\mu}^{expt} - a_{\mu}^{SM} = (295 \pm 88) \times 10^{-11} . \quad (1.37)$$

So this discrepancy motivates one to think of a beyond SM interactions contributing to a_{μ} value. In this thesis we will address this issue in an extended $U(1)$ model of the SM.

1.4 Observed 3.5 keV X-ray line by XMM-Newton Observatory

Recently the XMM-Newton observatory reported a $(3.55 - 3.57) \pm 0.03$ keV X-ray signal from the spectrum of 73 galaxy clusters [7]. There is more than 3σ confidence level of the detected X-ray. To verify that whether this line is originating from one of the dominating clusters in the sample

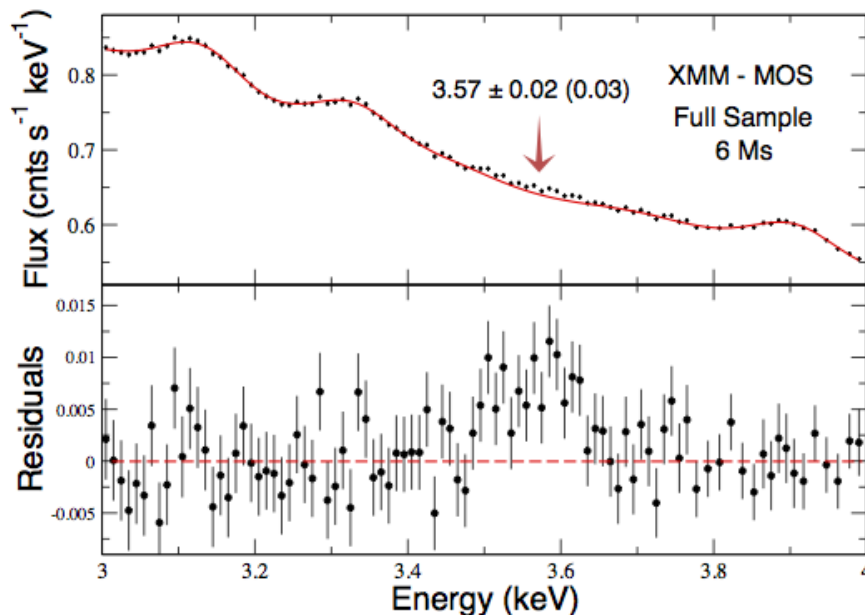


Figure 1.9: The excess of 3.5 keV line as observed in XMM Newton Observatory in the full sample of 73 cluster of galaxies. Picture is borrowed from [7].

a method is implemented by dividing the full sample into 3 different sub samples namely-Perseus, Centaurus + Coma + Ophiuchus, and all others, and then studying separately these 3 sub samples. In the results they conclude that the line was found in all these three sub samples with a flux of $1.6_{-0.4}^{+0.3} \times 10^{-5}$ photons per $\text{cm}^{-2} \text{s}^{-1}$ at 3.57 keV. The authors [7] also argued that this line does not correspond to any atomic transition present in the plasma. The possible origin could be a decaying

sterile neutrino. So this observation is also inviting physics beyond the SM to explain it. In this thesis we try to explain the origin of this signal due to a dipolar DM which will be explained in full detail in the next chapter.

1.5 Aim of the Thesis

From the discussions of the previous sections we conclude that the SM may not be sufficient to explain various experimental observations. To explain the various observed phenomena, such as existence of DM, non-zero masses of active light neutrinos, muon $g - 2$ anomaly, 3.5 KeV X-ray line *etc.* we need to explore physics beyond the SM while satisfying the existing experimental constraints. Our goal will be to build up models which can explain more than one phenomena simultaneously. As a result strong constraints on the model parameters can be emerged which can be measured at different experiments.

1.6 Thesis Overview

The thesis is organised as follows. In chapter 1 the basic introduction about the DM is presented. The evidence of DM from various experiments is discussed. The physics of DM and its freeze out from the thermal bath is also studied. The freeze out mechanism is presented in a lucid manner by solving the Boltzmann equation. A brief summary of the experimental detection of DM is discussed. The massiveness of the neutrinos is presented in various seesaw models. Then the anomalous magnetic moment of the muon and the observed 3.5 keV X-ray line by the XMM Newton observatory is mentioned. In chapter 2 a dipolar DM model is proposed in order to explain neutrino mass and DM. The model also explains the 3.5 keV X-ray signal as observed by XMM Newton observatory by introducing a transition magnetic moment operator. In chapter 3, a mixed singlet-doublet DM model is considered. The DM parameter space is explored in the model by considering different constraints from relic density of DM and direct detection experiments. In the same model the smallness of neutrino mass is also presented in a Type II seesaw scenario. In a further application of the model, the 750 GeV diphoton resonance is also explained by the model as claimed by CMS and ATLAS. In chapter 4, a $U(1)$ gauge extension of the SM is considered. In the model the new $U(1)$ gauge boson couples to the muon, and hence can contribute to the magnetic moment. So the anomaly of the muon magnetic moment is explained. In the same model the DM phenomenology as well as the neutrino mass are also explored. In chapter 5 conclusion is drawn in a very brief manner.

Chapter 2

Dipolar Dark Matter and 3.5 keV x-ray line

2.1 Introduction

In 2014, the XMM-Newton X-ray observatory reported an X-ray signal of 3.5 keV in the energy spectrum of 73 galaxy clusters [7, 30]. Since the galaxy clusters are huge sources of dark matter (DM) the origin of this line may be related to the DM. If confirmed by others this can give a strong hint for the non-gravitational interaction of DM. There are a few attempts in order to explain the origin of this X-ray line with relation to the DM. The possible processes which can give rise to such a signal are : (i) decaying dark matter or annihilating DM [31, 32, 33, 34, 35, 36, 37, 38, 39, 40, 41, 42], (ii) magnetic dipolar dark matter (via up scattering of DM into an excited states and subsequent decay of excited states into DM and an X-ray photon) [43, 44, 45, 46, 47, 48, 49], (iii) others [50, 51, 52, 53, 54, 55, 56, 57, 58, 59, 60, 61, 62, 63, 64, 65, 66, 67, 68, 69, 70, 71, 72, 73]. The decay/annihilation of a multi keV dark matter or the decay of next to lightest stable particle to the lightest stable particle with a keV mass splitting can explain the origin of the signal. However the SM does not accommodate such particles. So to explain such a phenomena we have to look beyond the SM scenario.

Apart from this, there is also evidence of new physics in order to explain the DM of the universe which is mentioned in chapter 1. Moreover, the small neutrino mass can not be explained in SM (see sec 1.2). To explain the various phenomena mentioned above in a single framework, we extended the SM by adding a new set of 3 right handed fermions (N_1, N_2, N_3), an extra Higgs doublet (Σ) and a singlet charged scalar H^+ . With these minimal set of particles a discrete symmetry $Z_2 \times Z'_2$ is also imposed, which does not allow a mixing in the right handed neutrinos(RHN) sector. A soft breaking of the discrete symmetry allows a mixing between N_1 and N_2 which creates a mass splitting between the two. This small mass splitting allows the next to lightest stable particle (NLSP) N_2 to decay N_1 through the electromagnetic dipole moment operator. If the mass splitting between the two is order of 3.5 keV, then the emitted photon can explain the findings of XMM-Newton observatory. Again the lifetime of N_2 is larger than the universe so that it is decaying in the current epoch and it can also contribute to the relic abundance of DM. The decay of N_2 to N_1 converts its density to N_1 while keeping the total DM density intact. Due to the presence of RHNs, a lepton number violating

Majorana mass term is possible for the heavy neutrinos. As a result the light neutrinos get sub-eV order of mass either in the tree level or in the loop level.

2.2 The Model

We extended the SM by adding three right handed SM singlet fermions(N_{iR}). A charged scalar particle (H^+) and a Higgs (Σ) are also added which transform like singlet and doublet under $SU(2)_L$ respectively. The masses of all these particles are \mathcal{O} (TeV). In order to stabilize the lightest singlet fermion a $Z_2 \times Z'_2$ symmetry is also imposed. As a result the lightest stable particle (LSP) serves as a viable DM candidate. The particle content of the Model and corresponding quantum numbers are displayed in the table. 2.1 The complete Lagrangian can be written as :

Table 2.1: Particle content of the proposed Model.

	Field	$SU(3)_C \times SU(2)_L \times U(1)_Y$	$Z_2 \times Z'_2$
Fermions	$Q_L \equiv (u, d)_L^T$	(3, 2, 1/6)	+ +
	u_R	(3, 1, 2/3)	+ +
	d_R	(3, 1, -1/3)	+ +
	$\ell_L \equiv (\nu, e)_L^T$	(1, 2, -1/2)	+ +
	e_R	(1, 1, -1)	+ +
	N_{1R}	(1, 1, 0)	- +
	N_{2R}	(1, 1, 0)	+ -
	N_{3R}	(1, 1, 0)	+ +
Scalars	Φ	(1, 2, +1/2)	+ +
	Σ	(1, 2, +1/2)	+ -
	H^+	(1, 1, +1)	- +

$$\mathcal{L} = \mathcal{L}_{\text{SM}} + \mathcal{L}_{\text{New}}$$

where \mathcal{L}_{SM} is the SM Lagrangian while the new physics Lagrangian \mathcal{L}_{New} contains all terms containing any of the new particles including the right handed neutrinos and is given by:

$$\begin{aligned} \mathcal{L}_{\text{New}} \ni & (Y_H)_{1\alpha} N_{1R}^T C \ell_{\alpha R} H^+ + (Y_\Sigma)_{\alpha 2} \overline{\ell_{\alpha L}} \tilde{\Sigma} N_{2R} \\ & + (Y_\nu)_{\alpha 3} \overline{\ell_{\alpha L}} \tilde{\Phi} N_{3R} + (Y_e)_{\alpha\beta} \overline{\ell_{\alpha L}} \Phi \ell_{\beta R} \\ & + \frac{1}{2} \overline{(N_{iR})^C} M_{Ni} N_{iR} + \text{h.c.} + V(\Phi, \Sigma, H^+) \end{aligned} \quad (2.1)$$

where the scalar potential can be given by:

$$\begin{aligned} V(\Phi, \Sigma, H^+) = & -\mu_\Phi^2 |\Phi|^2 + M_\Sigma^2 |\Sigma|^2 + M_H^2 |H^\pm|^2 \\ & + \lambda_\Phi |\Phi|^4 + \lambda_\Sigma |\Sigma|^4 + \lambda_H |H^\pm|^4 \\ & + \lambda_{\Phi H} (\Phi^\dagger \Phi) |H^\pm|^2 + \lambda_{\Sigma H} (\Sigma^\dagger \Sigma) |H^\pm|^2 \\ & + f |\Phi|^2 |\Sigma|^2 + \frac{\lambda_{\Phi\Sigma}}{2} [(\Phi^\dagger \Sigma)^2 + \text{h.c.}] . \end{aligned} \quad (2.2)$$

Since Σ is ascribed a positive mass squared term it does not get any vacuum expectation value

(vev). It is also assumed that the individual masses of the newly added scalar particles are greater than the right handed fermions i.e. $M_\Sigma, M_{H^\pm} > M$, with $M_1 \sim M_2 \sim M_3 = M$, so that the decays $N_1 \rightarrow \ell_R H^+$ and $N_2 \rightarrow \nu_L + \Sigma^0$ are kinematically forbidden. As a result N_1, N_2 are individually stable. However under $Z_2 \times Z'_2$ symmetry, N_3 goes to itself and hence it is not stable. It can decay through the process: $N_3 \rightarrow \nu_i \Phi^0$. The smallness of neutrino mass can be explained in a type I seesaw scenario by N_3 .

The mixing between N_1 and N_2 is forbidden by the $Z_2 \times Z'_2$ symmetry. A small mixing between them is generated by breaking $Z_2 \times Z'_2$ softly with:

$$\mathcal{L}_{\text{soft}} = [\mu_s \Sigma \Phi (H^+)^* + h.c.] , \quad (2.3)$$

where the scale of μ_s will be determined from the observed phenomenon. The $Z_2 \times Z'_2$ symmetry breaking term generates a mixing between N_1 and N_2 and as a result N_2 can decay via $N_2 \rightarrow N_1 + \gamma$. The emitted photon can be identified with the recent observation of 3.5 keV X-ray line signal by the XMM-Newton X-ray observatory.

2.2.1 Constraints on new particles

The scalar doublet Σ also has interaction with SM Z particle. As a result it can modify the decay width of the Z boson. In order to forbid the decay of Z to Σ we impose the constraint $M_\Sigma > M_Z/2$. As a result the decay is not kinematically allowed. In other words

$$M_\Sigma > 45\text{GeV} . \quad (2.4)$$

The mass of the singlet charged scalar H^\pm is lower bounded by LEP. It is given to be [74]

$$M_H > 80\text{GeV} . \quad (2.5)$$

2.2.2 Mass splitting between N_1 and N_2

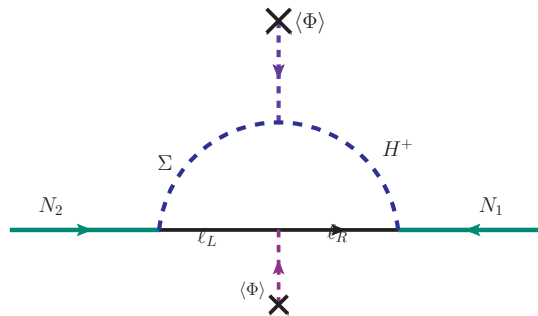


Figure 2.1: Mass splitting between N_1 and N_2 due to radiative correction through breaking of $Z_2 \times Z'_2$ symmetry.

The breaking of $Z_2 \times Z'_2$ symmetry generates a mixing between N_1 and N_2 as mentioned above.

The mixing can be calculated from the Fig. 2.1 as

$$\Delta M_{12} = -Y_{H1\alpha}^* Y_{\Sigma\alpha 2} \mu_s v_{ew} \int \frac{d^4 k}{(2\pi)^4} \frac{i(\not{p} - \not{k} + m_\ell)}{[(p-k)^2 - m_\ell^2 + i\epsilon]} \frac{i}{(k^2 - M_H^2)} \frac{i}{(k^2 - M_\Sigma^2)} \quad (2.6)$$

Before doing the integration we note that we will calculate this integral in the limit $p \rightarrow 0$. And the integration involving \not{k} will go to zero due to the symmetry argument. So we will end up with the expression :

$$\Delta M_{12} = iY_{H1\alpha}^* Y_{\Sigma\alpha 2} \mu_s v_{ew} \int \frac{d^4 k}{(2\pi)^4} \frac{m_\ell}{[k^2 - m_\ell^2 + i\epsilon]} \frac{1}{(k^2 - M_H^2)} \frac{1}{(k^2 - M_\Sigma^2)} \quad (2.7)$$

At this point we will perform the Wick rotation, so that we can go from Minkowski space to the Euclidean space by changing the variables to :

$$k^0 = ik_E^0, \quad \vec{k} = \vec{k}_E$$

Now the expression becomes:

$$\begin{aligned} \Delta M_{12} &= (iY_{H1\alpha}^* Y_{\Sigma\alpha 2} \mu_s v_{ew} m_\ell) \frac{-i}{(2\pi)^4} \int d^4 k_E \frac{1}{(k_E^2 + m_\ell^2)} \frac{1}{(k_E^2 + M_H^2)} \frac{1}{(k_E^2 + M_\Sigma^2)} \\ &= (Y_{H1\alpha}^* Y_{\Sigma\alpha 2} \mu_s v_{ew} m_\ell) \frac{1}{(2\pi)^4} (2\pi^2) \int_0^\infty k_E^2 dk_E \frac{1}{(k_E^2 + m_\ell^2)} \frac{1}{(k_E^2 + M_H^2)} \frac{1}{(k_E^2 + M_\Sigma^2)} \quad (2.8) \\ &= (Y_{H1\alpha}^* Y_{\Sigma\alpha 2} \mu_s v_{ew} m_\ell) \times \\ &\quad \frac{m_\ell^2(M_H^2 - M_\Sigma^2) \ln(m_\ell^2) + M_H^2(M_\Sigma^2 - m_\ell^2) \ln(M_H^2) + M_\Sigma^2(m_\ell^2 - M_H^2) \ln(M_\Sigma^2)}{(m_\ell^2 - M_H^2)(m_\ell^2 - M_\Sigma^2)(M_H^2 - M_\Sigma^2)} \end{aligned}$$

Since $m_\ell \ll M_{\Sigma, H}$, we can safely neglect the terms involving m_ℓ^2 . So the mixing is given by :

$$\Delta M_{12} = \frac{Y_{H1\alpha}^* Y_{\Sigma\alpha 2}}{16\pi^2} \frac{\mu_s v_{ew} m_\ell}{(M_\Sigma^2 - M_H^2)} \ln\left(\frac{M_\Sigma^2}{M_H^2}\right) \quad (2.9)$$

The Majorana mass matrix in the basis of (N_1, N_2, N_3) is given by:

$$\begin{pmatrix} M_1 & \Delta M_{12} & 0 \\ \Delta M_{12} & M_2 & 0 \\ 0 & 0 & M_3 \end{pmatrix} \quad (2.10)$$

Diagonalizing the mass matrix, we get the mass eigenvalues $M_1 + \Delta M_{12}$ and $M_2 - \Delta M_{12}$ and M_3 . Thus the mass splitting between the two eigenstates N_1 and N_2 is given by

$$\delta = 2\Delta M_{12}. \quad (2.11)$$

If mass of N_2 is heavier than N_1 then, the N_2 can decay to N_1 and a monochromatic photon with energy equal to the mass difference between the two. The lifetime of N_2 should be greater than the age of the universe so that it can decay in the current epoch. The recent observation of the X-ray

line can be explained if the mass splitting is ~ 3.5 keV. Using these information from eq. 2.9, we can estimate the soft symmetry breaking term to be:

$$\mu_s \simeq 1.6 \times 10^{-2} \text{GeV} \left(\frac{(M_\Sigma^2 - M_H^2)/\ln[M_\Sigma^2/M_H^2]}{10^4 \text{ GeV}^2} \right) \left(\frac{\Delta M_{12}}{3.5 \text{ keV}} \right) \left(\frac{0.5^2}{Y_H^* Y_\Sigma} \right) \left(\frac{246 \text{ GeV}}{v_{\text{EW}}} \right) \left(\frac{1.7 \text{ GeV}}{m_l} \right) \quad (2.12)$$

In the above equation the normalization of $\left(\frac{(M_\Sigma^2 - M_H^2)/\ln[M_\Sigma^2/M_H^2]}{10^4 \text{ GeV}^2} \right)$ holds for $M_\Sigma \sim M_H = \mathcal{O}(100)$ GeV and $M_\Sigma - M_H = \mathcal{O}(\text{keV-GeV})$. From eq. 2.12 we see that for $M_\Sigma \sim M_H \sim 100 \text{ GeV}$ the mixing between Σ and H particles is $\tan 2\theta \approx \mu_s v_{\text{EW}} / (M_\Sigma^2 - M_H^2) \approx \mathcal{O}(10^{-4})$.

2.3 Magnetic DM and explanation to 3.5 keV X-ray line

The RH neutrinos N_i are Majorana in nature. As a result the diagonal magnetic moment vanishes. But there is transition magnetic moment possible for them. The electromagnetic coupling for the heavy neutrinos with photons, via the dimension five effective magnetic dipole moment (MDM) operator is given by

$$\mathcal{L}_{\text{MDM}} = -\frac{i}{2} N_{Rj} C^{-1} \mu_{jk} \sigma_{\alpha\beta} N_{Rk} \mathcal{F}^{\alpha\beta} + \text{h.c.} \quad (j \neq k). \quad (2.13)$$

where $\mathcal{F}^{\alpha\beta}$ is the electromagnetic field tensor and μ_{12} is the transition magnetic moment between the first and second generation of heavy right-handed Majorana neutrinos N_2, N_1 . The possible Feynman diagrams which yield transitional magnetic moment μ_{12} and decay process $N_2 \rightarrow N_1 \gamma$ are shown in Fig. 2.2. The magnetic moment of DM is calculated from the figure as (see appendix B) :

$$\mu_{12} = -\frac{-e}{64 \pi^2} \frac{(Y_H^* Y_\Sigma \mu_s v_{\text{ew}})}{M_\Sigma^2 - M_H^2} \frac{m_l}{M_\Sigma^2} \mathcal{I}_{\text{tot}} \quad (2.14)$$

where

$$\mathcal{I}_{\text{tot}} \simeq \int_0^1 dx \left[\frac{x(1-x)^2}{(1-x)M_H^2/M_\Sigma^2 + x(x-1)M_2^2/M_\Sigma^2 + x} - \frac{x(1-x)^2}{(1-x) + x(x-1)M_2^2/M_\Sigma^2 + xM_H^2/M_\Sigma^2} \right]. \quad (2.15)$$

Since N_2 is little bit heavier than N_1 with a difference in mass lying in $\mathcal{O}(3.5 \text{ keV})$, the former can decay to later by emitting a monochromatic photon. The decay width is given by

$$\begin{aligned} \Gamma(N_2 \rightarrow N_1 \gamma) &= \frac{M_2^3}{8\pi} \left(1 - \frac{M_1^2}{M_2^2} \right)^3 |\mu_{12}|^2 \\ &= \frac{|\mu_{12}|^2}{\pi} \delta^3, \end{aligned} \quad (2.16)$$

where

$$\delta \equiv E_\gamma = \frac{M_2}{2} \left(1 - \frac{M_1^2}{M_2^2} \right) \quad (2.17)$$

is the energy of the emitted photon, which is nothing but the mass difference between N_1 and N_2 . To explain the observed X-ray line the we use $\delta = 3.5 \text{ keV}$, and the decay width to be $\Gamma(N_2 \rightarrow N_1 \gamma) = (0.36 - 3.3) \times 10^{-52} \text{ GeV} (M_2/3.5 \text{ keV})$ [7, 36, 49] for the decaying DM. Since the life time of

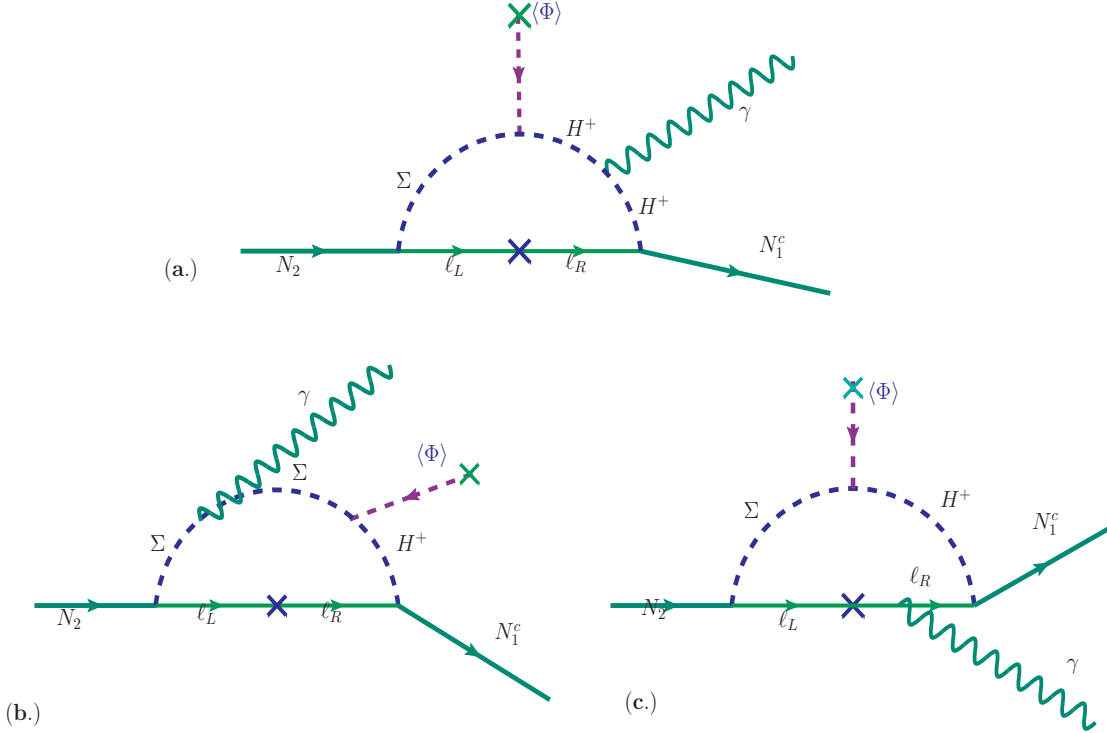


Figure 2.2: Feynman diagram for magnetic DM decay: $N_2 \rightarrow N_1 \gamma$.

the DM is longer than the age of the Universe, we get from the observed X-ray line an upper bound on the mass of DM to be $M_2 < (16 - 146)\text{TeV}$. This implies that a DM mass varying between a few keV to $\mathcal{O}(100)\text{TeV}$ can in principle give the observed X-ray line. In particular, for $M_2 = 100 \text{ GeV}$, the decay rate is $\mathcal{O}(10^{-44})\text{GeV}$. In other words the life time of N_2 is $\mathcal{O}(10^{19})\text{sec}$, which is longer than the age of the Universe. From Eq. (2.16) one can also estimate the required magnetic moment to be $\mu_{12} = \mathcal{O}(10^{-14})\text{GeV}^{-1}$, which is consistent with Eq. (2.14).

2.3.1 Estimation of the new physics scale and collider search

To estimate the scale of new physics, let us define a ratio $R \equiv \frac{\mu_{12}}{\delta}$. Using Eqs. (2.9), (2.11) and (2.14) we get

$$R = \frac{e}{8} \frac{1}{M_\Sigma^2} \frac{I_{\text{tot}}}{\ln(M_\Sigma^2/M_H^2)}. \quad (2.18)$$

In the above equation I_{tot} can be evaluated numerically. For a typical set of values, 350 GeV DM mass, using $\delta = 3.5\text{keV}$ and $\mu_{12} = 2.46 \times 10^{-14} \text{GeV}^{-1}$ we get $M_\Sigma \approx M_H = 380\text{GeV}$. Thus the mass scale of the new particles are not far from the electroweak scale and hence can be searched at colliders. In particular, the charged scalars H^\pm and Σ^\pm are important. These particles can be pair produced at LHC via the exchange of SM Higgs particle. For example, $pp \rightarrow h \rightarrow H^+ H^- \rightarrow e^+ e^- + \text{missing energy}$. Similarly, $pp \rightarrow h \rightarrow \Sigma^+ \Sigma^- \rightarrow e^+ e^- + \text{missing energy}$. Σ^\pm particles can also be detected through other decay processes, such as: $\Sigma^\pm \rightarrow W^\pm \Sigma^0 (\Sigma^{0*}) \rightarrow f \bar{f} f_1 \bar{f}_2$, where f, f_1, f_2 are SM fermions.

2.4 Neutrino mass

After the electro-weak phase transition one of the Yukawa term $(Y_\nu)_{\alpha 3} \bar{\ell}_{\alpha L} \tilde{\Phi} N_{3R}$ generates a Dirac mass term: $(M_D)_{\alpha 3} = (Y_\nu)_{\alpha 3} v_{ew}$, where $v_{ew} = \langle \Phi \rangle$ and $\alpha = e, \mu, \tau$. At the same time the N_3 particle also has a Majorana mass term $M_3 N_3 N_3$ which breaks the lepton number by two units. As a result a Majorana mass matrix for the light neutrinos is obtained which is

$$(m_\nu)_{\alpha\beta} = \frac{v^2}{M_3} (Y_\nu)_{\alpha 3} (Y_\nu)_{\beta 3} \quad (2.19)$$

After diagonalisation of the above mass matrix, the eigen values are given by $\text{Tr} [(Y_\nu)_{\alpha 3} (Y_\nu)_{\beta 3}] v_{ew}^2 / M_3$, 0, 0. Thus at tree level one of the light neutrinos say ν_3 gets mass. This is because of the exact $Z_2 \times Z'_2$ symmetry in the Lagrangian which prevents the Yukawa terms $\bar{\ell}_\alpha \Phi N_{1R}$ and $\bar{\ell}_\alpha \Phi N_{2R}$. On the other hand, the fact that $M_\Sigma^2 > 0$ prevents a vacuum expectation value for Σ field, we can not generate a Majorana mass of light neutrinos at the tree level through the coupling: $Y_{\Sigma\alpha 2} \bar{\ell}_{\alpha L} \tilde{\Sigma} N_{2R}$. However the light neutrinos can get mass in radiative corrections in one loop level. The diagram relevant for the neutrino mass generation is shown in fig. 2.3.

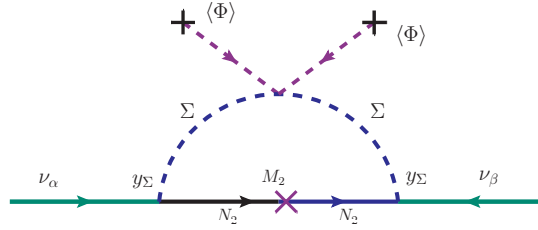


Figure 2.3: One loop diagram contributing to Majorana mass of light neutrinos.

Due to the presence of a quartic coupling $\frac{\lambda_{\Phi\Sigma}}{2} [(\Phi^\dagger \Sigma)^2 + h.c.]$, the electroweak phase transition generates a mass splitting: $\lambda_{\Phi\Sigma} v^2$ between the real (Σ_R^0) and imaginary (Σ_I^0) components of Σ^0 , the neutral component of Σ field. The neutrino mass matrix can be calculated from the diagram (see appendix A) [75]

$$(m_\nu^{\text{loop}})_{\alpha\beta} = \frac{(Y_\Sigma)_{\alpha 2} (Y_\Sigma)_{\beta 2} M_2}{16\pi^2} \left[\frac{M_{\Sigma_R}^2}{(M_{\Sigma_R}^2 - M_2^2)} \ln \left(\frac{M_{\Sigma_R}^2}{M_2^2} \right) - \frac{M_{\Sigma_I}^2}{(M_{\Sigma_I}^2 - M_2^2)} \ln \left(\frac{M_{\Sigma_I}^2}{M_2^2} \right) \right] \quad (2.20)$$

Diagonalizing the above radiative mass matrix we get only one of the state massive, say ν_2 . Since the origin of the masses of the two eigen states ν_2 and ν_3 are different they can easily satisfy the solar and atmospheric mass splitting constraint.

2.5 Relic abundance of DM

The lightest stable particle (LSP), which is odd under $Z_2 \times Z'_2$ symmetry, is N_1 and hence serves as a viable dark matter candidate. The next to lightest stable particle N_2 can decay to N_1 and a photon. But the Electromagnetic coupling of N_1 and N_2 with photon is too small, the life time of N_2

is large and is comparable with the age of the universe. Therefore N_2 is also stable on cosmological time scale. Hence N_2 can also be a DM candidate. When N_2 decays its density gets converted to N_1 keeping the net DM abundance intact.

The DM can not be in thermal equilibrium with so small an electromagnetic coupling. For the DM to be in thermal equilibrium the dipole moment required is $\mu_{12} \sim \mathcal{O}(10^{-4})\text{GeV}^{-1}$ [76]. So the only way the right handed neutrinos are in thermal equilibrium is through the interaction of N_1 with singlet charged Higgs(H^+) and right handed charged leptons (ℓ_R) and that of N_2 with the $SU(2)_L$ doublets ℓ_L and Σ . The \mathcal{O} (keV) mass splitting between the N_1 and N_2 is irrelevant for DM relic abundance. So for all practical purpose we assume $M_1 = M_2 = M_{\text{DM}}$. In order to calculate the relic abundance of DM we use the freeze out mechanism. When the temperature of the universe falls below the mass scale of DM it freezes out from the thermal bath and its number density in a comoving volume remains constant afterwards. The decoupling temperature is given by $T_f = M_{\text{DM}}/x_f$, where $x_f \approx 25$. The relic abundance obtained through co-annihilation of N_1 with H^+ and that of N_2 with Σ can be given by [77, 78]

$$\Omega_{\text{DM}}h^2 = \frac{1.09 \times 10^9 \text{GeV}^{-1}}{g_*^{1/2} M_{\text{Pl}}} \times \frac{1}{J(x_f)} \quad (2.21)$$

where

$$J(x_f) = \int_{x_f}^{\infty} \frac{\langle \sigma|v \rangle_{\text{eff}}}{x^2} dx \quad (2.22)$$

with

$$\langle \sigma|v \rangle_{\text{eff}} = \langle \sigma|v \rangle_{\text{eff}}^{N_1} + \langle \sigma|v \rangle_{\text{eff}}^{N_2}. \quad (2.23)$$

In the above equation the effective co-annihilation cross-sections of N_1 with H^+ and that of N_2 with that of Σ are given as:

$$\langle \sigma|v \rangle_{\text{eff}}^{N_i} = \langle \sigma|v \rangle^{N_i-X} g_i g_X (1 + \Delta_X)^{3/2} \times \left(\frac{e^{-x\Delta_X}}{g_{\text{eff}}^2} \right) \quad (2.24)$$

where $g_i, i = 1, 2$ represents the internal degrees of freedom of N_1 and N_2 , g_X represents the internal degrees of freedom of X -particle (H^+, Σ) co-annihilating with $N_i, i = 1, 2$ and

$$g_{\text{eff}} = g_i + g_X (1 + \Delta_X)^{3/2} e^{-x\Delta_X}. \quad (2.25)$$

where $\Delta_X = (M_X - M_{\text{DM}})/M_{\text{DM}}$. The various cross-sections relevant to the relic density are given below.

$$\langle \sigma|v \rangle(N_{1R} + H^+ \Leftrightarrow \ell_R + \Phi) = \frac{(Y_H)_{1\alpha}^2}{64\pi M_H (s - m_\alpha^2)^2} \frac{m_f^2}{\langle \phi \rangle^2} s\sqrt{s} \left(1 - \frac{M_\Phi^2}{s} \right)^2 \quad (2.26)$$

$$\langle \sigma|v \rangle(N_{1R} + H^+ \Leftrightarrow \ell_R + Z) = \frac{1}{32\pi M_H} \left(\frac{g(Y_H)_{1\alpha}(T_3 - \sin^2\theta_W Q)}{\cos\theta_W (s - m_\alpha^2 + i\epsilon)} \right)^2 s\sqrt{s} \left(1 - \frac{m_Z^2}{s} \right)^2 \quad (2.27)$$

$$\langle \sigma|v \rangle(N_{1R} + H^+ \Leftrightarrow \ell_R + \gamma) = \frac{e^2}{32\pi M_H} \frac{(Y_H)_{1\alpha}^2}{(s - m_\alpha^2)^2} s\sqrt{s} \quad (2.28)$$

where $\alpha = e, \mu, \tau$

The relic abundance of N_2 is obtained through its co-annihilation with Σ particles via the following processes are

$$\langle\sigma|v\rangle(N_{2R} + \Sigma^0 \Leftrightarrow l_L + W) = \frac{1}{64\pi M_\Sigma} \frac{g^2(Y_\Sigma)_{2\alpha}^2}{\sqrt{s}} \left(1 - \frac{m_W^2}{s}\right)^2 \quad (2.29)$$

$$\langle\sigma|v\rangle(N_{2R} + \Sigma^0 \Leftrightarrow \nu_L + Z) = \frac{1}{128\pi M_\Sigma} \frac{g^2(Y_\Sigma)_{2\alpha}^2}{\cos^2\theta_W\sqrt{s}} \left(1 - \frac{m_Z^2}{s}\right)^2 \quad (2.30)$$

$$\langle\sigma|v\rangle(N_{2R} + \Sigma^- \Leftrightarrow \nu_L + W) = \frac{1}{64\pi M_\Sigma} \frac{g^2(Y_\Sigma)_{2\alpha}^2}{(s - m_\alpha^2 + i\epsilon)^2} s\sqrt{s} \left(1 - \frac{m_W^2}{s}\right)^2 \quad (2.31)$$

$$\langle\sigma|v\rangle(N_{2R} + \Sigma^- \Leftrightarrow e_L + Z) = \frac{1}{32\pi M_\Sigma} \frac{g^2(Y_\Sigma)_{2\alpha}^2 (T_3 - \sin^2\theta_W Q)^2}{\cos^2\theta_W (s - m_\alpha^2 + i\epsilon)^2} s\sqrt{s} \left(1 - \frac{m_Z^2}{s}\right)^2 \quad (2.32)$$

$$\langle\sigma|v\rangle(N_{2R} + \Sigma^- \Leftrightarrow e_L + \gamma) = \frac{e^2(Y_\Sigma)_{2\alpha}^2}{32\pi M_\Sigma (s - m_\alpha^2 + i\epsilon)^2} s\sqrt{s} \quad (2.33)$$

$$\langle\sigma|v\rangle(N_{2R} + \Sigma^- \Leftrightarrow e_R + \Phi) = \frac{(Y_\Sigma)_{2\alpha}^2}{64\pi M_\Sigma (s - m_\alpha^2 + i\epsilon)^2} \frac{m_f^2}{\langle\Phi\rangle^2} s\sqrt{s} \left(1 - \frac{M_\Phi^2}{s}\right)^2 \quad (2.34)$$

The contribution to the relic density of DM can be estimated by defining the branching ratios as:

$$\begin{aligned} r_1 &= \frac{\langle\sigma|v\rangle_{N_1}}{\langle\sigma|v\rangle_{N_1} + \langle\sigma|v\rangle_{N_2}} \\ r_2 &= \frac{\langle\sigma|v\rangle_{N_2}}{\langle\sigma|v\rangle_{N_1} + \langle\sigma|v\rangle_{N_2}} \end{aligned} \quad (2.35)$$

A plot is shown in fig. 2.4 with r_1 and r_2 as a function of M_{DM} taking the couplings $Y_\Sigma = Y_H = Y$.

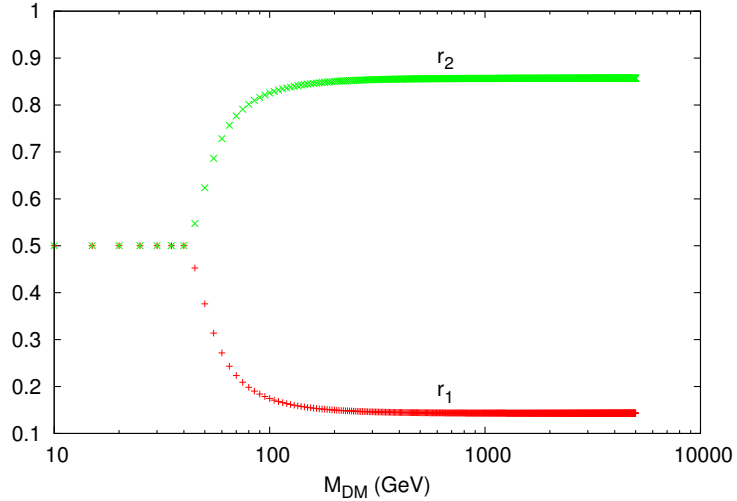


Figure 2.4: r_1 and r_2 as a function of M_{DM} for $Y_\Sigma = Y_H$. For simplicity we set $M_{\text{DM}} = M_X$.

For simplicity the masses of new scalars also assumed to be equal $M_{H^+} = M_\Sigma = M_X$. To see the effect of mass splitting between the coannihilation partner (M_X) and the DM (M_{DM}) on the relic abundance we plotted the $\Omega h^2 / (\Omega h^2)_{\text{deg}}$ as a function of $M_X - M_{\text{DM}}$ as shown in fig. 2.5. Where $(\Omega h^2)_{\text{deg}}$ is the relic abundance in the zero mass splitting limit. We can clearly read from the fig. 2.5,

the relic abundance increases as the mass splitting increases. It is because the coannihilation cross section depends on the mass splitting which suffers a Boltzmann suppression i.e $\langle\sigma|v|\rangle \propto e^{-x\Delta x}$. As a result the effective cross section decreases with increase in mass splitting hence leading to increase of relic abundance. To explore more on the parameter space we calculate the relic abundance of

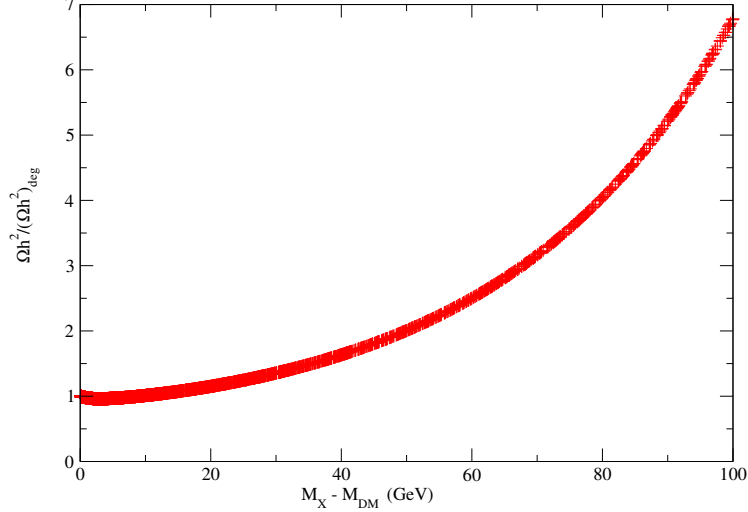


Figure 2.5: Ratio of DM abundance as a function of $M_X - M_{\text{DM}}$ for a typical mass of DM, $M_{\text{DM}} = 1000\text{GeV}$ and $Y_\Sigma = Y_H = 0.55$

DM for various couplings. This is shown in fig. 2.6. We have plotted the correct relic abundance as allowed by PLANCK as a function of M_{DM} and $\Delta M = M_X - M_{\text{DM}}$ for different Yukawa coupling strength $Y = 0.1, 0.5, 1.0, 2.0, 3.5$. The coannihilation cross-section is proportional to $e^{-\Delta M}$, as a

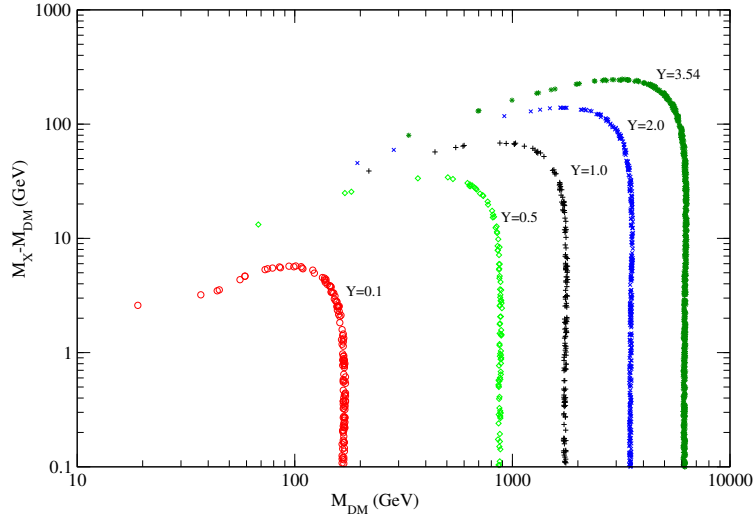


Figure 2.6: Scatter plots for observed relic abundance in the plane of $M_X - M_{\text{DM}}$ versus M_{DM} for different values of the Yukawa couplings: $Y = Y_\Sigma = Y_H$.

result for small value of mass splitting the cross-section will be large. That's why we get more points near $\Delta M \sim 0$ for the correct relic abundance. Again for a fixed DM mass, if the coupling increases we need large mass splitting so that the effective crosssection will be in the correct range as to give

the observed relic abundance. This can be read easily from the fig 2.6 as we increase the coupling from $Y = 0.1$ to $Y = 3.5$, the perturbative limit. For smaller DM mass, the crosssection increases with further decrease in DM mass. So we need a mass splitting of the order of 10 GeV in order to get the correct relic abundance.

Let us now discuss the compatibility of parameter space satisfying relic abundance as well as explaining the 3.5 keV X-ray line. As we have mentioned in section (2.3), the decay width of DM, giving the X-ray line, is given by: $\Gamma(N_2 \rightarrow N_1\gamma) = 0.36 - 3.3 \times 10^{-52} \text{GeV}(M_2/3.5\text{keV})$ [7, 36, 49]. This implies that for a decaying DM, the allowed mass range by observed X-ray line is about 7 keV to 146 TeV, where the lower bound is obtained from kinematics while the upper bound is obtained assuming the life time of DM is longer than the age of the Universe. On the other hand the relic abundance of DM allows one to go all the way to 6000 GeV in the perturbative limit. So, the mass of DM allowed by the correct relic abundance is a subset of the mass allowed by the observed X-ray line.

2.6 Direct Detection of DM

We know that the direct detection of DM is a very challenging task. The null observation of any signal through direct interaction with the nucleon thus puts a constraint on the effective nucleon-DM scattering cross-section. In this section we study the constraint on model parameters from the bound obtained in the LUX experiment [6]. We note that the mass splitting between N_2 and N_1 is only 3.5 keV, so for all practical purposes we consider the spin independent DM-nucleon interaction $N_1 n \rightarrow N_2 n$, mediated by SM Higgs exchange and photon to be elastic. The Feynman diagram for DM-nucleon interaction for direct detection is shown in Fig. 2.7.

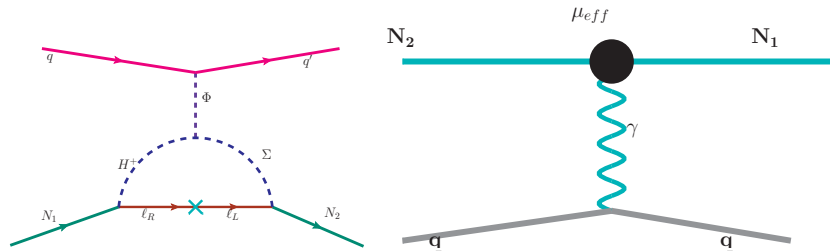


Figure 2.7: Elastic scattering of magnetic dipolar DM with target nuclei.

Contribution from Higgs exchange diagram

The diagram contributing to the direct detection via Higgs exchange is shown in the left panel of fig. 2.7. The effective coupling between $N_2 - N_1 - \Phi$ entering into this interaction can be given by:

$$\lambda_{\text{eff}} \simeq \frac{-\mu_S}{16\pi^2} Y_\Sigma Y_H^* m_\ell \mathcal{F}(M_H^2, M_\Sigma^2, m_\ell^2), \quad (2.36)$$

where

$$\mathcal{F}(M_H^2, M_\Sigma^2, m_\ell^2) = \frac{1}{M_H^2 - M_\Sigma^2} \times \left[\frac{1}{\frac{m_\ell^2}{M_H^2} - 1} \ln\left(\frac{m_\ell^2}{M_H^2}\right) - \frac{1}{\frac{m_\ell^2}{M_\Sigma^2} - 1} \ln\left(\frac{m_\ell^2}{M_\Sigma^2}\right) \right]. \quad (2.37)$$

The function $\mathcal{F}(M_H^2, M_\Sigma^2, m_\ell^2)$ follows from eq. 2.8. Thus the spin independent DM-nucleon cross-section can be given as:

$$\sigma_{SI} = \frac{\mu_n^2}{4\pi} \lambda_{\text{eff}}^2 \left(\frac{f_n m_n}{v_{\text{ew}}} \right)^2 \frac{1}{M_h^4} \quad (2.38)$$

where $\mu_n = M_{N_1} m_n / (M_{N_1} + m_n)$ is the reduced DM-nucleon mass with $m_n = 0.946\text{GeV}$ and $M_h = 125\text{GeV}$ is the SM Higgs mass. The effective coupling between the SM Higgs and nucleon is given by: $f_n m_n / v_{\text{ew}}$ which depend upon the quark content of the nucleon for each quark flavor. The Higgs-nucleon coupling f_n is given by:

$$f_n = \sum_q f_q = \frac{m_q}{m_n} \langle n | \bar{q}q | n \rangle \quad (2.39)$$

where the sum is over all quark flavors. In the present analysis, we have used $f_n = 0.32$ [79] though its value can lie within a range $f_n = 0.26 - 0.33$ [80]. Using $M_\Sigma \approx M_H = 100\text{GeV}$ and $Y_H = Y_\Sigma = 0.5$ we get $\sigma_{SI} \approx \mathcal{O}(10^{-59})\text{cm}^2$, which is much smaller than the current stringent limit: $\sigma_{SI} = 7.5 \times 10^{-46} \text{cm}^2$ from LUX.

Photon exchange contribution

From Fig. 2.7 (b) the spin independent DM-nucleon cross-section is given by

$$\sigma_{SI} = \frac{e^2 \mu_{12}^2}{16\pi} (Z f_p + (A - Z) f_n)^2 \quad (2.40)$$

where $f_p = f_n$ for the case of iso-spin conserving interaction and is given by Eq. (2.39). For LUX experiment $Z = 54$ while A varies between 74 to 80. Moreover, μ_{12} is given by Eq.(2.14). Using the same set of parameters used in section 2.3, we get $\sigma_{SI} \approx \mathcal{O}(10^{-57})\text{cm}^2$, which is much smaller than the current LUX limit. We note that, in this case, the LUX bound cannot be directly applied because the mediator is the massless photon that affects the event spectra of DM-nucleon scattering [81].

2.7 Summary and Outlook

In this chapter the minimal extension of the SM is presented to explain simultaneously the observed 3.5 keV X-ray line, neutrino mass as well as the DM phenomenology. Three right handed neutrinos (N_1, N_2, N_3) with two scalars, a charged singlet H^+ and a doublet Σ are added to the SM. The non trivial transformation of the new fields under a discrete $Z_2 \times Z_2'$ symmetry makes the lightest RHN (N_1) stable. Hence it serves as a viable DM candidate. The next to lightest stable particle (N_2) whose mass is only 3.5 keV greater than N_1 decays to $N_1 + \gamma$ in the present epoch. The number density of N_2 is then converted into N_1 while keeping the total DM abundance intact. The emerged

γ can be identified as the observed 3.5 keV X-ray line. Since N_3 couples to SM leptons and the Higgs doublet, a small Majorana mass is generated for one of the light neutrinos through canonical see-saw mechanism. The other neutrinos get their mass in one loop level. We have shown that the observed relic abundance requires the masses of the new scalars (H^+, Σ^+) are not far from electroweak scale. So these particles can be pair produced and their subsequent decay can be searched in LHC. The direct detection cross-section is very much suppressed. Hence there is no constraint coming from the LUX bound on the DM parameter space.

Chapter 3

Vector like mixed singlet-doublet fermionic Dark Matter and application to 750 GeV diphoton excess signal

3.1 Introduction

As mentioned in chapter 1 the SM is incomplete in the sense that it does not contain a dark matter (DM) particle. Again the smallness of neutrino mass is also not explained in the SM. So the limitation of SM theory suggests to look for physics in BSM frameworks.

In a simplistic approach to BSM scenario, a non-zero hypercharge particle generally gives large direct detection cross-section through the Z mediated DM-nucleon cross-section and hence ruled out unless some fine tune mechanism is employed to validate. Alternatively, a vector-like colourless fermion with zero hypercharge is a simple possibility to be considered as a candidate of DM in the BSM scenario. These fermions are similar to SM leptons even though they may not carry any leptonic charge. While the singlet and triplet leptons with hypercharge (Y) zero need an extra symmetry for their stability, the quintet fermion with $Y = 0$ is stable by itself [82]. The neutral component of these fermions can be a viable candidate of DM. Hence, the simplest fermionic DM is to introduce a singlet fermion (χ^0) odd under a Z_2 symmetry. However, without introducing additional fields, such DM can only have an effective interaction to the SM via a dimension five operator of the form $\bar{\chi}^0\chi^0 H^\dagger H/\Lambda$. In order to obtain a full theory of such an operator, one needs to introduce an additional scalar singlet (η) that mixes with the SM Higgs and thus yielding an effective Yukawa interactions of the fermionic DM to SM through terms like $\bar{\chi}^0\chi^0\eta \rightarrow \bar{\chi}^0\chi^0 h$ (see for example [83]). On the other hand, the neutral component of a vector-like doublet or a quartet lepton with non-zero hypercharge can not qualify itself to be a candidate of DM even in presence of an extra symmetry due to its large Z -mediated WIMP-nucleon elastic cross-section. However, a vector-like doublet DM can be reinstated in presence of a heavy scalar triplet [84, 85] where the relic

abundance mostly arises from an asymmetric component. The symmetric component of DM gets annihilated to the SM particles. On the other hand, if the SM is extended by multiple vector-like doublets and singlets, supplemented by a symmetry under which the new fermions are odd while all other SM fields are even, then the DM can emerge as an admixture of the neutral component of the doublets and singlets [86, 87, 88, 89, 90, 91, 92, 93, 94, 95, 96, 97]. We consider a model by augmenting the SM with two additional vector-like leptons: one doublet $N \equiv (N^0, N^-)^T$ and a singlet χ . A Z_2 symmetry is also imposed under which N and χ are odd while all other fields are even. As a result the DM emerges out to be a mixed state of singlet and neutral component of the doublet vector-like leptons.

In order to explain the smallness of neutrino mass as well as DM in the same model, a triplet scalar Δ is added with hypercharge 2 (for some earlier attempts, see [98, 99, 100, 101, 102, 103, 78]) on top of two additional vector-like leptons. We will see the effect of the scalar triplet on the DM phenomenology. Since the scalar triplet can be light, it contributes to the relic abundance of DM through s-channel resonance on top of Z and H mediation. Moreover, it relaxes the strong constraints coming from direct detection.

The triplet scalar not only couples to the SM lepton and Higgs doublets, but also to the additional vector-like lepton doublet N . The Majorana couplings of Δ with N , L and H is then be given by $f_N \Delta N N + f_L \Delta L L + \mu \Delta^\dagger H H$. Note that if the triplet is heavier than the DM and leptons, it can be integrated out and hence effectively generating the dimension five operators:

$$\left(\frac{LLHH}{\Lambda} + \frac{NNHH}{\Lambda} \right),$$

where $\Lambda \sim M_\Delta$. After EW symmetry breaking Δ acquires an induced vacuum expectation value (vev) of $\mathcal{O}(1)$ GeV which in turn give Majorana masses to light neutrinos as well as to N^0 . Since N^0 is a vector-like Dirac fermion, it can have a Dirac mass too. As a result N^0 splits up into two pseudo-Dirac fermions, with a mass splitting of sub-GeV order, whose elastic scattering with the nucleon mediated by Z -boson is forbidden. This feature of the model leads to a survival of larger region of parameter space from direct search constraints given by the latest data from Xenon-100 [12] and LUX [6]. On the other hand, the Higgs mediated elastic scattering of the DM with the nucleon gives an excellent opportunity to detect it at future direct search experiments such as XENON1T [104]. It is harder to see the signature of only DM production at collider as they need to recoil against an ISR jet for missing energy. However, the charged partner of the DM (which is next-to-lightest stable particle) can be produced copiously which eventually decays to DM giving rise to leptons and missing energy. More interestingly, the charged companion can also give large displaced vertex signature as we will elaborate.

3.2 The Model

The model contains two vector like fermions: a doublet $N^T (\equiv (N^0, N^-))$ (1,2,-1) and a singlet χ^0 (1,1,0), where the numbers inside the parentheses are the quantum numbers corresponding to the SM gauge group $SU(3)_c \times SU(2)_L \times U(1)_Y$ in addition to the SM particles. Since the particles

transform vector like under the SM gauge group, the anomaly is cancelled by exactly by the left and right component of the new fermions. As a result, the model is free from any gauge anomaly. A discrete symmetry Z_2 is also imposed under which N and χ^0 are odd, while all other fields are even. As a result the DM emerge as an admixture of N^0 and χ^0 . The relevant Lagrangian can be given as :

$$-\mathcal{L}_{\text{Yuk}} \supset M_N \bar{N} N + M_\chi \bar{\chi}^0 \chi^0 + \left[Y \bar{N} \tilde{H} \chi^0 + \text{h.c.} \right], \quad (3.1)$$

where M_N and M_χ are mass parameters corresponding to the doublet and singlet vector like leptons and Y denotes the interaction strength among them. Note here that due to vector-like nature, mass terms are perfectly gauge invariant. In Eq. (3.1), $\tilde{H} = i\tau_2 H^*$, where H is the SM Higgs iso-doublet

$H = \begin{pmatrix} H^+ \\ H_0 \end{pmatrix}$. After electroweak phase transition, the vacuum expectation value (vev) of SM Higgs

$\langle H \rangle = \begin{pmatrix} 0 \\ v \end{pmatrix}$ gives rise to a mixing between N^0 and χ^0 . In the basis (χ^0, N^0) , the mass matrix is

given by

$$\mathcal{M} = \begin{pmatrix} M_\chi & m_D \\ m_D & M_N \end{pmatrix}. \quad (3.2)$$

where $m_D = Yv$ and $v = 174$ GeV. Diagonalizing the above mass matrix we get two mass eigenvalues:

$$\begin{aligned} M_1 &\approx M_\chi - \frac{m_D^2}{M_N - M_\chi} \\ M_2 &\approx M_N + \frac{m_D^2}{M_N - M_\chi} \end{aligned} \quad (3.3)$$

where we have assumed $m_D \ll M_N, M_\chi$. The corresponding mass eigenstates are given by:

$$\begin{aligned} N_1 &= \cos \theta \chi^0 + \sin \theta N^0 \\ N_2 &= \cos \theta N^0 - \sin \theta \chi^0, \end{aligned} \quad (3.4)$$

where the mixing angle is:

$$\tan 2\theta = \frac{2m_D}{M_N - M_\chi}. \quad (3.5)$$

Note that N_2 is dominantly a doublet with a small admixture of singlet component. On the other hand, N_1 is dominantly a singlet with a small admixture of doublet component, which makes it a viable candidate of DM.

In the physical spectrum we also have a charged vector-like fermion N^\pm whose mass in terms of M_1 and M_2 and the mixing angle θ can be given as:

$$M^\pm = M_1 \sin^2 \theta + M_2 \cos^2 \theta \simeq M_N. \quad (3.6)$$

We will see later that the allowed values of the mixing angle is quite small, *i.e.* $\sin \theta \simeq 0.1$. Therefore, we have $M_2 \approx M_N$. This implies that the vector-like lepton N^\pm is almost degenerate to neutral

vector-like lepton N_2 , $M_2 \approx M^\pm$. Since $\sin \theta \sim 0.1$, we always get $M_N < M_2$ unless M_1 is quite large, say $M_1 > \mathcal{O}(10^4)$ GeV. For $M_1 \lesssim \mathcal{O}(10^4)$ GeV and $\sin \theta \lesssim 0.1$, we can have four possibilities in the mass spectrum of additional vector-like leptons as shown in the Fig. 3.1. From Fig. 3.1 (c) and (d) we see that the charged lepton is the lightest stable fermion and hence excluded from DM consideration. So, the remaining possibilities are Fig. 3.1 (a) and (b), where N_1 is the lightest stable particle (LSP) and is a suitable DM candidate. The next to lightest stable particle (NLSP) is the charged vector-like fermion N^- and next to next lightest stable particle (NNLSP) is N_2 . The mass splitting between N_1 and N^- is $(M_N - M_\chi) + m_D^2/(M_N - M_\chi)$, where as the mass splitting between N_1 and N_2 is $(M_N - M_\chi) + 2m_D^2/(M_N - M_\chi)$. Depending on the choice of M_1 and M_2 , the mass splitting between N_1 and N_2 can be either large (Fig. 3.1 (a)) or small (Fig.3.1 (b)).

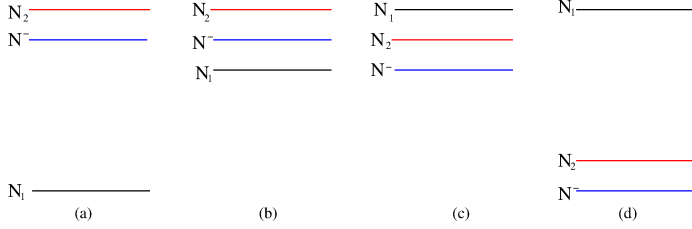


Figure 3.1: Pictorial presentation of the possible mass spectrum for additional vector-like leptons.

Let us now turn to the interaction terms in the mass basis of N_1 and N_2 . The Yukawa interaction term can be re-written as:

$$\begin{aligned} Y \bar{N} \tilde{H} \chi^0 + \text{h.c.} &\rightarrow Y \bar{N}^0 h \chi^0 + \text{h.c.} \\ &= Y [\sin 2\theta (\bar{N}_1 h N_1 - \bar{N}_2 h N_2) + \cos 2\theta (\bar{N}_1 h N_2 + \bar{N}_2 h N_1)] . \end{aligned} \quad (3.7)$$

Similarly the charge current and neutral current gauge interaction in the mass basis of N_1 and N_2 can be given as:

$$\frac{g}{\sqrt{2}} \bar{N}^0 \gamma^\mu W_\mu^+ N^- + \text{h.c.} \rightarrow \frac{g \sin \theta}{\sqrt{2}} \bar{N}_1 \gamma^\mu W_\mu^+ N^- + \frac{g \cos \theta}{\sqrt{2}} \bar{N}_2 \gamma^\mu W_\mu^+ N^- + \text{h.c.} , \quad (3.8)$$

$$\frac{g}{2 \cos \theta_w} \bar{N}^0 \gamma^\mu Z_\mu N^0 \rightarrow \frac{g}{2 \cos \theta_w} (\sin^2 \theta \bar{N}_1 \gamma^\mu Z_\mu N_1 + \sin \theta \cos \theta (\bar{N}_1 \gamma^\mu Z_\mu N_2 + \bar{N}_2 \gamma^\mu Z_\mu N_1) + \cos^2 \theta \bar{N}_2 \gamma^\mu Z_\mu N_2) . \quad (3.9)$$

The neutral current of N^- is not affected by the singlet-doublet mixing and is given by:

$$e \gamma^\mu \bar{N}^- A_\mu N^- + \frac{g}{2 \cos \theta_W} (1 - 2 \sin^2 \theta_W) \bar{N}^- \gamma^\mu Z_\mu N^- . \quad (3.10)$$

Essentially, the model contains three independent parameters in terms of

$$\{M_1, M_2, \sin \theta\} \quad \text{or} \quad \{Y, M_1, M_2\} \quad (3.11)$$

where, Y and $\sin \theta$ are related by

$$Y = \frac{\Delta M \sin 2\theta}{2v} , \quad (3.12)$$

as seen from Eq. (3.5).

We use $\sin\theta$ as an independent parameter in our analysis. We will see that the mixing angle plays a vital role in the DM phenomenology. In particular, the relic abundance of DM gives an upper bound on the singlet-doublet mixing angle to be $\sin\theta \lesssim 0.4$. For larger mixing angle the relic abundance is less than the observed value due to large annihilation cross-sections in almost all parameter space. We also found that a lower bound on $\sin\theta$ coming from the decay of N_2 and N^- after they freeze out from the thermal bath. In principle these particles can decay on, before or after the DM (N_1) freezes out depending on the mixing angle. In the worst case, N_2 and N^- have to decay before the onset of Big-Bang nucleosynthesis. In that case, the lower bound on the mixing angle is very much relaxed and the out-of-equilibrium decay of N_2 and N^- will produce an additional abundance of DM. Therefore, in what follows, we demand that N_2 and N^- decay on or before the freeze out of DM (N_1). As a result we get a stronger lower bound on $\sin\theta$, which of course depends on their masses.

If the mass splitting between N^- and N_1 is larger than W^\pm -boson mass, then N^- decay preferably through the two body process: $N^- \rightarrow N_1 + W^-$. However, if the mass splitting between N^- and N_1 is less than W^\pm -boson mass then N^- decay through the three body process: $N^- \rightarrow N_1 \ell^- \bar{\nu}_\ell$. For the latter case, we get a stronger lower bound on the mixing angle than the former. The three body decay width of N^- is given by (see appendix C):

$$\Gamma = \frac{G_F^2 \sin^2\theta}{24\pi^3} M_N^5 I \quad (3.13)$$

where G_F is the Fermi coupling constant and I is given as:

$$I = \frac{1}{4} \lambda^{1/2} (1, a^2, b^2) F_1(a, b) + 6F_2(a, b) \ln \left(\frac{2a}{1 + a^2 - b^2 - \lambda^{1/2}(1, a^2, b^2)} \right). \quad (3.14)$$

In the above Equation $F_1(a, b)$ and $F_2(a, b)$ are two polynomials of $a = M_1/M_N$ and $b = m_\ell/M_N$, where m_ℓ is the charged lepton mass. Up to $\mathcal{O}(b^2)$, these two polynomials are given by

$$\begin{aligned} F_1(a, b) &= (a^6 - 2a^5 - 7a^4(1 + b^2) + 10a^3(b^2 - 2) + a^2(12b^2 - 7) + (3b^2 - 1)) \\ F_2(a, b) &= (a^5 + a^4 + a^3(1 - 2b^2)). \end{aligned} \quad (3.15)$$

In Eq. (3.14), $\lambda^{1/2} = \sqrt{1 + a^4 + b^4 - 2a^2 - 2b^2 - 2a^2b^2}$ defines the phase space. In the limit $b = m_\ell/M_N \rightarrow 1 - a = \Delta M/M_N$, $\lambda^{1/2}$ goes to zero and hence $I \rightarrow 0$. The life time of N^- is then given by $\tau \equiv \Gamma^{-1}$. We take the freeze out temperature of DM to be $T_f = M_1/20$. Since the DM freezes out during radiation dominated era, the corresponding time of DM freeze-out is given by :

$$t_f = 0.301 g_\star^{-1/2} \frac{m_{\text{pl}}}{T_f^2}, \quad (3.16)$$

where g_\star is the effective massless degrees of freedom at a temperature T_f and m_{pl} is the Planck mass. Demanding that N^- should decay before the DM freezes out (i.e. $\tau \lesssim t_f$) we get

$$\sin\theta \gtrsim 1.1789 \times 10^{-5} \left(\frac{1.375 \times 10^{-5}}{I} \right)^{1/2} \left(\frac{200\text{GeV}}{M_N} \right)^{5/2} \left(\frac{g_\star}{106.75} \right)^{1/4} \left(\frac{M_1}{180\text{GeV}} \right). \quad (3.17)$$

Notice that the lower bound on the mixing angle depends on the mass of N^- and N_1 . For a typical value of $M_N = 200$ GeV, $M_1 = 180$ GeV, we get $\sin \theta \gtrsim 1.17 \times 10^{-5}$. Since τ is inversely proportional to M_N^5 , larger the mass, smaller will be the lower bound on the mixing angle.

3.3 Constraints on Model Parameters

3.3.1 Invisible Z-decay

The non observation of Z decay width to a fourth generation charged lepton pairs prohibit to $M^\pm > M_z/2$. As $M^\pm \simeq M_2 \simeq M_N$, this implies that the mass of N^- and N_2 has to be larger than 45 GeV. On the other hand M_1 can be as light as 1 GeV [105]. Due to singlet-doublet mixing, the Z-boson can decay to N_1 and N_2 . Since N_2 is heavier than $M_z/2$, the decay of Z to $N_2 N_2$ is also forbidden. Hence the relevant decay widths of the processes $Z \rightarrow N_1 N_1$ and $Z \rightarrow N_1 N_2$ can be given as:

$$\begin{aligned} \Gamma(Z \rightarrow N_1 N_1) &= \frac{1}{48\pi} M_Z \left(\frac{g^2 \sin^4 \theta}{\cos^2 \theta_w} \right) \left(1 + \frac{2M_1^2}{M_Z^2} \right) \left(1 - \frac{4M_1^2}{M_Z^2} \right)^{1/2} \\ \Gamma(Z \rightarrow N_1 N_2) &= \frac{1}{96\pi} M_Z \left(\frac{g^2 \sin^2 \theta \cos^2 \theta}{\cos^2 \theta_w} \right) \left(\left(1 - \frac{(M_1^2 + M_2^2)}{M_Z^2} \right) + \frac{6M_1 M_2}{M_Z^2} + \left(1 - \frac{(M_1^2 - M_2^2)^2}{M_Z^4} \right) \right) \\ &\quad \left(1 - 2 \frac{(M_1^2 + M_2^2)}{M_Z^2} + \frac{(M_1^2 - M_2^2)^2}{M_Z^4} \right)^{1/2} \end{aligned} \quad (3.18)$$

The invisible Z-decay width in the SM is $\Gamma(\text{invisible}) = 499 \pm 1.5 \text{ MeV}$ [106]. Therefore, if Z is allowed to decay to $N_1 N_1$ and $N_1 N_2$ then the decay width should not be more than 1.5 MeV. Under this condition we have shown the constraints on $\sin \theta$ for various values of M_1 in Fig. (3.2), while fixing $M_2 = M_z/2 = 45$ GeV, the minimum possible value, for simplicity. We see that the DM mass M_1 can be allowed below $M_z/2 = 45$ GeV only if $\sin \theta < 10^{-3}$.

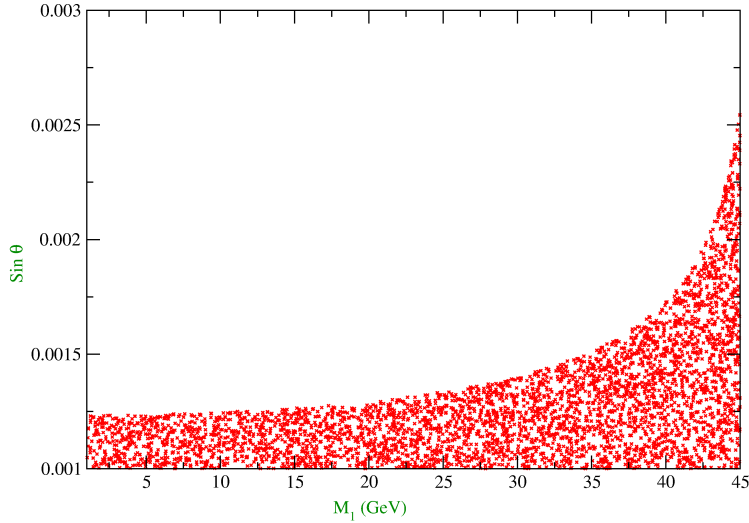


Figure 3.2: The allowed values of $\sin \theta$ for different DM mass $M_1 < M_z/2 = 45$ GeV from invisible Z decay constraints. We assume here $M_2 = M_z/2 = 45$ GeV.

3.3.2 Invisible Higgs decay

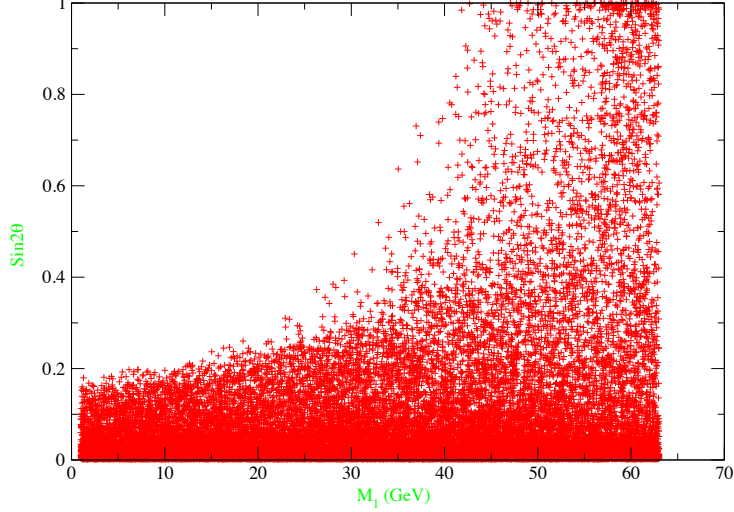


Figure 3.3: Scatter plot for allowed parameter space in $\sin 2\theta - M_1$ (GeV) plane from invisible Higgs decay. All possible values of M_2 used that keeps the decay chain open.

The SM Higgs can decay to N_1 and N_2 and therefore strongly constrained by the observation. In particular, the branching ratio for the invisible Higgs decay width is given by

$$\text{Br}_{\text{inv}} = \frac{\Gamma_h^{\text{inv}}}{\Gamma_h^{\text{SM}} + \Gamma_h^{\text{inv}}}, \quad (3.19)$$

where $\Gamma_h^{\text{SM}} = 4\text{MeV}$. The invisible Higgs decay width is given by:

$$\Gamma_h^{\text{inv}} = \Gamma(h \rightarrow N_1 N_1) + \Gamma(h \rightarrow N_2 N_2) + \Gamma(h \rightarrow N_1 N_2) \quad (3.20)$$

where

$$\begin{aligned} \Gamma(h \rightarrow N_i N_i) &= \frac{(Y \sin 2\theta)^2}{8\pi} M_h \left(1 - \frac{4M_i^2}{M_h^2}\right)^{3/2} \\ \Gamma(h \rightarrow N_i N_j) &= \frac{(Y \cos 2\theta)^2}{8\pi} M_h \left(1 - \frac{M_i^2 + M_j^2}{M_h^2} - \frac{2M_i M_j}{M_h^2}\right) \\ &\quad \times \left(1 - \frac{2(M_i^2 + M_j^2)}{M_h^2} + \frac{(M_i^2 - M_j^2)^2}{M_h^4}\right)^{1/2}. \end{aligned} \quad (3.21)$$

Taking $\text{Br}_{\text{inv}} < 0.3$ [107, 108, 109] we have shown the allowed region in the plane of $\sin 2\theta$ versus M_1 in Fig. (3.3). We saw that for small DM mass, typically $1 < M_1 < M_H/2 = 63$ GeV, $\sin 2\theta$ is strongly constrained, while for $M_1 \gtrsim 63$ GeV, large $\sin 2\theta$ is allowed from invisible Higgs decay constraints. In the scan, we are choosing all possible values of M_2 that keeps the decay chain open.

Clearly, the invisible Z -decay puts stronger constraint on the mixing angle than the invisible decay of Higgs does.

3.4 Constraint on Model parameters from Direct Search Experiments of DM

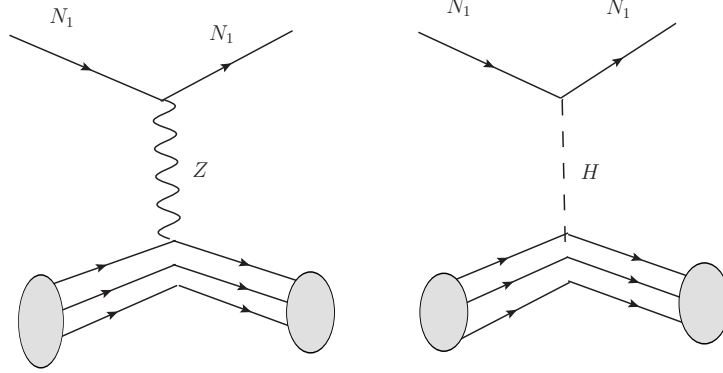


Figure 3.4: Feynman diagrams for direct detection of N_1 DM.

It is very difficult to probe the DM in direct search experiments. The non observation of DM signal in direct search experiments like XENON100 [12] and LUX [110] thus puts a stringent constraint on the effective nucleon-DM cross-section as a function of DM mass. As a result the direct search experiments also put a constraint over the model parameters. The relevant diagrams through which the DM interacts with the nuclei in this model is shown in Fig. 3.4. There is a constraint on mixing angle $\sin \theta$ for spin independent DM-nucleon interaction mediated via the Z -boson (see in the left of Fig. (3.4)). The cross-section per nucleon for Z mediation is given by [111, 112]

$$\sigma_{\text{SI}}^Z = \frac{1}{\pi A^2} \mu_r^2 |\mathcal{M}|^2 \quad (3.22)$$

where A is the mass number of the target nucleus, $\mu_r = M_1 m_n / (M_1 + m_n) \approx m_n$ is the reduced mass, m_n is the mass of nucleon (proton or neutron) and \mathcal{M} is the amplitude for Z -mediated DM-nucleon cross-section given by

$$\mathcal{M} = \sqrt{2} G_F [Z(f_p/f_n) + (A - Z)] f_n \sin^2 \theta, \quad (3.23)$$

where f_p and f_n are the interaction strengths (including hadronic uncertainties) of DM with proton and neutron respectively and Z is the atomic number of the target nucleus. For simplicity we assume conservation of isospin, *i.e.* $f_p/f_n = 1$. The value of f_n vary within a range: $0.14 < f_n < 0.66$ [113, 114, 115, 116]. If we take $f_n \simeq 1/3$, the central value, then from Eqs. (3.22) and (3.23), we get the Z -mediated cross-section per nucleon to be

$$\sigma_{\text{SI}}^Z \simeq 3.75 \times 10^{-39} \text{cm}^2 \sin^4 \theta. \quad (3.24)$$

In the above equation the only unknown is the $\sin \theta$ and hence can be constrained from observation. Using the data from Xenon-100 and LUX we have shown the allowed values of $\sin \theta$ in the left panel of Fig. (3.5) as a function of the DM mass.

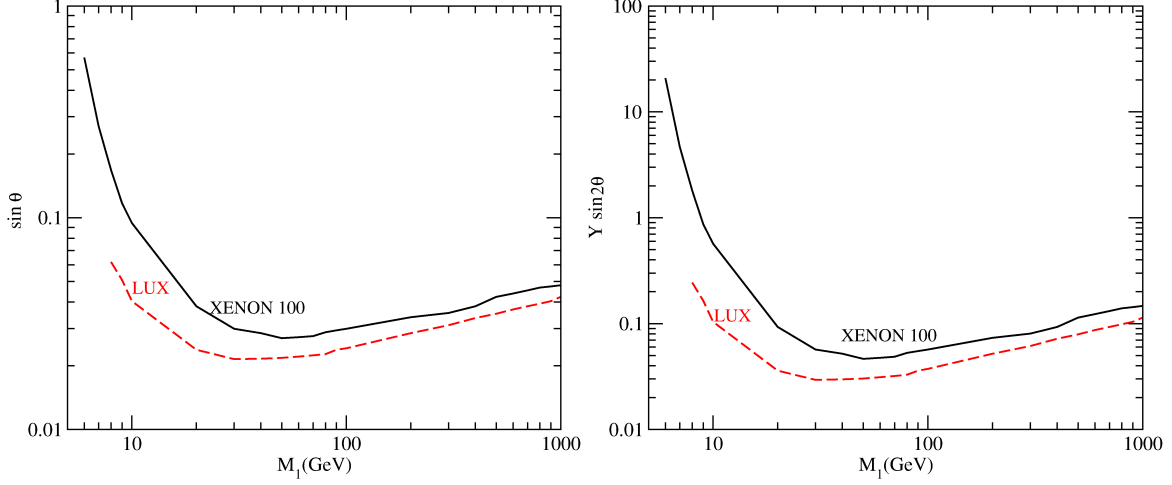


Figure 3.5: Constraint on $\sin \theta$ (left) from Z mediated direct detection process and $Y \sin 2\theta$ (right) from H mediated direct detection process using Xenon-100 and LUX data for different values of DM mass M_1 .

Another possibility of having spin-independent DM-nucleon interaction is through the exchange of SM Higgs (see in the right of Fig. (3.4)). The cross-section per nucleon is given by:

$$\sigma_{\text{SI}}^h = \frac{1}{\pi A^2} \mu_r^2 [Z f_p + (A - Z) f_n]^2 \quad (3.25)$$

where the effective interaction strengths of DM with proton and neutron are given by:

$$f_{p,n} = \sum_{q=u,d,s} f_{Tq}^{(p,n)} \alpha_q \frac{m_{(p,n)}}{m_q} + \frac{2}{27} f_{TG}^{(p,n)} \sum_{q=c,t,b} \alpha_q \frac{m_{p,n}}{m_q} \quad (3.26)$$

with

$$\alpha_q = \frac{Y \sin 2\theta}{M_h^2} \left(\frac{m_q}{v} \right). \quad (3.27)$$

In Eq. (3.26), the different coupling strengths between DM and light quarks are given by [117] $f_{Tu}^{(p)} = 0.020 \pm 0.004$, $f_{Td}^{(p)} = 0.026 \pm 0.005$, $f_{Ts}^{(p)} = 0.118 \pm 0.062$, $f_{Tu}^{(n)} = 0.014 \pm 0.004$, $f_{Td}^{(n)} = 0.036 \pm 0.008$, $f_{Ts}^{(n)} = 0.118 \pm 0.062$. The coupling of DM with the gluons in target nuclei is parameterized by

$$f_{TG}^{(p,n)} = 1 - \sum_{q=u,d,s} f_{Tq}^{(p,n)}. \quad (3.28)$$

Thus from Eqs. (3.25,3.26,3.27,3.28) the spin-independent DM-nucleon cross-section is given to be:

$$\sigma_{\text{SI}}^h = \frac{4}{\pi A^2} \mu_r^2 \frac{Y^2 \sin^2 2\theta}{M_h^4} \left[\frac{m_p}{v} \left(f_{Tu}^p + f_{Td}^p + f_{Ts}^p + \frac{2}{9} f_{TG}^p \right) + \frac{m_n}{v} \left(f_{Tu}^n + f_{Td}^n + f_{Ts}^n + \frac{2}{9} f_{TG}^n \right) \right]^2. \quad (3.29)$$

In the above equation the only unknown quantity is Y or $\sin 2\theta$ which can be constrained by requiring

that σ_{SI}^h is less than the current DM-nucleon cross-sections at Xenon-100 and LUX. This is shown in the right panel of Fig. (3.5).

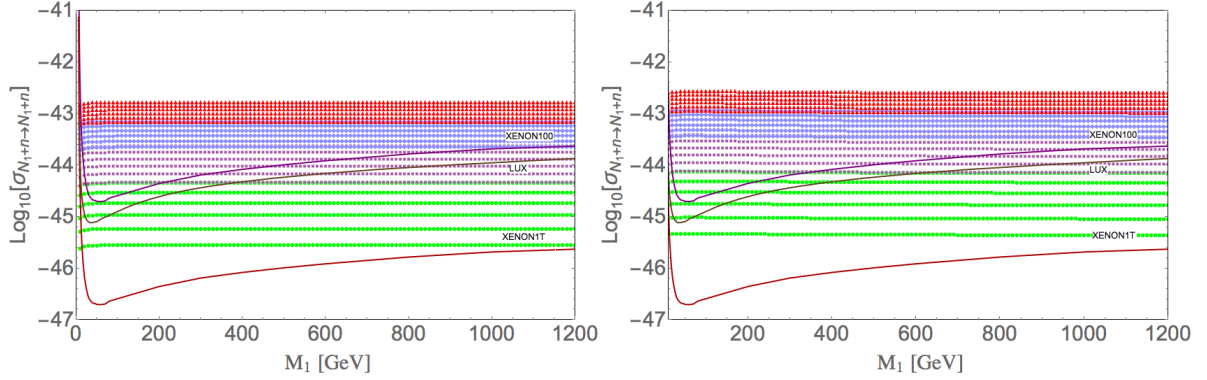


Figure 3.6: Spin independent direct detection cross-section for N_1 DM as a function of DM mass for $\sin \theta = \{0.05 - 0.1\}$ (Green), $\sin \theta = \{0.1 - 0.15\}$ (Purple), $\sin \theta = \{0.15 - 0.2\}$ (Lilac), $\sin \theta = \{0.2 - 0.25\}$ (Red). Fixed values of $\Delta M = \{100, 700\}$ GeV (left and right respectively) have been used. XENON 100, LUX data are shown with XENON 1 T prediction.

Now a combined analysis is made by taking into account both Z and H mediated diagrams together. The value of mixing angle $\sin \theta$ as well as DM mass are changed by keeping a fixed value of ΔM and hence changing $Y = \Delta M \sin 2\theta/2v$ accordingly. In Fig 3.6, we show the spin-independent cross-section for N_1 DM within its mass range $M_1 : 50 - 1200$ GeV. The plot is obtained by varying $\sin \theta$ within $\{0.05 - 0.25\}$ with $\sin \theta = \{0.05 - 0.1\}$ (Green), $\sin \theta = \{0.1 - 0.15\}$ (Purple), $\sin \theta = \{0.15 - 0.2\}$ (Lilac), $\sin \theta = \{0.2 - 0.25\}$ (Red) by choosing a fixed set of $\Delta M = \{100, 700\}$ GeV (left and right respectively). It clearly shows that the larger is $\sin \theta$, the stronger is the interaction strength (through larger contribution from Z mediation) and hence the larger is the DM-nucleon cross-section. Similarly, the larger is ΔM , the greater is the Y -value and hence larger is the DM-nucleon cross-section (through larger contribution from Higgs mediation). Hence, it turns out that direct search experiments constraints $\sin \theta$ to a great extent. For example, we see that with $\sin \theta = 0.1$, the DM mass $M_1 > 350$ GeV. The effect of ΔM on DM-nucleon cross-section is much smaller as we can see from the left and right panel of Fig. (3.6). However, we note that ΔM plays a dominant role in the relic abundance of DM. Approximately, $\sin \theta \leq 0.1$ (Green points) are allowed for most of the parameter space except for smaller DM masses. Further small mixing angles are still allowed and that will have a non-trivial outcome in collider search.

It is also noticed that there is a very tiny amount of spin-dependent cross-section arises through Z mediation, but the cross-section lies far far below than the observed limit and hence it effectively doesn't constrain the parameter space at all. For example, with $\{M_1 = 80, M_2 = 120, \sin \theta = 0.1\}$, the spin dependent cross-section for proton is as low as 3.2×10^{-49} pb compared to 4.2×10^{-9} pb for spin independent one.

3.5 Constraints from Electroweak precision tests on Vector-like leptons

Any vector like fermion doublet beyond SM framework contribute to the electroweak precision test parameters S , T and U [118, 119, 120, 121]. In fact, a more generalized set of parameters for electroweak precision test are \hat{S} , \hat{T} , W and Y [1], where the \hat{S} , \hat{T} are related to Peskin-Takeuchi parameters S , T as $\hat{S} = \alpha S/4 \sin^2 \theta_w$, $\hat{T} = \alpha T$, while W and Y are two new set of parameters. The observed values of these parameters at LEP-I and LEP-II set a lower bound on the mass scale of new fermions. Global fit of the electroweak precision parameters for a light Higgs [1]¹ is shown in the following Table.

	$10^3 \hat{S}$	$10^3 \hat{T}$	$10^3 W$	$10^3 Y$
Light Higgs	0.0 ± 1.3	0.1 ± 0.9	0.1 ± 1.2	-0.4 ± 0.8

Table 3.1: Global fit for the electroweak precision parameters taken from ref. [1].

In our present model, we have two neutral fermions N_1 , N_2 and a charged one N^- . Note that N_1 is dominantly a singlet and a small admixture of doublet component, while N_2 is dominantly a doublet and a small admixture of singlet component. Therefore, the mixing is important for their contribution to \hat{S} , \hat{T} , W and Y . In terms of M_1 , M_2 , M^\pm and $\sin \theta$ we can compute \hat{S} as [90]:

$$\begin{aligned} \hat{S} = & \frac{g^2}{16\pi^2} \left[\frac{1}{3} \left\{ \ln \left(\frac{\mu^2}{(M^\pm)^2} \right) - \cos^4 \theta \ln \left(\frac{\mu^2}{M_2^2} \right) - \sin^4 \theta \ln \left(\frac{\mu^2}{M_1^2} \right) \right\} - 2 \sin^2 \theta \cos^2 \theta \left\{ \ln \left(\frac{\mu^2}{M_1 M_2} \right) \right. \right. \\ & + \frac{M_1^4 - 8M_1^2 M_2^2 + M_2^4}{9(M_1^2 - M_2^2)^2} + \frac{(M_1^2 + M_2^2)(M_1^4 - 4M_1^2 M_2^2 + M_2^4)}{6(M_1^2 - M_2^2)^3} \ln \left(\frac{M_2^2}{M_1^2} \right) \\ & \left. \left. + \frac{M_1 M_2 (M_1^2 + M_2^2)}{2(M_1^2 - M_2^2)^2} + \frac{M_1^3 M_2^3}{(M_1^2 - M_2^2)^3} \ln \left(\frac{M_2^2}{M_1^2} \right) \right\} \right] \end{aligned} \quad (3.30)$$

where μ is at the EW scale. We have plotted \hat{S} as a function of M_2 for different values of the mixing angles while keeping $M_1 = 150$ GeV, in the left panel of fig. 3.7. On the other hand, in the right panel, we have shown the allowed values of \hat{S} in the plane of $M_2 - M^\pm$ versus M_2 for $\sin \theta = 0.05$. We observed that \hat{S} does not put strong constraints on M_1 and M_2 . Moreover, small values of $\sin \theta$ allows a small mass splitting between N_2 and N^- which relaxes the constraint on \hat{T} parameter as we discuss below. In terms of M_1 , M_2 , M^\pm and $\sin \theta$ one can compute \hat{T} as [90]:

$$\hat{T} = \frac{g^2}{16\pi^2 M_W^2} \left[2 \sin^2 \theta \cos^2 \theta \Pi(M_1, M_2, 0) - 2 \cos^2 \theta \Pi(M^\pm, M_2, 0) - 2 \sin^2 \theta \Pi(M^\pm, M_1, 0) \right], \quad (3.31)$$

where $\Pi(a, b, 0)$ is given by:

$$\begin{aligned} \Pi(a, b, 0) = & -\frac{1}{2}(M_a^2 + M_b^2) \left(\text{Div} + \ln \left(\frac{\mu^2}{M_a M_b} \right) \right) - \frac{1}{4}(M_a^2 + M_b^2) - \frac{(M_a^4 + M_b^4)}{4(M_a^2 - M_b^2)} \ln \frac{M_b^2}{M_a^2} \\ & + M_a M_b \left\{ \text{Div} + \ln \left(\frac{\mu^2}{M_a M_b} \right) + 1 + \frac{(M_a^2 + M_b^2)}{2(M_a^2 - M_b^2)} \ln \frac{M_b^2}{M_a^2} \right\} \end{aligned} \quad (3.32)$$

¹The value \hat{S} , \hat{T} , W and Y are obtained using a Higgs mass $m_h = 115$ GeV. However, we now know that the SM Higgs mass is 125 GeV. Therefore, the value of \hat{S} , \hat{T} , W and Y are expected to change. But this effect is nullified by the small values of $\sin \theta$.

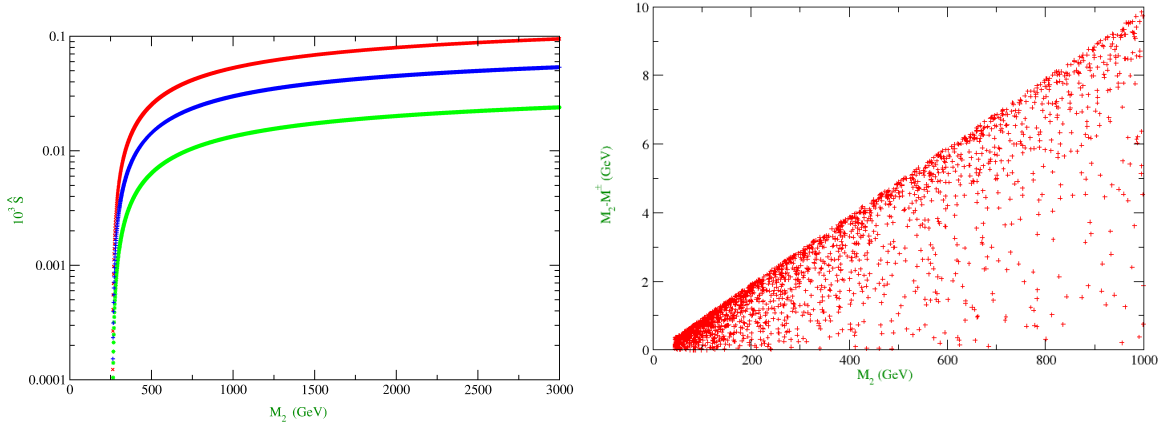


Figure 3.7: In the left panel, \hat{S} is shown as a function of M_2 for $M_1 = 150$ GeV and $\sin\theta = 0.05$ (Green colour, bottom), $\sin\theta = 0.075$ (Blue color, middle) and $\sin\theta = 0.1$ (Red color, top). In the right panel, allowed values of \hat{S} in the plane of $M_2 - M^\pm$ versus M_2 for $\sin\theta = 0.05$.

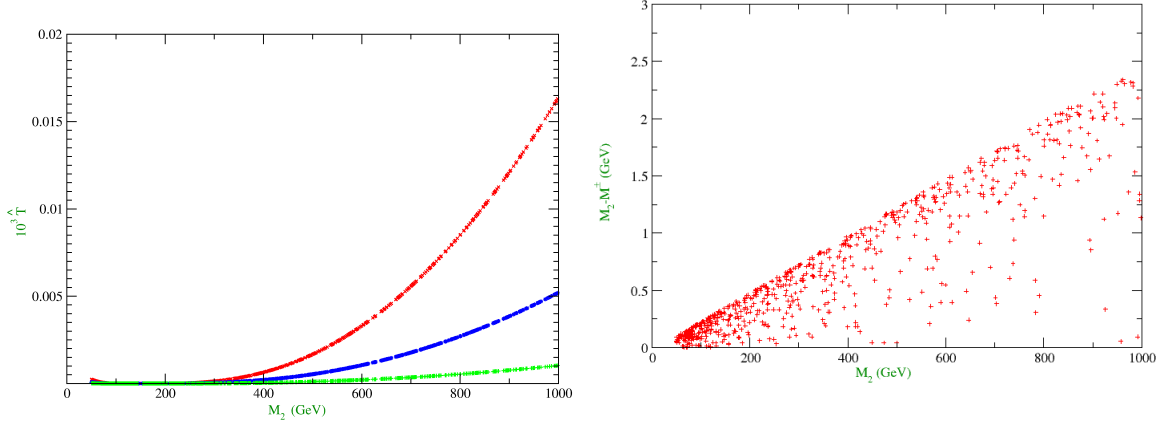


Figure 3.8: In the left panel, \hat{T} is shown as a function of M_2 for $M_1 = 150$ GeV and $\sin\theta = 0.05$ (Green colour, bottom), $\sin\theta = 0.075$ (Blue color, middle) and $\sin\theta = 0.1$ (Red color, top). In the right panel, allowed values of \hat{T} in the plane of $M_2 - M^\pm$ versus M_2 for $\sin\theta = 0.05$.

From the left panel of Fig. (3.8) we see that for $\sin\theta < 0.05$ we don't get strong constraints on M_2 and M_1 . Moreover, small values of $\sin\theta$ restricts the value of $M_2 - M^\pm$ to be less than a GeV. As a result large M_2 values are also allowed. Near $M_2 \approx M^\pm$, \hat{T} vanishes as expected. The value of Y and W are usually suppressed by the masses new fermions. Since the allowed masses of N_1 , N_2 and N^\pm are above 100 GeV by the relic density constraint, so Y and W are naturally suppressed.

3.6 Relic Abundance of DM

3.6.1 Relics of Inert fermion doublet DM

In the present model, there are potentially two possible DM candidates χ^0 and the neutral component N^0 . In absence of the singlet fermion χ^0 , the neutral component (N^0) of the fermion doublet is stable due to the imposed Z_2 symmetry. However, this does not guarantee that the N^0 alone is a viable DM candidate. Under this circumstance it is crucial to check if N^0 can give rise correct relic abundance observed by WMAP and PLANCK.

The relic abundance of a DM is characterised by the number changing processes in which the candidate is involved. In this case, on top of annihilations to SM particles, the DM (N_0) can also participate in co-annihilations with heavier particles N^\pm which are odd under the same Z_2 symmetry. The relevant annihilation and co-annihilation channels in order to keep the inert fermion doublet DM in the thermal equilibrium in the early universe are listed below.

$$\begin{aligned} N^0 \bar{N}^0 &\rightarrow hh, Zh, W^+W^-, ZZ, , f\bar{f} \\ N^0 N^\pm &\rightarrow W^\pm \gamma, W^\pm h, W^\pm Z, f' \bar{f}' \\ N^\pm N^\mp &\rightarrow W^\pm W^\mp, Zh, \gamma Z, \gamma\gamma, ZZ, f\bar{f}, \end{aligned}$$

where f, f' are SM fermions. The relic abundance is calculated using micrOMEGAs [122]. The relic

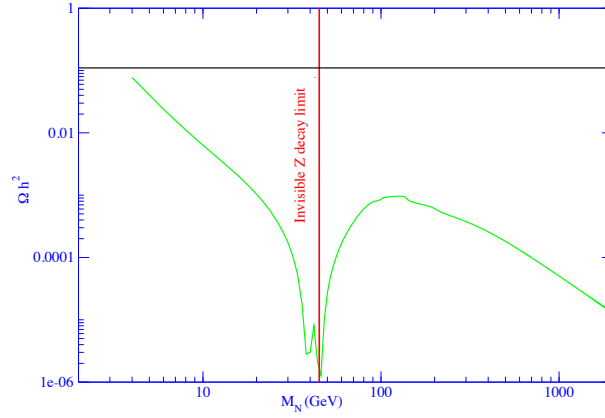


Figure 3.9: Relic abundance (green line) of N_0 , the neutral component of the doublet as DM, plotted as a function of doublet mass (M_N) in GeV. Black horizontal line shows the observed relic abundance by PLANCK data. The solid red vertical line is shown to mark $\frac{M_Z}{2} = 45$ GeV; for $M_N > \frac{M_Z}{2}$ the DM does not contribute to the invisible Z decay width.

abundance as a function of its mass is shown in Fig. 3.9. In a conservative limit we take the mass splitting between N^0 and its charged partner N^\pm to be 1 GeV. We see that the large annihilation and co-annihilation cross-sections always yield much smaller relic density than required and hence the model is ruled out with the mass range of the order of TeV. The dominant channels, contributing to the relic density, are $N^0 \bar{N}^0 \rightarrow hh, Zh, W^+W^-, ZZ$ and $N^\pm N^\mp \rightarrow W^\pm W^\mp$. We can also clearly spot the resonance at $M_N = \frac{M_Z}{2}$, where the relic density drops due to enhancement in the cross-

section due to s-channel Z mediation. Thus we infer that the neutral component of the doublet alone can not be a viable DM candidate as its relic abundance is much below the observed limit. Therefore, in the next section we will consider a mixed singlet-doublet state as the candidate of DM.

3.6.2 Relics of Singlet-Doublet mixed fermion DM

After the electroweak phase transition, the singlet (χ^0) and neutral component of the doublet (N^0) fermion mix with each other. In this scenario, the lightest particle $N_1 = \cos\theta\chi^0 + \sin\theta N^0$, which is stabilized by the imposed Z_2 symmetry, serves as a viable candidate of DM. In order to estimate the relic abundance of the N_1 DM, we need to calculate the various cross-sections through which N_1 abundance depletes.

The main annihilation processes have been indicated in Fig. 3.10. The dominant channels are $\overline{N_1}N_1 \rightarrow hh$ and $\overline{N_1}N_1 \rightarrow W^+W^-$. The other relevant channels are mainly coannihilation of N_1 with N_2 and N^\pm . We have shown $\overline{N_1}N_2 \rightarrow SM$ in Fig 3.11. The annihilation of $\overline{N_2}N_2 \rightarrow SM$ is very similar to $\overline{N_1}N_1 \rightarrow SM$ and are not shown explicitly. If N_1 is degenerate to N^\pm , then we find co annihilations of $\overline{N_1}N^\pm \rightarrow SM$ (in Fig. 3.12), $\overline{N_2}N^\pm \rightarrow SM$ (similar to $\overline{N_1}N^\pm \rightarrow SM$) and $N^\mp N^\pm \rightarrow SM$ (in Fig. 3.13) are also important for correct relic density of DM.

Relic abundance for N_1 is given by [77]

$$\Omega_{N_1} h^2 = \frac{1.09 \times 10^9 \text{Gev}^{-1}}{g_\star^{1/2} m_{\text{pl}}} \frac{1}{J(x_f)}, \quad (3.33)$$

where $J(x_f)$ is given by

$$J(x_f) = \int_{x_f}^{\infty} \frac{\langle \sigma|v| \rangle_{\text{eff}}}{x^2} dx, \quad (3.34)$$

where $\langle \sigma|v| \rangle_{\text{eff}}$ is thermal average of annihilation and coannihilation cross-sections of the DM particle. The expression for effective cross-section can be written as :

$$\begin{aligned} \langle \sigma|v| \rangle_{\text{eff}} = & \frac{g_1^2}{g_{\text{eff}}^2} \sigma(N_1 N_1) + 2 \frac{g_1 g_2}{g_{\text{eff}}^2} \sigma(N_1 N_2) (1 + \omega)^{3/2} \exp(-x\omega) \\ & + 2 \frac{g_1 g_3}{g_{\text{eff}}^2} \sigma(N_1 N^-) (1 + \omega)^{3/2} \exp(-x\omega) \\ & + 2 \frac{g_2 g_3}{g_{\text{eff}}^2} \sigma(N_2 N^-) (1 + \omega)^3 \exp(-2x\omega) + \frac{g_2^2}{g_{\text{eff}}^2} \sigma(N_2 N_2) (1 + \omega)^3 \exp(-2x\omega) \\ & + \frac{g_3^2}{g_{\text{eff}}^2} \sigma(N^- N^-) (1 + \omega)^3 \exp(-2x\omega). \end{aligned} \quad (3.35)$$

In this equation g_1, g_2, g_3 represent spin degrees of freedom for particles N_1, N_2, N^- respectively and their values are 2 for all. ω stands for the mass splitting ratio, given by $\omega = \frac{M_i - M_1}{M_1}$, where M_i is the mass of N_2 and N^\pm . The effective degrees of freedom denoted by g_{eff} , and is given by

$$g_{\text{eff}} = g_1 + g_2 (1 + \omega)^{3/2} \exp(-x\omega) + g_3 (1 + \omega)^{3/2} \exp(-x\omega) \quad (3.36)$$

Relic density of the DM is calculated using micrOMEGAs [122]. In Fig. 3.14, relic density of DM is plotted as a function of its mass for three different values of the mixing angle: $\sin\theta = 0.1, 0.2, 0.3$, shown in red (top), green (middle), purple (bottom) respectively. The mass difference $M_2 - M_1 =$

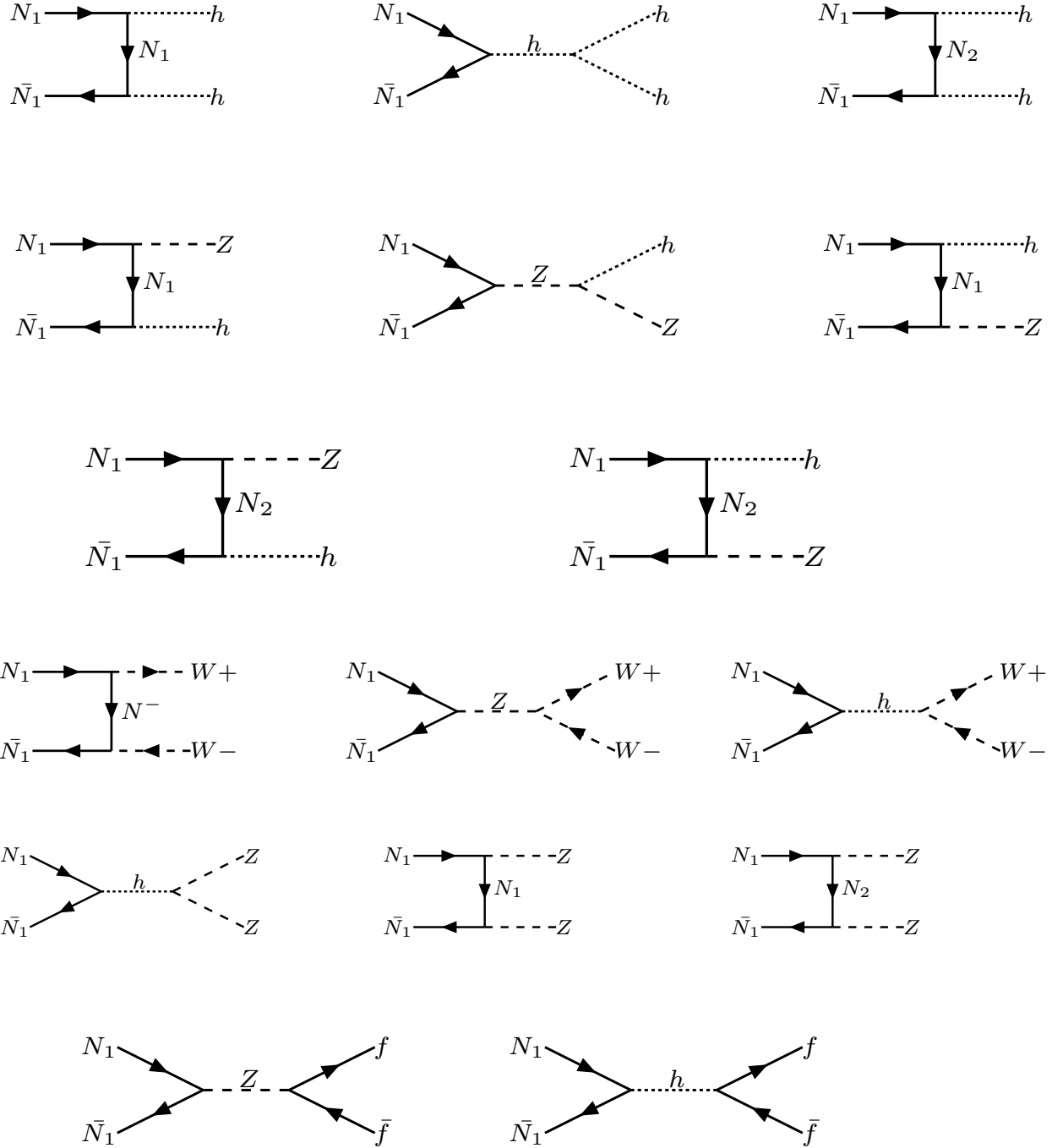


Figure 3.10: Dominant Annihilation processes to Higgs and gauge boson productions along with $f\bar{f}$, where f stands for all the SM fermions.

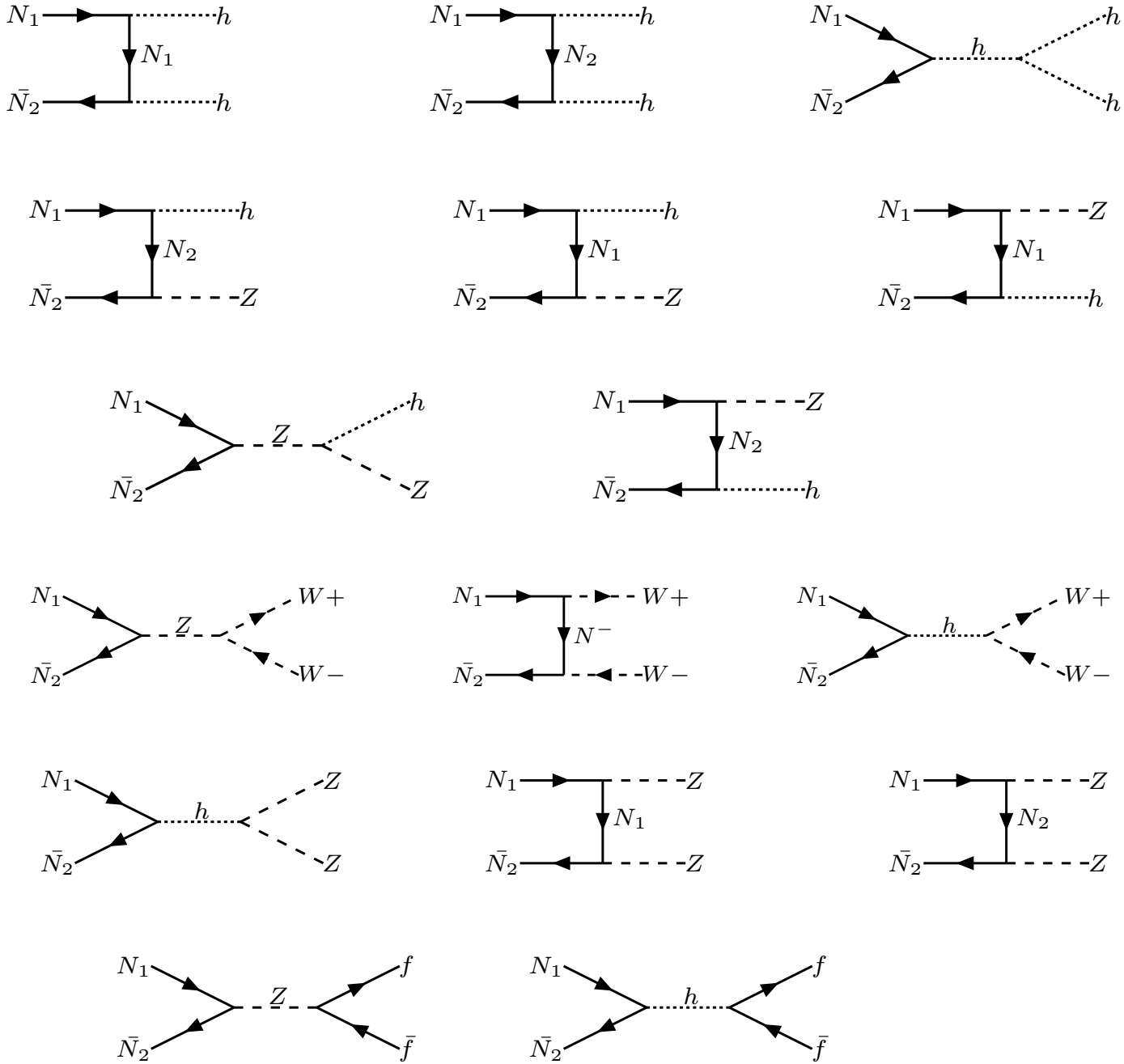


Figure 3.11: Dominant Coannihilation processes with N_2 to Higgs, gauge boson pair and $f\bar{f}$, where f stands for all fermions.

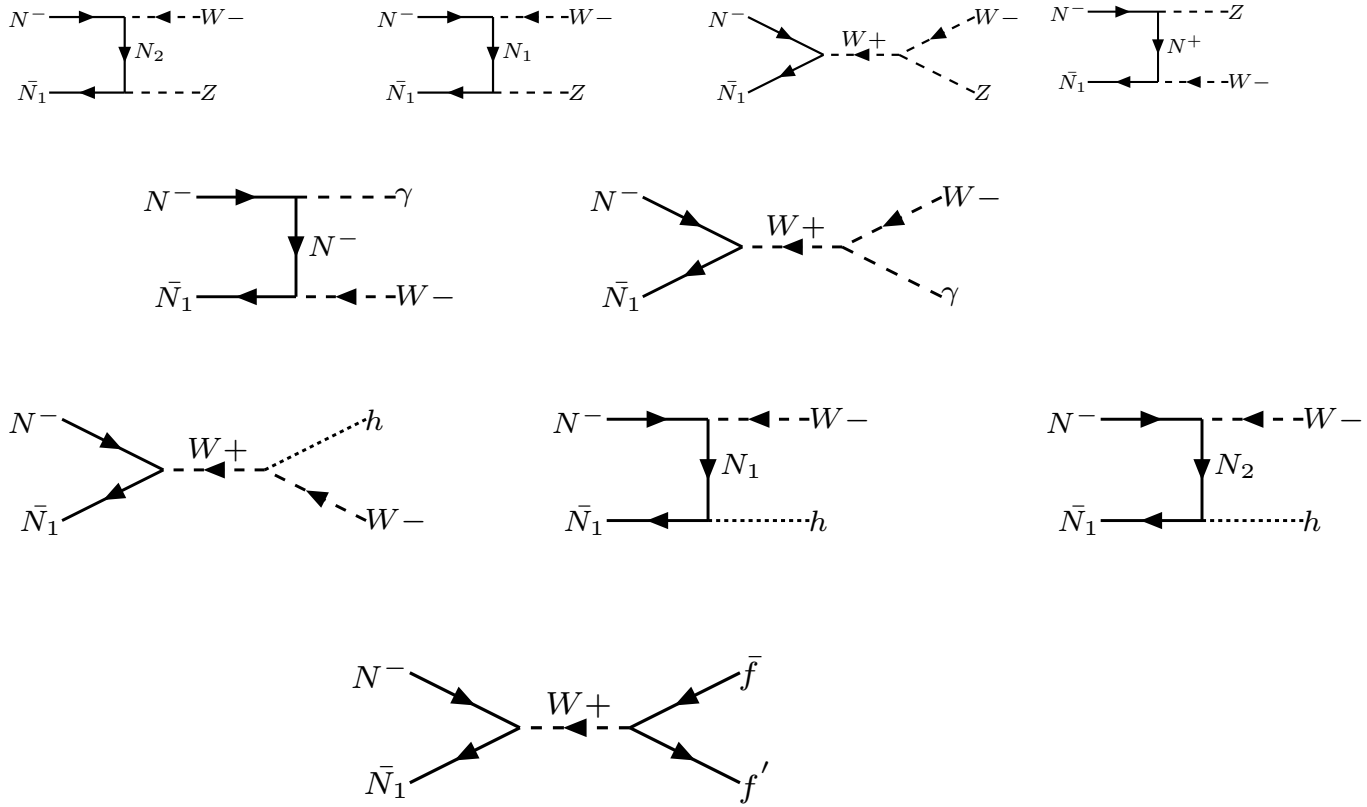


Figure 3.12: Dominant co-annihilation contributions from $N_1 N^-$ to Gauge boson and Higgs productions along with $f' \bar{f}$, where f stands for all the SM fermions.

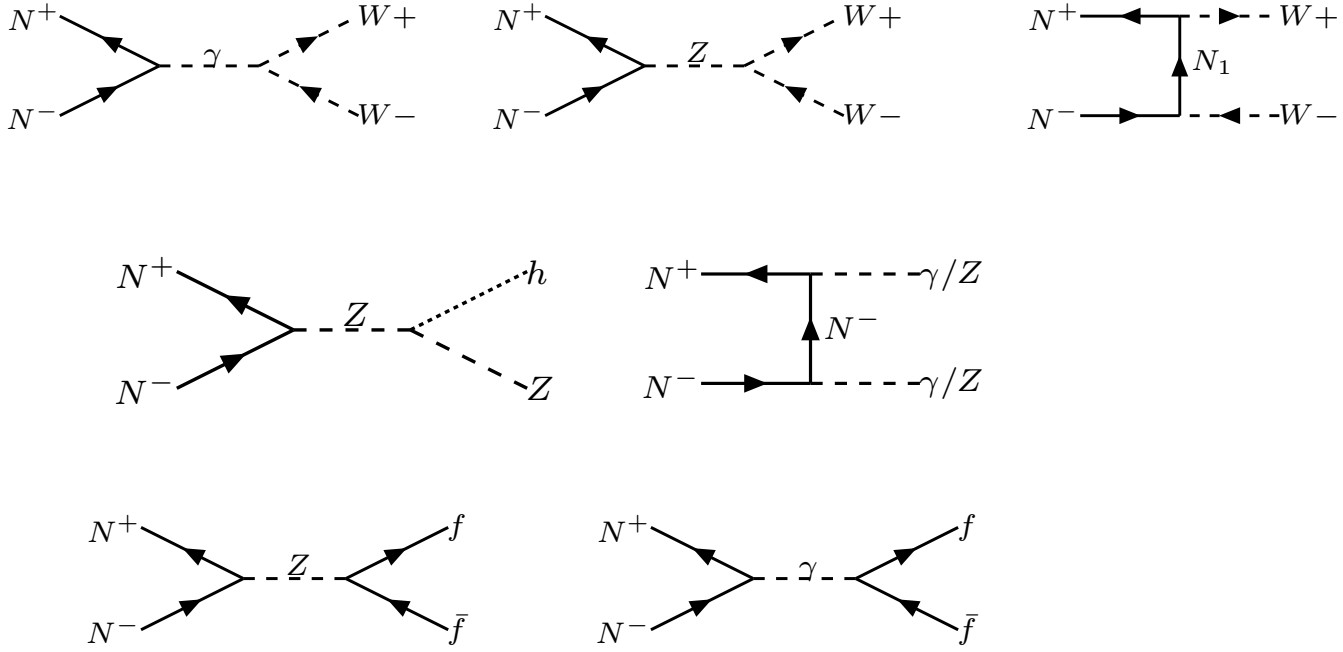


Figure 3.13: Dominant co-annihilation contributions from N^+N^- to Gauge boson and Higgs productions along with $f\bar{f}$, where f stands for all the SM fermions.

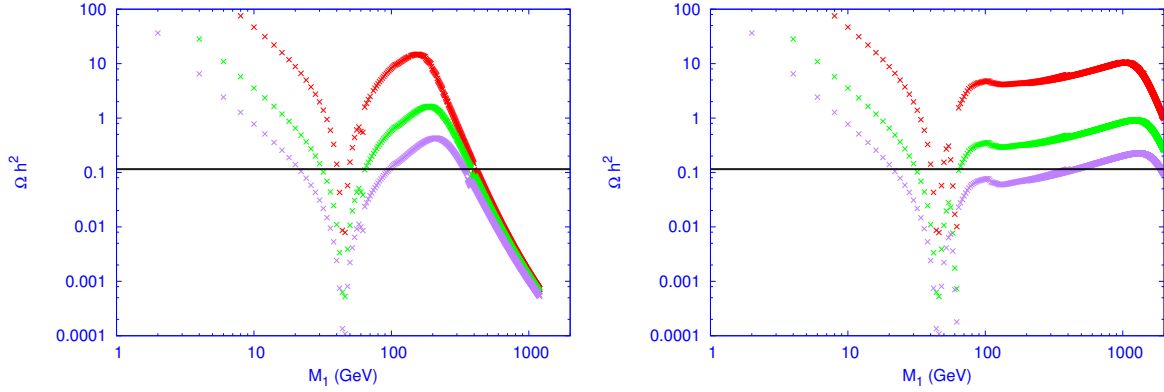


Figure 3.14: Relic density of DM as a function of its mass M_1 for different values of $\sin\theta = 0.1, 0.2, 0.3$, shown by red (top), green (middle) and purple (bottom) respectively. The value of the mass splitting: $M_2 - M_1 = 50, 500\text{GeV}$ is fixed respectively for left and right panel.

50, 500 GeV is fixed for left and right panel of Fig. 3.14. The black horizontal line corresponds to the observed relic density: $\Omega_{\text{DM}}h^2 = 0.1199$ by PLANCK [9]. As seen from the figure there is a sharp drop in relic density near two resonance points for s-channel mediated process through Z and h . Naturally, the right panel of fig. 3.14 with larger mass difference and hence a larger Yukawa

coupling Y shows more prominent h resonance. From these figures it is clear that as $\sin\theta$ increases relic density decreases. It is due to the fact that the Z mediated cross-section increases for increase in $\sin\theta$, and hence yield a low relic density. As the mass splitting between N_1 and N_2 is taken to be very large in the above cases, the dominant contribution to relic density comes from annihilation channels while co-annihilation channels are Boltzmann suppressed.

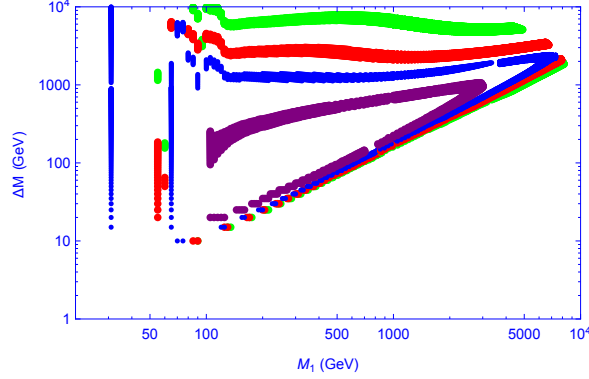


Figure 3.15: Scatter plot for correct relic density in the plane of M_1 and ΔM , shown by green, red, blue and purple coloured points for $\sin\theta = 0.1, 0.15, 0.2, 0.3$ respectively.

Now we will show how the mass splitting between N_1 and N_2 affects the relic density of the DM. In fig. 3.15, we have shown a scatter plot for correct relic density in the plane of M_1 and $\Delta M = M_2 - M_1$. Green, red, blue and purple coloured points satisfy the constraint of relic density for $\sin\theta = 0.1, 0.15, 0.2, 0.3$ respectively (from outermost to innermost contour). Let us first consider the vertical bars in the left hand side of the allowed parameter space. In this region of small DM mass, annihilation cross-section achieves large enhancement due to s-channel Z and h mediation at $M_{N_1} = \frac{M_Z}{2}$ and at $M_{N_1} = \frac{M_H}{2}$ respectively where the annihilation cross-section is independent of ΔM . Annihilation cross-sections contribute significantly for large ΔM to provide correct relic abundance. As the mass splitting decreases co-annihilation channels contribute significantly to add to the annihilation channels. As seen from the figure 3.15, we can divide the relic density allowed parameter space into two regions with same $\sin\theta$ value: i) The region in which ΔM is increasing with DM mass to satisfy correct relic density constraint. In this region, the contribution to relic density comes from both annihilation and dominantly from co-annihilation channels as the mass splitting is small. Here, due to small, ΔM , the Yukawa coupling Y (see Eq. 3.12) is small and so is the Higgs mediated cross-sections. Hence, co-annihilation channels provide with the rest of the requirement for correct relic density and allowed parameter space requires $\Delta M \sim M_1$. ii) The second region corresponds to a large ΔM while insensitive to DM mass satisfying the correct relic abundance. In this region, the dominant contribution to relic density comes from the annihilation channels (large ΔM indicates large Yukawa Y and large Higgs mediation cross-sections), and the co-annihilation channels are Boltzmann suppressed. Z mediated annihilation cross-sections are fixed by the choice of a specific mixing angle (in the DM mass region within $\sim \text{TeV}$). Therefore, the larger is the mixing the larger is the Z mediated annihilation. This correctly balances the Higgs mediated annihilation cross-sections to yield correct relic density. That is why we notice that a smaller mass splitting (ΔM) is required for larger $\sin\theta$ for a fixed value of DM mass. Hence green lines with

smaller mixing ($\sin \theta = 0.1$) requires larger ΔM and appears on top. With larger mixing, red, blue and purple lines, the required ΔM are smaller and appears below. It is easy to extend the analysis for even larger mixing angles, where the triangle becomes smaller and smaller in size and covers the innermost regions to yield the correct relic density. For $\sin \theta \gtrsim 0.5$ we can not get any relic abundance.

Points below “correct annihilation lines” (for a specific value of $\sin \theta$) provide more than required annihilation and hence those are under abundant regions. Similarly just above those, the annihilation will not be enough to produce correct density and hence are over abundant regions. Points below (above) the “correct co-annihilation regions” produce more (less) co-annihilations than required and hence depict under (over) abundant regions.

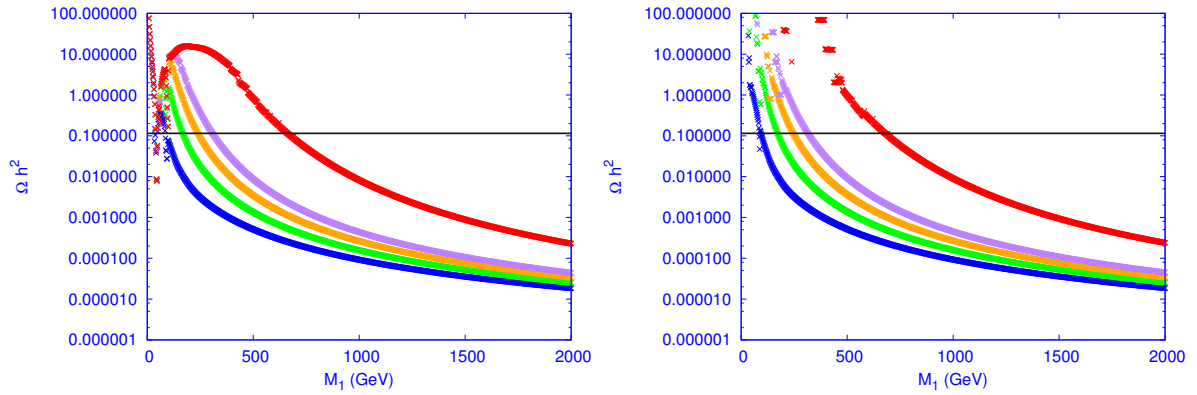


Figure 3.16: Left : Ωh^2 versus DM mass M_{DM} in GeV for $\sin \theta = 0.1$ and $\Delta M = 10, 20, 30, 40, 100$ GeV (Blue, Green, Orange, Purple, Red respectively from bottom to top). Right : Ωh^2 versus DM mass M_{DM} in GeV for $\sin \theta = 0.0001$ and $\Delta M = 10, 20, 30, 40, 100$ GeV (Blue, Green, Orange, Purple, Red respectively from bottom to top). Horizontal line shows the correct relic density.

The ΔM dependency on the relic density for a specific choice of mixing angle is shown in Fig. 3.16, particularly for small mixing regions where co-annihilations play a crucial role in yielding correct relic density. In the left panel we use $\sin \theta = 0.1$ and that in the right panel $\sin \theta = 0.0001$. We plot different slices with constant $\Delta M = 10, 20, 30, 40, 100$ GeV as shown in Blue, Green, Orange, Purple, Red respectively from bottom to top. We note here that with larger ΔM , the annihilation cross-section increases due to enhancement in Yukawa coupling $Y \propto \Delta M$. However, co-annihilation decreases due to increase in ΔM as $\sigma \propto e^{-\Delta M}$. Note that in the small $\sin \theta$ limit the dominant contribution to relic density comes from the channels involving only N_2 and N^\pm in the initial state going to SM gauge bosons, as mentioned in the beginning of this section. The processes involving $N_1 N_1 \rightarrow \text{SM}$ are heavily suppressed with small $\sin \theta$. As a result, we first get relics of N_2 and N^- which subsequently decay to N_1 before N_1 freezes out. In particular, if the mass splitting between N^- and N_1 is more than 80 GeV, then N^- decays through two body process: $N^- \rightarrow N_1 + W^-$. Notice that the mixing angles $\sin \theta = 0.1, 0.0001$ used simultaneously in the left and right-panel of Fig. (3.16) are much larger than the lower bound obtained on the singlet-doublet fermion mixing angle as given in eq. 3.17 by considering the 3-body decay of N^- , namely $\sin \theta > \mathcal{O}(10^{-5})$.

For large ΔM the co-annihilation cross-sections decrease, which are the dominant processes in the small $\sin\theta$ limit. As a result relic abundance increases for a particular value of M_1 with larger ΔM . Hence we require a larger mass difference ΔM for larger DM mass to account for correct co-annihilation so that the relic density will be in the observed limit.

3.7 Collider Signature

If the new leptons are $\simeq 500$ GeV, they can be produced at the Large Hadron Collider (LHC). They will eventually decay to the lightest stable particle N_1 . The DM N_1 is stable, charge neutral and will escape from the detector, while its charged partner N^\pm may give promising signature if it is produced. For example, N^\pm can be pair produced via the Drell-Yan process mediated by γ and Z -boson. Note that the production of N^\pm is independent of singlet-doublet mixing. So the small values of $\sin\theta$, required for evading Xenon-100 and LUX bound at direct detection of DM, does not affect the pair production of N^\pm . On the other hand, production of $N_1 N^\pm$ pair via the exchange of SM W^\pm will be suppressed by low values of $\sin\theta$. Therefore, in what follows we will discuss signature of vector-like charged fermions N^\pm , pair produced mainly through γ and Z mediated Drell-Yan process.

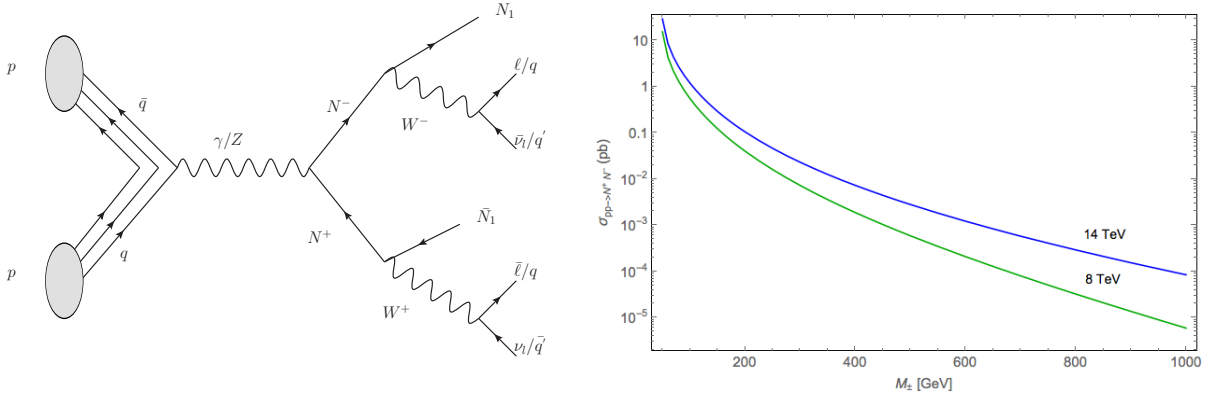


Figure 3.17: Left panel: Feynman graph producing $N^+ N^-$ pair at LHC and its subsequent decays. Right panel: Variation in production cross section $\sigma_{pp \rightarrow N^+ N^-}$ (pb) at LHC with respect to M_\pm for $E_{cm} = 8$ TeV (Green, below) and $E_{cm} = 14$ TeV (Blue, above).

Once the N^\pm is produced it decays via $N^\pm \rightarrow N_1 W^\pm$. If the mass splitting between N^\pm and N_1 , which is equivalent to $\Delta M = M_2 - M_1 \equiv M^\pm - M_1$, is larger than W mass, then the two body is favorable, otherwise the decay will proceed through off-shell W . So the relevant signatures in case of pair production of $N^+ N^-$ at LHC will be as follows: $pp \rightarrow N^+ N^- \rightarrow \bar{N}_1 N_1 W^+ W^-$; subsequently the possible final states are:

1. One lepton + Di-jet + Missing energy ($\ell 2j E_{\cancel{T}}$)
2. Two oppositely charged leptons + Missing energy ($2\ell E_{\cancel{T}}$)
3. 4 jets + Missing energy ($4j E_{\cancel{T}}$)

depending on whether the W 's decay hadronically or leptonically. See for example, the Feynman graph in the left of Fig. (3.17). We also show the variation in production cross-section $\sigma_{pp \rightarrow N^+ N^-}$

(pb) for N^+N^- at LHC with respect to $M_{\pm}(GeV)$ for $E_{cm} = 8$ TeV (Green, below) and $E_{cm} = 14$ TeV (Blue, above). Accordingly, we tabulate in Table (3.2) the production cross-sections as well as the cross-sections in hadronically quiet dilepton final state as well as in single lepton state for the benchmark points chosen above. For reference, contributions to the leptonic final states from dominant SM background; namely W^+W^- , ZZ , $t\bar{t}$ has also been tabulated in Table (3.3) and Table (3.4) for $E_{cm} = 8$ TeV and $E_{cm} = 14$ TeV respectively. It is seen that the only way to tame down the background is to put a very high missing energy cut, $E_{\cancel{T}} > 100$ GeV. The amount of signal that will be left after MET cut, depends on the amount of transverse momentum that is transferred to N_1 from the decay of N^{\pm} , which is proportional to the mass difference. However, as W^{\pm} is less massive than the DM, the significant part of the momentum will be carried by the DM. hence, it is expected that the peak of MET will be much higher than 100 GeV and a cut hence will retain a significant part of the signal. CalcHep [123] and Pythia [124] event generators have been used to produce the cross-sections. Just for clarifications, we also note here that missing energy is identified in terms of the visible momenta as follows: vector sum of the x and y components of the momenta separately for all visible objects form visible transverse momentum $(p_T)_{vis}$ and that is precisely the missing energy from momentum conservation.

$$(p_T)_{vis} = \sqrt{(\sum p_x)^2 + (\sum p_y)^2} = E_{\cancel{T}} \quad (3.37)$$

where, $\sum p_x = \sum (p_x)_{\ell} + \sum (p_x)_{jet}$ and similarly for $\sum p_y$.

What we see from the table, is that BP1 has a very small M_N and hence results with a huge cross-section. Hence, this point lies close to what has been discarded from non-observation of any excess in semi-leptonic or leptonic channels so far from 7 TeV data at LHC. However, for BP3 and BP4, there is a strong possibility that one might see an excess in the next run of LHC after careful background reduction. While for BP2, it seems very hard to see any excess in above channels unless we go to high luminosity LHC. The analysis presented here is more indicative than exhaustive. For generic collider implications of vector like DM, see [125, 126, 127], which also imply additional constraints on the DM parameter space.

Benchmark Points	$[\sigma_{pp \rightarrow N^+N^-}]_8$	$[\sigma_{\ell 2j E_{\cancel{T}}}]_8$	$[\sigma_{2\ell E_{\cancel{T}}}]_8$	$[\sigma_{pp \rightarrow N^+N^-}]_{14}$	$[\sigma_{\ell 2j E_{\cancel{T}}}]_{14}$	$[\sigma_{2\ell E_{\cancel{T}}}]_{14}$
BP1	284	80	12.5	700	197	31
BP2	0.58	0.16	0.025	3.3	0.93	0.15
BP3	10.13	2.85	0.45	35.1	9.88	1.55
BP4	27.02	7.6	1.19	82.5	23.2	3.64

Table 3.2: Production Cross-sections $\sigma_{pp \rightarrow N^+N^-}$ for the benchmark points at LHC for $E_{cm} = 8$ and 14 TeV. The leptonic final states $\sigma_{\ell 2j E_{\cancel{T}}}$ and $\sigma_{2\ell E_{\cancel{T}}}$ are also mentioned. All cross-sections are in fb.

There is another very interesting signature of the model. For example, if the mass splitting between N^{\pm} and N_1 is less than 90 GeV, then N^- will decay via three body suppressed process: $N^- \rightarrow N_1 \ell \nu_{\ell}$ and $N^- \rightarrow N_1 + di - jets$, due to small values of $\sin \theta$. The latter one may not be a suitable process to search at LHC, while the former one is useful to look for via a displaced vertex signature as discussed below. The decay rate is given in equation 3.13. In the left-panel of Fig. (3.18), we have shown $\Gamma^{-1}(cm)$ as a function of ΔM by taking $M_N = 150$ GeV and $m_{\ell} = 150$ MeV. We see that for small ΔM , say $\Delta M < 10$ GeV, we get a displaced vertex more than 1 cm. In

SM Background	$[\sigma_{\ell 2j E_{\cancel{T}}}]_8$	$[\sigma_{\ell 2j E_{\cancel{T}}}]_8, E_{\cancel{T}} > 100$	$[\sigma_{2\ell E_{\cancel{T}}}]_8$	$[\sigma_{2\ell E_{\cancel{T}}}]_8, E_{\cancel{T}} > 100$
WW	2.30	1.04	0.74	≤ 0.35
ZZ	0.38	0.005	10.4	≤ 0.5
$t\bar{t}$	5.43	0.16	0.09	$\simeq 0$

Table 3.3: SM background at LHC for $E_{cm} = 8$ TeV for $\ell 2j E_{\cancel{T}}$ and $2\ell E_{\cancel{T}}$ channels before and after missing energy cut $E_{\cancel{T}} > 100$ GeV. All cross-sections are in fb.

SM Background	$[\sigma_{\ell 2j E_{\cancel{T}}}]_{14}$	$[\sigma_{\ell 2j E_{\cancel{T}}}]_{14}, E_{\cancel{T}} > 100$	$[\sigma_{2\ell E_{\cancel{T}}}]_{14}$	$[\sigma_{2\ell E_{\cancel{T}}}]_{14}, E_{\cancel{T}} > 100$
WW	4.37	0.027	1.26	≤ 0.7
ZZ	0.83	0.01	16.9	≤ 1
$t\bar{t}$	21.4	0.88	0.41	≤ 0.1

Table 3.4: SM background at LHC for $E_{cm} = 14$ TeV for $\ell 2j E_{\cancel{T}}$ and $2\ell E_{\cancel{T}}$ channels before and after missing energy cut $E_{\cancel{T}} > 100$ GeV. All cross-sections are in fb.

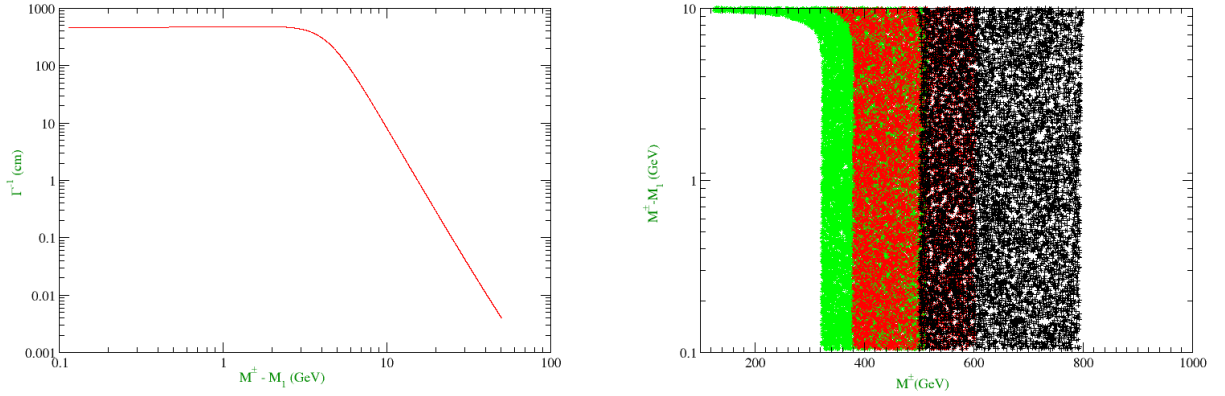


Figure 3.18: Left panel: Displaced vertex of N^- for $M^\pm = 150$ GeV, $m_\ell = 105$ MeV and $\sin \theta = 3 \times 10^{-4}$. Right panel: Γ^{-1} values varying between (1 - 10) cm in the plane of ΔM versus M^\pm for $\sin \theta = 3 \times 10^{-4}$ (in Green), 2×10^{-4} (in Red) and 10^{-4} (in Black) simultaneously from left to right.

the right panel of Fig.(3.18), we show Γ^{-1} values varying between (1 - 10) cm in the plane of ΔM versus M_N for $\sin \theta = 3 \times 10^{-4}$ (in Green), 2×10^{-4} (in Red) and 10^{-4} (in Black) simultaneously from left to right. The important point to be noted here is that to get a large displaced vertex we need a small mixing angle between the singlet and doublet. In the left panel of Fig. 3.19, a scatter plot is shown taking relic abundance as a function of DM mass keeping the mass splitting less than 50 GeV. Here, we fix the singlet-doublet mixing angle to be $\sin \theta = 3 \times 10^{-4}$, a moderately smaller value. We have also shown the correct relic abundance as allowed by the PLANCK data with a horizontal solid black line. We choose those set of points from the relic abundance data which are allowed by the PLANCK result and use them to calculate the displaced vertex signature of N^\pm (Γ^{-1}) and plotted as a function of M^\pm in the right-panel of Fig. (3.19). We observe that the displaced vertex becomes very small for larger values of M^\pm , as the inverse of decay width Γ^{-1} is inversely proportional to the mass of decaying charged particle. However, for smaller masses with

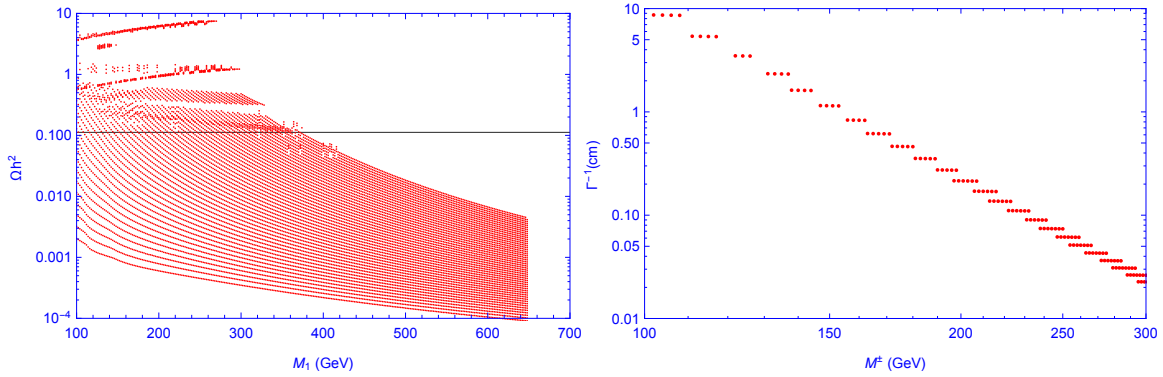


Figure 3.19: Left panel: Scatter plot showing relic abundance as a function of DM mass with mass splitting less than 50 GeV. Black solid line shows the correct relic abundance as allowed by PLANCK data. Right panel: Displaced vertex (Γ^{-1}) in cm as a function of M^\pm (GeV) for relic density allowed points. Value of mixing angle $\sin \theta = 3 \times 10^{-4}$ is used in both the plots for illustration.

$M^\pm \sim 200$ GeV, the displaced vertex can be as large as 2.5 mm to be detected in Large Hadron Collider (LHC). The important point to be noted here is that to get a large displaced vertex we need a small mixing angle between the singlet and doublet. In fact, the small mixing angle is favoured by all the constraints we discussed in previous sections, such as correct relic abundance and null detection of DM at direct search experiments. However, from Eq. (3.17) we also learnt that the singlet-doublet mixing can not be arbitrarily small and therefore, the displaced vertex can not be too large.

3.8 Addition of Scalar triplet to the Inert Fermion DM Model

In order to explain the neutrino mass and DM in a single framework, a scalar triplet $\Delta(1, 3, 2)$ is added to the inert fermion DM model. The numbers inside the parenthesis are quantum numbers under the SM gauge group $SU(3)_c \times SU(2)_L \times U(1)_Y$. After electroweak symmetry breaking when Δ gets an induced vev, neutrinos get mass through the coupling with triplet scalar Δ . In the presence of the scalar triplet, new channels open up for DM annihilation hence can alter the relic density of DM. As the DM also couples to Δ , a gauge invariant Majorana mass term is also possible for the DM. Hence it splits up into two Majorana states with a small mass splitting. As a result the direct detection cross-section through Z mediation is suppressed. We will address these issues in the subsequent sections.

The new terms possible in addition to the Lagrangian 3.1 is:

$$\mathcal{L}_{\text{new}} = (D^\mu \Delta)^\dagger (D_\mu \Delta) + \mathcal{L}_{yuk} - V(\Delta, H), \quad (3.38)$$

where D_μ is the covariant derivative involving $SU(2)$ (W_μ) and $U(1)_Y$ (B_μ) gauge bosons and is given by :

$$D_\mu = \partial_\mu - i\frac{g}{2}\tau \cdot W_\mu - ig'\frac{Y}{2}B_\mu.$$

The scalar potential involving SM doublet (H) and triplet (Δ) in Eq. (3.38) is given by

$$\begin{aligned}
V(\Delta, H) &= -\mu_H^2 H^\dagger H + \lambda_H (H^\dagger H)^2 + \mu_\Delta^2 (\Delta^\dagger \Delta) + \lambda_\Delta (\Delta^\dagger \Delta)^2 \\
&+ \lambda_{H\Delta} (H^\dagger H) (\Delta^\dagger \Delta) + \frac{1}{2} [\mu \Delta^\dagger H H + \text{h.c.}] ,
\end{aligned} \tag{3.39}$$

where Δ in matrix form is

$$\Delta = \begin{pmatrix} \frac{\Delta^+}{\sqrt{2}} & \Delta^{++} \\ \Delta^0 & -\frac{\Delta^+}{\sqrt{2}} \end{pmatrix} . \tag{3.40}$$

We assume that μ_Δ^2 is positive. So it doesn't acquire a vacuum expectation value (vev). But it gets an induced vev after EW phase transition. The vev of Δ is given by

$$\langle \Delta \rangle \equiv u_\Delta \approx -\frac{\mu v^2}{\sqrt{2}(\mu_\Delta^2 + \lambda_{H\Delta} v^2/2)} \tag{3.41}$$

where v is the vev of Higgs field and its value is 174 GeV.

The Yukawa interaction in Eq. (3.38) is given by:

$$\mathcal{L}_{yuk} = \frac{1}{\sqrt{2}} [(f_L)_{\alpha\beta} \overline{L}_\alpha^c i\tau_2 \Delta L_\beta + f_N \overline{N}^c i\tau_2 \Delta N + \text{h.c.}] , \tag{3.42}$$

where L is the SM lepton doublet and α, β denote family indices. The Yukawa interactions importantly inherit the source of neutrino masses.

3.8.1 Mixing in the scalar sector

There are two scalar particles in the model, one is a doublet and another is a triplet under SM gauge group. The quantum fluctuations around the vacuum is given as:

$$H^0 = \frac{1}{\sqrt{2}}(v + h^0 + i\xi^0), \Delta^0 = \frac{1}{\sqrt{2}}(u_\Delta + \delta^0 + i\eta^0) \tag{3.43}$$

The mass matrix is given as :

$$\mathcal{M}_{sc}^2 = \begin{pmatrix} M_H^2 & \mu v/2 \\ \mu v/2 & M_\Delta^2 \end{pmatrix} \tag{3.44}$$

where $M_\Delta^2 = \mu_\Delta^2 + \lambda_{H\Delta} v^2/2$ and $M_H^2 = 2\lambda_H v^2$. The two neutral Higgs fields (CP - even) mass eigenstates are given by

$$H_1 = \cos \theta_0 h^0 + \sin \theta_0 \delta^0, H_2 = -\sin \theta_0 h^0 + \cos \theta_0 \delta^0 \tag{3.45}$$

where H_1 is the SM like Higgs and H_2 is the triplet like Higgs. The mixing angle is given by

$$\tan 2\theta_0 = \frac{\mu v}{(M_\Delta^2 - M_H^2)} . \tag{3.46}$$

The corresponding mass eigenvalues are M_{H_1} (SM Higgs like) and M_{H_2} (triplet like) and are given as :

$$\begin{aligned} M_{H_1}^2 &\approx M_H^2 - \frac{(\mu v/2)^2}{M_\Delta^2 - M_H^2} \\ M_{H_2}^2 &\approx M_\Delta^2 + \frac{(\mu v/2)^2}{M_\Delta^2 - M_H^2}. \end{aligned} \quad (3.47)$$

Since the addition of a scalar triplet can modify the ρ parameter, which is not differing from SM value: $\rho = 1.00037 \pm 0.00023$ [128], so we have a constraint on the vev u_Δ as:

$$u_\Delta \leq 3.64 \text{ GeV}. \quad (3.48)$$

For different values of M_Δ we have shown μ as a function of $\sin \theta_0$ in Fig. (3.20). Here we see that smaller is the triplet scalar mass, the smaller is the dependence on mixing angle $\sin \theta_0$.

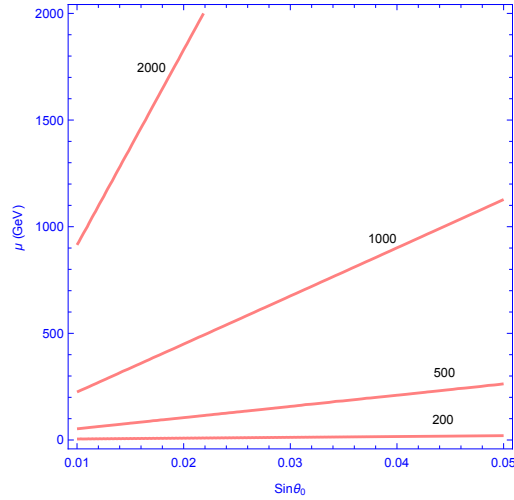


Figure 3.20: Contours of different values of M_Δ (in GeV) in the plane of μ versus $\sin \theta_0$.

From Eqs.(3.46), (3.41) and (3.48) we see that there exist an upper bound on the mixing angle

$$\sin \theta_0 < 0.02 \left(\frac{174 \text{ GeV}}{v} \right) \left(\frac{1}{1 - 0.39 \frac{(M_H/125 \text{ GeV})^2}{(M_\Delta/200 \text{ GeV})^2}} \right). \quad (3.49)$$

We may also get a constraint on $\sin \theta_0$ from the decay of SM Higgs to different channels. For example, let us take the decay of H_1 to $\tau\tau$ leptons. The decay width is given by:

$$\Gamma = \frac{M_{H_1}}{8\pi} \frac{m_\tau^2}{v^2} \left(1 - \frac{4m_\tau^2}{M_{H_1}^2} \right)^{3/2} (1 - \sin^2 \theta_0) \quad (3.50)$$

Comparing with the experimental branching fraction $Br(H_1 \rightarrow \tau\tau) = 6.272 \times 10^{-2}$, we found that $\sin \theta_0 = 0.176$. So any value of the mixing angle less than this will be allowed by the corresponding decay experiment. Similarly one can easily derive the limit on the doublet-triplet mixing from branching fraction of SM Higgs decaying to W^+W^{*-} , ZZ^* , which are much precisely measured at

LHC. For example, if we choose Higgs decay to W^+W^{-*} state, the observed branching fraction is $Br(H_1 \rightarrow W^+W^{-*}) : 2.317 \times 10^{-1}$. In order to obtain a limit on the doublet-triplet mixing angle $\sin \theta_0$, we need to calculate the decay width of this process as given in [129] :

$$\Gamma_{H_1 \rightarrow WW^* \rightarrow Wf\bar{f}'} = \frac{3g^4 M_{H_1}}{512\pi^3} (g \sin \theta_0 u_\Delta / (4M_w) - \cos \theta_0)^2 F(x), \quad (3.51)$$

where

$$F(x) = -|1-x^2| \left(\frac{47}{2}x^2 - \frac{13}{2} + \frac{1}{x^2} \right) + 3(1-6x^2+4x^4)|Ln(x)| + \frac{3(1-8x^2+20x^4)}{|\sqrt{4x^2-1}|} \arccos \left[\frac{3x^2-1}{2x^3} \right],$$

with $x = M_W/M_{H_1}$. In the small mixing limit $\sin \theta_0 \rightarrow 0$, the decay reproduces same branching ratio as that of the SM prediction. However, as we increase the value of the mixing angle, the branching ratio to this particular final state reduces due to larger triplet contributions. For example, with $\sin \theta_0 = 0.05, 0.07, 0.1$, $Br(H_1 \rightarrow WW^*)$ is changed by 0.27%, 0.51%, 1.04% respectively from the central value. Hence, in a conservative limit, if we take $\sin \theta_0 \sim 0.05$ or smaller, it is consistent with the experimental observation of Higgs decay to WW^* final state.

Thus we see that the bound obtained on the mixing angle from Higgs decay is less constraining than that from the ρ parameter. Therefore, we will use the constraint on the mixing angle, obtained from ρ parameter, while calculating the DM-nucleon elastic scattering in section (3.11.2). Since the doublet-triplet scalar mixing is found to be small we assume that the flavour eigenstates are the mass eigenstates and treat $M_{H_1} = M_H, M_{H_2} = M_\Delta$ through out the calculation.

We assume that there is no mixing between the neutral CP-odd states as well as in the charged states. So that the ξ^0 is absorbed in the unitary gauge by the gauge bosons after the symmetry breaking and the charged triplet scalar fields will remain as the mass eigen fields.

3.9 Small neutrino mass

The coupling of scalar triplet Δ to SM lepton and Higgs doublets combinely break the lepton number by two units as given in Eq. (3.42). As a result the $\Delta L_\alpha L_\beta$ coupling yields Majorana masses to three flavors of active neutrinos as [130, 131, 132, 133, 134, 135, 136]:

$$(M_\nu)_{\alpha\beta} = \sqrt{2}(f_L)_{\alpha\beta} \langle \Delta \rangle \approx (f_L)_{\alpha\beta} \frac{-\mu v^2}{\sqrt{2}M_\Delta^2}. \quad (3.52)$$

Taking $\mu \simeq M_\Delta \simeq \mathcal{O}(10^{14})$ GeV, we can explain neutrino masses of order 0.1eV with a coupling strength $f_L \simeq 1$. However, the scale of M_Δ can be brought down to TeV scales by taking the smaller couplings.

To get the neutrino mass eigen values, the above mass matrix can be diagonalised by the usual U_{PMNS} matrix as :

$$M_\nu = U_{PMNS} M_\nu^{diag} U_{PMNS}^T, \quad (3.53)$$

where U_{PMNS} is given by

$$U_{PMNS} = \begin{pmatrix} c_{12}c_{13} & s_{12}c_{13} & s_{13}e^{-i\delta_{13}} \\ -s_{12}c_{23} - c_{12}s_{23}s_{13}e^{i\delta_{13}} & c_{12}c_{23} - s_{12}s_{23}s_{13}e^{i\delta_{13}} & s_{23}c_{13} \\ s_{12}s_{23} - c_{12}c_{23}s_{13}e^{i\delta_{13}} & -c_{12}s_{23} - s_{12}c_{23}s_{13}e^{i\delta_{13}} & c_{23}c_{13} \end{pmatrix} \cdot U_{ph}, \quad (3.54)$$

with c_{ij} , s_{ij} stand for $\cos\theta_{ij}$ and $\sin\theta_{ij}$ respectively and U_{ph} is given by

$$U_{ph} = \text{Diag}(e^{-i\gamma_1}, e^{-i\gamma_2}, 1). \quad (3.55)$$

Where γ_1 , γ_2 are two Majorana phases. The diagonal matrix $M_\nu^{diag} = \text{Diag}(m_1, m_2, m_3)$ with diagonal entries are the mass eigen values for the neutrinos. The current neutrino oscillation data at 3σ confidence level give the constraint on mixing angles [128] :

$$0.259 < \sin^2\theta_{12} < 0.359, \quad 0.374 < \sin^2\theta_{23} < 0.628, \quad 0.0176 < \sin^2\theta_{13} < 0.0295 \quad (3.56)$$

However little information is available about the CP violating Dirac phase δ as well as the Majorana phases. Although the absolute mass of neutrinos is not measured yet, the mass square differences have already been measured to a good degree of accuracy :

$$\begin{aligned} \Delta m_0^2 &\equiv m_2^2 - m_1^2 = (6.99 - 8.18) \times 10^{-5} \text{eV}^2 \\ |\Delta m_{atm}^2| &\equiv |m_3^2 - m_1^2| = (2.23 - 2.61) \times 10^{-3} \text{eV}^2 \end{aligned} \quad (3.57)$$

One of the main issues of neutrino physics lies in the sign of the atmospheric mass square difference $|\Delta m_{atm}^2| \equiv |m_3^2 - m_1^2|$, which is still unknown. This yields two possibilities: normal hierarchy (NH) ($m_1 < m_2 < m_3$) or inverted hierarchy (IH) ($m_3 < m_1 < m_2$). Another possibility, yet allowed, is to have a degenerate (DG) neutrino mass spectrum ($m_1 \sim m_2 \sim m_3$). Assuming that the neutrinos are Majorana, the mass matrix can be written as :

$$M_\nu = \begin{pmatrix} a & b & c \\ b & d & e \\ c & e & f \end{pmatrix} \quad (3.58)$$

Using equations 3.53, 3.54, 3.56 and 3.57, we can estimate the unknown parameters in neutrino mass matrix of Eq. (3.58). To estimate the parameters in NH, we use the best fit values of the oscillation parameters. For a typical value of $m_1 = 0.0001$ eV, we get the mass parameters (in eV) as :

$$\begin{aligned} a &= 0.003833, \quad b = 0.00759, \quad c = 0.002691 \\ d &= 0.023865, \quad e = 0.02083, \quad f = 0.03038 \end{aligned} \quad (3.59)$$

Similarly for IH case, choosing $m_3 = 0.001$ eV, we get the mass parameters (in eV) as :

$$\begin{aligned} a &= 0.0484, \quad b = -0.00459, \quad c = -0.00573 \\ d &= 0.02893, \quad e = -0.02366, \quad f = 0.02303 \end{aligned} \quad (3.60)$$

In both the cases, we put the Dirac and Majorana phases to be zero for simplicity.

The mass of the scalar triplet can also be brought down to TeV scale by choosing appropriate Yukawa coupling. If the mass is order of a few hundreds of GeV, then it can give interesting dilepton signals in the collider. See for example, [137, 138, 139, 140, 141, 142] for a detailed discussion regarding the dilepton signatures at collider.

We would like to note that the presence of scalar triplet addresses the issue of generating neutrino masses as we discussed here, and has minor dependence on DM relic density. However, the scalar triplet plays a major role in the direct detection by forbidding Z-mediated DM-nucleon interaction and thereby increasing the limit on singlet-doublet mixing as we will discuss shortly.

3.10 Pseudo-Dirac nature of DM

3.10.1 Pseudo-Dirac nature of Inert fermion doublet DM

Let us assume the case where the singlet fermion χ^0 is absent in the spectrum. In this case, the imposed Z_2 symmetry stabilizes the neutral component of the fermion doublet $N \equiv (N^0, N^-)^T$. From Eq. (3.42) we see that after EW phase transition the induced vev of the triplet yields a Majorana mass to N^0 and is given by:

$$m = \sqrt{2}f_N \langle \Delta \rangle \approx f_N \frac{-\mu v^2}{\sqrt{2}M_\Delta^2}. \quad (3.61)$$

Thus the N^0 has a large Dirac mass M_N as given in Eq. (3.38) and a small Majorana mass m as shown in the above Eq. (3.61). Therefore, we get a mass matrix in the basis $\{N_L^0, (N_R^0)^c\}$ as:

$$\mathcal{M} = \begin{pmatrix} m & M_N \\ M_N & m \end{pmatrix} \quad (3.62)$$

The presence of small Majorana mass of the doublet DM splits the Dirac state N^0 into two pseudo-Dirac states: $\psi_{1,2}^0$, whose mass eigenvalues are given by $M_N \pm m$ for mixing angle $\pi/4$, which is the maximal mixing. Hence the mass splitting between the two states $\{N_L^0, (N_R^0)^c\}$ is:

$$\delta M = 2m = 2\sqrt{2}f_N u_\Delta. \quad (3.63)$$

Notice that the above mass splitting $\delta M \ll M_N$ and hence does not play any role in the relic abundance calculation, where both the components act as degenerate DM components. However, the small mass splitting between the two pseudo-Dirac states prohibits N_0 to interact to the detector through Z mediation in the non-relativistic inelastic scattering limit and is crucial to escape from the strong direct detection constraints mediated via Z -boson. For example, to explain the DAMA signal through the inelastic scattering of DM with the nuclei the required mass splitting should be $\mathcal{O}(100\text{keV})$ [85, 84, 143].

A crucial observation from Eq. (3.52) and (3.61) is that the ratio:

$$R = \frac{(M_\nu)}{m} = \frac{f_L}{f_N} \quad (3.64)$$

is extremely small. In particular, if $M_\nu \sim \mathcal{O}(\text{eV})$ and $m \sim \mathcal{O}(100\text{KeV})$ then $R \sim 10^{-5}$. In other words the triplet scalar coupling to SM sector is highly suppressed in comparison to the DM sector.

3.10.2 Pseudo-Dirac nature of singlet-doublet fermion DM

Next we adhere to the actual scenario where DM is the lightest one among the mixed states of singlet and doublet fermions χ^0 and N^0 . As discussed in section 3.2, the DM is assumed to be $N_1 = \cos\theta\chi^0 + \sin\theta N^0$ with a Dirac mass M_1 . However, from Eq. (3.42) we see that the vev of Δ induces a Majorana mass to N_1 due to singlet-doublet mixing and is given by:

$$m_1 = \sqrt{2}f_N \sin^2\theta \langle \Delta \rangle \approx f_N \sin^2\theta \frac{-\mu v^2}{\sqrt{2}M_\Delta^2}. \quad (3.65)$$

Thus the Majorana mass m_1 splits the Dirac spinor N_1 into two pseudo-Dirac states $\psi_1^{a,b}$ with masses $M_1 \pm m_1$. The mass splitting between the two pseudo-Dirac states ($\psi_1^{a,b}$) is given by

$$\delta M_1 = 2m_1 = 2\sqrt{2}f_N \sin^2\theta u_\Delta \quad (3.66)$$

Note that again $\delta M_1 \ll M_1$ from the estimate of induced vev of the triplet and hence does not play any role in the relic abundance calculation. However, the sub-GeV order mass splitting plays a crucial role in direct detection by forbidding the Z-boson mediated DM-nucleon elastic scattering. We will come back to this issue while discussing the inelastic scattering of DM with nucleon in sec. 3.11.1. Now from Eq. (3.52) and (3.65) we see that the ratio:

$$R = \frac{(M_\nu)}{m_1} = \frac{f_L}{f_N \sin^2\theta}. \quad (3.67)$$

Thus in comparison to Eq. (3.64), we see that the ratio between the two couplings $R = f_L/f_N$ is improved by two orders of magnitude (*i.e.* $R \sim 10^{-3}$) if we assume $\sin\theta = 0.1$, which is the rough order of magnitude of singlet-doublet mixing being used in relic abundance calculation as we demonstrate in the next section.

3.10.3 Relics of Singlet-Doublet mixed fermion DM in presence of scalar triplet

In the presence of light scalar triplet Δ , there will be additional s-channel processes through Δ^0 mediation as well as processes involving Δ particles in the final states in addition to the channels mentioned in sec 3.6. The relevant processes are :

$$\begin{aligned} N_1 \bar{N}_1 &\xrightarrow{\Delta^0} f\bar{f}, hh, W^+W^-, ZZ \\ N_1 \bar{N}_1 &\rightarrow \Delta^{++}\Delta^{--}, \Delta^+\Delta^-\Delta^0\Delta^0, W^\pm\Delta^\pm, \Delta^0 H, \Delta^0 Z \\ N_1 \bar{N}_2 &\xrightarrow{\Delta^0} f\bar{f}, hh, W^+W^-, ZZ \\ N_1 \bar{N}_2 &\rightarrow \Delta^{++}\Delta^{--}, \Delta^0\Delta^0, \Delta^+\Delta^-, W^\pm\Delta^\pm, \Delta^0 h, \Delta^0 Z \\ N_1 N^+ &\rightarrow \Delta^-\Delta^{++}, W^-\Delta^{++}, \Delta^0\Delta^+, h\Delta^+, Z\Delta^+, \gamma\Delta^+, W^+\Delta^0 \\ N_2 \bar{N}_2 &\xrightarrow{\Delta^0} f\bar{f}, hh, W^+W^-, ZZ \\ N_2 \bar{N}_2 &\rightarrow \Delta^{++}\Delta^{--}, \Delta^+\Delta^-\Delta^0\Delta^0, W^\pm\Delta^\pm, \Delta^0 H, \Delta^0 Z \end{aligned}$$

$N_2 N^+ \rightarrow \Delta^- \Delta^{++}, W^- \Delta^{++}, \Delta^0 \Delta^+, h \Delta^+, Z \Delta^+, \gamma \Delta^+, W^+ \Delta^0$
 $N^\pm N^\pm \rightarrow \Delta^{++} \Delta^{--}, \Delta^+ \Delta^-, W^+ \Delta^-, Z \Delta^0,$
 where f' 's are SM fermions and γ is the photon field.

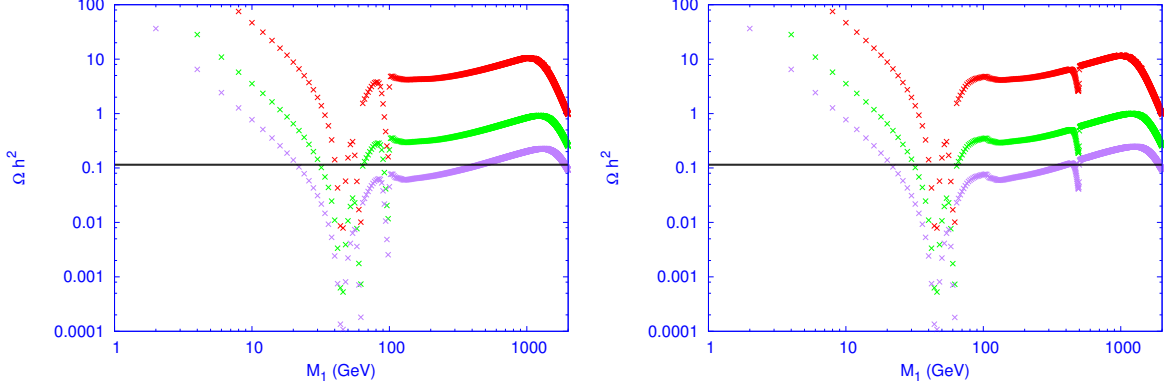


Figure 3.21: Relic density of DM as a function of its mass M_1 for different values of $\sin \theta = 0.1, 0.2, 0.3$, shown by red (top), green (middle) and purple (bottom) respectively. The value of the triplet mass: $M_\Delta = 200, 1000 \text{ GeV}$ is fixed respectively for left and right panel. All these plots are generated keeping a fixed value of the mass splitting $M_2 - M_1 = 500 \text{ GeV}$. Ratio of Majorana couplings are fixed at : $\frac{f'_L}{f'_N} = 10^{-3}$ for illustration.

Relic density of the DM is calculated using micrOMEGAs [122]. In Fig. 3.21, relic density of DM is plotted as a function of its mass keeping the mass difference fixed at $M_2 - M_1 = 500 \text{ GeV}$, for three different values of the mixing angle: $\sin \theta = 0.1, 0.2, 0.3$, shown in red (top), green (middle), purple (bottom) respectively. In the left panel of the fig. 3.21 we use $M_\Delta = 200 \text{ GeV}$, whereas in the right panel of fig. 3.21 we use $M_\Delta = 1000 \text{ GeV}$. The black horizontal line corresponds to the observed relic density: $\Omega_{\text{DM}} h^2 = 0.1199 \pm 0.0027$ by PLANCK [9]. For both the plots in fig 3.21 we fix the ratio of Majorana couplings to be: $\frac{f'_L}{f'_N} = 10^{-3}$. The analysis is same here as presented in sec 3.6.2. For a comparison see fig 3.14. From the plots in the fig. 3.21, it can be seen that the contribution of Δ field to the relic density is coming only near the resonance points. The triplet scalar does not contribute significantly apart from the resonant annihilation through s-channel process mediated via Δ^0 . This is because the total cross-section is dominated by $N_1 \bar{N}_1 \rightarrow W^+ W^-$ and the Δ -mediated s-channel contribution is suppressed due to the large triplet scalar mass present in the propagator. Therefore, we can not expect any change in relic density allowed parameter space if we vary the ratio of Majorana couplings: $\frac{f'_L}{f'_N}$. The cross-sections involving scalar triplet in the final states also do not affect the relic abundance since those are suppressed by phase space due to heavy triplet masses and as in this region of parameter space ($M_1 > M_\Delta$) the cross-sections involving gauge bosons in the final state dominate. In summary, we don't see almost any difference in relic density of DM in left and right panel of Fig. 3.21 due to change in triplet masses. We can however see that the resonance drop due to s-channel triplet mediation is reduced for large triplet mass $M_\Delta = 1000 \text{ GeV}$ (shown in right panel) in comparison to $M_\Delta = 200 \text{ GeV}$ (shown in left panel) for obvious reasons. As the mass splitting between N_1 and N_2 is taken to be very large in the above cases, the dominant contribution to relic density comes from annihilation channels while co-annihilation channels are

Boltzmann suppressed.

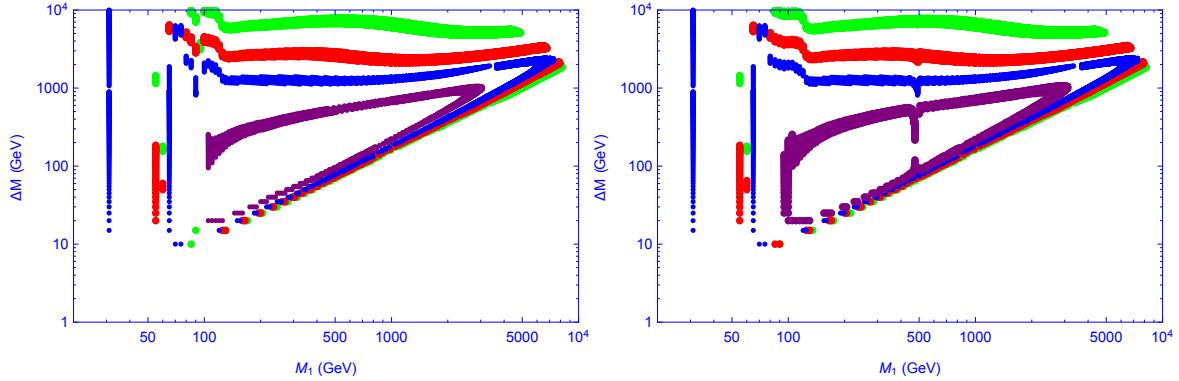


Figure 3.22: Scatter plot for correct relic density in the plane of M_1 and ΔM , shown by green, red, blue and purple coloured points for $\sin \theta = 0.1, 0.15, 0.2, 0.3$ respectively. Two different triplet masses are chosen $M_\Delta = 200$, and 1000 GeV respectively for the left and right panel plots. We fixed the value of Majorana coupling ratio: $f_L/f_N = 10^{-3}$ in both the figures for illustration.

Now we will show how the mass splitting between N_1 and N_2 affects the relic density of the DM. In fig. 3.22, we have shown a scatter plot for correct relic density in the plane of M_1 and $\Delta M = M_2 - M_1$. Green, red, blue and purple coloured points satisfy the constraint of relic density for $\sin \theta = 0.1, 0.15, 0.2, 0.3$ respectively (from outermost to innermost contour). The mass of scalar triplet $M_\Delta = 200, 1000$ GeV is used in left and right panel respectively. There is not much difference in the parameter space if we vary the scalar triplet mass except few points in the resonance region. Also the fig 3.22 is not much differing than fig 3.15 apart from Δ^0 resonance points and hence the analysis. It can be clearly seen in left and right panel of the fig. 3.22 with scalar triplet mass 200 GeV and 1000 GeV respectively. The Yukawa coupling ratio $f_L/f_N = 10^{-3}$ is fixed for both the plots. Again, if we change this ratio to a different value, no significant change in the allowed parameter space is expected.

3.11 Direct Detection in presence of the scalar triplet

In the presence of the scalar triplet, a Majorana mass term is possible for the DM. As a result, the Majorana mass splits the Dirac state into two Majorana states. Due to which the DM interactions with the nucleus becomes inelastic through Z boson mediation. However elastic scattering is still be possible through scalar mediation. We will discuss the details in the following.

3.11.1 Direct Detection of DM through inelastic scattering with the nuclei

As we have seen in section (3.6.1), the inert fermion doublet N^0 alone does not produce correct relic abundance. Therefore, we refrain ourselves to consider the inelastic scattering of N^0 only with the

nuclei mediated via Z boson. Rather we will consider the inelastic scattering of DM N_1 , which is an admixture of doublet N^0 and singlet χ^0 .

From Eq. (3.38), the relevant interaction for scattering of N_1 with nucleon mediated via the Z -boson is given by

$$\mathcal{L}_{Z\text{-DM}} \supset \overline{N_1} (\gamma^\mu \partial_\mu + ig_z \gamma^\mu Z_\mu) N_1, \quad (3.68)$$

where $g_z = \frac{g}{2 \cos \theta_w} \sin^2 \theta$. However the presence of scalar triplet, as discussed in section (3.10.2), splits the Dirac state N_1 into two pseudo-Dirac states $\psi_1^{a,b}$ with a small mass splitting m_1 . Therefore, the above interaction in terms of the new eigenstates $\psi_1^{a,b}$ can be rewritten as:

$$\mathcal{L}_{Z\text{-DM}} \supset \overline{\psi_1^a} i \gamma^\mu \partial_\mu \psi_1^a + \overline{\psi_1^b} i \gamma^\mu \partial_\mu \psi_1^b + ig_z \overline{\psi_1^a} \gamma^\mu \psi_1^b Z_\mu. \quad (3.69)$$

One can notice from the above equation that the dominant gauge interaction is off-diagonal, while the diagonal interaction vanishes. As a result there will be inelastic scattering of DM with the nucleus is possible. Note that the mass splitting between the two mass eigen states $\psi_1^{a,b}$ is given by: $\delta M_1 = 2\sqrt{2} f_N \sin^2 \theta u_\Delta$. In this case, the minimum velocity of the DM needed to register a recoil inside the detector is given by [144, 145, 85, 84, 143] :

$$v_{\min} = c \sqrt{\frac{1}{2m_n E_R} \left(\frac{m_n E_R}{\mu_r} + \delta M_1 \right)}, \quad (3.70)$$

where E_R is the recoil energy of the nucleon and μ_r is the reduced mass. If the mass splitting is above a few hundred keV, then it will be difficult to excite ψ_1^b with the largest possible kinetic energy of the DM ψ_1^a . So the inelastic scattering mediated by Z -boson will be forbidden. As a result constraints coming from direct detection can be relaxed significantly. This is an important consequence in presence of the scalar triplet Δ in this model, which makes a sharp distinction with the existing analysis in this direction.

3.11.2 Direct Detection of DM through elastic scattering with the nuclei

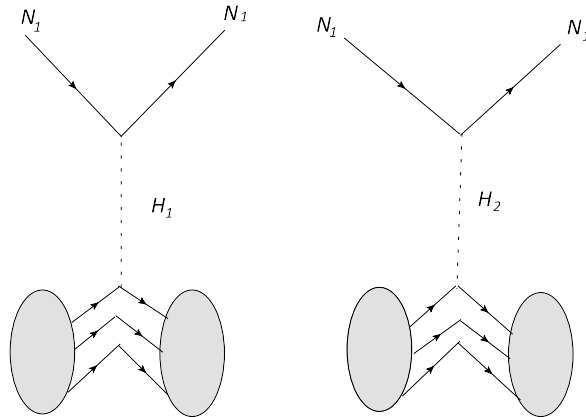


Figure 3.23: Feynman diagrams for direct detection of N_1 DM via Higgs mediation.

The Z mediated DM-nuclei scattering becomes inelastic, but the elastic interaction is still be possible through the scalar mediation. The relevant diagram through which N_1 talks to the nucleus

is shown in Fig. 3.23. The constraint on the model parameters as coming from the experiments like Xenon-100 [12] and LUX [6] which at present give strongest constraint on spin-independent DM-nucleon cross-section from the null detection of DM yet. In our model, this in turn puts a stringent constraint on the singlet-doublet mixing angle $\sin\theta$ for spin independent DM-nucleon interaction mediated via the H_1 and H_2 -bosons (see in the Fig. (3.23)). The cross-section per nucleon is given by [111, 112]

$$\sigma_{\text{SI}} = \frac{1}{\pi A^2} \mu_r^2 |\mathcal{M}|^2 \quad (3.71)$$

where A is the mass number of the target nucleus, $\mu_r = M_1 m_n / (M_1 + m_n) \approx m_n$ is the reduced mass, m_n is the mass of nucleon (proton or neutron) and \mathcal{M} is the amplitude for DM-nucleon cross-section. There are two t-channel processes through which DM can interact with the nucleus which is shown in the fig 3.23. The amplitude is given by:

$$\mathcal{M} = \sum_{i=1,2} [Z f_p^i + (A - Z) f_n^i] \quad (3.72)$$

where the effective interaction strengths of DM with proton and neutron are given by:

$$f_{p,n}^i = \sum_{q=u,d,s} f_{Tq}^{(p,n)} \alpha_q^i \frac{m_{(p,n)}}{m_q} + \frac{2}{27} f_{TG}^{(p,n)} \sum_{q=c,t,b} \alpha_q^i \frac{m_{p,n}}{m_q} \quad (3.73)$$

with

$$\alpha_q^1 = \frac{Y \sin 2\theta \cos^2 \theta_0}{M_H^2} \left(\frac{m_q}{v} \right) \quad (3.74)$$

$$\alpha_q^2 = -\frac{Y \sin 2\theta \sin^2 \theta_0}{M_\Delta^2} \left(\frac{m_q}{v} \right). \quad (3.75)$$

In Eq. (3.26), the different coupling strengths between DM and light quarks are given by [117] $f_{Tu}^{(p)} = 0.020 \pm 0.004$, $f_{Td}^{(p)} = 0.026 \pm 0.005$, $f_{Ts}^{(p)} = 0.118 \pm 0.062$, $f_{Tu}^{(n)} = 0.014 \pm 0.004$, $f_{Td}^{(n)} = 0.036 \pm 0.008$, $f_{Ts}^{(n)} = 0.118 \pm 0.062$. The coupling of DM with the gluons in target nuclei is parameterized by

$$f_{TG}^{(p,n)} = 1 - \sum_{q=u,d,s} f_{Tq}^{(p,n)}. \quad (3.76)$$

We have plotted the spin independent direct detection cross-section as a function of DM mass in the Fig.3.24 by taking the value of $M_\Delta = 200$ GeV for two different values of $M_2 - M_1 = 100, 500$ GeV in the left and right panel respectively. The plot is generated using different values of the singlet-doublet mixing angle: $\sin\theta = \{0.05-0.1\}$ (Purple), $\sin\theta = \{0.1-0.15\}$ (Pitch), $\sin\theta = \{0.15-0.2\}$ (Green), $\sin\theta = \{0.2-0.25\}$ (Gray), $\sin\theta = \{0.25-0.3\}$ (Orange), $\sin\theta = \{0.3-0.35\}$ (Red). The top Black dotted line shows the experimental limit on the SI nuclei-DM cross-section with DM mass predicted from LUX 2016 and the one below shows the sensitivity of XENON1T. The constraint from XENON 100 is loose and weaker than the LUX data and hence not shown in the figure. One of the main outcome of the figure in the left panel is that with larger $\sin\theta$, due to larger Yukawa coupling direct search cross-section through Higgs mediation is larger. Hence, LUX data constrains the singlet-doublet mixing to $\sin\theta \sim 0.3$ for DM mass ~ 600 GeV with $\Delta M = 100$ GeV (on the left hand side of Fig. 3.24). The constraint on the mixing is even more weaker for larger DM mass

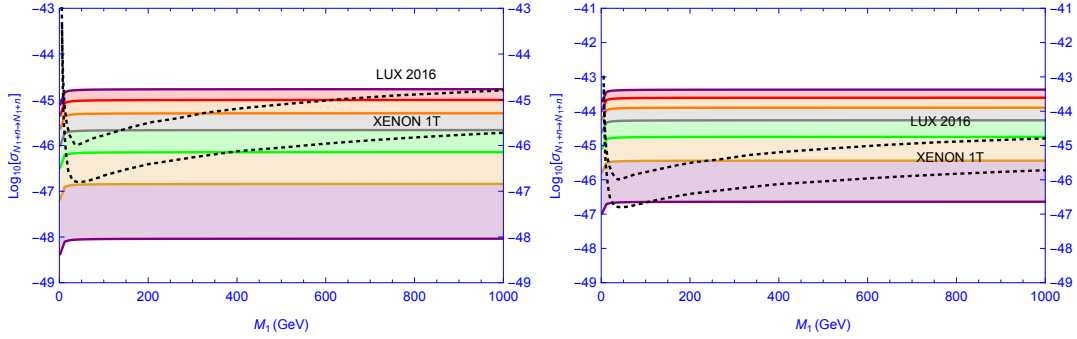


Figure 3.24: Spin Independent direct detection cross-section for DM as a function of DM mass for $\sin \theta = \{0.05-0.1\}$ (Purple), $\sin \theta = \{0.1-0.15\}$ (Pitch), $\sin \theta = \{0.15-0.2\}$ (Green), $\sin \theta = \{0.2-0.25\}$ (Gray), $\sin \theta = \{0.25-0.3\}$ (Orange), $\sin \theta = \{0.3-0.35\}$ (Red). Black dotted curves show the data from LUX and XENON 1T prediction. Value of $\Delta M = 100, 500$ GeV are fixed for left and right panel figures respectively. The scalar triplet mass is fixed at $M_\Delta = 200$ GeV and scalar mixing angle is fixed at $\sin \theta_0 = 0.05$ for the calculation.

~ 900 GeV and can be as large as $\sin \theta \sim 0.4$. This presents a strikingly different outcome than what we obtained in absence of scalar triplet, the mixing angle was constrained there significantly to $\sin \theta \leq 0.1$ to account for the null observation in LUX data. Again this is simply due to the absence of Z mediated direct search processes due to the mass splitting generated by the triplet as discussed in the above section and hence allows the DM to live in a much larger region of relic density allowed parameter space. In the right panel of the Fig. 3.24 with larger $\Delta M = 500$ GeV, the constraint on $\sin \theta$ is more stringent than the left one. It is because the SI cross-section is enhanced due to the increase in Yukawa coupling $Y \propto \Delta M$ for larger ΔM as expected. In the right panel, for DM mass of ~ 300 GeV: $\sin \theta \sim 0.1$ and for DM mass around ~ 1000 GeV and above: $\sin \theta \sim 0.15$ can be accommodated. Since the mixing between $\Delta - h$ is small: $\sin \theta_0 < 5 \times 10^{-2}$, the contribution to the cross-section by the H_2 mediated diagram is suppressed. This is also further suppressed by the large mass of M_Δ present in the propagator. For this reason no striking difference in direct search cross-section for higher values of M_Δ is found as the cross-section is dominated by H_1 mediation only.

3.12 Summary of constraints of the model

We summarize the constraints on the parameters in Fig. 3.25, where we have shown the allowed values in the plane of $M_1 - M_2$ using $\sin \theta = 0.1$ in the left and for $\sin \theta = 0.3$ on the right. The green points are allowed by the relic abundance of DM by taking the constraint from PLANCK data. The main constraint comes from non observation of DM from direct search data of LUX experiment. On the left, for small $\sin \theta = 0.1$, direct search constraint is less severe as has already been discussed and the whole relic density allowed points are consistent with direct search bound. However, for larger $\sin \theta = 0.3$, on the right hand side of Fig. 3.25, a significant part of the relic density allowed space is submerged into direct search bound excepting for the low DM mass region upto ~ 400 GeV. The direct search bound gets more stringent with larger ΔM and that is one of

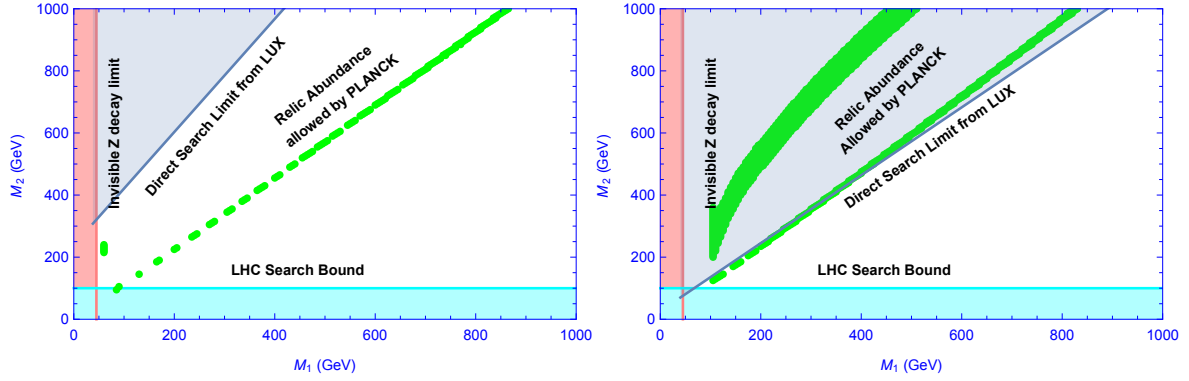


Figure 3.25: Summary of all constraints in the plane of $M_1 - M_2$ using $\sin\theta = 0.1$ (left) and $\sin\theta = 0.3$ (right).

the primary reasons that relic density allowed parameter space with large $\sin\theta = 0.3$ is disfavoured. This is still significantly new in contrast to the model without the triplet, where larger mixing ≥ 0.1 , was completely forbidden by direct search data. There are other small regions which are disfavoured by various experimental searches. For example, the region in cyan colour is disfavoured by the collider search of N^\pm and hence the allowed values are given by $M^\pm \sim M_2 > 100$ GeV. The mass of N_1 (DM), i.e., $M_1 > 45$ GeV, is required in order to relax the severe constraints from the invisible Z boson decay. The charged partner of the DM gives interesting signatures at colliders if $M^\pm - M_1 \lesssim 80$ GeV. As a result the two body decay of N^\pm is forbidden. The only way it can decay is the three body decay. For example, the notable one is $N^- \rightarrow N_1 \ell^- \bar{\nu}_\ell$. In the small singlet-doublet mixing limit we get a displaced vertex of 10 cm for $M^\pm \sim 100$ GeV and a mass splitting of few tens of GeV while satisfying the constraint from observed relic abundance.

3.13 Application to Diphoton Excess

Recently CMS and ATLAS detectors at the Large Hadron Collider (LHC) experiment [146, 147, 148] reported an excess of $\gamma\gamma$ events in the proton-proton collision with centre-of-mass energy ($E_{cm} = \sqrt{s}$) 13 TeV. In fact, CMS reported the excess around 750 GeV with a local significance of 2.6σ , while ATLAS reported the same excess around 750 GeV with a local significance of 3.6σ in the invariant mass distribution of $\gamma\gamma$. This excess could be simply due to the statistical fluctuations or due to the presence of a new Physics and needs future data for its verification. From ATLAS [147] and CMS [148] experiments, the production cross-section times the branching ratio of any resonance X with a mass around 750 GeV is given as:

$$\begin{aligned}\sigma_{\text{ATLAS}}(pp \rightarrow X) \text{Br}(X \rightarrow \gamma\gamma) &\simeq (10 \pm 3) \text{fb}, \\ \sigma_{\text{CMS}}(pp \rightarrow X) \text{Br}(X \rightarrow \gamma\gamma) &\simeq (6 \pm 3) \text{fb}.\end{aligned}$$

Amazingly the diphoton excesses observed by the two experiments are at the same energy bin. This gives enough indication for new physics beyond the SM which can be confirmed or ruled out by future data. In the following we consider the diphoton excess observed at LHC to be a signature

of new physics and provide a viable solution.

If the diphoton events observed at LHC are due to a resonance, then the Landau-Yang's theorem [149, 150] implies that the spin of the resonance can not be 1. In other words the resonance could be a spin zero scalar or a spin two tensor similar to graviton. Another feature of the resonance is that the production cross-section times branching ratio is quite large ($\approx 10\text{fb}$), which indicates its production is due to strongly interacting particles. The most important feature of the resonance is that its width is quite large ($\approx 45\text{ GeV}$). For large width of the resonance, the branching fraction to $\gamma\gamma$ events decreases significantly. Therefore, the main challenge for any theory beyond the SM is to find a large production cross-section: $\sigma(pp \rightarrow X \rightarrow \gamma\gamma)$ to fit the data. For earlier attempts to explain the signal see [151, 152, 153, 154, 155, 156, 157, 158, 159, 160, 161, 162, 163, 164, 165, 166, 167, 168, 169, 170, 171, 172, 173, 174, 175, 176, 177, 178, 179, 180, 181, 182, 183, 184, 185, 186, 187, 188, 189, 190, 191, 192, 193, 194, 195, 196, 197, 198, 199, 200, 201, 202, 203, 204, 205, 206, 207, 208, 209, 210, 211, 212, 213, 214, 215, 216, 217, 218, 219, 220, 221, 222, 223, 224, 225, 226, 227, 228, 229, 230, 231, 232, 233, 234, 235, 236, 237, 238, 239, 240, 241, 242, 243, 244, 245, 246, 247, 248, 249, 250, 251, 252, 253, 254, 255, 256, 257, 258, 259, 260, 261, 262, 263, 264, 265, 266, 267, 268, 269, 270, 271, 272, 273, 274, 275, 276, 277, 278, 279, 280, 281, 282, 283, 284, 285, 286, 287, 288, 289, 290, 291, 292, 293, 294, 295, 296, 297, 298, 299, 300]

In this section we will try to explain the diphoton excess by the resonant decay of a scalar particle. To explain the signal we add a scalar and a vector like quark to the singlet-doublet DM model.

3.14 The Model for Dark Assisted scalar decay

We extend the SM with a scalar singlet $S(1, 1, 0)$ and a dark sector, comprising of a vector like lepton doublet $N^T = (N^0, N^-)$ (1,2,-1) and a leptonic singlet χ^0 (1,1,0), where the quantum numbers in the parentheses are under the gauge group $SU(3)_c \times SU(2)_L \times U(1)_Y$. In addition to the SM gauge symmetry, we impose a discrete symmetry Z_2 under which the dark sector fermions: N and χ^0 are odd, while all other fields are even. The motivation for introducing such a dark sector is two fold: i) firstly, the linear combination of the neutral component of the lepton doublet (N^0) and singlet (χ^0) becomes a viable candidate of DM, ii) secondly, the charged component of the vector like lepton doublet assists the scalar resonance S to give rise the diphoton excess of invariant mass 750 GeV.

The relevant Lagrangian can be given as:

$$\begin{aligned}
-\mathcal{L} \quad \supset \quad & M_N \bar{N}N + f_N S \bar{N}N + M_\chi \bar{\chi}^0 \chi^0 + f_\chi S \bar{\chi}^0 \chi^0 \\
& + \left[Y \bar{N} \tilde{H} \chi^0 + \text{h.c.} \right] + V(S, H),
\end{aligned} \tag{3.77}$$

where H is the SM Higgs isodoublet and $\tilde{H} = i\tau_2 H^*$. The scalar potential in Eq. (3.77) is given by

$$\begin{aligned}
V(S, H) \quad = \quad & \mu_H^2 H^\dagger H + \lambda_H (H^\dagger H)^2 + \frac{1}{2} \mu_S^2 S^2 + \frac{\lambda_S}{4} S^4 \\
& + \frac{\lambda_{SH}}{2} (H^\dagger H) S^2 + \mu_{SH} S H^\dagger H,
\end{aligned} \tag{3.78}$$

where $\lambda_H, \lambda_S > 0$ and $\lambda_{SH} > -2\sqrt{\lambda_S \lambda_H}$ is required for vacuum stability. We assume that $\mu_S^2 > 0$ and $\mu_H^2 < 0$, so that S does not acquire a vacuum expectation value (vev) before electroweak phase transition. After H acquires a vev: $\langle H \rangle = v = \sqrt{-\mu_H^2/2\lambda_H}$, S gets an induced vev which we neglect

in the following calculation.

After electroweak phase transition, S mixes with the H through the tri-linear term $SH^\dagger H$. Due to the mixing we get the mass matrix for the scalar fields as:

$$\mathcal{M}^2 = \begin{pmatrix} 2\lambda_H v^2 & \mu_{SH} v \\ \mu_{SH} v & \mu_S^2 + \lambda_{SH} v^2 \end{pmatrix}, \quad (3.79)$$

where the trilinear parameter μ_{SH} (with mass dimension one) decides the mixing between the two scalar fields, which can be parameterized by a mixing angle θ_{hS} as

$$\tan \theta_{hS} = \frac{\mu_{SH} v}{\mu_S^2 + \lambda_{SH} v^2 - 2\lambda_H v^2}. \quad (3.80)$$

The above equation shows that the mixing angle θ_{hS} between the two scalar fields vanishes if $\mu_{SH} \rightarrow 0$. For finite mixing, the masses of the physical Higgses can be obtained by Diagonalizing the mass matrix (3.79) and is given by:

$$\begin{aligned} M_h^2 &= \left(\lambda_H v^2 + \frac{1}{2}\mu_S^2 + \frac{1}{2}\lambda_{SH} v^2 \right) + \frac{1}{2}D \\ M_S^2 &= \left(\lambda_H v^2 + \frac{1}{2}\mu_S^2 + \frac{1}{2}\lambda_{SH} v^2 \right) - \frac{1}{2}D, \end{aligned} \quad (3.81)$$

where $D = \sqrt{(2\lambda_H v^2 - \mu_S^2 - \lambda_{SH} v^2)^2 + 4(\mu_{SH} v)^2}$, corresponding to the mass eigenstates h and S , where we identify h as the SM Higgs with $M_h = 125$ GeV and S is the new scalar with $M_S = 750$ GeV. Using Eq.(3.81) we have plotted contours for $M_h = 125$ GeV and $M_S = 750$ GeV in the plane of $\sqrt{2\lambda_H} v$ and $\sqrt{\mu_S^2 + \lambda_{SH} v^2}$ for different choices of $\mu_{SH} = \{10, 750, 1400\}$ GeV (Red thick, Blue dashed and Green dotted lines respectively), as shown in Fig.3.26. We observe that for small mixing ($\mu_{SH} = 10$ GeV, represented by red solid line) contours of $M_S = 750$ GeV and $M_h = 125$ GeV intersect vertically as expected while for larger mixing, $\mu_{SH} > 1400$ GeV, we can not get simultaneous solution for $M_S = 750$ GeV and $M_h = 125$ GeV. This implies that the largest allowed mixing for which we get the simultaneous solution is $\sin \theta_{hS} \approx 0.467$. However, such large values of the mixing angles are strongly constrained from other observations (See for instance [203]).

The electroweak phase transition also gives rise a mixing between N^0 and χ^0 as mentioned in sec. 3.2. In the physical spectrum we also have a charged fermion ψ^\pm whose mass in terms of the masses of $N_{1,2}$ ($M_{1,2}$) and the mixing angle θ is given by

$$M^\pm = M_1 \sin^2 \theta + M_2 \cos^2 \theta \quad (3.82)$$

In the limit of vanishing mixing in the dark sector, $\sin \theta \rightarrow 0$, $M^\pm = M_N$. Therefore, a non-zero mixing also gives rise to a mass splitting between N^\pm and N_2 is given by $\Delta M = \frac{m_D^2}{M_N - M_X}$.

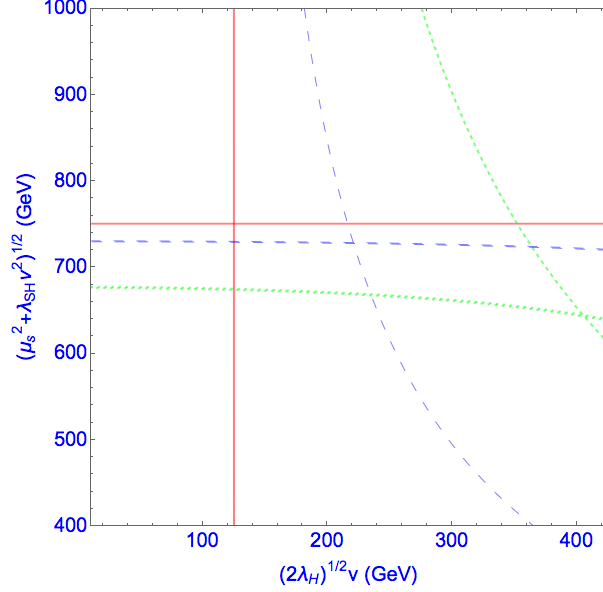


Figure 3.26: Contours of $M_h = 125$ GeV and $M_S = 750$ GeV in the plane of $\sqrt{2\lambda_H}v$ and $\sqrt{\mu_S^2 + \lambda_{SH}v^2}$ for $\mu_{SH} = 10$ GeV (Solid red), $\mu_{SH} = 750$ GeV (Dashed blue), and $\mu_{SH} = 1400$ GeV (Dotted green).

3.14.1 Explanation for Diphoton Excess

$S \rightarrow \gamma\gamma$ and production of S through mixing with the SM Higgs

The LHC search strategy for diphoton events, if possible via a scalar resonance S with mass around 750 GeV, is mostly decided by the production and subsequent decay of the resonant particle to $\gamma\gamma$, which can be parameterised as:

$$\sigma_{\text{ATLAS/CMS}}(pp \rightarrow S \rightarrow \gamma\gamma) \simeq \sigma_{\text{prod}}(pp \rightarrow S) \cdot \text{Br.}(S \rightarrow \gamma\gamma). \quad (3.83)$$

The above cross-section has to be compared with the experimental data

$$\sigma_{\text{ATLAS}}(pp \rightarrow X \rightarrow \gamma\gamma) \simeq (10 \pm 3)\text{fb}, \quad (3.84)$$

$$\sigma_{\text{CMS}}(pp \rightarrow X \rightarrow \gamma\gamma) \simeq (6 \pm 3)\text{fb}. \quad (3.85)$$

In absence of the additional vector-like fermions, the production of S and its subsequent decay to $\gamma\gamma$ can occur through the mixing with the SM Higgs, which can be given as:

$$\sigma(pp \rightarrow S \rightarrow \gamma\gamma) \simeq \sigma_{\text{prod}}(pp \rightarrow h) \cdot \sin^4 \theta_{hS} \cdot \frac{\Gamma(h \rightarrow \gamma\gamma)}{\Gamma(S \rightarrow \text{All})}, \quad (3.86)$$

where $\Gamma(S \rightarrow \text{All}) \approx 45$ GeV as indicated by ATLAS data [147]. Within the SM, the decay width: $h \rightarrow \gamma\gamma$ can be estimated to be $\approx 4 \times 10^{-6}$ GeV for $M_h = 125$ GeV and $\Gamma(h \rightarrow \text{All}) = 4$ MeV. The total production cross-section of Higgs at centre of mass energy of 13 TeV is given by ≈ 50 pb [301]. Thus with a maximal mixing between the SM Higgs and S , *i.e.* ($\sin \theta_{hS} \approx 0.4$), we see that $\sigma(pp \rightarrow S \rightarrow \gamma\gamma) \approx 10^{-4}$ fb, which is much smaller than the required value given in Eq. (3.84).

Therefore, we conclude that the production of the scalar resonance S giving diphoton excess at LHC can not be possible through its mixing with the SM Higgs.

In the following sub-section 3.14.1 we set the $S - h$ mixing to be zero and adopt an alternative scenario for $\sigma(pp \rightarrow S \rightarrow \gamma\gamma)$ using vector-like quarks.

Dark sector assisted S decays

Since S is a singlet scalar, it can not directly couple to the gauge bosons. On the other hand, S can couple to vector-like dark sector fermions which can couple to SM gauge bosons as discussed in the previous section. As the charged component of the Z_2 -odd fermion doublet assist the decay of S , we term it as dark sector assisted decay. Defining $B_{\mu\nu}$ and $W_{\mu\nu}^i$ as the respective field strength tensors for the gauge group $U(1)_Y$ and $SU(2)_L$, one can write down the effective operators for coupling between the scalar S and the vector bosons by integrating out the vector-like fermions in the loop as:

$$\mathcal{L}_{\text{EFT}} \supset \kappa_2 S W_{\mu\nu}^i W^{i,\mu\nu} + \kappa_1 S B_{\mu\nu} B^{\mu\nu} \quad (3.87)$$

where the effective couplings κ_1 and κ_2 can be expressed in terms of Yukawa coupling f_N connecting scalar with vector-like fermion N as [179]:

$$k_1 = \frac{f_N g_Y^2}{32\pi^2 M_N} \quad \text{and} \quad k_2 = \frac{3f_N g^2}{64\pi^2 M_N} \quad (3.88)$$

Since the vector-like dark sector particles carry no color charge and hence, can not contribute to the decay of $S \rightarrow gg$ and $gg \rightarrow S$ for production of scalar particle. However, one can produce large cross-section for scalar S via gluon fusion process by introducing additional vector-like particle carrying color charge, for example, see ref. [157, 164]. We will also adopt a similar strategy that will be discussed in the next sub-section. After rotation to the physical gauge boson states the decay rates can be given as:

$$\begin{aligned} \Gamma(S \rightarrow WW) &= \frac{1}{16\pi} \left[2 + \left(1 - \frac{M_S^2}{2M_W^2} \right)^2 \right] \\ &\quad \left(1 - \frac{4M_W^2}{M_S^2} \right)^{1/2} k_{WW}^2 M_S^3 \\ \Gamma(S \rightarrow ZZ) &= \frac{1}{32\pi} \left[2 + \left(1 - \frac{M_S^2}{2M_Z^2} \right)^2 \right] \\ &\quad \left(1 - \frac{4M_Z^2}{M_S^2} \right)^{1/2} k_{ZZ}^2 M_S^3 \\ \Gamma(S \rightarrow Z\gamma) &= \frac{3}{16\pi} \left(1 - \frac{M_Z^2}{M_S^2} \right) k_{Z\gamma}^2 M_S^3 \\ \Gamma(S \rightarrow \gamma\gamma) &= \frac{1}{8\pi} k_{\gamma\gamma}^2 M_S^3 \end{aligned} \quad (3.89)$$

where the effective couplings are given by [179]:

$$\begin{aligned}
k_{WW} &= \frac{g^2}{32\pi^2} \frac{f_N}{M_N} A_{1/2}(x_N) \\
k_{\gamma\gamma} &= \frac{e^2}{16\pi^2} Q_N^2 \frac{f_N}{M_N} A_{1/2}(x_N) \\
k_{ZZ} &= k_{WW}(1 - \tan^2 \theta_W) + k_{\gamma\gamma} \tan^2 \theta_W \\
k_{Z\gamma} &= k_{WW} \cos 2\theta_W \tan \theta_W - k_{\gamma\gamma} 2 \tan \theta_W
\end{aligned} \tag{3.90}$$

The factors involved in Eq. (3.90) are given by

$$\begin{aligned}
A_{1/2}(x_N) &= 2x_N [1 + (1 - x_N)f(x_N)] , \\
x_N &= \frac{4M_N^2}{M_S^2} , \\
f(x) &= \begin{cases} \arcsin^2 \sqrt{x} & x \leq 1 \\ -\frac{1}{4} \left[\ln \left(\frac{1+\sqrt{1-x}}{1-\sqrt{1-x}} \right) - i\pi \right]^2 & x \geq 1. \end{cases}
\end{aligned} \tag{3.91}$$

Dark sector assisted $S \rightarrow \gamma\gamma$ and quark-like vector particles for $gg \rightarrow S$

As discussed in section 3.14.1, we see that the required cross-section for the scalar resonance S production can not be achieved through S-h mixing. As an alternative, we introduce an iso-singlet quark-like vector fermion Q of mass M_Q to the framework discussed in the above section. The main reason for introducing additional quark-like vector particle is to provide the large production cross-section for scalar S via gluon gluon fusion process as shown in the left-panel of Fig. 3.27 even with $\theta_{hS} \rightarrow 0$. The subsequent decay $S \rightarrow \gamma\gamma$ mediated by N^\pm is shown in right-panel of Fig. 3.27.

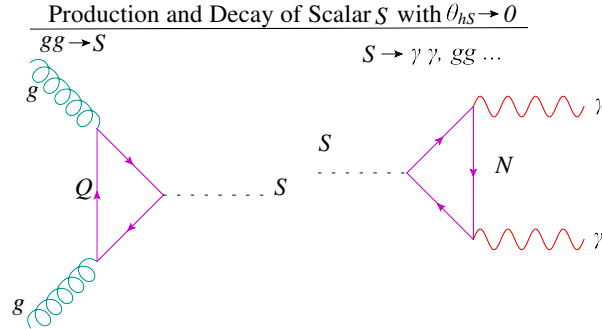


Figure 3.27: Feynman diagrams for production of scalar S through gluon gluon fusion mediated by quark-like vector particle Q and its subsequent decay to SM particles mediated by the dark sector particle N^\pm . The other decay modes of S via its mixing with the SM Higgs are suppressed in the limit $\theta_{hS} \rightarrow 0$.

The Yukawa coupling of the scalar S to Q can be given as $f_Q S \bar{Q} Q$. This coupling helps in producing S via gluon gluon fusion process. The production of scalar S , arising from gluon gluon fusion process, and its subsequent decay to $\gamma\gamma$ can be expressed in terms of the decay rate $\Gamma(S \rightarrow gg)$

as [302, 161]:

$$\sigma(pp \rightarrow S \rightarrow \gamma\gamma) = \frac{1}{M_S \hat{s}} C_{gg} \Gamma(S \rightarrow gg) \text{Br}(S \rightarrow \gamma\gamma) \quad (3.92)$$

where $\sqrt{\hat{s}} = 13$ TeV is the centre of mass energy at which LHC is collecting data. The dimensionless coupling

$$C_{gg} = \frac{\pi^2}{8} \int_{M_S^2/\hat{s}}^1 \frac{dx}{x} g(x) g(M_S^2/\hat{s}x). \quad (3.93)$$

At $\sqrt{\hat{s}} = 13$ TeV, $C_{gg} = 2137$ [161]. In Eq. (3.92), the decay rate $\Gamma(S \rightarrow gg)$ is given by:

$$\Gamma(S \rightarrow gg) = \frac{1}{8\pi} k_{gg}^2 M_S^3 \quad (3.94)$$

where the effective coupling of S to gg through the exchange of Q in the loop is given by

$$k_{gg} = \frac{g_S^2}{16\pi^2} \frac{f_Q}{M_Q} N_c A_{1/2}(x_Q) \quad (3.95)$$

where $A_{1/2}(x)$ is given by Eq. (3.91).

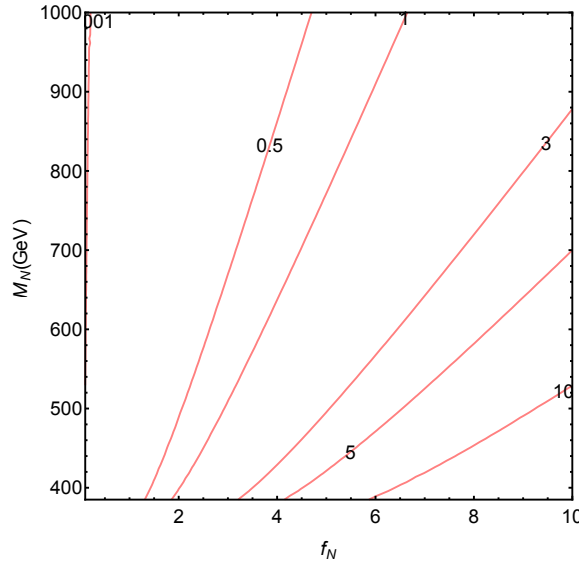


Figure 3.28: Contours of $\sigma(pp \rightarrow S \rightarrow \gamma\gamma)$ in the plane of f_N versus M_N for $f_N = f_Q$, $M_N = M_Q$ and $\sin \theta_{hS} = 0$.

In Fig. (3.28), we have shown the contours of $\sigma(pp \rightarrow S \rightarrow \gamma\gamma)$ in the plane of f_N versus M_N by assuming that $f_N = f_Q$ and $M_N = M_Q$. From Fig. (3.28), we see that to get a production cross-section of 10 fb, we need the S coupling to $f_N = f_Q > 5$. The mass of these vector-like fermions are chosen to be larger than 375 GeV in order to avoid the tree level decay of $S \rightarrow \bar{Q}Q$. The corresponding total decay width and branching fraction are shown in Fig. (3.29) and (3.30). We see that the total decay width can be as large as 30 GeV, while the branching fraction is order of 10^{-4} . Since the mass of the vector-like fermions are heavier than 375 GeV, the decay of S to SM particles occurs via the triangle loop constituting N^\pm . However, the tree level decay of S to hh is allowed. It may increase the total width depending on the mixing between SM Higgs and S .

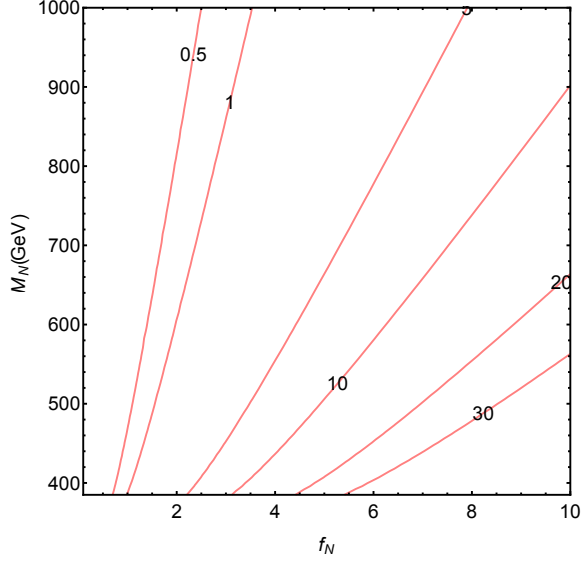


Figure 3.29: Contours of $\Gamma(S \rightarrow \text{All})$ (in GeV) in the plane of f_N versus M_N for $f_N = f_Q$, $M_N = M_Q$ and $\sin \theta_{hS} = 0$.

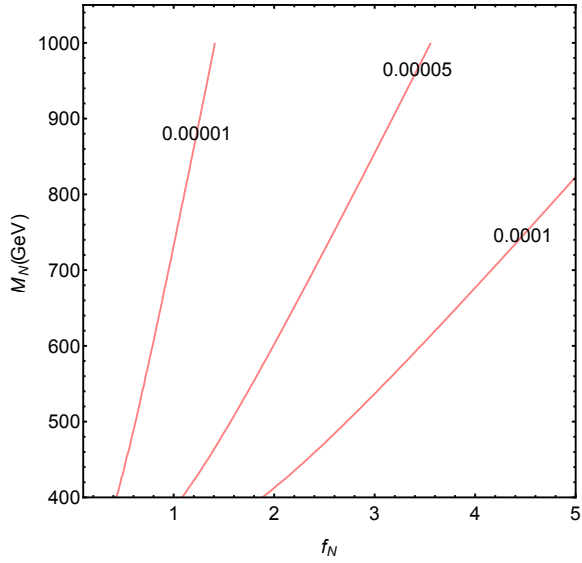


Figure 3.30: Contours of $\text{Br}(S \rightarrow \gamma\gamma)$ in the plane of f_N versus M_N for $f_Q = 5$ and $M_Q = 600$ GeV. We set $\sin \theta_{hS} = 0$.

However, we have checked that for $\sin \theta_{hS} < 0.1$, the tree level decay of S to hh does not affect the above result.

3.15 Summary and Outlook

A vector like mixed singlet-doublet fermion is studied as a DM candidate in a BSM framework. The model contains a doublet(N) and singlet(χ^0) fermion under $SU(2)$ group which are odd under a Z_2 symmetry. Thus there are 3 physical states in the model $N_1 = \cos \theta \chi^0 + \sin \theta N^0$ and $N_2 =$

$\cos\theta N^0 - \sin\theta\chi^0$ and N^\pm the charged partner of N^0 , where θ is the mixing angle. The lightest among the three physical states which is N_1 and is stable by the imposed Z_2 symmetry, hence a suitable candidate of DM. The relevant constraints on $\sin\theta$ from the invisible Z and Higgs decay, electroweak precision data and direct detection of DM are discussed. For $M_1 < 45$ GeV, N_1 is strongly constrained by the invisible Z -decay width, while for $M_1 > 45$ GeV, the direct detection of N_1 DM at Xenon-100 and LUX give the strongest constraint on $\sin\theta$, thus ruling out its viability for $\sin\theta \gtrsim 0.1$. However this constraint is also affected by the presence of a scalar triplet. We found that the constraint from null detection of DM at direct search experiments and relic abundance can be satisfied in a large region of parameter space for mixing angle: $\sin\theta \sim 0.3$ and smaller values. If the scalar triplet is light, say $M_\Delta \lesssim 500$ GeV, then it contributes to relic abundance only near the resonance i.e with $M_{N_1} \sim \frac{M_\Delta}{2}$. On the other hand, if $M_\Delta \gtrsim 1$ TeV, then it decouples and hence does not contribute to relic abundance of DM.

The scalar triplet couples symmetrically to lepton doublets as well as to the doublet component of the DM. Therefore, when the scalar triplet acquires an induced vev, it not only gives Majorana masses to the light neutrinos but also induce a sub-GeV Majorana mass to the DM. As a result the DM, which was originally a vector-like Dirac fermion splits into two pseudo-Dirac fermions with a mass separation of sub-GeV order. Due to this reason the Z -mediated inelastic scattering of the DM with nucleon is suppressed. However, we found that the spin independent direct detection of DM through the SM Higgs mediation is in the right ballpark of Xenon-1T. The absence of Z mediated DM-nucleon cross-section relaxes the constraint on mixing angle $\sin\theta$ as we can go as high as $\sin\theta = 0.3$ for DM mass $M_1 > 400$ GeV for small mass splitting $\Delta M < 100$ GeV. This high value of $\sin\theta$ is also well satisfied by the correct relic abundance. So the spin independent direct detection cross-section does not put stronger constraint on the mixing angle if the mass splitting is not so large and allows large region of parameter space unlike the model in absence of a triplet.

The ρ parameter in the SM restricts the vev of scalar triplet to $u_\Delta \leq 3.64$ GeV. This in turn gives the mixing between the SM Higgs and Δ to be $\sin\theta_0 \mathcal{O}(10^{-2})$ even if the $M_\Delta \lesssim 500$ GeV. Therefore, Δ does not contribute significantly to the spin independent direct detection cross-section.

We have illustrated how the recent diphoton excess signal $pp \rightarrow S \rightarrow \gamma\gamma$ around an invariant mass of 750 GeV can be accounted by a Dark sector assisted scalar decay. The framework considered is a simple extension of SM with additional scalar singlet S having mass around 750 GeV, an iso-singlet vector-like quark Q and a dark sector constituted by a vector-like lepton doublet N and a neutral singlet χ^0 . We argue that the extra particles added in this framework are minimal when we explain diphoton excess signal and DM component of the Universe. We note that the masses of the new particles added are below TeV scale, but above $M_S/2 = 375$ GeV.

Chapter 4

Muon $g-2$ anomaly, neutrino mass and DM phenomenology in $U(1)$ gauged extension of standard model

4.1 Introduction

The incompatibility of the SM with various experimental observations like neutrino mass, anomalous muon magnetic moment, presence of DM, etc. motivates us to look for physics beyond the SM. A gauged $U(1)$ model has been paid much attention. Among various $U(1)$ extended models, the differences between two lepton flavours, i.e., $L_i - L_j$, with $i, j = e, \mu, \tau$, are anomaly free and can be gauged without any addition of extra fermions to the SM [303]. The most discussed model among these is the gauged $L_\mu - L_\tau$ model [304, 305, 306, 307, 308, 309, 310, 311, 312, 313, 314, 315, 316, 317, 318, 319, 320, 321, 322, 323, 324, 325, 326, 327, 328, 329, 330, 331, 332, 333, 334, 335, 336]. The interactions of the corresponding gauge boson Z' are restricted to only μ and τ families of leptons and therefore it significantly contributes to muon $g - 2$ anomaly, which is a discrepancy between the observation and SM prediction with more than 3σ confidence level. Moreover, Z' does not have any coupling with the electron family. Therefore, it can easily avoid the LEP bound: $M'_{Z'}/g' > 6$ TeV [337]. So, in this scenario a Z' - mass can vary from a few MeV to TeV which can in principle be probed at LHC and at future energy frontiers.

Gauged $U(1)_{L_\mu - L_\tau}$ models have been discussed extensively in the literature in light of sub-eV neutrino masses [316, 317, 318, 319, 320, 321, 322, 323, 324, 325, 326, 327, 328, 329, 330, 331] and DM phenomenology [33, 332, 333, 334, 335, 336]. All these models are devoted to predict either non-zero neutrino masses or DM content of the Universe, while satisfying the constraints from muon $g - 2$ anomaly. We noticed that all the $U(1)_{L_\mu - L_\tau}$ models discussing DM phenomenology [33, 332, 333, 334, 335, 336] predict a candidate of DM, which is elastic in nature.

In this chapter we revisit the gauged $U(1)_{L_\mu - L_\tau}$ model in light of muon $g - 2$ anomaly, non-zero neutrino mass and DM phenomenology simultaneously, while including the latest constraints

from various observations. We found that the DM is required to be inelastic to reconcile the relic abundance constraints with null detection of DM at direct search experiments. We augment the SM by including three right handed neutrinos: N_e , N_μ and N_τ , which are singlets under the SM gauge group, and a vector like colorless neutral fermion χ . We also add an extra SM singlet scalar S . All these particles except N_e , are charged under $U(1)_{L_\mu-L_\tau}$, though singlets under the SM gauge group. When S acquires a vacuum expectation value (vev), the $U(1)_{L_\mu-L_\tau}$ breaks to identity and gives masses to Z' as well as to the neutral fermions N_e, N_μ, N_τ . We also impose an additional Z_2 symmetry under which χ is odd and all other fields are even. As a result χ serves as a candidate of DM. The smallness of neutrino mass is also explained using type-I see-saw with the presence of right handed neutrinos N_e, N_μ and N_τ , whose masses are generated from the vev of scalar field S .

In this model the relic abundance of DM (χ) is obtained via its annihilation to muon and tauon family of leptons through the exchange of $U(1)_{L_\mu-L_\tau}$ gauge boson Z' . We show that the relic density crucially depends on $U(1)_{L_\mu-L_\tau}$ gauge boson mass $M_{Z'}$ and its coupling g' . In particular, we find that the observed relic density requires $g' \gtrsim 5 \times 10^{-3}$ for $M_{Z'} \gtrsim 100$ MeV. However, if $g' \lesssim 5 \times 10^{-3}$ then we get an over abundance of DM, while these couplings are compatible with the observed muon $g-2$ anomaly. We resolve this conflict by adding an extra singlet scalar η , doubly charged under $U(1)_{L_\mu-L_\tau}$, which can drain out the large DM abundance via the annihilation process: $\bar{\chi}\chi \rightarrow \eta^\dagger\eta$. As a result, the parameter space of the model satisfying muon $g-2$ anomaly can be reconciled with the observed relic abundance of DM. We also show that the acceptable region of parameter space for observed relic density and muon $g-2$ anomaly is further constrained by null detection of DM at Xenon-100 [12] and LUX [110]. Moreover, we noticed that the allowed parameter space is severely constrained by the neutrino trident production [8], the creation of a muon pair from the scattering of muon-neutrino off the coulomb field of a target nucleus. The neutrino trident production cross-section, reported by CHARM-II ($\sigma_{CHARM}/\sigma_{SM} = 1.58 \pm 0.57$) [338] and CCFR ($\sigma_{CCFR}/\sigma_{SM} = 0.82 \pm 0.28$) [339] collaborations, does not seem to deviate significantly from the SM prediction. On the other hand, a new Z' gauge boson, corresponding to a $U(1)_{L_\mu-L_\tau}$ gauge symmetry, contributes constructively to the production cross-section of the above mentioned process. In fact, combine constraints from muon $g-2$ anomaly and neutrino trident production restricts $M_{Z'} \lesssim 400$ MeV [8]. However, in a large region of the parameter space spanned by $M_{Z'} \gtrsim 400$ MeV and $g' \gtrsim 10^{-3}$, where contribution to muon $g-2$ anomaly comes partially and yet not ruled out by neutrino trident production, the positron excess, observed at PAMELA [16, 17], Fermi-LAT [340] and AMS-02 [15, 2], can be explained via the DM annihilation.

4.2 The model

We extend the gauge sector of the SM by introducing a $U(1)_{L_\mu-L_\tau}$ gauge symmetry (from now on referred to as “gauged $U(1)_{L_\mu-L_\tau}$ model”) where the difference between muon and tau lepton numbers is defined as a local gauge symmetry [303, 304, 305, 306, 307, 308, 309, 310, 311, 312, 313, 314, 315, 316, 317, 318, 319, 320, 321, 322, 323, 324, 325, 326, 327, 328, 329, 330, 331, 33, 332, 333, 334, 335, 336]. The advantage of considering the gauged $U(1)_{L_\mu-L_\tau}$ model is that the theory is free from any gauge anomaly, so there is no need for introduction of additional fermions. The non zero neutrino mass can be explored after breaking the gauge symmetry. A Z_2 is also imposed under

which χ is odd while all other fields are even. Thus the discrete symmetry imposed makes χ stable and as a result it serves as a candidate of DM.

4.2.1 Spontaneous breaking of gauge symmetry

The spontaneous symmetry breaking of gauged $U(1)_{L_\mu-L_\tau}$ model is given by:

$$\mathcal{G}_{L_\mu-L_\tau} \xrightarrow{\langle S \rangle, \langle \eta \rangle} \mathcal{G}_{SM} \xrightarrow{\langle H \rangle} SU(3)_C \times U(1)_{em}, \quad (4.1)$$

where

$$\begin{aligned} \mathcal{G}_{L_\mu-L_\tau} &\equiv SU(3)_C \times SU(2)_L \times U(1)_Y \times U(1)_{L_\mu-L_\tau}, \\ \mathcal{G}_{SM} &\equiv SU(3)_C \times SU(2)_L \times U(1)_Y \end{aligned}$$

At first, the spontaneous symmetry breaking of $\mathcal{G}_{L_\mu-L_\tau} \rightarrow \mathcal{G}_{SM}$ is achieved by assigning non-zero vacuum expectation values (vevs) to complex scalar field S and η . The subsequent stage of symmetry breaking $\mathcal{G}_{SM} \rightarrow SU(3)_C \times U(1)_{em}$ is obtained with the SM Higgs H providing masses to known charged fermions.

	Field	$SU(3)_C \times SU(2)_L \times U(1)_Y$	L_μ	L_τ	$L_\mu - L_\tau$
Quarks	$Q_L \equiv (u, d)_L^T$	$(\mathbf{3}, \mathbf{2}, 1/6)$	0	0	0
	u_R	$(\mathbf{3}, \mathbf{1}, 2/3)$	0	0	0
	d_R	$(\mathbf{3}, \mathbf{1}, -1/3)$	0	0	0
Leptons	$L_e \equiv (\nu_e, e^-)_L^T$	$(\mathbf{1}, \mathbf{2}, -1/2)$	0	0	0
	$L_\mu \equiv (\nu_\mu, \mu^-)_L^T$	$(\mathbf{1}, \mathbf{2}, -1/2)$	1	0	1
	$L_\tau \equiv (\nu_\tau, \tau^-)_L^T$	$(\mathbf{1}, \mathbf{2}, -1/2)$	0	1	-1
	e_R	$(\mathbf{1}, \mathbf{1}, -1)$	0	0	0
	μ_R	$(\mathbf{1}, \mathbf{1}, -1)$	1	0	1
	τ_R	$(\mathbf{1}, \mathbf{1}, -1)$	0	1	-1
	N_e	$(\mathbf{1}, \mathbf{1}, 0)$	0	0	0
N_μ	$(\mathbf{1}, \mathbf{1}, 0)$	1	0	1	
N_τ	$(\mathbf{1}, \mathbf{1}, 0)$	0	1	-1	
χ	$(\mathbf{1}, \mathbf{1}, 0)$	-	-	1	
Scalars	H	$(\mathbf{1}, \mathbf{2}, 1/2)$	-	-	0
	S	$(\mathbf{1}, \mathbf{1}, 0)$	-	-	1
	η	$(\mathbf{1}, \mathbf{1}, 0)$	-	-	2

Table 4.1: Particle content of the minimal $U(1)_{L_\mu-L_\tau}$ gauge extension of the SM and their transformation under the SM gauge group.

The complete model with all details of the particles and their corresponding quantum numbers under the gauge group $SU(3)_C \times SU(2)_L \times U(1)_Y \times U(1)_{L_\mu-L_\tau}$ is written in the Table 4.1. Apart from the SM quarks and leptons, three neutral fermions N_e, N_μ, N_τ are added to explain the light neutrino mass via seesaw mechanism and a Z_2 odd vector like Dirac fermion χ is also added, which acts as DM candidate.

4.2.2 Interaction Lagrangian

The complete interaction Lagrangian for the gauged $U(1)_{L_\mu-L_\tau}$ model is given by

$$\begin{aligned}
\mathcal{L}_{L_\mu-L_\tau} = & i\bar{N}_e \not{\partial} N_e + i\bar{N}_\mu (\not{\partial} + i g_{\mu\tau} Z'_\mu \gamma^\mu) N_\mu + i\bar{N}_\tau (\not{\partial} - i g_{\mu\tau} Z'_\mu \gamma^\mu) N_\tau \\
& - g_{\mu\tau} (\bar{\mu} \gamma^\mu \mu + \bar{\nu}_\mu \gamma^\mu P_L \nu_\mu - \bar{\tau} \gamma^\mu \tau - \bar{\nu}_\tau \gamma^\mu P_L \nu_\tau) Z'_\mu \\
& - M_{ee} \bar{N}_e^c N_e - (\lambda_{e\mu} S^* \bar{N}_e^c N_\mu + h.c) - (\lambda_{e\tau} S \bar{N}_e^c N_\tau + h.c) \\
& - (\lambda_{\mu\mu} \eta^* \bar{N}_\mu^c N_\mu + h.c) - (\lambda_{\tau\tau} \eta \bar{N}_\tau^c N_\tau + h.c) \\
& - \left(Y_{ee} \bar{L}_e \tilde{H} N_e + Y_{\mu\mu} \bar{L}_\mu \tilde{H} N_\mu + Y_{\tau\tau} \bar{L}_\tau \tilde{H} N_\tau + h.c \right) \\
& + i\bar{\chi} (\not{\partial} + i g_{\mu\tau} Z'_\mu \gamma^\mu) \chi - M_\chi \bar{\chi} \chi - f_\chi \bar{\chi}^c \chi \eta^* \\
& - \frac{1}{4} F_{Z'}^{\mu\nu} F_{\mu\nu}^{Z'} + \frac{\epsilon}{4} F_{Z'}^{\mu\nu} F_{\mu\nu} \\
& + |(\partial_\mu + i g_{\mu\tau} Z'_\mu) S|^2 - \mu_S^2 S^\dagger S + \lambda_S (S^\dagger S)^2 + |(\partial_\mu + i 2g_{\mu\tau} Z'_\mu) \eta|^2 - \mu_\eta^2 \eta^\dagger \eta + \lambda_\eta (\eta^\dagger \eta)^2 \\
& + \lambda_{HS} (H^\dagger H) (S^\dagger S) + \lambda_{H\eta} (H^\dagger H) (\eta^\dagger \eta) + \lambda_{\eta S} (\eta^\dagger \eta) (S^\dagger S) + \mu_{\eta S} S S \eta^* + \mathcal{L}_{\text{SM}}, \tag{4.2}
\end{aligned}$$

where \mathcal{L}_{SM} is the SM Lagrangian. We denote here Z'_μ as the new gauge boson for $U(1)_{L_\mu-L_\tau}$ and the corresponding field strength tensor as $F_{\mu\nu}^{Z'} = \partial_\mu Z'_\nu - \partial_\nu Z'_\mu$. The gauge coupling corresponding to $U(1)_{L_\mu-L_\tau}$ is defined as $g_{\mu\tau} \equiv g'$ (as mentioned in sec. 4.1.)

4.2.3 Scalar masses and mixing

The scalar potential of the model is given by

$$\begin{aligned}
\mathcal{V}(H, S) = & -\mu_H^2 H^\dagger H + \lambda_H (H^\dagger H)^2 - \mu_\eta^2 \eta^\dagger \eta + \lambda_\eta (\eta^\dagger \eta)^2 - \mu_S^2 S^\dagger S + \lambda_S (S^\dagger S)^2 \\
& + \lambda_{SH} (H^\dagger H) (S^\dagger S) + \lambda_{H\eta} (H^\dagger H) (\eta^\dagger \eta) + \lambda_{\eta S} (\eta^\dagger \eta) (S^\dagger S) + \mu_{\eta S} S S \eta^* \tag{4.3}
\end{aligned}$$

where H is the SM Higgs doublet and S, η are the complex scalar singlets under SM, while charged under $U(1)_{L_\mu-L_\tau}$. The neutral complex scalars H^0, S and η can be parameterised as follows:

$$\begin{aligned}
H^0 &= \frac{1}{\sqrt{2}}(v_H + h) + \frac{i}{\sqrt{2}}G^0, \\
S &= \frac{1}{\sqrt{2}}(v_S + s) + \frac{i}{\sqrt{2}}A, \\
\eta &= \frac{1}{\sqrt{2}}(v_\eta + \eta) + \frac{i}{\sqrt{2}}B, \tag{4.4}
\end{aligned}$$

The mass matrix for the neutral scalars is given by

$$\mathcal{M}^2 = \begin{pmatrix} 2\lambda_H v_H^2 & \lambda_{SH} v_H v_S & \lambda_{H\eta} v_H v_\eta \\ \lambda_{SH} v_H v_S & 2\lambda_S v_S^2 & \lambda_{\eta S} v_S v_\eta + \mu_{\eta S} v_S \\ \lambda_{H\eta} v_H v_\eta & \lambda_{\eta S} v_S v_\eta + \mu_{\eta S} v_S & 2\lambda_\eta v_\eta^2 \end{pmatrix} \tag{4.5}$$

This is a symmetric mass matrix. So it can be diagonalized by a unitary matrix:

$$V^\dagger \mathcal{M}^2 V = \text{Diagonal}(M_h^2, M_S^2, M_\eta^2) \quad (4.6)$$

We identify M_h as the physical mass of the SM Higgs, while M_S and M_η are the masses of additional scalars S and η respectively. Since S and η are singlets, their masses can vary from sub-GeV to TeV region. For a typical set of values: $v_H = 174\text{GeV}$, $v_S = 1200\text{GeV}$, $v_\eta = 50\text{GeV}$, $\lambda_H = 0.2585$, $\lambda_{SH} = 0.0005$, $\lambda_S = 0.4$, $\lambda_\eta = 0.00021$, $\lambda_{\eta H} = 0.00001$, $\lambda_{\eta S} = 0.0015$, $\mu_{\eta S} = 0.1\text{GeV}$, the physical masses are found to be $M_h = 125\text{ GeV}$, $M_S = 1073\text{ GeV}$, $M_\eta = 1\text{ GeV}$ and the mixing between h and η field is $\sin\theta_{\eta h} = 5.56 \times 10^{-6}$. We will study the importance of η field while calculating the relic abundance of DM. The mixing between η and h field is required to be small as it plays a dominant role in the direct detection of DM. We will show in Fig.4.5 that if the mixing angle is large then it will kill almost all the relic abundance parameter space.

4.2.4 Mixing in the Gauge sector

The Z' boson becomes massive after the spontaneous breaking of $U(1)_{L_\mu-L_\tau}$ symmetry, when η and S gets vev. In the tree level there is no mixing between the SM gauge boson Z and Z' . However at one loop level, the mixing is possible through the exchange of muon and tauon families of leptons as shown in fig. 4.1. The loop factor can be estimated as (see appendix D)

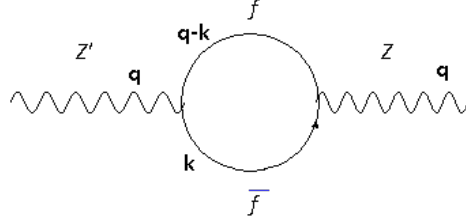


Figure 4.1: The mixing between the SM gauge boson Z and the $U(1)_{L_\mu-L_\tau}$ gauge boson Z' arising through the exchange of muon and tauon families of leptons.

$$\Pi^{\mu\nu}(q^2) = (q^2 g^{\mu\nu} - q^\mu q^\nu) \frac{4}{3} \frac{1}{16\pi^2} \left(g_{\mu\tau} \frac{C_V g}{2 \cos\theta_W} \right) \text{Log} \left(\frac{m_f^2}{\Lambda^2} \right) \quad (4.7)$$

where θ_W is the Weinberg angle, C_V is the vector coupling of SM fermions with Z boson, Λ is the cut off scale of the theory and m_f is the mass of the charged fermion running in the loop. In the gauge basis, the mass matrix is given by

$$\mathcal{M}_2^2 = \begin{pmatrix} M_{Z_0}^2 & \Pi \\ \Pi & \tilde{M}_{Z'}^2 \end{pmatrix} \quad (4.8)$$

where Π is given by $\Pi = \Pi^{\mu\nu} * g_{\mu\nu}$ and $M_{Z_0} = 91.1876\text{ GeV}$. Thus the mixing angle is given by

$$\tan 2\theta_Z = \frac{2\Pi}{\tilde{M}_{Z'}^2 - M_{Z_0}^2} \quad (4.9)$$

Diagonalizing the mass matrix (4.8) we get the eigen values:

$$\begin{aligned} M_Z^2 &= \frac{M_{Z^0}^2 - M_{Z'}^2 \sin^2 \theta_Z}{\cos^2 \theta_Z} \\ M_{Z'}^2 &= \frac{\tilde{M}_{Z'}^2 - M_Z^2 \sin^2 \theta_Z}{\cos^2 \theta_Z} \end{aligned} \quad (4.10)$$

where M_Z and $M_{Z'}$ are the physical masses of Z and Z' gauge bosons. The mixing angle θ_Z has to be chosen in such a way that the physical mass of Z -boson should be obtained within the current uncertainty of the SM Z boson mass [106]. It can be computed from equation (4.10) as follows:

$$\frac{M_Z - M_{Z^0}}{M_{Z^0}} = \frac{M_{Z^0}^2 - M_{Z'}^2}{2M_{Z^0}^2} \tan^2 \theta_Z \leq 4.6 \times 10^{-5} \quad (4.11)$$

For $M_{Z'} - M_{Z^0} \gtrsim M_{Z^0}$ we get $\tan \theta_Z \lesssim 10^{-2}$.

4.3 BBN constraint on η - h mixing

The scalar η does not decay to SM particles directly. However it can decay to SM fermions through η - h mixing. The decay width is given by

$$\Gamma_\eta \simeq \sum_{2m_f < M_\eta} \frac{M_\eta}{8\pi} \theta_{\eta h}^2 \frac{2m_f^2}{v_H^2}, \quad (4.12)$$

where m_f is the mass of the SM fermion. Thus lifetime of η is estimated to be

$$\tau_\eta \simeq 1s \times \left(\frac{\theta_{\eta h}}{10^{-6}} \right)^{-2} \left(\frac{1\text{GeV}}{M_\eta} \right). \quad (4.13)$$

For η to decay before big bang nucleosynthesis (BBN) we demand that $\tau_\eta \lesssim \tau_{BBN} \sim 1$ s [341, 342, 343, 344], so that it does not affect the predictions of BBN. Therefore we get $\theta_{\eta h} \gtrsim \mathcal{O}(10^{-6})$ for $M_\eta \gtrsim 1\text{GeV}$. We will see that the parameter space is well compatible with BBN constraint for direct detection as well as the relic abundance of DM in subsequent sections.

4.4 Muon $g - 2$ anomaly

As mentioned in the chapter 1 that there is a discrepancy between the experimental result [28] and the SM prediction [29] of the magnetic moment of muon. The result is an agreement in 3σ range and is given as

$$\Delta a_\mu = a_\mu^{expt} - a_\mu^{SM} = (295 \pm 88) \times 10^{-11}. \quad (4.14)$$

In this gauged extension of the SM, the new gauge field Z' couples to the muon, hence can contribute to its magnetic moment. Its contribution is given by [336]

$$\Delta a_\mu = \frac{\alpha'}{2\pi} \int_0^1 dx \frac{2m_\mu^2 x^2 (1-x)}{x^2 m_\mu^2 + (1-x) M_{Z'}^2} \approx \frac{\alpha'}{2\pi} \frac{2m_\mu^2}{3M_{Z'}^2}, \quad (4.15)$$

where $\alpha' = g_{\mu\tau}^2/4\pi$.

The above equation implies that the discrepancy between the experimental measurement [28] and the SM prediction [29] of a_μ value can be explained in a large region of parameter space as shown by black shaded region in Fig. (4.3). Thus any value of $(g_{\mu\tau}, M_{Z'})$ below the black shaded region is insufficient to account for anomalous $g - 2$ values, while the corresponding points above the black shaded region give excess $g - 2$ values.

However the allowed parameter space is severely constrained by the neutrino trident production [8], the creation of a muon pair from the scattering of muon-neutrino off the coulomb field of a target nucleus. The neutrino trident production cross-section, reported by CHARM-II ($\sigma_{CHARM}/\sigma_{SM} = 1.58 \pm 0.57$) [338] and CCFR ($\sigma_{CCFR}/\sigma_{SM} = 0.82 \pm 0.28$) [339] collaborations, does not seem to deviate much from the SM prediction. On the other hand, a new Z' gauge boson, corresponding to a $U(1)_{L_\mu-L_\tau}$ gauge symmetry, contributes constructively to the production cross-section of the above mentioned process. In fact, combining the constraints from muon $g-2$ anomaly and neutrino trident production restricts $M_{Z'} \lesssim 400\text{MeV}$ and $g' \lesssim 10^{-3}$ [8]. However, this region does not produce the correct relic abundance of DM. We will discuss it more in sec 4.6.

4.5 Neutrino mass

The additional neutral fermions $N_e(0), N_\mu(1), N_\tau(-1)$ where the quantum numbers in the parentheses are the $L_\mu - L_\tau$ charge, can generate small neutrino masses in a Type I seesaw mechanism. The relevant Yukawa interactions are given by :

$$\begin{aligned} \mathcal{L} = & -\frac{1}{2}M_{ee}\overline{N}_e^c N_e - \frac{1}{2}M_{\mu\tau}\overline{N}_\mu^c N_\tau - (\lambda_{e\mu}S^*\overline{N}_e^c N_\mu + h.c) - (\lambda_{e\tau}S\overline{N}_e^c N_\tau + h.c) \\ & - (\lambda_{\mu\mu}\eta^*\overline{N}_\mu^c N_\mu + h.c) - (\lambda_{\tau\tau}\eta\overline{N}_\tau^c N_\tau + h.c) \\ & - (Y_{ee}\overline{L}_e\tilde{H}N_e + Y_{\mu\mu}\overline{L}_\mu\tilde{H}N_\mu + Y_{\tau\tau}\overline{L}_\tau\tilde{H}N_\tau + h.c) \\ = & -\frac{1}{2}N_\alpha^T C^{-1}M_{R\alpha\beta}N_\beta + M_{D\alpha\beta}\overline{\nu}_\alpha N_\beta + h.c. \end{aligned} \quad (4.16)$$

where the Dirac and Majorana neutrino mass matrices are given by

$$M_R = \begin{pmatrix} M_{ee} & \lambda_{e\mu}v_S & \lambda_{e\tau}v_S \\ \lambda_{e\mu}v_S & \lambda_{\mu\mu}v_\eta & M_{\mu\tau} \\ \lambda_{e\tau}v_S & M_{\mu\tau} & \lambda_{\tau\tau}v_\eta \end{pmatrix}, \quad M_D = \begin{pmatrix} Y_{ee}v_H & 0 & 0 \\ 0 & Y_{\mu\mu}v_H & 0 \\ 0 & 0 & Y_{\tau\tau}v_H \end{pmatrix} \quad (4.17)$$

Using seesaw approximation, the light neutrino mass matrix can be read as

$$m_\nu \simeq -M_D M_R^{-1} M_D^T. \quad (4.18)$$

We point out here that the resulting Dirac neutrino mass matrix is not only diagonal but also degenerate. As a result, we can express $M_D = m_d \mathbb{I}_{3 \times 3}$. One can express heavy Majorana neutrino mass matrix in terms of light neutrino mass matrix as

$$M_R = m_d^2 m_\nu^{-1}. \quad (4.19)$$

Thus, one can reconstruct M_R using neutrino oscillation parameters and $m_d \simeq 10^{-4}$ GeV. As we know that light neutrino mass matrix is diagonalized by the PMNS mixing matrix as

$$m_\nu^{\text{diag.}} = U_{\text{PMNS}}^\dagger m_\nu U_{\text{PMNS}}^* = \text{diag.}\{m_1, m_2, m_3\}$$

where m_i are the light neutrino mass eigenvalues. The PMNS mixing matrix is generally parameterized as

$$U_{\text{PMNS}} = \begin{pmatrix} c_{12}c_{13} & s_{12}c_{13} & s_{13}e^{-i\delta} \\ -s_{12}c_{23} - c_{12}s_{13}s_{23}e^{i\delta} & c_{12}c_{23} - s_{12}s_{13}s_{23}e^{i\delta} & c_{13}s_{23} \\ s_{12}s_{23} - c_{12}s_{13}c_{23}e^{i\delta} & -c_{12}s_{23} - s_{12}s_{13}c_{23}e^{i\delta} & c_{13}c_{23} \end{pmatrix} \cdot P \quad (4.20)$$

where $c_{ij} \equiv \cos \theta_{ij}$, $s_{ij} \equiv \sin \theta_{ij}$ (for $ij = 12, 13, 23$), and $P = \text{diag.}\{1, e^{i\alpha}, e^{i\beta}\}$. Here we denoted Dirac phase as δ and Majorana phases as α, β .

For a numerical example, we consider the best-fit values of the oscillation parameters, the atmospheric mixing angle $\theta_a \equiv \theta_{23} \simeq 41.2^\circ$, solar angle $\theta_s \equiv \theta_{12} \simeq 34.2^\circ$, the reactor mixing angle $\theta_r \equiv \theta_{13} \simeq 9^\circ$, and the Dirac CP phase $\delta = 0.8\pi$ (Majorana phases assumed to be zero here for simplicity i.e., $\alpha, \beta = 0$). The PMNS mixing matrix for this best-fit oscillation parameters is estimated to be

$$U_{\text{PMNS}} = \begin{pmatrix} 0.8168 & 0.5552 & -0.1265 - 0.0919i \\ -0.3461 - 0.0510i & 0.6604 - 0.0347i & 0.6634 \\ 0.4551 - 0.0563i & -0.5028 - 0.0382i & 0.7316 \end{pmatrix}. \quad (4.21)$$

We also use the best-fit values of mass squared differences $\Delta m_s^2 \equiv m_2^2 - m_1^2 = 7.56 \times 10^{-5} \text{eV}^2$ and $\Delta m_a^2 \equiv |m_3^2 - m_1^2| = 2.5 \times 10^{-3} \text{eV}^2$. As we do not know the sign of Δm_a^2 , the pattern of light neutrinos could be normal hierarchy (NH) with $m_1 < m_2 < m_3$,

$$m_2 = \sqrt{m_1^2 + \Delta m_s^2}, \quad m_3 = \sqrt{m_1^2 + \Delta m_a^2},$$

or, the inverted hierarchy (IH) with $m_3 < m_1 < m_2$,

$$m_1 = \sqrt{m_3^2 + \Delta m_a^2}, \quad m_2 = \sqrt{m_3^2 + \Delta m_a^2 + \Delta m_s^2}.$$

Now, one can use these oscillation parameters and $m_d \simeq 10^{-4}$ GeV, the mass matrix for heavy neutrinos is expressed as

$$M_R = 10^{-8} \text{GeV}^2 (U_{\text{PMNS}} m_\nu^{\text{diag.}} U_{\text{PMNS}}^T)^{-1}. \quad (4.22)$$

Using $m_1 = 0.001$ eV, the masses for heavy neutrinos are found to be $M_{N_1} \simeq 100$ GeV, $M_{N_2} \simeq 1000$ GeV and $M_{N_3} \simeq 8000$ GeV. The same algebra can be extended for inverted hierarchy and quasi-degenerate pattern of light neutrinos for deriving structure of M_R .

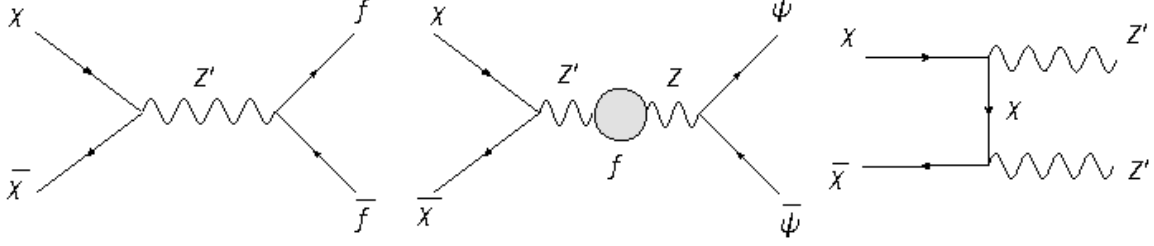


Figure 4.2: Possible annihilation channels for relic abundance of DM, where f represents muon and tauon families of leptons while ψ represents the SM fermion.

4.6 Relic Abundance of DM

The discrete Z_2 symmetry makes the χ particle stable and hence can serve a DM candidate in our present model. We explore the parameter space in two different scenarios, in the absence and in the presence of the singlet scalar η .

4.6.1 Relic abundance in absence of η

For simplicity we assume that the right handed neutrinos N_μ and N_τ as well as the scalar field S are heavier than the χ mass. So the annihilation of DM to these fields is kinematically forbidden. In the absence of η , the relevant diagrams that contribute to the relic density are shown in Fig. 4.2. The first two channels are s-channel processes through which DM annihilates to SM fermions and the third one is a t-channel process to Z', Z' final state. The second one is suppressed compared to the first one due to the small mixing angle between $Z - Z'$ is small ($\tan \theta_Z < 10^{-2}$), the constraint is coming from the non observation of DM signal in direct detection in Xenon-100 and LUX experiments. So the dominant contribution to relic abundance, below the threshold of Z' , comes from the s-channel annihilation: $\bar{\chi}\chi \rightarrow \bar{\psi}\psi, \bar{f}f$ through the exchange of Z' . Due to the resonance effect this cross-section dominates. We have shown in Fig. 4.3, the correct relic abundance of DM in the plane of $M_{Z'}$ and $g_{\mu\tau}$. Below the red line the annihilation cross-section through Z' exchange is small due to small gauge coupling and therefore, we always get an over abundance of DM. The constraints from muon $g - 2$ anomaly, shown by black shaded region, and direct detection of DM via $Z - Z'$ mixing, shown by green shaded region using $Z - Z'$ mixing to be 10^{-3} , are given in the same plot for comparison purpose. We note that region above green line is allowed by direct detection if $Z - Z'$ mixing is less than 10^{-3} . We have also shown the constraint from the neutrino trident production [8] by the brown dashed curve. The region above the brown dashed curve is ruled out due to the mismatch between experimental observation [338, 339] and SM prediction induced by large gauge coupling ($g_{\mu\tau}$). This implies that the combine constraints from muon $g - 2$ anomaly and neutrino trident production rules out Z' mass more than 400 MeV and $g_{\mu\tau} \gtrsim 10^{-3}$. On the other hand, for $M_{Z'} \lesssim 400\text{MeV}$ and $g_{\mu\tau} \lesssim 10^{-3}$ we get an overabundance of DM. We resolve this issue by adding an extra singlet scalar field $\eta(2)$, where the number inside the parenthesis is the charge under $U(1)_{L_\mu - L_\tau}$.

4.6.2 Relic abundance in presence of η

In presence of the SM singlet scalar field $\eta(2)$, the new annihilation channels $\bar{\chi}\chi \rightarrow \eta^\dagger\eta$, shown in Fig. 4.4, and $\bar{\chi}\chi \rightarrow h\eta$ open up in addition to the earlier mentioned channels, shown in fig. (4.2).

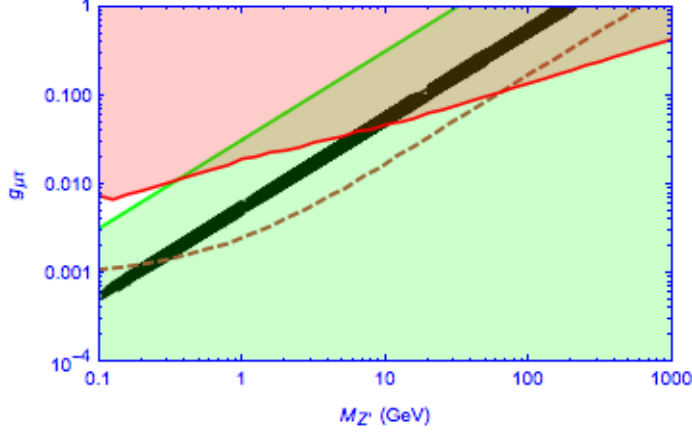


Figure 4.3: Parameter space for Z' boson. The region above the red line is allowed by the correct relic abundance of DM, the green shaded region is allowed by null detection of DM at LUX using $Z - Z'$ mixing to be 10^{-3} . Black shaded region is allowed by muon $g - 2$ anomaly. Neutrino trident production [8] forbids the region above the dashed brown curve.

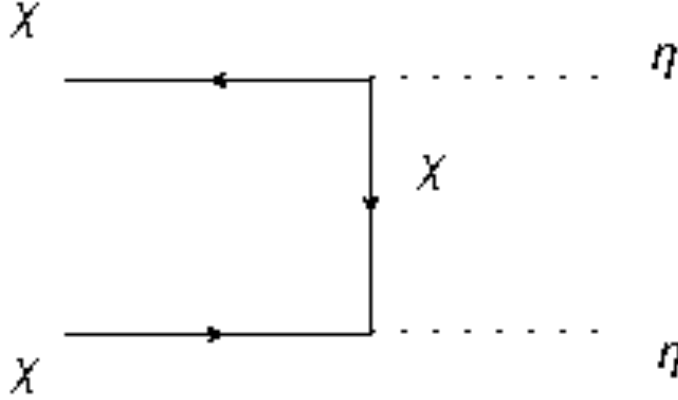


Figure 4.4: Dominant annihilation channel for relic abundance of DM in the region of small $g_{\mu\tau}$.

However, in the region of small gauge coupling $g_{\mu\tau}$, the dominant channel for the relic abundance of DM is $\bar{\chi}\chi \rightarrow \eta^\dagger\eta$. The other channel: $\bar{\chi}\chi \rightarrow h\eta$ is suppressed due to the small mixing angle $\sin\theta_{\eta h}$, required by null detection of DM at direct search experiments. We assume that the mass of η to be order of a GeV as discussed in section 4.2.3. The analytic expression for the cross-section of $\bar{\chi}\chi \rightarrow \eta^\dagger\eta$ is given by:

$$\langle\sigma|v\rangle(\chi\chi \rightarrow \eta\eta) = \frac{1}{128\pi} \frac{1}{\left(1 - \frac{M_\eta^2}{2M_\chi^2}\right)^2} \frac{f_\chi^4}{M_\chi^2} \left(1 - \frac{M_\eta^2}{M_\chi^2}\right)^{3/2} \quad (4.23)$$

The cross-section of the above process goes as $\frac{f_\chi^4}{M_\chi^2}$ for $M_\eta \ll M_\chi$. The allowed parameter space in the plane of M_η/M_χ and f_χ for the correct relic abundance as allowed by PLANCK is shown in Fig. 4.5 for a fixed value of $M_\eta = 1$ GeV. The green points show the value of analytic approximation (4.23) while the red points reveal the result from full calculation using `micrOMEGAs` [122]. The matching of both points ensures that the contribution to relic density is solely coming from the

$\bar{\chi}\chi \rightarrow \eta^\dagger\eta$ channel. It is also clear from the Fig. 4.5 that as the ratio $\frac{M_\eta}{M_\chi}$ decreases, in other words as M_χ increases for a fixed value of M_η , we need a large coupling to get the correct relic abundance. For comparison, we also show the DM-nucleon spin independent elastic cross-section: $\chi n \rightarrow \chi n$ mediated through the $\eta - h$ mixing, in the same plot. We find that the allowed mixing angle by LUX data is quite small. Typically, for $M_\eta \gtrsim 1$ GeV, we need $\theta_{\eta h} \lesssim \mathcal{O}(10^{-5})$ to reconcile the relic abundance with LUX data.

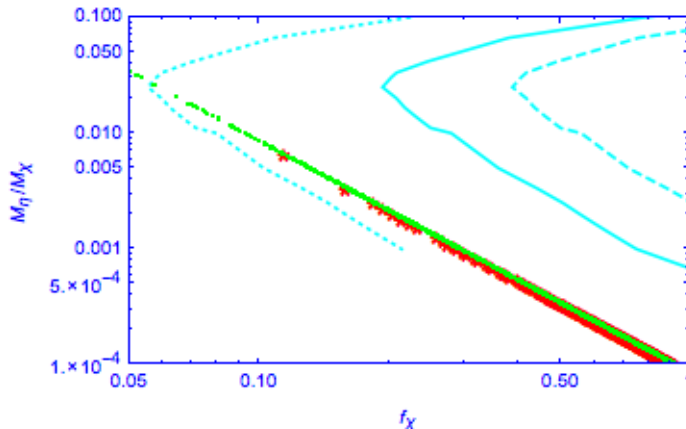


Figure 4.5: Constraints on the parameter space satisfying correct relic abundance (shown by Green and Red points) and null detection of dark matter at LUX (shown by Cyan lines). For $M_\eta = 1$ GeV, we have used $\sin \theta_{\eta h} = 5 \times 10^{-6}$ (dashed-line), 1×10^{-5} (solid-line) and 3.5×10^{-5} (dotted-line).

4.7 Constraints from Detection of DM in Direct Search Experiments

The non observation of DM signal in direct search experiments such as Xenon-100 [12] and LUX [110] put a constraint on the model parameters. We study the constraint coming from the direct detection of DM in the experiments in the following two cases:

- a. In the absence of η
- b. In the presence of η .

We show that in absence of η field, the elastic scattering of DM with nucleon through $Z - Z'$ mixing give stringent constraint on the model parameters: $M_{Z'}$ and $g_{\mu\tau}$, as depicted in fig. (4.3). On the other hand, in the presence of η field, the elastic scattering will be possible through the $\eta - h$ mixing, while inelastic scattering with nucleon will be possible via $Z - Z'$ mixing. In the following we discuss in details the possible constraints on model parameters.

4.7.1 Direct Detection in absence of η

The direct detection of DM signal through its elastic scattering with the nuclei is a very challenging task. The current sensitivity of present direct DM detection experiments sets stringent limits on parameters of the model, or hopefully enable the observation of signals in near future. In absence of η field, the elastic scattering between singlet fermion DM with nuclei is displayed in Fig. 4.6.

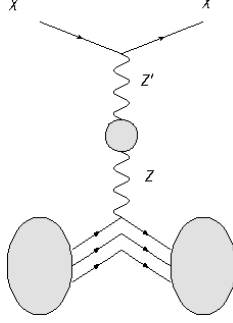


Figure 4.6: Feynman diagrams for direct detection of DM through scattering with nuclei via the exchange of $Z - Z'$ mixing.

The spin independent DM-nucleon cross-section mediated via the loop induced $Z - Z'$ mixing is given by [111, 112]

$$\sigma_{\text{SI}}^Z = \frac{1}{64\pi A^2} \mu_r^2 \tan^2 \theta_Z \frac{G_F}{2\sqrt{2}} \frac{g_{\mu\tau}^2}{M_{Z'}^2} \left[Z \frac{f_p}{f_n} + (A - Z) \right]^2 f_n^2, \quad (4.24)$$

where A is the mass number of the target nucleus, $\mu_r = M_\chi m_n / (M_\chi + m_n) \approx m_n$ is the reduced mass, m_n is the mass of nucleon (proton or neutron) and f_p and f_n are the interaction strengths (including hadronic uncertainties) of DM with proton and neutron respectively. Here Z is the atomic number of the target nucleus.

For simplicity we assume conservation of isospin, *i.e.* $f_p/f_n = 1$. The value of f_n is varied within the range: $0.14 < f_n < 0.66$ [113, 114, 115]. If we take $f_n \simeq 1/3$, the central value, then from Eqn. (3.22) we get the total cross-section per nucleon to be

$$\sigma_{\text{SI}}^Z \simeq 7.6 \times 10^{-46} \text{cm}^2 \tan^2 \theta_Z \frac{g_{\mu\tau}^2}{M_{Z'}^2}. \quad (4.25)$$

for the DM mass of 33 GeV.

The Z -boson mass puts a stringent constraint on the mixing parameter $\tan \theta_Z$ to be $\tan \theta_Z < 10^{-2}$ [345, 346]. For $\tan \theta_Z = 10^{-3}$ we show the allowed values of $g_{\mu\tau}$ and $M_{Z'}$ in fig (4.3) by choosing LUX limit on spin independent direct DM detection cross-section to be $7.6 \times 10^{-46} \text{cm}^2$ (at a DM mass of 33 GeV). The plot follows a straight line as expected from equation (3.22) and shown by the green line in fig. (4.3). Any values below that line will be allowed by the LUX limit. However the space above the green line will also be allowed if we choose $\tan \theta_Z < 10^{-3}$. In other words, the parameters $g_{\mu\tau}$ and $M_{Z'}$ are not severely constrained by the direct detection of DM.

4.7.2 Direct Detection in Presence of η

In presence of η field, the elastic scattering of the DM with the nuclei is mediated through $\eta - h$ mixing. On the other hand the inelastic scattering of the DM with the nuclei is mediated through the $Z - Z'$ mixing.

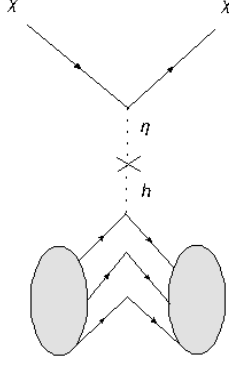


Figure 4.7: Elastic scattering of DM with nuclei through $\eta - h$ mixing.

Elastic scattering of DM

The spin-independent scattering of DM with nuclei is a t-channel exchange diagram as shown in Fig. 4.7 through the mixing of scalar singlet η with the SM Higgs H . The elastic scattering cross section $\sigma_{SI}^{\eta h}$ off a nucleus is given by [111, 112] :

$$\sigma_{SI}^{\eta h} = \frac{\mu_r^2}{\pi A^2} [Z f_p + (A - Z) f_n]^2 \quad (4.26)$$

where μ_r is the reduced mass, Z and A are respectively atomic and mass number of the target nucleus. In the above equation f_p and f_n are the effective interaction strengths of the DM with the proton and neutron of the target nucleus and are given by:

$$f_{p,n} = \sum_{q=u,d,s} f_{T_q}^{p,n} \alpha_q \frac{m_{p,n}}{m_q} + \frac{2}{27} f_{TG}^{p,n} \sum_{q=c,t,b} \alpha_q \frac{m_{p,n}}{m_q} \quad (4.27)$$

with

$$\alpha_q = \frac{f_\chi \sin \theta_{\eta h}}{M_\eta^2} \left(\frac{m_q}{v_H} \right) \quad (4.28)$$

In Eq. (4.27), the different coupling strengths between the DM and light quarks are given by [117, 3, 347, 348] $f_{T_u}^{(p)} = 0.020 \pm 0.004$, $f_{T_d}^{(p)} = 0.026 \pm 0.005$, $f_{T_s}^{(p)} = 0.118 \pm 0.062$, $f_{T_u}^{(n)} = 0.014 \pm 0.004$, $f_{T_d}^{(n)} = 0.036 \pm 0.008$, $f_{T_s}^{(n)} = 0.118 \pm 0.062$. The coupling of DM with the gluons in target nuclei is parameterized by

$$f_{TG}^n = 1 - \sum_{q=u,,d,s} f_{T_q}^n. \quad (4.29)$$

Thus from Eqs. 4.26, 4.27, 4.28, 3.28, the spin-independent DM-nucleon interaction through $\eta - h$ mixing is given by:

$$\begin{aligned} \sigma_{SI}^{\eta h} &= \frac{\mu_r^2 f_\chi^2 \sin^2 \theta_{\eta h}}{\pi A^2 M_\eta^4} \\ &\times \left[Z \frac{m_p}{v_H} \left(f_{T_u}^p + f_{T_d}^p + f_{T_s}^p + \frac{2}{9} f_{TG}^p \right) + (A - Z) \frac{m_n}{v_H} \left(f_{T_u}^n + f_{T_d}^n + f_{T_s}^n + \frac{2}{9} f_{TG}^n \right) \right]^2 \quad (4.30) \end{aligned}$$

In the above equation, the unknowns are f_χ , $\sin \theta_{\eta h}$ and M_η . So using the current limit on spin-independent scattering cross-section from Xenon-100 [12] and LUX [110] one can constrain these

parameters f_χ and M_η for a fixed value of mixing angle $\sin\theta_{\eta h}$. Here we use LUX bound and the corresponding contour lines are drawn in the fig.4.5 by choosing $M_\eta = 1\text{GeV}$ (cyan lines). We have drawn three contour lines for three different values of mixing angles: $\sin\theta_{\eta h} = 5 \times 10^{-6}$ (dashed), $\sin\theta_{\eta h} = 10^{-5}$ (solid) and $\sin\theta_{\eta h} = 3.5 \times 10^{-5}$ (dotted). The regions on the right of the respective lines are excluded by LUX data. From fig. (4.5), we see that for a constant value of M_η , if $\sin\theta_{\eta h}$ decreases then the curves shift towards higher value of f_χ . Thus for a typical value of η mass: $M_\eta = 1\text{ GeV}$, we need $\theta_{\eta h} \lesssim \mathcal{O}(10^{-5})$ to be compatible with relic abundance as well as direct search of DM at LUX. This constraint is also in agreement with bound from BBN as discussed in section 4.3.

Inelastic scattering of DM

As we discussed above, the inelastic scattering [144] of the DM with the target nuclei is also possible via $Z - Z'$ mixing. Let us rewrite the DM Lagrangian in presence of η field as [145, 85, 84, 143] :

$$\begin{aligned} \mathcal{L}_{DM} = & i\bar{\chi}(\not{\partial} + ig_{\mu\tau}Z'_\mu\gamma^\mu)\chi \\ & -M_\chi\bar{\chi}\chi - \frac{1}{2}f_1\left(\bar{\chi}^CP_L\chi + \text{h.c.}\right)\eta^* - \frac{1}{2}f_2\left(\bar{\chi}^CP_R\chi + \text{h.c.}\right)\eta^*, \end{aligned} \quad (4.31)$$

where f_1 and f_2 are the interaction strengths to left and right components of the vector-like fermion χ . When η gets a vev, the DM gets small Majorana mass $m_L = f_1v_\eta$ and $m_R = f_2v_\eta$. The presence of small Majorana mass terms for the DM split the Dirac state into two real Majorana states χ_1 and χ_2 . The Lagrangian in terms of the new eigenstates is given as

$$\begin{aligned} \mathcal{L}_{DM} = & \frac{1}{2}\bar{\chi}_1i\gamma^\mu\partial_\mu\chi_1 - \frac{1}{2}M_1\bar{\chi}_1\chi_1 + \frac{1}{2}\bar{\chi}_2i\gamma^\mu\partial_\mu\chi_2 - \frac{1}{2}M_2\bar{\chi}_2\chi_2 + ig_{\mu\tau}\bar{\chi}_2\gamma^\mu\chi_1Z'_\mu \\ & + \frac{1}{2}g_{\mu\tau}\frac{m_-}{M_\chi}\left(\bar{\chi}_2\gamma^\mu\gamma^5\chi_2 - \bar{\chi}_1\gamma^\mu\gamma^5\chi_1\right)Z'_\mu + \mathcal{O}\left(\frac{m_-^2}{M_\chi^2}\right) \\ & + \frac{1}{2}\left(f_1\cos^2\theta - f_2\sin^2\theta\right)\bar{\chi}_1\chi_1\eta + \frac{1}{2}\left(f_2\cos^2\theta - f_1\sin^2\theta\right)\bar{\chi}_2\chi_2\eta, \end{aligned} \quad (4.32)$$

where $\sin\theta$ is the mixing angle, M_1 and M_2 are the two mass eigenvalues and are given by

$$M_1 = M_\chi - m_+, M_2 = M_\chi + m_+ \quad (4.33)$$

$$m_\pm = \frac{m_L \pm m_R}{2} \quad (4.34)$$

From the above expression the dominant gauge interaction is off-diagonal, and the diagonal interaction is suppressed as $\frac{m_-}{M_\chi} \ll 1$. The mass splitting between the two mass eigen states is given by:

$$\delta = M_2 - M_1 = 2m_+ = (f_1 + f_2)v_\eta. \quad (4.35)$$

The inelastic scattering with the target nucleus due to $Z - Z'$ mixing is shown in Fig. 4.8. The occurrence of this process solely depends on the mass splitting between the two states. In fact, the minimum velocity of the DM needed to register a recoil inside the detector is given by [144, 145, 85, 84, 143] :

$$v_{\min} = c\sqrt{\frac{1}{2m_nE_R}\left(\frac{m_nE_R}{\mu_r} + \delta\right)}, \quad (4.36)$$

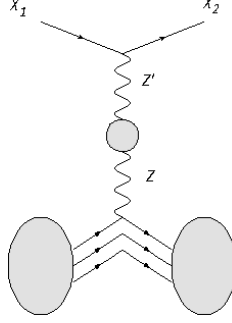


Figure 4.8: Inelastic scattering of DM with the target nucleus through the $Z - Z'$ mixing.

where E_R is the recoil energy of the nucleon. If the mass splitting is above a few hundred keV, then it will be difficult to excite χ_2 . So the inelastic scattering will be forbidden.

4.8 Indirect detection of DM

We now look at the compatibility of the present framework with indirect detection signals of DM and in particular AMS-02 positron data. Recently, the AMS-02 experiment reported the results of high precision measurement of the cosmic ray positron fraction in the energy range of 0.5–500 GeV[15, 2]. This result further confirmed the measurement of an excess in the positron fraction above 10 GeV as observed by PAMELA[16, 17] and FERMI-LAT[340]. The usual explanation for this excess is through DM annihilation producing the required flux of positrons. However such an excess was not observed in the antiproton flux by PAMELA[349], thus suggesting a preference for leptonic annihilation channels. Recently AMS-02 also announced results from their measurement of the antiproton flux, which suggests a slight excess above 100 GeV[350]. But this was found to be within error of the modelling of secondary astrophysical production[351]. In this context we consider the $L_\mu - L_\tau$ symmetry where the DM dominantly annihilates to muons which then subsequently decay to produce electrons. This ensures a softer distribution of positrons thereby providing a better fit to the experimental data.

For theoretical explanation for AMS-02 positron excess through DM annihilations in the $L_\mu - L_\tau$ symmetric extension of SM we have to calculate propagation of cosmic rays in the galaxy. In order to do this calculation, the propagation of cosmic rays is treated as a diffusion process and one therefore solves the appropriate diffusion equation. Here we calculate the flux of the cosmic ray electrons (primary and secondary) as well as secondary positrons at the position of the sun after propagating through the galaxy. The propagation equation for charged cosmic rays is given by[352]

$$\begin{aligned} \frac{\partial \psi(\vec{r}, p)}{\partial t} = & q + \vec{\nabla} \cdot (D_{xx} \vec{\nabla} \psi - \vec{V}_c \psi) + \frac{\partial}{\partial p} p^2 D_{pp} \frac{\partial}{\partial p} \frac{1}{p^2} \psi - \frac{\partial}{\partial p} \left[\dot{p} \psi - \frac{p}{3} (\vec{\nabla} \cdot \vec{V}_c) \psi \right] \\ & - \frac{1}{\tau_f} \psi - \frac{1}{\tau_r} \psi \end{aligned} \quad (4.37)$$

where ψ is the cosmic ray density, \dot{p} gives the energy loss of cosmic rays, $D_{xx(pp)}$ is the diffusion coefficient in spatial (momentum) coordinates while the last two terms represent the fragmentation and radioactive decay of cosmic ray nuclei. The diffusion coefficient is parameterized as $D_{xx} =$

	M_χ (GeV)	$M_{Z'}$ (GeV)	$g_{\mu\tau}$	Ωh^2	Boost factor
BP1	710	838	0.35	0.116	720
BP2	800	782	0.4	0.113	800

Table 4.2: Benchmark point which satisfies relic density and fits the AMS2 positron fraction data[2].

$D_{0xx}E^{-\gamma_e-\delta}$. The primary spectrum of cosmic ray electrons is modeled by

$$\psi = \frac{N}{2} \frac{L}{D_{0xx}} E^{-\gamma_e-\delta} \quad (4.38)$$

where N is a normalization constant and L is the half height of the cylindrical diffusion zone. The parameters for propagation of cosmic rays are D_0 , δ , N , L , v_a (Alfven velocity), V_c and γ_e . We use the GALPROP package [353, 354] to solve the diffusion equation in Eq. 4.37 using a diffusive re-acceleration model of diffusion. The cosmic ray primary and secondary electron flux as well as the secondary positron flux which constitute the astrophysical background are thus obtained. The positron flux from DM annihilations is calculated using micrOMEGAs[122] while the gauged $U(1)_{L_\mu-L_\tau}$ model is implemented in micrOMEGAs with the help of LanHEP[355]. The ratio of the DM positron signal thus obtained, to the total astrophysical background gives the positron fraction.

The key feature of this model is that the DM does not couple to quarks at tree level and hence we do not see any observable contribution to the antiproton flux. We therefore focus on the possible explanation of positron fraction. However, from fig. 4.3, we noticed that the combine constraints from muon $g-2$ anomaly and neutrino trident production restricts the $M_{Z'} \lesssim 400\text{MeV}$ and $g_{\mu\tau} \lesssim 10^{-3}$. In this limited parameter space, the DM annihilation cross section $\langle\sigma|v|\rangle(\chi^\dagger\chi \rightarrow \mu^+\mu^-, \tau^+\tau^-) \ll \langle\sigma|v|\rangle_F \equiv 3 \times 10^{-26}\text{cm}^3/\text{s}$. Therefore, to explain the observed positron excess one needs an unnaturally large boost factor. As we describe below, the most favorable cross-section for DM annihilation to positrons that explains the AMS-02 positron excess occurs near the resonance, Z' mass of $2M_\chi$, with the $DM-Z'$ coupling $\sim 10^{-1}$, which is now ruled out by the combine constraints from $g-2$ anomaly and neutrino trident production. Thus one finds that a reasonable explanation of the AMS-02 positron excess in the $L_\mu-L_\tau$ model under consideration is ruled out. However, if we choose any point below the dashed brown curve of fig. 4.3, then these points are not ruled out by neutrino trident production though contribute partially to anomalous $g-2$ values. In this region of parameter space, the DM annihilation can explain the observed positron excess while being compatible with relic density and direct detection limits. We consider two benchmark points which satisfy the relic density constraint from PLANCK[5]. The parameters for the two chosen benchmark points are listed in Table 4.2. We find that for the best fit to AMS-02 data in the current scenario requires $M_\chi \gtrsim 500$ GeV. Also for satisfying the relic density constraint we need $M_{Z'} \sim 500$ GeV for $M_\chi \gtrsim 500$ GeV.

4.9 Conclusion and Outlook

In this chapter we discussed the muon $g-2$ anomaly, light non-zero neutrino mass and DM phenomenology in a gauged $U(1)_{L_\mu-L_\tau}$ extension of the SM. We augmented the SM with three right handed neutrinos N_e, N_μ, N_τ and a Dirac fermion χ which have non zero charges under $U(1)_{L_\mu-L_\tau}$ symmetry except N_e which is a complete singlet fermion. The $U(1)_{L_\mu-L_\tau}$ was allowed to break

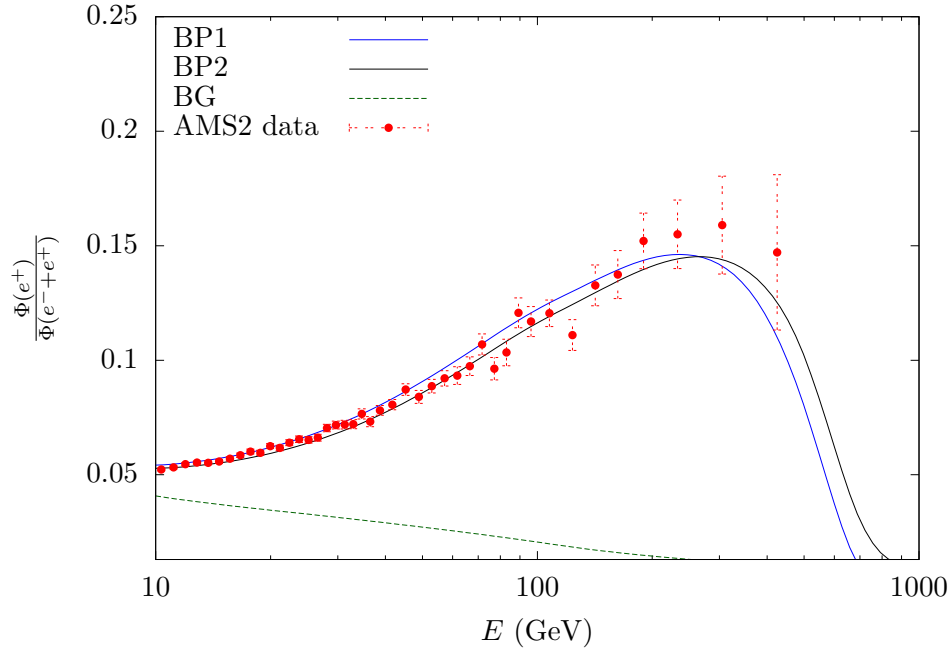


Figure 4.9: Ratio of positron flux to the total ($e^- + e^+$) flux against energy of the cosmic rays with AMS-02(2014) data[2] for benchmark points listed in Table 4.2. The blue curve is for the benchmark point BP1 while the black curve is for BP2.

completely at a TeV scale by giving vev to a SM singlet scalar S which bears an unit $L_\mu - L_\tau$ charge. The vev of S gave masses not only to the additional gauge boson Z' , but also to the right handed neutrinos: N_e, N_μ, N_τ . As a result, below electroweak symmetry breaking, the light neutrinos acquired masses through the type-I seesaw mechanism. A discrete symmetry Z_2 is also imposed under which, χ is chosen to be odd while all other fields are even. As a result the stability of χ is ensured. Hence it serves as a viable DM candidate.

The relic abundance of DM is obtained via its annihilation to muon and tauon families with Z' exchanged s-channel processes. To obtain the correct relic abundance we require mass of Z' to be greater than 100 MeV and the gauge coupling to leptons: $g_{\mu\tau} > 5 \times 10^{-3}$. On the other hand, the muon $g-2$ anomaly requires smaller values of the gauge coupling $g_{\mu\tau}$ for Z' mass greater than 100 MeV (see fig. 4.3). So the two problems could not be solved simultaneously. Therefore, a new SM singlet scalar field η is introduced into the model having 2 units of charge under $U(1)_{L_\mu - L_\tau}$ group. Due to the presence of η field, new annihilation channel $\bar{\chi}\chi \rightarrow \eta^\dagger\eta$ opens up. As a result we found a large region of parameter space in which the constraints from muon $g-2$ anomaly and relic abundance of DM could be satisfied simultaneously. The hitherto null detection of DM at direct search experiments, such as LUX, is also discussed in Fig. 4.3. We found that the constraints from muon $g-2$ anomaly and LUX experiment are compatible in a large parameter space.

The combine constraints from muon $g-2$ anomaly and neutrino trident production restricts $M_{Z'} \lesssim 400\text{MeV}$ and $g_{\mu\tau} \lesssim 10^{-3}$. This restricted parameter space is compatible with muon $g-2$ anomaly, latest direct detection limits from LUX and relic abundance of DM in presence of η field. In this limited parameter space the annihilation cross-section of DM to muon and tauon pairs through the exchange of Z' is much smaller than the DM relic abundance cross-section. So one needs

unnaturally large boost factor to explain the observed positron flux by PAMELA, Fermi-LAT and recently by AMS-02 in the cosmic ray shower. However, if we consider the parameter space in the plane of $g_{\mu\tau}$ versus $M_{Z'}$, which is not constrained by neutrino trident production, *i.e.*, points below the brown dashed curve, then we can explain the observed positron excess by DM annihilation with suppressed anti-proton flux, as in our model the DM annihilates only to lepton pairs. Note that these points in the plane of $g_{\mu\tau}$ versus $M_{Z'}$ contribute partially to the anomalous $g - 2$ anomaly. Thus, while explaining the observed positron excess, we need to sacrifice the explanation for $g - 2$ anomaly and vice versa.

Chapter 5

Conclusion

In this thesis, different models by extending the SM has been proposed in order to explore the possibility of a DM candidate as well as the small neutrino mass. The viability of the model is also verified by taking the results of various experiments from LHC, direct and indirect DM detection experiments like LUX and XENON. The smallness of neutrino mass is also explained in the models using seesaw mechanism.

In chapter 1, the existence of the DM is presented from results of various experiments like galaxy rotation curve, gravitational lensing, CMBR fluctuation observed by PLANCK. The production of the DM in the early universe is also studied by solving the Boltzmann equation in a freeze out mechanism. The method used in this case is only applicable for cold DM which differs from other possible DM candidates like warm and hot. The status of DM detection in various experiments like direct and indirect detection is also mentioned. A small review of the neutrino mass as well as the anomalous magnetic moment of muon particle is also presented. The motivation thus received in chapter 1 is carried out in various BSM frameworks in subsequent chapters 2,3 and 4.

In chapter 2, a dipolar DM model is studied simultaneously explaining the DM and neutrino mass. We augmented the SM by adding three right handed neutrinos and two scalars, a doublet and a charged singlet. The LSP among the right handed neutrinos serves as a DM candidate in the model. A transition magnetic moment is developed between the NLSP and the LSP. As a result the former can decay to later by emitting a monochromatic photon of 3.5 keV energy. This photon can explain the X-ray signal as observed by the XMM Newton observatory. The life time of the NLSP is of the order of age of the universe, hence it is decaying in the current epoch. As the life time is so large NLSP also gives contribution to the DM relic abundance. The neutrinos also get mass in a Type I seesaw scenario.

In chapter 3, a mixed singlet-doublet vector like fermionic DM model is proposed. The model contains two vector like fermions: a singlet and a doublet under $SU(2)_L$, in addition to the SM. We argued that a singlet or the neutral component of the doublet alone can not serve as DM candidates. But after electroweak transition both neutral particles mix together and the lightest of them becomes a viable candidate of DM. The stability of the DM is ensured by the imposed Z_2 symmetry. We explore the model parameters, considering combined constraints from collider, relic density of DM as well as null result from direct detection of DM experiments. The possibility of a displaced vertex signature in the colliders by the charged companion of DM is also studied. The model is further

extended by adding a scalar triplet under $SU(2)$. The scalar triplet couples to both SM leptons and fourth generation lepton. After the symmetry breaking, the neutral component of the triplet gets an induced vev. As a result the neutrinos get mass in a Type II seesaw scenario. Again the DM phenomenology is also affected by the presence of the scalar triplet. It is seen that the DM becomes inelastic due to the small Majorana mass induced by the scalar triplet. Hence the Z mediated direct detection process is forbidden. As a result the constraint on the singlet-doublet mixing angle is little bit relaxed. In a very brief way, the diphoton resonance at 750 GeV energy as claimed by CMS and ATLAS is also explained by adding a singlet scalar of mass 750 GeV and a vector like quark to the singlet-doublet vector like fermion model.

The inadequacy of SM in order to explain the muon anomalous magnetic moment is considered in chapter 4. The motivation received in chapter 1 is carried out further to explain the muon $g - 2$ anomaly, neutrino mass as well as the DM in a unified model. The SM is gauged by a new $U(1)_{L_\mu - L_\tau}$ symmetry, where the new symmetry is built under the basis of difference of lepton number between the muon and tauon lepton number. The model contains 3 neutral fermions in addition to the DM which are all a singlets under $SU(2)_L$. The DM has non trivial charge under the new gauge symmetry and is stabilized by a Z_2 symmetry. Two singlet scalars under $SU(2)_L$ but having charge in 1 and 2 units, under the imposed gauge symmetry are also added in order to explain neutrino mass as well as DM phenomenology. The magnetic moment of muon receives additional contribution from the new gauge field in addition to the SM, hence can explain the anomaly. In the absence of the double charge scalar under new gauge symmetry, the direct detection of DM is possible through $Z - Z'$ mixing. However in its presence, a Majorana mass term is possible for the DM. As a result the DM field splits into two Majorana fields with a small mass splitting between them. Since due to the inelastic nature the direct detection through $Z - Z'$ mixing is forbidden. But the elastic scattering is still be possible through the mixing in the scalar sector. The indirect detection of DM is also explored by considering the data of AMS-02.

In this work, new beyond standard model frameworks have been explored. The various features of the model in order to explain the cold DM is also carefully studied. The analysis is also further carried out, not only to the neutrino sector, but also to explain the muon anomalous magnetic moment and various astrophysical observations. The astrophysical observations include 3.5 keV X-ray line observed in the Newton XMM observatory, the positron excess observed by PAMELA, Fermi-LAT and AMS-02. Extensive study of these models also adds one step towards better understanding of our universe, especially the testability of DM in near future.

Appendices

Appendix A

Radiative Neutrino Mass

Now let us calculate the radiative neutrino mass. The mass matrix can be read from the fig. 2.3 as

$$(m_\nu)_{\alpha\beta} = i(Y_\Sigma)_{\alpha 2} P_R (I_R - I_I) P_R i(Y_\Sigma)_{\beta 2} \quad (\text{A.1})$$

where

$$I_R = \int \frac{d^4 k}{(2\pi)^4} \frac{i}{(p-k)^2 - M_{\Sigma R}^2} \frac{i(\not{k} + M_2)}{k^2 - M_2^2} \quad (\text{A.2})$$

with I_I being same as I_R if we replace $M_{\Sigma I}$ in place of $M_{\Sigma R}$. The relative sign between the two terms is due to the fact that the imaginary component of Σ field gets a minus sign when squared. And again the term containing \not{k} will also goes to zero considering the symmetric and antisymmetric argument of the integral in terms of k . We will calculate this integral in the limit $p \rightarrow 0$. So the expression for I_R becomes

$$I_R = - \int \frac{d^4 k}{(2\pi)^4} \frac{1}{k^2 - M_{\Sigma R}^2} \frac{M_2}{k^2 - M_2^2} \quad (\text{A.3})$$

We use the Feynman parameter x and later we will insert the M_2 in denominator of I_R , and arrive at the expression

$$\begin{aligned} \frac{1}{k^2 - M_{\Sigma R}^2} \frac{1}{k^2 - M_2^2} &= \int_0^1 dx \frac{1}{[x(k^2 - M_2^2) + (1-x)(k^2 - M_{\Sigma R}^2)]^2} \\ &= \int_0^1 dx \frac{1}{[k^2 - \Delta]^2} \end{aligned} \quad (\text{A.4})$$

where $\Delta = x(M_2^2 - M_{\Sigma R}^2) + M_{\Sigma R}^2$. Now I_R becomes

$$I_R = - \int_0^1 dx \int \frac{d^4 k}{(2\pi)^4} \frac{1}{[k^2 - \Delta]^2}. \quad (\text{A.5})$$

To do the k integration we perform a Wick rotation by changing $k^0 = ik_E^0$ and $\vec{k} = \vec{k}_E$. So the

integral becomes

$$\begin{aligned}
I_R &= - \int_0^1 dx \frac{i}{(2\pi)^4} \int d\Omega \int_0^\infty dk_E k_E^3 \frac{1}{[k_E^2 + \Delta]^2} \\
&= - \frac{i}{(2\pi)^4} \int_0^1 dx (2\pi^2) \int_0^\infty dk_E k_E^3 \frac{1}{[k_E^2 + \Delta]^2} \\
&= - \frac{i}{(16\pi^2)} \int_0^1 dx \int_0^\infty dk_E^2 k_E^2 \frac{1}{[k_E^2 + \Delta]^2}
\end{aligned} \tag{A.6}$$

The integral has ultraviolet divergence. But this divergence will be cancelled out by the contribution from I_I term. The expression for I_I will be exactly the same as I_R with $M_{\Sigma R}$ is replaced by $M_{\Sigma I}$. So our expression now becomes

$$\begin{aligned}
I_R - I_I &= - \frac{i}{(16\pi^2)} \int_0^1 dx \int_0^\infty dk_E^2 k_E^2 \left(\frac{1}{[k_E^2 + \Delta_R]^2} - \frac{1}{[k_E^2 + \Delta_I]^2} \right) \\
&= - \frac{i}{(16\pi^2)} \int_0^1 dx [(-\ln\Delta_R) - (-\ln\Delta_I)]
\end{aligned} \tag{A.7}$$

where $\Delta_{R,I} = x(M_2^2 - M_{\Sigma R,I}^2) + M_{\Sigma R,I}^2$. The phase appearing in the expression can be absorbed by redefining the SM neutrino field. So we can drop this phase. Now the dx integration is straight forward. After few algebraic manipulation we will arrive at the expression for neutrino mass matrix as

$$\begin{aligned}
(m_\nu^{\text{loop}})_{\alpha\beta} &= \frac{(Y_\Sigma)_{\alpha 2} (Y_\Sigma)_{\beta 2} M_2}{16\pi^2} \left[\frac{M_{\Sigma R}^2}{(M_{\Sigma R}^2 - M_2^2)} \ln \left(\frac{M_{\Sigma R}^2}{M_2^2} \right) \right. \\
&\quad \left. - \frac{M_{\Sigma I}^2}{(M_{\Sigma I}^2 - M_2^2)} \ln \left(\frac{M_{\Sigma I}^2}{M_2^2} \right) \right]
\end{aligned} \tag{A.8}$$

Appendix B

Magnetic Moment of Dipolar DM

Let us assign the four-vector momenta of N_2 , N_1 and photon by p_1 , p_2 and k , respectively. The Feynman amplitude for the magnetic DM decay shown in Fig. 2.2(c.) can be written as

$$\begin{aligned}
\mathcal{M}^{(\mathbf{c}.)} &= \int \frac{d^4k}{(2\pi)^4} \overline{u(p_2)} (i Y_H^* P_R) S_\ell(k-q) (-i e \gamma_\mu \epsilon^\mu(q)) S_\ell(k) (i Y_\Sigma P_R) u^c(p_1) \\
&\quad \times \Delta_H(p_1 - k) (\mu_s v_{\text{ew}}) \Delta_\Sigma(p_1 - k) \\
&= \overline{u(p_2)} \left(i \Gamma_\mu^{(\mathbf{c}.)} \right) \epsilon^\mu(q) u^c(p_1), \tag{B.1}
\end{aligned}$$

where $i \Gamma_\mu^{(\mathbf{c}.)}$ is factored out to be

$$\begin{aligned}
i \Gamma_\mu^{(\mathbf{c}.)} &= (-e Y_H^* Y_\Sigma \mu_s v_{\text{ew}}) \times \\
&\quad \int \frac{d^4k}{(2\pi)^4} \frac{P_R(\not{k} - \not{q} + m_\ell) \gamma_\mu (\not{k} + m_\ell) P_R}{\{[(k-q)^2 - m_\ell^2]\{k^2 - m_\ell^2\}\{(p_1 - k)^2 - M_H^2\}\{(p_1 - k)^2 - M_\Sigma^2\}\}} \\
&= (-e Y_H^* Y_\Sigma \mu_s v_{\text{ew}}) \int \frac{d^4k}{(2\pi)^4} \mathcal{D}^{-1} \cdot \mathcal{N}_\mu \tag{B.2}
\end{aligned}$$

We denote \mathcal{D}^{-1} and \mathcal{N}_μ as follows

$$\mathcal{D}^{-1} = \frac{1}{\{[(k-q)^2 - m_\ell^2]\{k^2 - m_\ell^2\}\{(p_1 - k)^2 - M_H^2\}\{(p_1 - k)^2 - M_\Sigma^2\}\}} \tag{B.3}$$

$$\mathcal{N}_\mu = P_R(\not{k} - \not{q} + m_\ell) \gamma_\mu (\not{k} + m_\ell) P_R. \tag{B.4}$$

After doing some simpler algebra, we get

$$\begin{aligned}
\Gamma_\mu^{(\mathbf{c}.)} &= \frac{(-e Y_H^* Y_\Sigma \mu_s v_{\text{ew}})}{M_\Sigma^2 - M_H^2} \times \int \frac{d^4k}{(2\pi)^4} \left[\frac{N_\mu}{\{[(k-q)^2 - m_\ell^2]\{k^2 - m_\ell^2\}\{(p_1 - k)^2 - M_\Sigma^2\}\}} \right. \\
&\quad \left. - \frac{N_\mu}{\{(k-q)^2 - m_\ell^2\}\{k^2 - m_\ell^2\}\{(p_1 - k)^2 - M_H^2\}\}} \right] \\
&= \frac{(-e Y_H^* Y_\Sigma \mu_s v_{\text{ew}})}{M_\Sigma^2 - M_H^2} [I_1 - I_2] \tag{B.5}
\end{aligned}$$

The integral now becomes

$$\begin{aligned}
I_1 &= \frac{m_\ell}{16\pi^2} \int_0^1 dx \int_0^{1-x} dy S_1^{-2} [2(qx + p_1 y)_\mu - \not{x}\gamma_\mu] P_R \\
&= \frac{1}{16\pi^2} \frac{m_\ell}{M_\Sigma^2} \int_0^1 dx \int_0^{1-x} dy \Omega_1 [2y p_{1\mu} - 2p_{1\mu}] P_R \\
&= \frac{1}{8\pi^2} \frac{m_\ell}{M_\Sigma^2} p_{1\mu} \int_0^1 dx \int_0^{1-x} dy \Omega_1 [y - 1] P_R
\end{aligned}$$

Here $S_1^{-2} = M_\Sigma^{-2} \Omega_1$, $\Omega_1 = [Z_N (y - y^2 - xy) - (1 - y)Z_\ell - y]^{-1}$. Since the term proportional to $p_{2\mu} - p_{1\mu}$ gives vanishing contribution and writing $p_{1\mu} = \frac{1}{2}[p_{2\mu} + p_{1\mu} + q_\mu]$, the integral becomes

$$I_1 = \frac{1}{16\pi^2} \frac{m_\ell}{M_\Sigma^2} (p_1 + p_2)_\mu \int_0^1 dx \int_0^{1-x} dy \Omega_1 [y - 1] P_R \quad (\text{B.6})$$

Similarly, one can express the second integral \mathcal{I}_2 by replacing M_Σ by M_H .

Now we can write the loop factor as

$$\begin{aligned}
i\Gamma_\mu^{(\text{c.})} &= \frac{(-e Y_H^* Y_\Sigma \mu_s v_{\text{ew}})}{M_\Sigma^2 - M_H^2} \left[\frac{1}{16\pi^2} \frac{m_\ell}{M_\Sigma^2} (p_1 + p_2)_\mu \int_0^1 dx \int_0^{1-x} dy \Omega_1 (y - 1) P_R \right. \\
&\quad \left. - \frac{1}{16\pi^2} \frac{m_\ell}{M_\Sigma^2} (p_1 + p_2)_\mu \int_0^1 dx \int_0^{1-x} dy \Omega_2 (y - 1) P_R \right] \\
&= \frac{-e}{16\pi^2} \frac{(Y_H^* Y_\Sigma \mu_s v_{\text{ew}})}{M_\Sigma^2 - M_H^2} \frac{m_\ell}{M_\Sigma^2} \mathcal{I} (p_1 + p_2)_\mu P_R \\
&= \mathcal{A}_{12}^{(\text{c.})} (p_1 + p_2)_\mu
\end{aligned} \quad (\text{B.7})$$

where the integral \mathcal{I} is

$$\mathcal{I} = \int_0^1 dx \int_0^{1-x} dy (y - 1) [\Omega_1 - \Omega_2]$$

and

$$\mathcal{A}_{12}^{(\text{c.})} = \frac{-e}{16\pi^2} \frac{(Y_H^* Y_\Sigma \mu_s v_{\text{ew}})}{M_\Sigma^2 - M_H^2} \frac{m_\ell}{M_\Sigma^2} \mathcal{I}$$

From Gordon Identity, we can write

$$\mathcal{A}_{12}^{(\text{c.})} \overline{u(p_2)} (p_1 + p_2)_\mu u(p_1) = \mathcal{A}_{12}^{(\text{c.})} \overline{u(p_2)} [2M_N \gamma_\mu - i \sigma_{\mu\nu} (p_2 - p_1)^\nu] u(p_1) \quad (\text{B.8})$$

The analytical expression for transitional magnetic moment between two nearly degenerate heavy RH neutrinos, as derived from the effective operator $\mathcal{A}_{12}^{(\text{c.})} \overline{N_1} \sigma^{\mu\nu} N_2 F_{\mu\nu}$ following Feynman diagram Fig. 2.2(c.), as

$$\mathcal{A}_{12}^{(\text{c.})} = \frac{-e}{16\pi^2} \frac{(Y_H^* Y_\Sigma \mu_s v_{\text{ew}})}{M_\Sigma^2 - M_H^2} \frac{m_\ell}{M_\Sigma^2} \mathcal{I} \quad (\text{B.9})$$

Using the same formalism of Feynman calculations as discussed in Fig. 2.2(c.), one can derive the relevant contributions of transition magnetic moment depicted in Fig. 2.2(a.) where the photon is emitted from H -vertex and Fig. 2.2(b.) with the emitted photon from Σ -vertex. At the end, the analytical expression for transitional magnetic moment including relevant Feynman diagrams can

be put in the following expression

$$\begin{aligned}
\mu_{12} &= \mathcal{A}_{12}^{(\mathbf{a})} + \mathcal{A}_{12}^{(\mathbf{b})} + \mathcal{A}_{12}^{(\mathbf{c})} \\
&\simeq \frac{-e}{16\pi^2} \frac{(Y_H^* Y_\Sigma \mu_s v_{\text{ew}})}{M_\Sigma^2 - M_H^2} \frac{m_\ell}{M_\Sigma^2} \mathcal{I}_{\text{tot}}.
\end{aligned} \tag{B.10}$$

where \mathcal{I}_{tot} is the loop factor accounting all these contributions.

Appendix C

3-Body Decay of N^-

Kinematics

The three body decay width is given by

$$d\Gamma = \frac{1}{2M_N} \prod_{i=1}^3 \left[\frac{d^3 p_i}{(2\pi)^3 2E_i} \right] \times (2\pi)^4 \delta^4 \left[P - \sum_{i=1}^3 p_i \right] |\mathcal{M}|^2, \quad (\text{C.1})$$

where P is the four momentum of the decaying particle and p_i are the four momenta of final state particles. We choose p_2, p_3 to be the momenta of SM leptons. \mathcal{M} is the amplitude matrix element for the decay. We introduce an invariant mass $s = (p_2 + p_3)^2$ of the SM leptons via the relation

$$\begin{aligned} 1 &= \int ds \delta(s - p^2) d^4 p \delta^4(p - p_2 - p_3) \\ &= \int ds \frac{d^3 p}{2E_p} \delta^4(p - p_2 - p_3) \end{aligned} \quad (\text{C.2})$$

we get

$$\begin{aligned} \Gamma &= \int \frac{1}{2M_N} \frac{ds}{2\pi} \left[\frac{d^3 p}{(2\pi)^3 2E_p} \frac{d^3 p_1}{(2\pi)^3 2E_1} (2\pi)^4 \delta^4(P - p_1 - p) \right] \\ &\times \left[\frac{d^3 p_2}{(2\pi)^3 2E_2} \frac{d^3 p_3}{(2\pi)^3 2E_3} (2\pi)^4 \delta^4(p - p_2 - p_3) \right] |\mathcal{M}|^2 \\ &= \int \frac{1}{2M_N} \frac{1}{(2\pi)^5} ds [d_2(P \rightarrow p_1, p) \times d_2(p \rightarrow p_2, p_3)] |\mathcal{M}|^2, \end{aligned} \quad (\text{C.3})$$

where d_2 represents the two body phase space factor and is given by

$$d_2(A \rightarrow B, C) = \frac{\pi}{2M_A^2} \lambda^{1/2}(M_A^2, M_B^2, M_C^2) \frac{d\Omega}{4\pi}, \quad (\text{C.4})$$

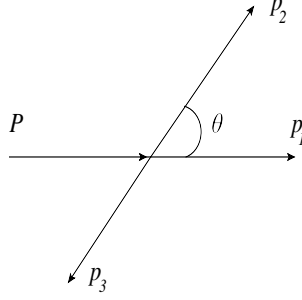


Figure C.1: Momentum configuration of N^- decay in ℓ, ν_ℓ COM frame.

with $\lambda(a, b, c) = a^2 + b^2 + c^2 - 2ab - 2bc - 2ca$. Now using the above expression in eq. C.3, we get

$$\begin{aligned} \Gamma &= \int \frac{1}{2M_N} \frac{ds}{(2\pi)^5} \frac{\pi}{2M_N^2} \lambda^{1/2}(M_N^2, m_1^2, s) \frac{d\Omega}{4\pi} \\ &\times \frac{\pi}{2s} \lambda^{1/2}(s, m_2^2, m_3^2) \frac{d\Omega}{4\pi} |\mathcal{M}|^2 \\ &= \int \frac{1}{2^8 M_N^3 \pi^3 s} \lambda^{1/2}(M_N^2, m_1^2, s) \times \lambda^{1/2}(s, m_2^2, m_3^2) \frac{1}{4\pi} \times 2\pi d\cos\theta |\mathcal{M}|^2 \end{aligned} \quad (\text{C.5})$$

or,

$$\frac{d\Gamma}{ds d\cos\theta} = \frac{1}{2^9 M_N^3 \pi^3 s} \lambda^{1/2}(M_N^2, m_1^2, s) \times \lambda^{1/2}(s, m_2^2, m_3^2) |\mathcal{M}|^2. \quad (\text{C.6})$$

This is the basic equation for decay width. Now we will calculate the $|\mathcal{M}|^2$ for the process

$$N^-(P) \rightarrow N^0(p_1) l^-(p_2) \nu_l(p_3) \quad (\text{C.7})$$

The amplitude for this process is given by

$$\begin{aligned} i\mathcal{M} &= \frac{ig \sin\theta}{\sqrt{2}} [\bar{v}(p_1) \gamma^\mu u(P)] \left(\frac{-ig_{\mu\nu}}{q^2 - M_W^2 + i\epsilon} \right) \frac{ig}{2\sqrt{2}} [\bar{u}(p_3) \gamma^\nu P_L v(p_2)] \\ &= i \frac{g^2 \sin\theta}{4(q^2 - M_W^2 + i\epsilon)} [\bar{v}(p_1) \gamma^\mu u(P)] [\bar{u}(p_3) \gamma^\nu P_L v(p_2)]. \end{aligned} \quad (\text{C.8})$$

Considering the two spin states of N^- , doing a spin sum of the spinors and squaring the amplitude, we get

$$|\mathcal{M}|^2 = \frac{g^4 \sin^2\theta}{32(q^2 - M_W^2 + i\epsilon)^2} \text{Tr}[(\not{P} - M_1) \gamma^\mu (\not{P} + M_N) \gamma^\nu] \text{Tr}[(\not{p}_3 + m_3) \gamma_\mu P_L (\not{p}_2 - m_2) \gamma_\nu P_L] \quad (\text{C.9})$$

After doing a little algebra with the trace we end up with the expression

$$|\mathcal{M}|^2 = \frac{g^4 \sin^2\theta}{(q^2 - M_W^2 + i\epsilon)^2} \times 2[(p_1 \cdot p_3)(p_2 \cdot P) + (p_1 \cdot p_2)(p_3 \cdot P) + M_1 M_N (p_3 \cdot p_2)] \quad (\text{C.10})$$

To calculate various products of momenta, we choose the center of mass frame of l^- and ν_l (see fig. C.1).

$$P = (E, 0, 0, \vec{p})$$

$$\begin{aligned}
p_1 &= (E_1, 0, 0, \vec{p}) \\
p_2 &= (E_2, 0, 0, \vec{p}') \\
p_3 &= (E_3, 0, 0, -\vec{p}')
\end{aligned}$$

and

$$s = (p_2 + p_3)^2 = (P - p_1)^2, \text{ hence}$$

$$s_{min} = (m_3 + m_2)^2, \quad s_{max} = (M_N - M_1)^2.$$

Now the products of momenta are given as

$$\begin{aligned}
P \cdot p_2 &= EE_2 - |\vec{p}'||\vec{p}'| \cos \theta \\
p_1 \cdot p_3 &= E_1 E_3 + |\vec{p}'||\vec{p}'| \cos \theta \\
p_1 \cdot p_2 &= E_1 E_2 - |\vec{p}'||\vec{p}'| \cos \theta \\
P \cdot p_3 &= EE_3 + |\vec{p}'||\vec{p}'| \cos \theta \\
p_2 \cdot p_3 &= \frac{s - m_2^2 - m_3^2}{2}.
\end{aligned} \tag{C.11}$$

The energy and momenta can be expressed in terms of masses and s like

$$\begin{aligned}
E &= \frac{M_N^2 - M_1^2 + s}{2\sqrt{s}} \\
E_1 &= \frac{M_N^2 - M_1^2 - s}{2\sqrt{s}} \\
E_2 &= \frac{s + m_2^2 - m_3^2}{2\sqrt{s}} \\
E_3 &= \frac{s + m_3^2 - m_2^2}{2\sqrt{s}} \\
|\vec{p}| &= \frac{1}{2\sqrt{s}} \lambda^{1/2}(M_N^2, M_1^2, s) \\
|\vec{p}'| &= \frac{1}{2\sqrt{s}} \lambda^{1/2}(s, m_2^2, m_3^2)
\end{aligned} \tag{C.12}$$

We use these relations in $|\mathcal{M}|^2$,

$$\begin{aligned}
|\mathcal{M}|^2 &= \frac{g^4 \sin^2 \theta}{(s - M_W^2 + i\epsilon)^2} \times 2 \left[\left((E_1 E_3 + |\vec{p}'||\vec{p}'| \cos \theta)(EE_2 - |\vec{p}'||\vec{p}'| \cos \theta) \right) \right. \\
&\quad \left. + (E_1 E_2 - |\vec{p}'||\vec{p}'| \cos \theta)(EE_3 + |\vec{p}'||\vec{p}'| \cos \theta) + M_1 M_N \left(\frac{s - m_2^2 - m_3^2}{2} \right) \right]
\end{aligned}$$

Doing a $d \cos \theta$ integration eq C.6 becomes

$$\begin{aligned}
\frac{d\Gamma}{ds} &= \frac{1}{2^9 M_N^3 \pi^3 s} \lambda^{1/2}(M_N^2, m_1^2, s) \times \lambda^{1/2}(s, m_2^2, m_3^2) \times \frac{g^4 \sin^2 \theta}{(s - M_W^2 + i\epsilon)^2} \\
&\quad \left[4EE_1 E_2 E_3 - \frac{4}{3} |\vec{p}'|^2 |\vec{p}'|^2 + M_N M_1 (s - m_2^2 - m_3^2) \right]
\end{aligned} \tag{C.13}$$

Now we will put the neutrino mass to be zero *i.e* $m_2 = 0$, and $m_3 = m_\ell$. Again in the limit of small momentum transfer, the denominator of the propagator $\rightarrow M_W^4$ and hence we can approximate it to Fermi constant with the usual relation $\frac{G_F}{\sqrt{2}} = \frac{g^2}{8M_W^2}$. The ds integration is performed using

Mathematica and after a little lengthy algebra, we get the final result

$$\Gamma = \frac{G_F^2 \sin^2 \theta}{24\pi^3} M_N^5 I \quad (\text{C.14})$$

where G_F is the Fermi coupling constant and I is given as:

$$I = \frac{1}{4} \lambda^{1/2} (1, a^2, b^2) F_1(a, b) + 6F_2(a, b) \ln \left(\frac{2a}{1 + a^2 - b^2 - \lambda^{1/2}(1, a^2, b^2)} \right). \quad (\text{C.15})$$

In the above Equation $F_1(a, b)$ and $F_2(a, b)$ are two polynomials of $a = M_1/M_N$ and $b = m_\ell/M_N$, where m_ℓ is the charged lepton mass. Upto $\mathcal{O}(b^2)$, these two polynomials are given by

$$\begin{aligned} F_1(a, b) &= (a^6 - 2a^5 - 7a^4(1 + b^2) + 10a^3(b^2 - 2) + a^2(12b^2 - 7) + (3b^2 - 1)) \\ F_2(a, b) &= (a^5 + a^4 + a^3(1 - 2b^2)). \end{aligned} \quad (\text{C.16})$$

Appendix D

Calculation of $Z - Z'$ mixing

The loop factor is given as

$$\begin{aligned}
i\Pi^{\mu\nu} &= -1 \int \frac{d^4k}{(2\pi)^4} Tr \left[(ig_{\mu\tau})\gamma^\mu \frac{i(\not{k} + m_f)}{k^2 - m_f^2 + i\epsilon} \left(i\frac{g}{2\cos\theta_W} \right) \gamma^\nu (C_V - C_A\gamma^5) \frac{i(\not{k} + \not{q} + m_f)}{(k+q)^2 - m_f^2 + i\epsilon} \right] \\
&= -\frac{g_{\mu\tau}g}{2\cos\theta_W} \int \frac{d^4k}{(2\pi)^4} \frac{1}{k^2 - m_f^2 + i\epsilon} \frac{1}{(k+q)^2 - m_f^2 + i\epsilon} \\
&\quad Tr [\gamma^\mu (\not{k} + m_f) \gamma^\nu (C_V - C_A\gamma^5) (\not{k} + \not{q} + m_f)] \\
&= -\frac{g_{\mu\tau}g}{2\cos\theta_W} \int \frac{d^4k}{(2\pi)^4} \frac{1}{D} N^{\mu\nu}, \tag{D.1}
\end{aligned}$$

Where $\frac{1}{D} = \frac{1}{k^2 - m_f^2 + i\epsilon} \frac{1}{(k+q)^2 - m_f^2 + i\epsilon}$ and $N^{\mu\nu}$ we will evaluate now

$$\begin{aligned}
N^{\mu\nu} &= Tr [\gamma^\mu (\not{k} + m_f) \gamma^\nu (C_V - C_A\gamma^5) (\not{k} + \not{q} + m_f)] \\
&= Tr [\gamma^\mu \not{k} \gamma^\nu (C_V - C_A\gamma^5) (\not{k} + \not{q})] + Tr [\gamma^\mu m_f \gamma^\nu (C_V - C_A\gamma^5) m_f] \\
&= C_V Tr [\gamma^\mu \not{k} \gamma^\nu \not{k} + \gamma^\mu \not{k} \gamma^\nu \not{q}] - C_A Tr [\gamma^\mu \not{k} \gamma^\nu \gamma^5 \not{k} + \gamma^\mu \not{k} \gamma^\nu \gamma^5 \not{q}] + C_V m_f^2 Tr [\gamma^\mu \gamma^\nu] \\
&= 4[(k^\mu k^\nu - k^2 g^{\mu\nu} + k^\nu k^\mu) + (k^\mu q^\nu - k_\rho q^\rho g^{\mu\nu} + k^\nu q^\mu)] \\
&\quad - 4C_A \varepsilon^{\rho\mu\sigma\nu} q_\rho k_\sigma + 4m_f^2 C_V g^{\mu\nu} \tag{D.2}
\end{aligned}$$

Now for the denominator part we have to use the Feynmann parameterization formulae :

$$\frac{1}{AB} = \int_0^1 dx \frac{1}{[xA + (1-x)B]^2} \tag{D.3}$$

Now

$$\begin{aligned}
\frac{1}{D} &= \int_0^1 dx \frac{1}{[(k^2 - m_f^2)(1-x) + ((k+q)^2 - m_f^2)x]^2} \\
&= \int_0^1 dx \frac{1}{[(k^2 - m_f^2)(1-x) + (k^2 + q^2 + 2k \cdot q - m_f^2)x]^2} \\
&= \int_0^1 dx \frac{1}{[k^2 + 2xk \cdot q + xq^2 - m_f^2]^2} \\
&= \int_0^1 dx \frac{1}{[l^2 - \Delta]^2} \tag{D.4}
\end{aligned}$$

where $l = k + xq$ and $\Delta = -x(1-x)q^2 + m_f^2$. Now we will change also the variable in numerator $N^{\mu\nu}$ to l .

$$N^{\mu\nu} = 4C_V \left[\left(\frac{2}{d} - 1\right) l^2 g^{\mu\nu} + 2x(x-1)q^\mu q^\nu - (x^2q^2 - xq^2 - m_f^2)g^{\mu\nu} \right] \tag{D.5}$$

In the expression above we have used $l^\mu l^\nu \rightarrow \frac{1}{d} l^2 g^{\mu\nu}$ with dimension of space is d . We have neglected the term containing antisymmetric tensor ε in the eq. D.2 for symmetric arguments since it contains terms linear in l^μ . The Feynmann integrals involving four momenta integration are :

$$\int \frac{d^d l}{(2\pi)^d} \frac{l^2}{(l^2 - \Delta)^2} = \frac{-i}{(4\pi)^{d/2}} \frac{d}{2} \frac{\Gamma(1 - \frac{d}{2})}{\Gamma(2)} \left(\frac{1}{\Delta}\right)^{1-d/2} \tag{D.6}$$

$$\int \frac{d^d l}{(2\pi)^d} \frac{1}{(l^2 - \Delta)^2} = \frac{i}{(4\pi)^{d/2}} \frac{d}{2} \frac{\Gamma(2 - \frac{d}{2})}{\Gamma(2)} \left(\frac{1}{\Delta}\right)^{2-d/2} \tag{D.7}$$

Using these integrals and after a bit algebraic manipulations we will end up with the expression

$$i\Pi^{\mu\nu} = -i \frac{g_{\mu\tau} g}{2 \cos \theta_W} 4C_V \int_0^1 dx \frac{1}{(4\pi)^{d/2}} \frac{\Gamma(2 - \frac{d}{2})}{\Delta^{2-d/2}} \times [-g^{\mu\nu}(x^2q^2 - xq^2 - m_f^2) + 2x(x-1)q^\mu q^\nu - \Delta g^{\mu\nu}] \tag{D.8}$$

Using the expression for Δ , the equation above can be rewritten as.

$$\begin{aligned}
i\Pi^{\mu\nu} &= -i \frac{g_{\mu\tau} g}{2 \cos \theta_W} 4C_V \int_0^1 dx \frac{1}{(4\pi)^{d/2}} \frac{\Gamma(2 - \frac{d}{2})}{\Delta^{2-d/2}} \\
&\quad \times [-g^{\mu\nu}(x^2q^2 - xq^2 - m_f^2 + x^2q^2 - xq^2 + m_f^2) + 2x(x-1)q^\mu q^\nu] \\
&= -i \frac{g_{\mu\tau} g}{2 \cos \theta_W} 4C_V \int_0^1 dx \frac{1}{(4\pi)^{d/2}} \frac{\Gamma(2 - \frac{d}{2})}{\Delta^{2-d/2}} \\
&\quad [g^{\mu\nu} 2x(x-1)q^2 - 2x(1-x)q^\mu q^\nu] \\
&= (q^2 g^{\mu\nu} - q^\mu q^\nu) \pi_2(q^2) \tag{D.9}
\end{aligned}$$

where

$$\pi_2(q^2) = -i \frac{g_{\mu\tau} g}{2 \cos \theta_W} 4C_V 2 \int_0^1 dx x(1-x) \frac{1}{(4\pi)^{d/2}} \frac{\Gamma(2 - \frac{d}{2})}{\Delta^{2-d/2}} \tag{D.10}$$

Using $\overline{\text{MS}}$ scheme, we can use

$$\frac{1}{(4\pi)^{d/2}} \frac{\Gamma(2 - \frac{d}{2})}{\Delta^{2-d/2}} \rightarrow \frac{1}{(4\pi)^2} \left[-\text{Log} \left(\frac{\Delta}{\Lambda^2} \right) \right] \quad (\text{D.11})$$

where Λ is the cutoff scale having mass dimension 1. Using the above formula in Eq. D.10

$$\begin{aligned} \pi_2(q^2) &= -i \frac{g_{\mu\tau} g}{2 \cos \theta_W} 8C_V \int_0^1 dx x(1-x) \frac{1}{(4\pi)^2} \left[-\text{Log} \left(\frac{\Delta}{\Lambda} \right) \right] \\ &= -i \frac{g_{\mu\tau} g}{2 \cos \theta_W} 8C_V \frac{1}{(4\pi)^2} \int_0^1 dx x(1-x) \text{Log} \left(\frac{-x(1-x)q^2 + m_f^2}{\Lambda^2} \right) \end{aligned} \quad (\text{D.12})$$

In the limit $q \rightarrow 0$, the above equation becomes

$$\begin{aligned} \pi_2(q^2) &= -i \frac{g_{\mu\tau} g}{2 \cos \theta_W} 8C_V \frac{1}{6} \text{Log} \left(\frac{m_f^2}{\Lambda^2} \right) \\ &= -i \frac{g_{\mu\tau} g}{2 \cos \theta_W} C_V \frac{4}{3} \text{Log} \left(\frac{m_f^2}{\Lambda^2} \right) \end{aligned} \quad (\text{D.13})$$

List of Publications

1. Sudhanwa Patra, **Nirakar Sahoo**, and Narendra Sahu, "*Dipolar dark matter in light of the 3.5 keV X-ray line, neutrino mass, and LUX data*", [Phys.Rev.D91, \(2015\) 115013](#), arXiv:1412.4253.
2. Subhaditya Bhattacharya, **Nirakar Sahoo**, and Narendra Sahu, "*Minimal Vector-like leptonic Dark Matter and Signatures at the LHC*", [Phys.Rev.D93,\(2016\), 115040](#), arXiv:1510.02760.
3. Subhaditya Bhattacharya, Sudhanwa Patra, **Nirakar Sahoo** and Narendra Sahu, "*750 GeV Di-Photon Excess at CERN LHC from a Dark Sector Assisted Scalar Decay*", [Journal of Cosmology and Astroparticle Physics, Volume 2016, June 2016](#), arXiv:1601.01569.
4. Sudhanwa Patra, Soumya Rao, **Nirakar Sahoo** and Narendra Sahu, "*Gauged $U(1)_{L_\mu-L_\tau}$ model in light of muon $g-2$ anomaly, neutrino mass and dark matter phenomenology*", [Nuclear Physics B, Vol 917, 2017](#), arXiv:1607.04046.
5. Subhaditya Bhattacharya, **Nirakar Sahoo**, and Narendra Sahu, "*Singlet-Doublet Fermionic Dark Matter, Neutrino Mass and Collider Signatures*", [Phys.Rev.D96, \(2017\), 035010](#), arXiv:1704.03417.

References

- [1] R. Barbieri, A. Pomarol, R. Rattazzi, and A. Strumia. Electroweak symmetry breaking after LEP-1 and LEP-2. *Nucl. Phys.* **B703**, (2004) 127-146.
- [2] L. Accardo et al. High Statistics Measurement of the Positron Fraction in Primary Cosmic Rays of 0.5500 GeV with the Alpha Magnetic Spectrometer on the International Space Station. *Phys. Rev. Lett.* **113**, (2014) 121101.
- [3] G. Jungman, M. Kamionkowski, and K. Griest. Supersymmetric dark matter. *Phys. Rept.* **267**, (1996) 195-373.
- [4] D. Clowe, M. Bradac, A. H. Gonzalez, M. Markevitch, S. W. Randall, C. Jones, and D. Zaritsky. A direct empirical proof of the existence of dark matter. *Astrophys. J.* **648**, (2006) L109-L113.
- [5] N. Aghanim et al. Planck 2015 results. XI. CMB power spectra, likelihoods, and robustness of parameters. *Astron. Astrophys.* **594**, (2016) A11.
- [6] D. S. Akerib et al. Results from a search for dark matter in the complete LUX exposure. *Phys. Rev. Lett.* **118**, (2017) 021303.
- [7] E. Bulbul, M. Markevitch, A. Foster, R. K. Smith, M. Loewenstein, and S. W. Randall. Detection of An Unidentified Emission

- Line in the Stacked X-ray spectrum of Galaxy Clusters. *Astrophys. J.* **789**, (2014) 13.
- [8] W. Altmannshofer, S. Gori, M. Pospelov, and I. Yavin. Neutrino Trident Production: A Powerful Probe of New Physics with Neutrino Beams. *Phys. Rev. Lett.* **113**, (2014) 091801.
- [9] P. A. R. Ade et al. Planck 2013 results. XVI. Cosmological parameters. *Astron. Astrophys.* **571**, (2014) A16.
- [10] G. Hinshaw et al. Nine-Year Wilkinson Microwave Anisotropy Probe (WMAP) Observations: Cosmological Parameter Results. *Astrophys. J. Suppl.* **208**, (2013) 19.
- [11] E. W. Kolb and M. S. Turner. The Early Universe. *Front. Phys.* **69**, (1990) 1-547.
- [12] E. Aprile et al. Dark Matter Results from 225 Live Days of XENON100 Data. *Phys. Rev. Lett.* **109**, (2012) 181301.
- [13] P. Agnes et al. Results from the first use of low radioactivity argon in a dark matter search. *Phys. Rev.* **D93**, (2016) 081101. [Addendum: *Phys. Rev.*D95,no.6,069901(2017)].
- [14] A. Tan et al. Dark Matter Results from First 98.7 Days of Data from the PandaX-II Experiment. *Phys. Rev. Lett.* **117**, (2016) 121303.
- [15] M. Aguilar et al. First Result from the Alpha Magnetic Spectrometer on the International Space Station: Precision Measurement of the Positron Fraction in Primary Cosmic Rays of 0.5350 GeV. *Phys. Rev. Lett.* **110**, (2013) 141102.
- [16] O. Adriani et al. An anomalous positron abundance in cosmic rays with energies 1.5-100 GeV. *Nature* **458**, (2009) 607-609.

- [17] O. Adriani et al. A statistical procedure for the identification of positrons in the PAMELA experiment. *Astropart. Phys.* **34**, (2010) 1-11.
- [18] S. Fukuda et al. Constraints on neutrino oscillations using 1258 days of Super-Kamiokande solar neutrino data. *Phys. Rev. Lett.* **86**, (2001) 5656-5660.
- [19] Q. R. Ahmad et al. Direct evidence for neutrino flavor transformation from neutral current interactions in the Sudbury Neutrino Observatory. *Phys. Rev. Lett.* **89**, (2002) 011301.
- [20] J. N. Bahcall and C. Pena-Garay. Solar models and solar neutrino oscillations. *New J. Phys.* **6**, (2004) 63.
- [21] K. Abe et al. Indication of Electron Neutrino Appearance from an Accelerator-produced Off-axis Muon Neutrino Beam. *Phys. Rev. Lett.* **107**, (2011) 041801.
- [22] P. Adamson et al. Improved search for muon-neutrino to electron-neutrino oscillations in MINOS. *Phys. Rev. Lett.* **107**, (2011) 181802.
- [23] Y. Abe et al. Indication of Reactor $\bar{\nu}_e$ Disappearance in the Double Chooz Experiment. *Phys. Rev. Lett.* **108**, (2012) 131801.
- [24] F. P. An et al. Observation of electron-antineutrino disappearance at Daya Bay. *Phys. Rev. Lett.* **108**, (2012) 171803.
- [25] J. K. Ahn et al. Observation of Reactor Electron Antineutrino Disappearance in the RENO Experiment. *Phys. Rev. Lett.* **108**, (2012) 191802.
- [26] Q. R. Ahmad et al. Measurement of day and night neutrino energy spectra at SNO and constraints on neutrino mixing parameters. *Phys. Rev. Lett.* **89**, (2002) 011302.

- [27] S. Weinberg. Baryon and Lepton Nonconserving Processes. *Phys. Rev. Lett.* **43**, (1979) 1566-1570.
- [28] G. W. Bennett et al. Final Report of the Muon E821 Anomalous Magnetic Moment Measurement at BNL. *Phys. Rev.* **D73**, (2006) 072003.
- [29] J. P. Miller, E. de Rafael, and B. L. Roberts. Muon (g-2): Experiment and theory. *Rept. Prog. Phys.* **70**, (2007) 795.
- [30] A. Boyarsky, O. Ruchayskiy, D. Iakubovskyi, and J. Franse. Unidentified Line in X-Ray Spectra of the Andromeda Galaxy and Perseus Galaxy Cluster. *Phys. Rev. Lett.* **113**, (2014) 251301.
- [31] K. N. Abazajian. Resonantly Produced 7 keV Sterile Neutrino Dark Matter Models and the Properties of Milky Way Satellites. *Phys. Rev. Lett.* **112**, (2014) 161303.
- [32] S. Baek and H. Okada. 7 keV Dark Matter as X-ray Line Signal in Radiative Neutrino Model. *arXiv* 1403.1710.
- [33] B. Shuve and I. Yavin. Dark matter progenitor: Light vector boson decay into sterile neutrinos. *Phys. Rev.* **D89**, (2014) 113004.
- [34] T. Tsuyuki. Neutrino masses, leptogenesis, and sterile neutrino dark matter. *Phys. Rev.* **D90**, (2014) 013007.
- [35] F. Bezrukov and D. Gorbunov. Relic Gravity Waves and 7 keV Dark Matter from a GeV scale inflaton. *Phys. Lett.* **B736**, (2014) 494-498.
- [36] K. P. Modak. 3.5 keV X-ray Line Signal from Decay of Right-Handed Neutrino due to Transition Magnetic Moment. *JHEP* **03**, (2015) 064.

- [37] D. J. Robinson and Y. Tsai. Dynamical framework for KeV Dirac neutrino warm dark matter. *Phys. Rev.* **D90**, (2014) 045030.
- [38] S. Chakraborty, D. K. Ghosh, and S. Roy. 7 keV Sterile neutrino dark matter in $U(1)_{R-}$ lepton number model. *JHEP* **10**, (2014) 146.
- [39] A. Abada, G. Arcadi, and M. Lucente. Dark Matter in the minimal Inverse Seesaw mechanism. *JCAP* **1410**, (2014) 001.
- [40] R. Krall, M. Reece, and T. Roxlo. Effective field theory and keV lines from dark matter. *JCAP* **1409**, (2014) 007.
- [41] H. Ishida, K. S. Jeong, and F. Takahashi. 7 keV sterile neutrino dark matter from split flavor mechanism. *Phys. Lett.* **B732**, (2014) 196-200.
- [42] S. Patra and P. Pritimita. 7 keV sterile neutrino Dark Matter in extended seesaw framework. *arXiv* 1409.3656.
- [43] D. P. Finkbeiner and N. Weiner. X-ray line from exciting dark matter. *Phys. Rev.* **D94**, (2016) 083002.
- [44] C. El Aisati, T. Hambye, and T. Scarn. Can a millicharged dark matter particle emit an observable gamma-ray line? *JHEP* **08**, (2014) 133.
- [45] M. T. Frandsen, F. Sannino, I. M. Shoemaker, and O. Svendsen. X-ray Lines from Dark Matter: The Good, The Bad, and The Unlikely. *JCAP* **1405**, (2014) 033.
- [46] R. Allahverdi, B. Dutta, and Y. Gao. keV Photon Emission from Light Nonthermal Dark Matter. *Phys. Rev.* **D89**, (2014) 127305.

- [47] J. M. Cline, Y. Farzan, Z. Liu, G. D. Moore, and W. Xue. 3.5 keV x rays as the 21 cm line of dark atoms, and a link to light sterile neutrinos. *Phys. Rev.* **D89**, (2014) 121302.
- [48] H. Okada and T. Toma. 3.55 keV X-ray Line Signal from Excited Dark Matter in Radiative Neutrino Model. *Phys. Lett.* **B737**, (2014) 162-166.
- [49] H. M. Lee. Magnetic dark matter for the X-ray line at 3.55 keV. *Phys. Lett.* **B738**, (2014) 118-122.
- [50] T. Higaki, K. S. Jeong, and F. Takahashi. The 7 keV axion dark matter and the X-ray line signal. *Phys. Lett.* **B733**, (2014) 25-31.
- [51] J. Jaeckel, J. Redondo, and A. Ringwald. 3.55 keV hint for decaying axionlike particle dark matter. *Phys. Rev.* **D89**, (2014) 103511.
- [52] H. M. Lee, S. C. Park, and W.-I. Park. Cluster X-ray line at 3.5 keV from axion-like dark matter. *Eur. Phys. J.* **C74**, (2014) 3062.
- [53] M. Cicoli, J. P. Conlon, M. C. D. Marsh, and M. Rummel. 3.55 keV photon line and its morphology from a 3.55 keV axionlike particle line. *Phys. Rev.* **D90**, (2014) 023540.
- [54] A. G. Dias, A. C. B. Machado, C. C. Nishi, A. Ringwald, and P. Vaudrevange. The Quest for an Intermediate-Scale Accidental Axion and Further ALPs. *JHEP* **06**, (2014) 037.
- [55] J. P. Conlon and F. V. Day. 3.55 keV photon lines from axion to photon conversion in the Milky Way and M31. *JCAP* **1411**, (2014) 033.
- [56] J.-C. Park, S. C. Park, and K. Kong. X-ray line signal from 7 keV axino dark matter decay. *Phys. Lett.* **B733**, (2014) 217-220.

- [57] K.-Y. Choi and O. Seto. X-ray line signal from decaying axino warm dark matter. *Phys. Lett.* **B735**, (2014) 92-94.
- [58] S. P. Liew. Axino dark matter in light of an anomalous X-ray line. *JCAP* **1405**, (2014) 044.
- [59] C. Kolda and J. Unwin. X-ray lines from R-parity violating decays of keV sparticles. *Phys. Rev.* **D90**, (2014) 023535.
- [60] N. E. Bomark and L. Roszkowski. 3.5 keV x-ray line from decaying gravitino dark matter. *Phys. Rev.* **D90**, (2014) 011701.
- [61] S. V. Demidov and D. S. Gorbunov. SUSY in the sky or a keV signature of sub-GeV gravitino dark matter. *Phys. Rev.* **D90**, (2014) 035014.
- [62] K. Nakayama, F. Takahashi, and T. T. Yanagida. The 3.5 keV X-ray line signal from decaying moduli with low cutoff scale. *Phys. Lett.* **B735**, (2014) 338-339.
- [63] K. Nakayama, F. Takahashi, and T. T. Yanagida. Anomaly-free flavor models for NambuGoldstone bosons and the 3.5keV X-ray line signal. *Phys. Lett.* **B734**, (2014) 178-182.
- [64] F. S. Queiroz and K. Sinha. The Poker Face of the Majoron Dark Matter Model: LUX to keV Line. *Phys. Lett.* **B735**, (2014) 69-74.
- [65] E. Dudas, L. Heurtier, and Y. Mambrini. Generating X-ray lines from annihilating dark matter. *Phys. Rev.* **D90**, (2014) 035002.
- [66] K. S. Babu and R. N. Mohapatra. 7 keV Scalar Dark Matter and the Anomalous Galactic X-ray Spectrum. *Phys. Rev.* **D89**, (2014) 115011.

- [67] Y. Farzan and A. R. Akbarieh. Decaying Vector Dark Matter as an Explanation for the 3.5 keV Line from Galaxy Clusters. *JCAP* **1411**, (2014) 015.
- [68] A. Abada, V. De Romeri, and A. M. Teixeira. Effect of sterile states on lepton magnetic moments and neutrinoless double beta decay. *JHEP* **09**, (2014) 074.
- [69] Z. Kang, P. Ko, T. Li, and Y. Liu. Natural X-ray Lines from the Low Scale Supersymmetry Breaking. *Phys. Lett.* **B742**, (2015) 249-255.
- [70] A. Boyarsky, O. Ruchayskiy, and M. Shaposhnikov. The Role of sterile neutrinos in cosmology and astrophysics. *Ann. Rev. Nucl. Part. Sci.* **59**, (2009) 191-214.
- [71] A. Kusenko. Sterile neutrinos: The Dark side of the light fermions. *Phys. Rept.* **481**, (2009) 1-28.
- [72] A. Adulpravitchai and M. A. Schmidt. A Fresh Look at keV Sterile Neutrino Dark Matter from Frozen-In Scalars. *JHEP* **01**, (2015) 006.
- [73] J. M. Cline and A. R. Frey. Consistency of dark matter interpretations of the 3.5 keV x-ray line. *Phys. Rev.* **D90**, (2014) 123537.
- [74] J. Beringer et al. Review of Particle Physics (RPP). *Phys. Rev.* **D86**, (2012) 010001.
- [75] E. Ma. Verifiable radiative seesaw mechanism of neutrino mass and dark matter. *Phys. Rev.* **D73**, (2006) 077301.
- [76] E. Masso, S. Mohanty, and S. Rao. Dipolar Dark Matter. *Phys. Rev.* **D80**, (2009) 036009.

- [77] K. Griest and D. Seckel. Three exceptions in the calculation of relic abundances. *Phys. Rev.* **D43**, (1991) 3191-3203.
- [78] A. Chatterjee and N. Sahu. Resurrecting L-type sneutrino dark matter in light of neutrino masses and LUX data. *Phys. Rev.* **D90**, (2014) 095021.
- [79] J. Giedt, A. W. Thomas, and R. D. Young. Dark matter, the CMSSM and lattice QCD. *Phys. Rev. Lett.* **103**, (2009) 201802.
- [80] Y. Mambrini. Higgs searches and singlet scalar dark matter: Combined constraints from XENON 100 and the LHC. *Phys. Rev.* **D84**, (2011) 115017.
- [81] T. Li, S. Miao, and Y.-F. Zhou. Light mediators in dark matter direct detections. *Journal of Cosmology and Astroparticle Physics* **2015**, (2015) 032.
- [82] M. Cirelli, N. Fornengo, and A. Strumia. Minimal dark matter. *Nucl. Phys.* **B753**, (2006) 178-194.
- [83] Y. G. Kim, K. Y. Lee, and S. Shin. Singlet fermionic dark matter. *JHEP* **05**, (2008) 100.
- [84] C. Arina, J.-O. Gong, and N. Sahu. Unifying darko-lepto-genesis with scalar triplet inflation. *Nucl. Phys.* **B865**, (2012) 430-460.
- [85] C. Arina and N. Sahu. Asymmetric Inelastic Inert Doublet Dark Matter from Triplet Scalar Leptogenesis. *Nucl. Phys.* **B854**, (2012) 666-699.
- [86] N. Arkani-Hamed, S. Dimopoulos, and S. Kachru. Predictive landscapes and new physics at a TeV. *hep-th/* 0501082.
- [87] R. Mahbubani and L. Senatore. The Minimal model for dark matter and unification. *Phys. Rev.* **D73**, (2006) 043510.

- [88] F. D’Eramo. Dark matter and Higgs boson physics. *Phys. Rev.* **D76**, (2007) 083522.
- [89] R. Enberg, P. J. Fox, L. J. Hall, A. Y. Papaioannou, and M. Papucci. LHC and dark matter signals of improved naturalness. *JHEP* **11**, (2007) 014.
- [90] G. Cynolter and E. Lendvai. Electroweak Precision Constraints on Vector-like Fermions. *Eur. Phys. J.* **C58**, (2008) 463-469.
- [91] T. Cohen, J. Kearney, A. Pierce, and D. Tucker-Smith. Singlet-Doublet Dark Matter. *Phys. Rev.* **D85**, (2012) 075003.
- [92] C. Cheung and D. Sanford. Simplified Models of Mixed Dark Matter. *JCAP* **1402**, (2014) 011.
- [93] D. Restrepo, A. Rivera, M. Sanchez-Pelez, O. Zapata, and W. Tangarife. Radiative Neutrino Masses in the Singlet-Doublet Fermion Dark Matter Model with Scalar Singlets. *Phys. Rev.* **D92**, (2015) 013005.
- [94] L. Calibbi, A. Mariotti, and P. Tziveloglou. Singlet-Doublet Model: Dark matter searches and LHC constraints. *JHEP* **10**, (2015) 116.
- [95] G. Cynolter, J. Kovcs, and E. Lendvai. Doubletsinglet model and unitarity. *Mod. Phys. Lett.* **A31**, (2016) 1650013.
- [96] A. Freitas, S. Westhoff, and J. Zupan. Integrating in the Higgs Portal to Fermion Dark Matter. *JHEP* **09**, (2015) 015.
- [97] N. Bizot and M. Frigerio. Fermionic extensions of the Standard Model in light of the Higgs couplings. *JHEP* **01**, (2016) 036.

- [98] S. Bhattacharya, B. Karmakar, N. Sahu, and A. Sil. Flavor origin of dark matter and its relation with leptonic nonzero θ_{13} and Dirac CP phase δ . *JHEP* **05**, (2017) 068.
- [99] S. Bhattacharya, B. Karmakar, N. Sahu, and A. Sil. Unifying the flavor origin of dark matter with leptonic nonzero θ_{13} . *Phys. Rev.* **D93**, (2016) 115041.
- [100] S. Bhattacharya, S. Jana, and S. Nandi. Neutrino Masses and Scalar Singlet Dark Matter. *Phys. Rev.* **D95**, (2017) 055003.
- [101] N. Sahu and U. Sarkar. Predictive model for dark matter, dark energy, neutrino masses and leptogenesis at the TeV scale. *Phys. Rev.* **D76**, (2007) 045014.
- [102] J. McDonald, N. Sahu, and U. Sarkar. Type-II Seesaw at Collider, Lepton Asymmetry and Singlet Scalar Dark Matter. *JCAP* **0804**, (2008) 037.
- [103] N. Sahu and U. Sarkar. Extended Zee model for Neutrino Mass, Leptogenesis and Sterile Neutrino like Dark Matter. *Phys. Rev.* **D78**, (2008) 115013.
- [104] E. Aprile et al. Physics reach of the XENON1T dark matter experiment. *JCAP* **1604**, (2016) 027.
- [105] B. W. Lee and S. Weinberg. Cosmological Lower Bound on Heavy Neutrino Masses. *Phys. Rev. Lett.* **39**, (1977) 165-168.
- [106] K. A. Olive et al. Review of Particle Physics. *Chin. Phys.* **C38**, (2014) 090001.
- [107] G. Aad et al. Search for invisible decays of a Higgs boson using vector-boson fusion in pp collisions at $\sqrt{s} = 8$ TeV with the ATLAS detector. *JHEP* **01**, (2016) 172.

- [108] S. Baek, P. Ko, and W.-I. Park. Invisible Higgs Decay Width vs. Dark Matter Direct Detection Cross Section in Higgs Portal Dark Matter Models. *Phys. Rev.* **D90**, (2014) 055014.
- [109] A. Djouadi, O. Lebedev, Y. Mambrini, and J. Quevillon. Implications of LHC searches for Higgs–portal dark matter. *Phys. Lett.* **B709**, (2012) 65-69.
- [110] D. S. Akerib et al. First results from the LUX dark matter experiment at the Sanford Underground Research Facility. *Phys. Rev. Lett.* **112**, (2014) 091303.
- [111] M. W. Goodman and E. Witten. Detectability of Certain Dark Matter Candidates. *Phys. Rev.* **D31**, (1985) 3059.
- [112] R. Essig. Direct Detection of Non-Chiral Dark Matter. *Phys. Rev.* **D78**, (2008) 015004.
- [113] R. Koch. A New Determination of the πN Sigma Term Using Hyperbolic Dispersion Relations in the (ν^*2, t) Plane. *Z. Phys.* **C15**, (1982) 161-168.
- [114] J. Gasser, H. Leutwyler, and M. E. Sainio. Form-factor of the sigma term. *Phys. Lett.* **B253**, (1991) 260-264.
- [115] M. M. Pavan, I. I. Strakovsky, R. L. Workman, and R. A. Arndt. The Pion nucleon Sigma term is definitely large: Results from a G.W.U. analysis of pi nucleon scattering data. *PiN Newslett.* **16**, (2002) 110-115.
- [116] A. Bottino, F. Donato, N. Fornengo, and S. Scopel. Interpreting the recent results on direct search for dark matter particles in terms of relic neutralino. *Phys. Rev.* **D78**, (2008) 083520.

- [117] G. Bertone, D. Hooper, and J. Silk. Particle dark matter: Evidence, candidates and constraints. *Phys. Rept.* **405**, (2005) 279-390.
- [118] L. Lavoura and J. P. Silva. The Oblique corrections from vector - like singlet and doublet quarks. *Phys. Rev.* **D47**, (1993) 2046-2057.
- [119] F. del Aguila, J. de Blas, and M. Perez-Victoria. Effects of new leptons in Electroweak Precision Data. *Phys. Rev.* **D78**, (2008) 013010.
- [120] J. Erler and P. Langacker. Precision Constraints on Extra Fermion Generations. *Phys. Rev. Lett.* **105**, (2010) 031801.
- [121] M. E. Peskin and T. Takeuchi. Estimation of oblique electroweak corrections. *Phys. Rev. D* **46**, (1992) 381–409.
- [122] G. Blanger, F. Boudjema, A. Pukhov, and A. Semenov. micrOMEGAs4.1: two dark matter candidates. *Comput. Phys. Commun.* **192**, (2015) 322-329.
- [123] A. Belyaev, N. D. Christensen, and A. Pukhov. CalcHEP 3.4 for collider physics within and beyond the Standard Model. *Comput. Phys. Commun.* **184**, (2013) 1729-1769.
- [124] T. Sjostrand, S. Mrenna, and P. Z. Skands. PYTHIA 6.4 Physics and Manual. *JHEP* **05**, (2006) 026.
- [125] R. Dermisek, J. P. Hall, E. Lunghi, and S. Shin. Limits on Vector-like Leptons from Searches for Anomalous Production of Multi-Lepton Events. *JHEP* **12**, (2014) 013.
- [126] R. Dermisek, E. Lunghi, and S. Shin. Contributions of flavor violating couplings of a Higgs boson to $pp \rightarrow WW$. *JHEP* **08**, (2015) 126.

- [127] R. Dermisek, E. Lunghi, and S. Shin. Two Higgs doublet model with vectorlike leptons and contributions to $pp \rightarrow WW$ and $H \rightarrow WW$. *JHEP* **02**, (2016) 119.
- [128] C. Patrignani et al. Review of Particle Physics. *Chin. Phys.* **C40**, (2016) 100001.
- [129] W.-Y. Keung and W. J. Marciano. HIGGS SCALAR DECAYS: $H \rightarrow W^{+-} X$. *Phys. Rev.* **D30**, (1984) 248.
- [130] M. Magg and C. Wetterich. Neutrino Mass Problem and Gauge Hierarchy. *Phys. Lett.* **94B**, (1980) 61-64.
- [131] G. Lazarides, Q. Shafi, and C. Wetterich. Proton Lifetime and Fermion Masses in an SO(10) Model. *Nucl. Phys.* **B181**, (1981) 287-300.
- [132] R. N. Mohapatra and G. Senjanovic. Neutrino Masses and Mixings in Gauge Models with Spontaneous Parity Violation. *Phys. Rev.* **D23**, (1981) 165.
- [133] E. Ma and U. Sarkar. Neutrino masses and leptogenesis with heavy Higgs triplets. *Phys. Rev. Lett.* **80**, (1998) 5716-5719.
- [134] W. Konetschny and W. Kummer. Nonconservation of Total Lepton Number with Scalar Bosons. *Phys. Lett.* **70B**, (1977) 433-435.
- [135] J. Schechter and J. W. F. Valle. Neutrino Masses in SU(2) x U(1) Theories. *Phys. Rev.* **D22**, (1980) 2227.
- [136] T. P. Cheng and L.-F. Li. Neutrino Masses, Mixings and Oscillations in SU(2) x U(1) Models of Electroweak Interactions. *Phys. Rev.* **D22**, (1980) 2860.

- [137] A. G. Akeroyd, M. Aoki, and H. Sugiyama. Probing Majorana Phases and Neutrino Mass Spectrum in the Higgs Triplet Model at the CERN LHC. *Phys. Rev.* **D77**, (2008) 075010.
- [138] J. Garayoa and T. Schwetz. Neutrino mass hierarchy and Majorana CP phases within the Higgs triplet model at the LHC. *JHEP* **03**, (2008) 009.
- [139] E. J. Chun, K. Y. Lee, and S. C. Park. Testing Higgs triplet model and neutrino mass patterns. *Phys. Lett.* **B566**, (2003) 142-151.
- [140] M. Kadastik, M. Raidal, and L. Rebane. Direct determination of neutrino mass parameters at future colliders. *Phys. Rev.* **D77**, (2008) 115023.
- [141] P. Fileviez Perez, T. Han, G.-y. Huang, T. Li, and K. Wang. Neutrino Masses and the CERN LHC: Testing Type II Seesaw. *Phys. Rev.* **D78**, (2008) 015018.
- [142] S. K. Majee and N. Sahu. Dilepton Signal of a Type-II Seesaw at CERN LHC: Reveals a TeV Scale B-L Symmetry. *Phys. Rev.* **D82**, (2010) 053007.
- [143] C. Arina, R. N. Mohapatra, and N. Sahu. Co-genesis of Matter and Dark Matter with Vector-like Fourth Generation Leptons. *Phys. Lett.* **B720**, (2013) 130-136.
- [144] D. Tucker-Smith and N. Weiner. Inelastic dark matter. *Phys. Rev.* **D64**, (2001) 043502.
- [145] Y. Cui, D. E. Morrissey, D. Poland, and L. Randall. Candidates for Inelastic Dark Matter. *JHEP* **05**, (2009) 076.
- [146] J. Olsen and M. Kado. ATLAS and CMS physics results from Run 2 - 2015. Talks by CERN, December 15. <https://indico.cern.ch/event/442432/> .

- [147] The ATLAS collaboration, Search for resonances decaying to photon pairs in 3.2 fb^{-1} of pp collisions at $\sqrt{s} = 13 \text{ TeV}$ with the ATLAS detector. <https://atlas.web.cern.ch/Atlas/GROUPS/PHYSICS/CONFNOTES/ATLAS-CONF-2015-081/> .
- [148] CMS Collaboration, Search for new physics in high mass diphoton events in proton-proton collisions at 13TeV . <http://cms-results.web.cern.ch/cms-results/public-results/preliminary-results/EXO-15-004/> .
- [149] L. Landau. *Dokl. Akad. Nauk Ser. Fizika* **60**, (1948) 207-209.
- [150] C.-N. Yang. *Phys. Rev.* **D77**, (1950) 242.
- [151] S. Di Chiara, L. Marzola, and M. Raidal. First interpretation of the 750 GeV diphoton resonance at the LHC. *Phys. Rev.* **D93**, (2016) 095018.
- [152] A. Pilaftsis. Diphoton Signatures from Heavy Axion Decays at the CERN Large Hadron Collider. *Phys. Rev.* **D93**, (2016) 015017.
- [153] S. Knapen, T. Melia, M. Papucci, and K. Zurek. Rays of light from the LHC. *Phys. Rev.* **D93**, (2016) 075020.
- [154] M. Backovic, A. Mariotti, and D. Redigolo. Di-photon excess illuminates Dark Matter. *JHEP* **03**, (2016) 157.
- [155] E. Molinaro, F. Sannino, and N. Vignaroli. Minimal Composite Dynamics versus Axion Origin of the Diphoton excess. *Mod. Phys. Lett.* **A31**, (2016) 1650155.
- [156] R. S. Gupta, S. Jger, Y. Kats, G. Perez, and E. Stamou. Interpreting a 750 GeV Diphoton Resonance. *JHEP* **07**, (2016) 145.

- [157] J. Ellis, S. A. R. Ellis, J. Quevillon, V. Sanz, and T. You. On the Interpretation of a Possible ~ 750 GeV Particle Decaying into $\gamma\gamma$. *JHEP* **03**, (2016) 176.
- [158] T. Higaki, K. S. Jeong, N. Kitajima, and F. Takahashi. The QCD Axion from Aligned Axions and Diphoton Excess. *Phys. Lett.* **B755**, (2016) 13-16.
- [159] Y. Mambrini, G. Arcadi, and A. Djouadi. The LHC diphoton resonance and dark matter. *Phys. Lett.* **B755**, (2016) 426-432.
- [160] D. Buttazzo, A. Greljo, and D. Marzocca. Knocking on new physics door with a scalar resonance. *Eur. Phys. J.* **C76**, (2016) 116.
- [161] R. Franceschini, G. F. Giudice, J. F. Kamenik, M. McCullough, A. Pomarol, R. Rattazzi, M. Redi, F. Riva, A. Strumia, and R. Torre. What is the $\gamma\gamma$ resonance at 750 GeV? *JHEP* **03**, (2016) 144.
- [162] A. Angelescu, A. Djouadi, and G. Moreau. Scenarii for interpretations of the LHC diphoton excess: Two Higgs doublets and vector-like quarks and leptons. *Phys. Lett.* **B756**, (2016) 126-132.
- [163] B. Bellazzini, R. Franceschini, F. Sala, and J. Serra. Goldstones in Diphotons. *JHEP* **04**, (2016) 072.
- [164] S. D. McDermott, P. Meade, and H. Ramani. Singlet Scalar Resonances and the Diphoton Excess. *Phys. Lett.* **B755**, (2016) 353-357.
- [165] M. Low, A. Tesi, and L.-T. Wang. A pseudoscalar decaying to photon pairs in the early LHC Run 2 data. *JHEP* **03**, (2016) 108.
- [166] C. Petersson and R. Torre. 750 GeV Diphoton Excess from the Goldstino Superpartner. *Phys. Rev. Lett.* **116**, (2016) 151804.

- [167] Q.-H. Cao, Y. Liu, K.-P. Xie, B. Yan, and D.-M. Zhang. A Boost Test of Anomalous Diphoton Resonance at the LHC. *arXiv* 1512.05542.
- [168] A. Kobakhidze, F. Wang, L. Wu, J. M. Yang, and M. Zhang. 750 GeV diphoton resonance in a top and bottom seesaw model. *Phys. Lett.* **B757**, (2016) 92-96.
- [169] P. Agrawal, J. Fan, B. Heidenreich, M. Reece, and M. Strassler. Experimental Considerations Motivated by the Diphoton Excess at the LHC. *JHEP* **06**, (2016) 082.
- [170] W. Chao, R. Huo, and J.-H. Yu. The minimal scalar-vectorlike top interpretation of the diphoton excess. *Eur. Phys. J. Plus* **132**, (2017) 27.
- [171] S. Fichtel, G. von Gersdorff, and C. Royon. Scattering light by light at 750 GeV at the LHC. *Phys. Rev.* **D93**, (2016) 075031.
- [172] D. Curtin and C. B. Verhaaren. Quirky Explanations for the Diphoton Excess. *Phys. Rev.* **D93**, (2016) 055011.
- [173] C. Csaki, J. Hubisz, and J. Terning. Minimal model of a diphoton resonance: Production without gluon couplings. *Phys. Rev.* **D93**, (2016) 035002.
- [174] D. Aloni, K. Blum, A. Dery, A. Efrati, and Y. Nir. On a possible large width 750 GeV diphoton resonance at ATLAS and CMS. *JHEP* **08**, (2016) 017.
- [175] S. V. Demidov and D. S. Gorbunov. On sgoldstino interpretation of the diphoton excess. *JETP Lett.* **103**, (2016) 219-222. [Pisma Zh. Eksp. Teor. Fiz.103,no.4,241(2016)].

- [176] J. M. No, V. Sanz, and J. Setford. See-saw composite Higgs model at the LHC: Linking naturalness to the 750 GeV diphoton resonance. *Phys. Rev.* **D93**, (2016) 095010.
- [177] Y. Bai, J. Berger, and R. Lu. 750 GeV dark pion: Cousin of a dark G -parity odd WIMP. *Phys. Rev.* **D93**, (2016) 076009.
- [178] S. Matsuzaki and K. Yamawaki. 750 GeV Diphoton Signal from One-Family Walking Technipion. *Mod. Phys. Lett.* **A31**, (2016) 1630016.
- [179] B. Dutta, Y. Gao, T. Ghosh, I. Gogoladze, and T. Li. Interpretation of the diphoton excess at CMS and ATLAS. *Phys. Rev.* **D93**, (2016) 055032.
- [180] D. Beirevi, E. Bertuzzo, O. Sumensari, and R. Zukanovich Funchal. Can the new resonance at LHC be a CP-Odd Higgs boson? *Phys. Lett.* **B757**, (2016) 261-267.
- [181] P. Cox, A. D. Medina, T. S. Ray, and A. Spray. Implications of diphoton searches for a Radion in the Bulk-Higgs Scenario. *Int. J. Mod. Phys.* **A32**, (2017) 1750020.
- [182] R. Martinez, F. Ochoa, and C. F. Sierra. Diphoton decay for a 750 GeV scalar boson in a $U(1)_X$ model. *Nucl. Phys.* **B913**, (2016) 64-78.
- [183] L. Bian, N. Chen, D. Liu, and J. Shu. Hidden confining world on the 750 GeV diphoton excess. *Phys. Rev.* **D93**, (2016) 095011.
- [184] J. Chakraborty, A. Choudhury, P. Ghosh, S. Mondal, and T. Srivastava. Di-photon resonance around 750 GeV: shedding light on the theory underneath. *arXiv*: 1512.05767.

- [185] A. Ahmed, B. M. Dillon, B. Grzadkowski, J. F. Gunion, and Y. Jiang. Implications of the absence of high-mass radion signals. *Phys. Rev.* **D95**, (2017) 095019.
- [186] F. F. Deppisch, C. Hati, S. Patra, P. Pritimita, and U. Sarkar. Implications of the diphoton excess on leftright models and gauge unification. *Phys. Lett.* **B757**, (2016) 223-230.
- [187] A. E. Carcamo Hernandez, I. de Medeiros Varzielas, and E. Schumacher. The 750 GeV diphoton resonance in the light of a 2HDM with S_3 flavour symmetry. *arXiv*: 1601.00661.
- [188] B. Dutta, Y. Gao, T. Ghosh, I. Gogoladze, T. Li, Q. Shafi, and J. W. Walker. Diphoton Excess in Consistent Supersymmetric SU(5) Models with Vector-like Particles. *arXiv*: 1601.00866.
- [189] T. Modak, S. Sadhukhan, and R. Srivastava. 750 GeV diphoton excess from gauged BL symmetry. *Phys. Lett.* **B756**, (2016) 405-412.
- [190] U. Danielsson, R. Enberg, G. Ingelman, and T. Mandal. Heavy photophilic scalar at the LHC from a varying electromagnetic coupling. *Nucl. Phys.* **B919**, (2017) 569-582.
- [191] W. Chao. The Diphoton Excess from an Exceptional Supersymmetric Standard Model. *arXiv* 1601.00633.
- [192] C. Csaki, J. Hubisz, S. Lombardo, and J. Terning. Gluon versus photon production of a 750 GeV diphoton resonance. *Phys. Rev.* **D93**, (2016) 095020.
- [193] A. Karozas, S. F. King, G. K. Leontaris, and A. K. Meadowcroft. 750 GeV diphoton excess from E_6 in F-theory GUTs. *Phys. Lett.* **B757**, (2016) 73-78.

- [194] K. Ghorbani and H. Ghorbani. The 750 GeV Diphoton Excess from a Pseudoscalar in Fermionic Dark Matter Scenario. *arXiv* 1601.00602.
- [195] X.-F. Han, L. Wang, L. Wu, J. M. Yang, and M. Zhang. Explaining 750 GeV diphoton excess from top/bottom partner cascade decay in two-Higgs-doublet model extension. *Phys. Lett.* **B756**, (2016) 309-316.
- [196] P. Ko, Y. Omura, and C. Yu. Diphoton Excess at 750 GeV in leptophobic $U(1)'$ model inspired by E_6 GUT. *JHEP* **04**, (2016) 098.
- [197] T. Nomura and H. Okada. Four-loop Neutrino Model Inspired by Diphoton Excess at 750 GeV. *Phys. Lett.* **B755**, (2016) 306-311.
- [198] E. Ma. Diphoton Revelation of the Utilitarian Supersymmetric Standard Model. *arXiv* 1512.09159.
- [199] E. Palti. Vector-Like Exotics in F-Theory and 750 GeV Diphotons. *Nucl. Phys.* **B907**, (2016) 597-616.
- [200] C. T. Potter. Pseudoscalar Gluinonia to 750 GeV LHC Diphotons. *arXiv* 1601.00240.
- [201] S. Jung, J. Song, and Y. W. Yoon. How Resonance-Continuum Interference Changes 750 GeV Diphoton Excess: Signal Enhancement and Peak Shift. *JHEP* **05**, (2016) 009.
- [202] L. Marzola, A. Racioppi, M. Raidal, F. R. Urban, and H. Veerme. Non-minimal CW inflation, electroweak symmetry breaking and the 750 GeV anomaly. *JHEP* **03**, (2016) 190.
- [203] A. Falkowski, O. Slone, and T. Volansky. Phenomenology of a 750 GeV Singlet. *JHEP* **02**, (2016) 152.

- [204] Y. Nakai, R. Sato, and K. Tobioka. Footprints of New Strong Dynamics via Anomaly and the 750 GeV Diphoton. *Phys. Rev. Lett.* **116**, (2016) 151802.
- [205] K. Harigaya and Y. Nomura. Composite Models for the 750 GeV Diphoton Excess. *Phys. Lett.* **B754**, (2016) 151-156.
- [206] U. Ellwanger and M. Rodriguez-Vazquez. Discovery Prospects of a Light Scalar in the NMSSM. *JHEP* **02**, (2016) 096.
- [207] D. Palle. On the possible new 750 GeV heavy boson resonance at the LHC. *arXiv* 1601.00618.
- [208] A. Dasgupta, M. Mitra, and D. Borah. Minimal Left-Right Symmetry Confronted with the 750 GeV Di-photon Excess at LHC. *arXiv* 1512.09202.
- [209] N. Bizot, S. Davidson, M. Frigerio, and J. L. Kneur. Two Higgs doublets to explain the excesses $pp \rightarrow \gamma\gamma(750 \text{ GeV})$ and $h \rightarrow \tau^\pm \mu^\mp$. *JHEP* **03**, (2016) 073.
- [210] F. Goertz, J. F. Kamenik, A. Katz, and M. Nardecchia. Indirect Constraints on the Scalar Di-Photon Resonance at the LHC. *JHEP* **05**, (2016) 187.
- [211] J. E. Kim. Is an axizilla possible for di-photon resonance? *Phys. Lett.* **B755**, (2016) 190-195.
- [212] N. Craig, P. Draper, C. Kilic, and S. Thomas. Shedding Light on Diphoton Resonances. *Phys. Rev.* **D93**, (2016) 115023.
- [213] K. Cheung, P. Ko, J. S. Lee, J. Park, and P.-Y. Tseng. Higgs precision study of the 750 GeV diphoton resonance and the 125 GeV standard model Higgs boson with Higgs-singlet mixing. *Phys. Rev.* **D94**, (2016) 033010.

- [214] B. C. Allanach, P. S. B. Dev, S. A. Renner, and K. Sakurai. 750 GeV diphoton excess explained by a resonant sneutrino in R-parity violating supersymmetry. *Phys. Rev.* **D93**, (2016) 115022.
- [215] W. Altmannshofer, J. Galloway, S. Gori, A. L. Kagan, A. Martin, and J. Zupan. 750 GeV diphoton excess. *Phys. Rev.* **D93**, (2016) 095015.
- [216] W.-C. Huang, Y.-L. S. Tsai, and T.-C. Yuan. Gauged Two Higgs Doublet Model confronts the LHC 750 GeV diphoton anomaly. *Nucl. Phys.* **B909**, (2016) 122-134.
- [217] A. Belyaev, G. Cacciapaglia, H. Cai, T. Flacke, A. Parolini, and H. Serdio. Singlets in composite Higgs models in light of the LHC 750 GeV diphoton excess. *Phys. Rev.* **D94**, (2016) 015004.
- [218] W. Liao and H.-q. Zheng. Scalar resonance at 750 GeV as composite of heavy vector-like fermions. *Commun. Theor. Phys.* **66**, (2016) 219-223.
- [219] J. Chang, K. Cheung, and C.-T. Lu. Interpreting the 750 GeV diphoton resonance using photon jets in hidden-valley-like models. *Phys. Rev.* **D93**, (2016) 075013.
- [220] M.-x. Luo, K. Wang, T. Xu, L. Zhang, and G. Zhu. Squarkonium, diquarkonium, and octetonium at the LHC and their diphoton decays. *Phys. Rev.* **D93**, (2016) 055042.
- [221] K. Kaneta, S. Kang, and H.-S. Lee. Diphoton channel at the LHC experiments to find a hint for a new heavy gauge boson. *Int. J. Mod. Phys.* **A31**, (2016) 1650159.
- [222] A. E. Crcamo Hernandez. A novel and economical explanation for SM fermion masses and mixings. *Eur. Phys. J.* **C76**, (2016) 503.

- [223] I. Low and J. Lykken. Implications of Gauge Invariance on a Heavy Diphoton Resonance. *arXiv* 1512.09089.
- [224] P. V. Dong and N. T. K. Ngan. Phenomenology of the simple 3-3-1 model with inert scalars. *arXiv* 1512.09073.
- [225] S. Kanemura, N. Machida, S. Odori, and T. Shindou. Diphoton excess at 750 GeV in an extended scalar sector. *arXiv* 1512.09053.
- [226] S. Kanemura, K. Nishiwaki, H. Okada, Y. Orikasa, S. C. Park, and R. Watanabe. LHC 750 GeV diphoton excess in a radiative seesaw model. *PTEP* **2016**, (2016) 123B04.
- [227] S. K. Kang and J. Song. Top-phobic heavy Higgs boson as the 750 GeV diphoton resonance. *Phys. Rev.* **D93**, (2016) 115012.
- [228] C.-W. Chiang, M. Ibe, and T. T. Yanagida. Revisiting Scalar Quark Hidden Sector in Light of 750-GeV Diphoton Resonance. *JHEP* **05**, (2016) 084.
- [229] L. E. Ibanez and V. Martin-Lozano. A Megaxion at 750 GeV as a First Hint of Low Scale String Theory. *JHEP* **07**, (2016) 021.
- [230] X.-J. Huang, W.-H. Zhang, and Y.-F. Zhou. A 750 GeV dark matter messenger at the Galactic Center. *Phys. Rev.* **D93**, (2016) 115006.
- [231] Y. Hamada, T. Noumi, S. Sun, and G. Shiu. An O(750) GeV Resonance and Inflation. *Phys. Rev.* **D93**, (2016) 123514.
- [232] L. A. Anchordoqui, I. Antoniadis, H. Goldberg, X. Huang, D. Lust, and T. R. Taylor. 750 GeV diphotons from closed string states. *Phys. Lett.* **B755**, (2016) 312-315.

- [233] X.-J. Bi, R. Ding, Y. Fan, L. Huang, C. Li, T. Li, S. Raza, X.-C. Wang, and B. Zhu. A Promising Interpretation of Diphoton Resonance at 750 GeV. *Phys. Rev.* **D94**, (2016) 015012.
- [234] W. Chao. Neutrino Catalyzed Diphoton Excess. *Nucl. Phys.* **B911**, (2016) 231-245.
- [235] C. Cai, Z.-H. Yu, and H.-H. Zhang. 750 GeV diphoton resonance as a singlet scalar in an extra dimensional model. *Phys. Rev.* **D93**, (2016) 075033.
- [236] J. Cao, L. Shang, W. Su, F. Wang, and Y. Zhang. Interpreting The 750 GeV Diphoton Excess Within Topflavor Seesaw Model. *Nucl. Phys.* **B911**, (2016) 447-470.
- [237] Y.-L. Tang and S.-h. Zhu. NMSSM extended with vectorlike particles and the diphoton excess at the LHC. *Phys. Rev.* **D94**, (2016) 035010.
- [238] P. S. B. Dev, R. N. Mohapatra, and Y. Zhang. Quark Seesaw, Vectorlike Fermions and Diphoton Excess. *JHEP* **02**, (2016) 186.
- [239] J. Gao, H. Zhang, and H. X. Zhu. Diphoton excess at 750 GeV: gluon-gluon fusion or quark-antiquark annihilation? *Eur. Phys. J.* **C76**, (2016) 348.
- [240] Q.-H. Cao, Y. Liu, K.-P. Xie, B. Yan, and D.-M. Zhang. Diphoton excess, low energy theorem, and the 331 model. *Phys. Rev.* **D93**, (2016) 075030.
- [241] F. Wang, W. Wang, L. Wu, J. M. Yang, and M. Zhang. Interpreting 750 GeV diphoton resonance as degenerate Higgs bosons in NMSSM with vector-like particles. *arXiv* 1512.08434.
- [242] H. An, C. Cheung, and Y. Zhang. Broad Diphotons from Narrow States. *arXiv* 1512.08378.

- [243] M. Son and A. Urbano. A new scalar resonance at 750 GeV: Towards a proof of concept in favor of strongly interacting theories. *JHEP* **05**, (2016) 181.
- [244] G. Li, Y.-n. Mao, Y.-L. Tang, C. Zhang, Y. Zhou, and S.-h. Zhu. Pseudoscalar Decaying Only via Loops as an Explanation for the 750 GeV Diphoton Excess. *Phys. Rev. Lett.* **116**, (2016) 151803.
- [245] A. Salvio and A. Mazumdar. Higgs Stability and the 750 GeV Diphoton Excess. *Phys. Lett.* **B755**, (2016) 469-474.
- [246] J.-C. Park and S. C. Park. Indirect signature of dark matter with the diphoton resonance at 750 GeV. *Phys. Dark Univ.* **14**, (2016) 4-10.
- [247] H. Han, S. Wang, and S. Zheng. Dark Matter Theories in the Light of Diphoton Excess. *arXiv* 1512.07992.
- [248] L. J. Hall, K. Harigaya, and Y. Nomura. 750 GeV Diphotons: Implications for Supersymmetric Unification. *JHEP* **03**, (2016) 017.
- [249] J. A. Casas, J. R. Espinosa, and J. M. Moreno. The 750 GeV Diphoton Excess as a First Light on Supersymmetry Breaking. *Phys. Lett.* **B759**, (2016) 159-165.
- [250] J. Zhang and S. Zhou. Electroweak Vacuum Stability and Diphoton Excess at 750 GeV. *Chin. Phys.* **C40**, (2016) 081001.
- [251] J. Liu, X.-P. Wang, and W. Xue. LHC diphoton excess from colorful resonances. *arXiv* 1512.07885.
- [252] K. Das and S. K. Rai. 750 GeV diphoton excess in a U(1) hidden symmetry model. *Phys. Rev.* **D93**, (2016) 095007.

- [253] H. Davoudiasl and C. Zhang. 750 GeV messenger of dark conformal symmetry breaking. *Phys. Rev.* **D93**, (2016) 055006.
- [254] M. Cveti, J. Halverson, and P. Langacker. String Consistency, Heavy Exotics, and the 750 GeV Diphoton Excess at the LHC. *Fortsch. Phys.* **64**, (2016) 748-782.
- [255] S. Chakraborty, A. Chakraborty, and S. Raychaudhuri. Diphoton resonance at 750 GeV in the broken R -symmetric MSSM. *Phys. Rev.* **D94**, (2016) 035014.
- [256] M. Badziak. Interpreting the 750 GeV diphoton excess in minimal extensions of Two-Higgs-Doublet models. *Phys. Lett.* **B759**, (2016) 464-470.
- [257] K. M. Patel and P. Sharma. Interpreting 750 GeV diphoton excess in SU(5) grand unified theory. *Phys. Lett.* **B757**, (2016) 282-288.
- [258] S. Moretti and K. Yagyu. 750 GeV diphoton excess and its explanation in two-Higgs-doublet models with a real inert scalar multiplet. *Phys. Rev.* **D93**, (2016) 055043.
- [259] J. Gu and Z. Liu. Physics implications of the diphoton excess from the perspective of renormalization group flow. *Phys. Rev.* **D93**, (2016) 075006.
- [260] Q.-H. Cao, S.-L. Chen, and P.-H. Gu. Strong CP Problem, Neutrino Masses and the 750 GeV Diphoton Resonance. *arXiv* 1512.07541.
- [261] G. M. Pelaggi, A. Strumia, and E. Vigiani. Trinification can explain the di-photon and di-boson LHC anomalies. *JHEP* **03**, (2016) 025.
- [262] U. K. Dey, S. Mohanty, and G. Tomar. 750 GeV resonance in the dark leftright model. *Phys. Lett.* **B756**, (2016) 384-389.

- [263] A. E. C. Hernandez and I. Niandi. LHC diphoton resonance at 750 GeV as an indication of $SU(3)_L \times U(1)_X$ electroweak symmetry. *Eur. Phys. J.* **C76**, (2016) 380.
- [264] C. W. Murphy. Vector Leptoquarks and the 750 GeV Diphoton Resonance at the LHC. *Phys. Lett.* **B757**, (2016) 192-198.
- [265] J. de Blas, J. Santiago, and R. Vega-Morales. New vector bosons and the diphoton excess. *Phys. Lett.* **B759**, (2016) 247-252.
- [266] P. S. B. Dev and D. Teresi. Asymmetric dark matter in the Sun and diphoton excess at the LHC. *Phys. Rev.* **D94**, (2016) 025001.
- [267] S. M. Boucenna, S. Morisi, and A. Vicente. The LHC diphoton resonance from gauge symmetry. *Phys. Rev.* **D93**, (2016) 115008.
- [268] K. Kulkarni. Extension of ν MSM model and possible explanations of recent astronomical and collider observations. *arXiv* 1512.06836.
- [269] M. Chala, M. Duerr, F. Kahlhoefer, and K. Schmidt-Hoberg. Tricking LandauYang: How to obtain the diphoton excess from a vector resonance. *Phys. Lett.* **B755**, (2016) 145-149.
- [270] M. Bauer and M. Neubert. Flavor anomalies, the 750 GeV diphoton excess, and a dark matter candidate. *Phys. Rev.* **D93**, (2016) 115030.
- [271] J. M. Cline and Z. Liu. LHC diphotons from electroweakly pair-produced composite pseudoscalars. *arXiv* 1512.06827.
- [272] L. Berthier, J. M. Cline, W. Shepherd, and M. Trott. Effective interpretations of a diphoton excess. *JHEP* **04**, (2016) 084.

- [273] J. S. Kim, K. Rolbiecki, and R. Ruiz de Austri. Model-independent combination of diphoton constraints at 750 GeV. *Eur. Phys. J.* **C76**, (2016) 251.
- [274] X.-J. Bi, Q.-F. Xiang, P.-F. Yin, and Z.-H. Yu. The 750 GeV diphoton excess at the LHC and dark matter constraints. *Nucl. Phys.* **B909**, (2016) 43-64.
- [275] J. J. Heckman. 750 GeV Diphotons from a D3-brane. *Nucl. Phys.* **B906**, (2016) 231-240.
- [276] F. P. Huang, C. S. Li, Z. L. Liu, and Y. Wang. Diphoton and dark matter from cascade decay. *Phys. Rev.* **D94**, (2016) 055025.
- [277] J. Cao, C. Han, L. Shang, W. Su, J. M. Yang, and Y. Zhang. Interpreting the 750 GeV diphoton excess by the singlet extension of the ManoharWise model. *Phys. Lett.* **B755**, (2016) 456-463.
- [278] F. Wang, L. Wu, J. M. Yang, and M. Zhang. 750 GeV diphoton resonance, 125 GeV Higgs and muon $g - 2$ anomaly in deflected anomaly mediation SUSY breaking scenarios. *Phys. Lett.* **B759**, (2016) 191-199.
- [279] O. Antipin, M. Mojaza, and F. Sannino. Minimal Coleman-Weinberg theory explains the diphoton excess. *Phys. Rev.* **D93**, (2016) 115007.
- [280] X.-F. Han and L. Wang. Implication of the 750 GeV diphoton resonance on two-Higgs-doublet model and its extensions with Higgs field. *Phys. Rev.* **D93**, (2016) 055027.
- [281] R. Ding, L. Huang, T. Li, and B. Zhu. Interpreting 750 GeV diphoton excess with R -parity violating supersymmetry. *Int. J. Mod. Phys.* **A32**, (2017) 1750014.

- [282] I. Chakraborty and A. Kundu. Diphoton excess at 750 GeV: Singlet scalars confront triviality. *Phys. Rev.* **D93**, (2016) 055003.
- [283] D. Barducci, A. Goudelis, S. Kulkarni, and D. Sengupta. One jet to rule them all: monojet constraints and invisible decays of a 750 GeV diphoton resonance. *JHEP* **05**, (2016) 154.
- [284] W. S. Cho, D. Kim, K. Kong, S. H. Lim, K. T. Matchev, J.-C. Park, and M. Park. 750 GeV Diphoton Excess May Not Imply a 750 GeV Resonance. *Phys. Rev. Lett.* **116**, (2016) 151805.
- [285] T.-F. Feng, X.-Q. Li, H.-B. Zhang, and S.-M. Zhao. The LHC 750 GeV diphoton excess in supersymmetry with gauged baryon and lepton numbers .
- [286] D. Bardhan, D. Bhatia, A. Chakraborty, U. Maitra, S. Raychaudhuri, and T. Samui. Radion Candidate for the LHC Diphoton Resonance. *arXiv* 1512.06674.
- [287] H. Han, S. Wang, and S. Zheng. Scalar Explanation of Diphoton Excess at LHC. *Nucl. Phys.* **B907**, (2016) 180-186.
- [288] M. Dhuria and G. Goswami. Perturbativity, vacuum stability, and inflation in the light of 750 GeV diphoton excess. *Phys. Rev.* **D94**, (2016) 055009.
- [289] S. Chang. A Simple $U(1)$ Gauge Theory Explanation of the Diphoton Excess. *Phys. Rev.* **D93**, (2016) 055016.
- [290] C. Han, H. M. Lee, M. Park, and V. Sanz. The diphoton resonance as a gravity mediator of dark matter. *Phys. Lett.* **B755**, (2016) 371-379.
- [291] M. T. Arun and P. Saha. Gravitons in multiply warped scenarios: At 750 GeV and beyond. *Pramana* **88**, (2017) 93.

- [292] W. Chao. Symmetries behind the 750 GeV diphoton excess. *Phys. Rev.* **D93**, (2016) 115013.
- [293] J. Bernon and C. Smith. Could the width of the diphoton anomaly signal a three-body decay? *Phys. Lett.* **B757**, (2016) 148-153.
- [294] L. M. Carpenter, R. Colburn, and J. Goodman. Supersoft SUSY models and the 750 GeV diphoton excess, beyond effective operators. *Phys. Rev.* **D94**, (2016) 015016.
- [295] E. Megias, O. Pujolas, and M. Quiros. On dilatons and the LHC diphoton excess. *JHEP* **05**, (2016) 137.
- [296] A. Alves, A. G. Dias, and K. Sinha. The 750 GeV S -cion: Where else should we look for it? *Phys. Lett.* **B757**, (2016) 39-46.
- [297] E. Gabrielli, K. Kannike, B. Mele, M. Raidal, C. Spethmann, and H. Veerme. A SUSY Inspired Simplified Model for the 750 GeV Diphoton Excess. *Phys. Lett.* **B756**, (2016) 36-41.
- [298] J. S. Kim, J. Reuter, K. Rolbiecki, and R. Ruiz de Austri. A resonance without resonance: scrutinizing the diphoton excess at 750 GeV. *Phys. Lett.* **B755**, (2016) 403-408.
- [299] R. Benbrik, C.-H. Chen, and T. Nomura. Higgs singlet boson as a diphoton resonance in a vectorlike quark model. *Phys. Rev.* **D93**, (2016) 055034.
- [300] Y. Jiang, Y.-Y. Li, and T. Liu. 750 GeV resonance in the gauged $U(1)'$ -extended MSSM. *Phys. Lett.* **B759**, (2016) 354-360.
- [301] The ATLAS collaboration, Measurements of the total cross sections for Higgs boson production combining the $H \rightarrow \gamma\gamma$ and $H \rightarrow ZZ^* \rightarrow 4\ell$ decay channels at 7, 8 and 13 TeV center-of-mass energies with the ATLAS detector.

<https://atlas.web.cern.ch/Atlas/GROUPS/PHYSICS/CONFNOTES/ATLAS-CONF-2015-069/> .

- [302] A. Djouadi. The Anatomy of electro-weak symmetry breaking. I: The Higgs boson in the standard model. *Phys. Rept.* **457**, (2008) 1-216.
- [303] X. G. He, G. C. Joshi, H. Lew, and R. R. Volkas. NEW Z-prime PHENOMENOLOGY. *Phys. Rev.* **D43**, (1991) 22-24.
- [304] X.-g. He. A Light Z-prime boson. In The Albuquerque meeting. Proceedings, 8th Meeting, Division of Particles and Fields of the American Physical Society, Albuquerque, USA, August 2-6, 1994. Vol. 1,2. 1994 1149–1152.
- [305] S. Baek, N. G. Deshpande, X. G. He, and P. Ko. Muon anomalous $g-2$ and gauged $L(\text{muon}) - L(\text{tau})$ models. *Phys. Rev.* **D64**, (2001) 055006.
- [306] W. Altmannshofer, M. Carena, and A. Crivellin. $L_\mu - L_\tau$ theory of Higgs flavor violation and $(g - 2)_\mu$. *Phys. Rev.* **D94**, (2016) 095026.
- [307] W. Altmannshofer, S. Gori, M. Pospelov, and I. Yavin. Quark flavor transitions in $L_\mu - L_\tau$ models. *Phys. Rev.* **D89**, (2014) 095033.
- [308] J. Heeck. Lepton flavor violation with light vector bosons. *Phys. Lett.* **B758**, (2016) 101-105.
- [309] K. Fuyuto, W.-S. Hou, and M. Kohda. Z -induced FCNC decays of top, beauty, and strange quarks. *Phys. Rev.* **D93**, (2016) 054021.
- [310] A. Crivellin, G. D’Ambrosio, and J. Heeck. Addressing the LHC flavor anomalies with horizontal gauge symmetries. *Phys. Rev.* **D91**, (2015) 075006.

- [311] A. Crivellin, G. D'Ambrosio, and J. Heeck. Explaining $h \rightarrow \mu^\pm \tau^\mp$, $B \rightarrow K^* \mu^+ \mu^-$ and $B \rightarrow K \mu^+ \mu^- / B \rightarrow K e^+ e^-$ in a two-Higgs-doublet model with gauged $L_\mu - L_\tau$. *Phys. Rev. Lett.* **114**, (2015) 151801.
- [312] J. Heeck, M. Holthausen, W. Rodejohann, and Y. Shimizu. Higgs in Abelian and non-Abelian flavor symmetry models. *Nucl. Phys.* **B896**, (2015) 281-310.
- [313] E. Ma and D. P. Roy. Anomalous neutrino interaction, muon $g-2$, and atomic parity nonconservation. *Phys. Rev.* **D65**, (2002) 075021.
- [314] K. Harigaya, T. Igari, M. M. Nojiri, M. Takeuchi, and K. Tobe. Muon $g-2$ and LHC phenomenology in the $L_\mu - L_\tau$ gauge symmetric model. *JHEP* **03**, (2014) 105.
- [315] F. Elahi and A. Martin. Constraints on $L_\mu - L_\tau$ interactions at the LHC and beyond. *Phys. Rev.* **D93**, (2016) 015022.
- [316] E. Ma, D. P. Roy, and S. Roy. Gauged $L(\mu) - L(\tau)$ with large muon anomalous magnetic moment and the bimaximal mixing of neutrinos. *Phys. Lett.* **B525**, (2002) 101-106.
- [317] J. Heeck and W. Rodejohann. Gauged $L_\mu - L_\tau$ Symmetry at the Electroweak Scale. *Phys. Rev.* **D84**, (2011) 075007.
- [318] J. Heeck and W. Rodejohann. Neutrino Phenomenology of gauged $L_\mu - L_\tau$: MINOS and beyond. *AIP Conf. Proc.* **1382**, (2011) 144-146.
- [319] J. Heeck and W. Rodejohann. Gauged $L_\mu - L_\tau$ and different Muon Neutrino and Anti-Neutrino Oscillations: MINOS and beyond. *J. Phys.* **G38**, (2011) 085005.

- [320] T. Ota and W. Rodejohann. Breaking of $L(\mu) - L(\tau)$ Flavor Symmetry, Lepton Flavor Violation and Leptogenesis. *Phys. Lett.* **B639**, (2006) 322-331.
- [321] W. Rodejohann and M. A. Schmidt. Flavor symmetry $L(\mu) - L(\tau)$ and quasi-degenerate neutrinos. *Phys. Atom. Nucl.* **69**, (2006) 1833-1841.
- [322] Z.-z. Xing and Z.-h. Zhao. A review of $\mu - \tau$ flavor symmetry in neutrino physics. *Rept. Prog. Phys.* **79**, (2016) 076201.
- [323] D. C. Rivera-Agudelo and A. Prez-Lorenzana. Leptonic CP phases near the $\mu - \tau$ symmetric limit. *Phys. Lett.* **B760**, (2016) 153-157.
- [324] S. Choubey and W. Rodejohann. A Flavor symmetry for quasi-degenerate neutrinos: $L(\mu) - L(\tau)$. *Eur. Phys. J.* **C40**, (2005) 259-268.
- [325] X.-G. He, G. C. Joshi, H. Lew, and R. R. Volkas. Simplest Z' -prime model. *Phys. Rev.* **D44**, (1991) 2118-2132.
- [326] T. Araki, F. Kaneko, T. Ota, J. Sato, and T. Shimomura. MeV scale leptonic force for cosmic neutrino spectrum and muon anomalous magnetic moment. *Phys. Rev.* **D93**, (2016) 013014.
- [327] E. Salvioni, A. Strumia, G. Villadoro, and F. Zwirner. Non-universal minimal Z' models: present bounds and early LHC reach. *JHEP* **03**, (2010) 010.
- [328] B. Adhikary. Soft breaking of $L(\mu) - L(\tau)$ symmetry: Light neutrino spectrum and Leptogenesis. *Phys. Rev.* **D74**, (2006) 033002.
- [329] N. F. Bell and R. R. Volkas. Bottom up model for maximal muon-neutrino - tau-neutrino mixing. *Phys. Rev.* **D63**, (2001) 013006.

- [330] K. Fuki and M. Yasue. Two Categories of Approximately mu-tau Symmetric Neutrino Mass Textures. *Nucl. Phys.* **B783**, (2007) 31-56.
- [331] S. Baek, H. Okada, and K. Yagyu. Flavour Dependent Gauged Radiative Neutrino Mass Model. *JHEP* **04**, (2015) 049.
- [332] P.-f. Yin, J. Liu, and S.-h. Zhu. Detecting light leptophilic gauge boson at BESIII detector. *Phys. Lett.* **B679**, (2009) 362-368.
- [333] X.-J. Bi, X.-G. He, and Q. Yuan. Parameters in a class of leptophilic models from PAMELA, ATIC and FERMI. *Phys. Lett.* **B678**, (2009) 168-173.
- [334] J.-C. Park, J. Kim, and S. C. Park. Galactic center GeV gamma-ray excess from dark matter with gauged lepton numbers. *Phys. Lett.* **B752**, (2016) 59-65.
- [335] S. Baek. Dark matter and muon ($g - 2$) in local $U(1)_{L_\mu-L_\tau}$ -extended Ma Model. *Phys. Lett.* **B756**, (2016) 1-5.
- [336] S. Baek and P. Ko. Phenomenology of $U(1)(L(\mu)-L(\tau))$ charged dark matter at PAMELA and colliders. *JCAP* **0910**, (2009) 011.
- [337] M. Carena, A. Daleo, B. A. Dobrescu, and T. M. P. Tait. Z' gauge bosons at the Tevatron. *Phys. Rev.* **D70**, (2004) 093009.
- [338] D. Geiregat et al. First observation of neutrino trident production. *Phys. Lett.* **B245**, (1990) 271-275.
- [339] S. R. Mishra et al. Neutrino tridents and W Z interference. *Phys. Rev. Lett.* **66**, (1991) 3117-3120.

- [340] M. Ackermann et al. Measurement of separate cosmic-ray electron and positron spectra with the Fermi Large Area Telescope. *Phys. Rev. Lett.* **108**, (2012) 011103.
- [341] M. Kawasaki, K. Kohri, and T. Moroi. Big-Bang nucleosynthesis and hadronic decay of long-lived massive particles. *Phys. Rev. D* **71**, (2005) 083502.
- [342] K. Jedamzik and M. Pospelov. Big Bang Nucleosynthesis and Particle Dark Matter. *New J. Phys.* **11**, (2009) 105028.
- [343] C. Arina, F.-X. Josse-Michaux, and N. Sahu. A Tight Connection Between Direct and Indirect Detection of Dark Matter through Higgs Portal Couplings to a Hidden Sector. *Phys. Rev. D* **82**, (2010) 015005.
- [344] M. Kaplinghat, S. Tulin, and H.-B. Yu. Direct Detection Portals for Self-interacting Dark Matter. *Phys. Rev. D* **89**, (2014) 035009.
- [345] A. Hook, E. Izaguirre, and J. G. Wacker. Model Independent Bounds on Kinetic Mixing. *Adv. High Energy Phys.* **2011**, (2011) 859762.
- [346] K. S. Babu, C. F. Kolda, and J. March-Russell. Implications of generalized Z - Z-prime mixing. *Phys. Rev. D* **57**, (1998) 6788-6792.
- [347] A. Crivellin, M. Hoferichter, and M. Procura. Accurate evaluation of hadronic uncertainties in spin-independent WIMP-nucleon scattering: Disentangling two- and three-flavor effects. *Phys. Rev. D* **89**, (2014) 054021.
- [348] M. Hoferichter, J. Ruiz de Elvira, B. Kubis, and U.-G. Meiner. High-Precision Determination of the Pion-Nucleon σ Term from Roy-Steiner Equations. *Phys. Rev. Lett.* **115**, (2015) 092301.

- [349] O. Adriani et al. PAMELA results on the cosmic-ray antiproton flux from 60 MeV to 180 GeV in kinetic energy. *Phys. Rev. Lett.* **105**, (2010) 121101.
- [350] AMS-02 Collaboration, Talks at the AMS Days at CERN, 15-17 April, 2015. <https://indico.cern.ch/event/381134/timetable/#20150415.detailed> .
- [351] G. Giesen, M. Boudaud, Y. Gnolini, V. Poulin, M. Cirelli, P. Salati, and P. D. Serpico. AMS-02 antiprotons, at last! Secondary astrophysical component and immediate implications for Dark Matter. *JCAP* **1509**, (2015) 023.
- [352] A. W. Strong, I. V. Moskalenko, and V. S. Ptuskin. Cosmic-ray propagation and interactions in the Galaxy. *Ann. Rev. Nucl. Part. Sci.* **57**, (2007) 285-327.
- [353] I. V. Moskalenko and A. W. Strong. Production and propagation of cosmic ray positrons and electrons. *Astrophys. J.* **493**, (1998) 694-707.
- [354] A. E. Vladimirov, S. W. Digel, G. Johannesson, P. F. Michelson, I. V. Moskalenko, P. L. Nolan, E. Orlando, T. A. Porter, and A. W. Strong. GALPROP WebRun: an internet-based service for calculating galactic cosmic ray propagation and associated photon emissions. *Comput. Phys. Commun.* **182**, (2011) 1156-1161.
- [355] A. V. Semenov. LanHEP: A Package for automatic generation of Feynman rules in gauge models. <http://theory.sinp.msu.ru/semenov/lanhep.html> .